Effect of Multiple Holes on Stress Concentrations and Damage Initiation in a Quasi-Isotropic Composite Laminate

by

Matthew K. Pirkle

A thesis submitted in partial fulfillment
of the requirements for the degree of
Master of Science in Engineering
(Automotive Systems Engineering)
in the University of Michigan-Dearborn
2020

Master's Thesis Committee:

Professor Pankaj K. Mallick, Chair
Associate Professor German Reyes-Villanueva
Lecturer James Boileau

DEDICATION

Dedicated to William, Lauren, and Rachel Pirkle

ACKNOWLEDGEMENTS

This work is dedicated to my family, whose love and support have seen me up to this point in my life and education.

It is with admiration that I give thanks to my father, Dr. William H. Pirkle. His career as a professor at the University of Illinois at Urbana-Champaign, and lifelong dedication to the field of organic chemistry has inspired me. At a young age I developed a great love, appreciation, and respect for science. I attribute much of this to his influence. He helped me to explore and develop my curiosity and fascination for all things mechanical. This has led me to pursue an education in engineering.

I would like to give thanks to my mother, Lauren S. Pirkle, whose career as a librarian and passion for reading helped to expose me to many wonderful and interesting topics, some of which included science. The myriad books she brought home from the Champaign Public Library kept the family consistently busy reading and learning, which was a fun and engaging experience. Her journey through education brought her two Master's degrees from the University of Illinois at Urbana-Champaign.

I would like to give thanks to my sister, Rachel Pirkle Langdon, whose interest in science led her to study cellular and molecular biology for her undergraduate degree. She went on to obtain her MBA at the University of Illinois at Urbana-Champaign, where she now works as the Director of Donor Relations and Stewardship in the Grainger College of Engineering. Her achievements in life have been inspiring. The completion of this work comes shortly after her marriage, and it is with a full heart that I look forward to the shared joy and memories that will undoubtedly fill and enrich her life.

I would like to extend my sincere gratitude to my advisor, Dr. P.K. Mallick, for the opportunity to create this work. His guidance and support of my education has helped me to develop a better mastery and deeper knowledge of engineering, which has been fulfilling. Dr. Mallick was never too busy to spend time with me discussing and explaining advanced engineering concepts, which I greatly value.

I would like to thank my committee member Dr. James Boileau, for his additional guidance and insight. The influence which was brought from his experience as an industry expert and research scientist in metallurgy at Ford was a valuable asset. His enthusiasm and interest in this thesis was very welcome, and it has been a rewarding experience to work with him.

I would like to thank my committee member Dr. German Reyes-Villanueva for his willingness to be on the committee. His background in composites, and expert knowledge therein, was a valuable addition to the group.

I would like to thank the department secretary, Sherry Boyd for her help in making sure the procedure and requisite archival deadlines for this thesis were made known to me. Her support in my awareness of the process for graduation and associated deadlines was also very welcome.

I would like to give thanks to Dr. L. Daniel Metz. I greatly value the years I have known him and his family, through which I have derived much inspiration and many fond memories. The influence from a lifelong passion for his career as both a professor at the University of Illinois at Urbana-Champaign, and practicing automotive engineer played greatly into choices I made for the direction of my education.

I would like to give thanks to all the graduate student members of my father's research group at the University of Illinois Urbana-Champaign, "The Pirkle Zoo". Some of their sporadic and often unpredictable practical jokes kept me on my toes while I passed the hours at Roger Adams Laboratory during my formative years. They were a source of motivation, and their mercurial behavior helped to show me that science could be tremendous fun, and that life should not be taken too seriously at times. Most specifically, I wish to thank Dr. Christopher J. Welch and Dr. Cody R. Cole for their friendship to our family throughout the years, and for their mentorship and inspiration.

TABLE OF CONTENTS

LIST OF FIGURES

LIST OF TABLES

ABSTRACT

The purpose of this study was to investigate the effects of multiple holes on stress concentrations in a continuous fiber reinforced quasi-isotropic laminate using a current industry standard finite element analysis software. The hole configurations included two asymmetric and two axisymmetric square holes with different corner radii and circular holes. The hole edge-to-edge distance was varied to study the effects of their proximity on stress concentration factors. The influence of stress concentrations upon damage initiation in the composite laminate was also studied using Hashin's composite failure criteria.

The stress concentration factor increases with decreasing hole-to-hole proximity. Similarly, the stress concentration factor increases with decreasing hole edge-to-laminate edge distance. Further, the stress concentration factor increases to an even greater degree when both the "hole-to-hole proximity effect" and the "edge effect" are present. As the corner radius in the square hole is increased, the stress concentration is reduced. Square holes with sufficiently rounded corners elicit lower stress concentration factors than circular holes of equivalent dimension.

Damage initiates in the general location of stress concentration regions in any given lamina, which is always found at the periphery of a hole or holes, and is independent of hole geometry. Further, damage initiates sooner for holes that are within a sufficiently close distance of one another. The severity of the "hole-to-hole proximity effect" and the "edge effect" dictate the damage initiation time.

CHAPTER 1: INTRODUCTION

An introduction to composite materials is given, followed by a background of the research topics. The research problem and objective are then established, and lastly the outline of the thesis is given.

1.1 Introduction

Composites are thought to have found their initial use in 1500 B.C., when the some of the first Egyptians and Mesopotamian settlers combined mud and straw to form a material which proved to be useful in the construction of tougher, more substantial buildings [1]. By definition, a composite is any combination of at least two chemically distinct materials, where the new material possesses properties superior to that of its constituents. The use of composites in engineering and related fields began in the 1940s, when glass fiber reinforced polymers were used in marine applications to replace traditional construction materials such as wood and metal [2]. This was due mainly to their low weight and ability to resist redox reactions (corrosion). Well recognized for their versatility, composites enjoy an increasing presence in engineering industries such as aerospace, automotive, civil, and mechanical. Tremendous variety exists in the choice of fiber and matrix, which, when coupled with the ability to alter the fiber direction and stacking sequence, allows for a tailored approach to composite design. This substantial degree of control lends itself significantly to their appeal as either an existing material substitute, or an initial design choice. Widely used in engineering industries due to superior material properties such as high strength, low density, and low coefficient of thermal expansion, it becomes of greater importance to fully understand their capabilities, and perhaps most importantly, their failure. Fiber reinforced composites benefit from high strength-to-weight ratios, high modulus-to-weight ratios, and high internal damping characteristics. The choice to use composites over their conventional metallic counterparts (e.g. steel, aluminum, cast iron, etc.) is usually governed by the constituent properties and resulting characteristics, and typically limited by material and manufacturing costs, or deficiencies which exist in the understanding of their mechanical

behavior. Mallick [3] pointed out that the effective design, process development, and subsequent implementation of composites is based upon judicious practice, and a full grasp of their attributes.

Holes are perhaps one of the most commonly used features in engineering design. The practical use of composites requires the presence of holes to enable joining via mechanical fastening hardware. Further, holes are often implemented in order to provide accessibility (which can facilitate serviceability efforts), or routing for electrical wiring. Additionally, the removal of material from components serves to reduce mass (and hence weight), which is a common practice in engineering design. Such efforts, as well as the inherent properties of composites, translate directly into greater fuel economy and higher performing systems when applied to the automotive and aerospace industries (among others). Examples of square holes in composites and other materials used in engineering industries can be seen below in Figs. 1.1 and 1.2. It is worth recognizing that in Fig. 1.2b, both the "hole-to-hole proximity effect" and the "edge effect" are of concern, as thermal stresses due to electronics and battery discharge can be present.

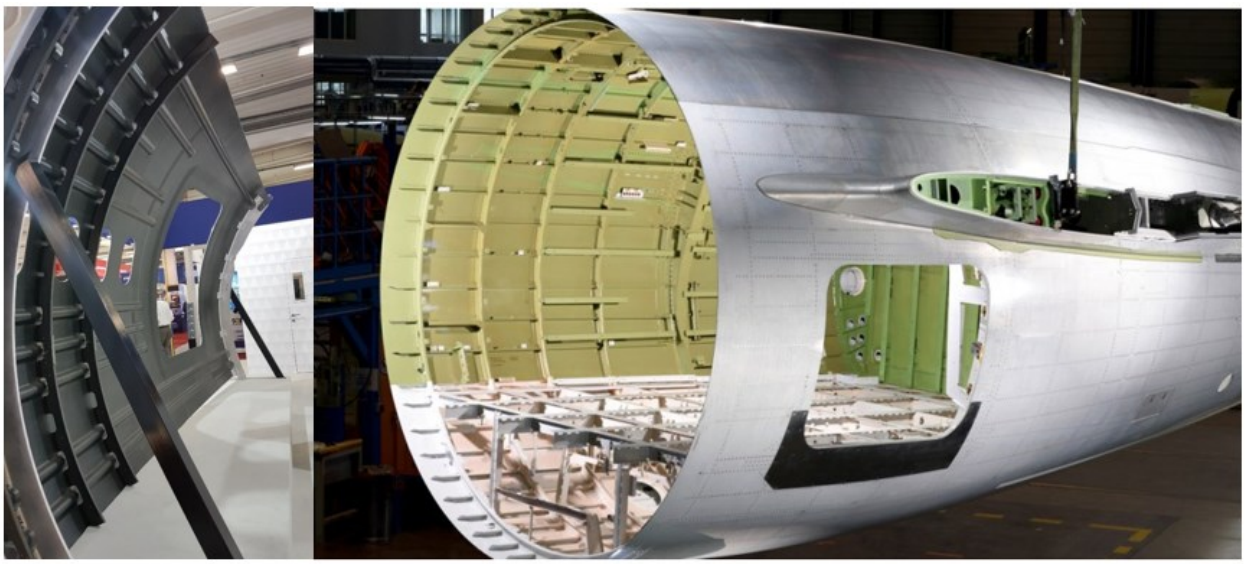

(a) (b)

Figure 1.1: Examples of square holes in aerospace engineering: (a) elongated square holes with rounded corners in a carbon fiber aircraft fuselage, (b) square hole with rounded corners in an aircraft aft fuselage.

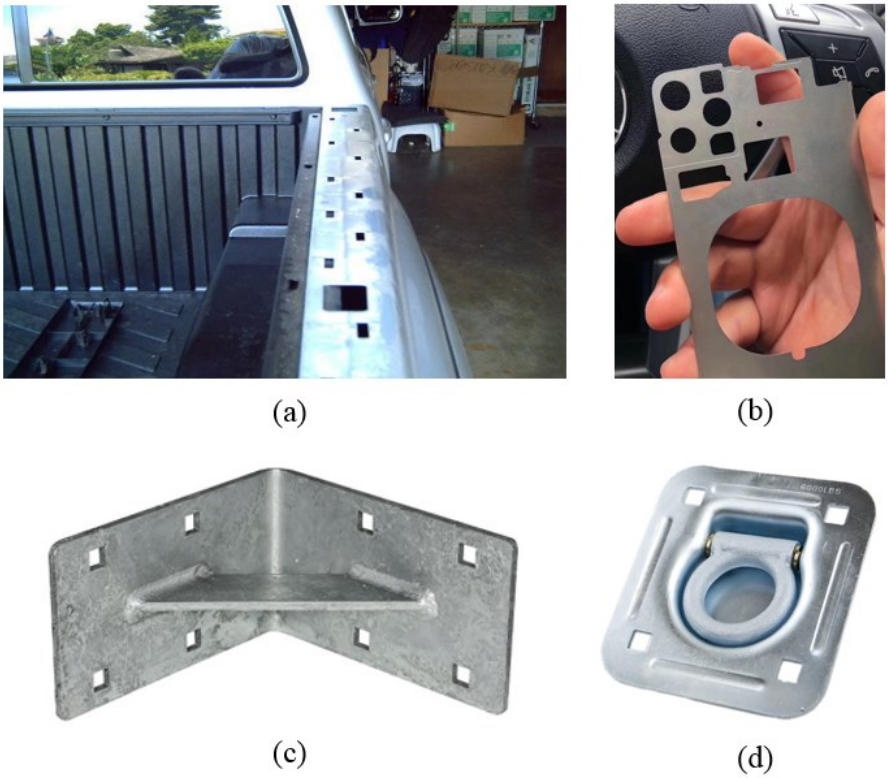

Figure 1.2: Examples of square holes in engineering: (a) square anchor holes in a truck frame, (b) square hole with rounded corners and circular holes in a 2019 iPhone chassis, (c) square holes in a reinforced bracket, (d) square holes in a tiedown.

1.2 Background

The use of holes in engineering design is very common. Invariably, the presence of a hole, notch, cutout, or other discontinuity in any material results in a redistribution and localization of stresses, when subjected to external loading. Stress concentrations surrounding holes are of great practical concern, since they are usually the leading cause of failure. Stress concentrations in continuous fiber reinforced composites which contain multiple holes are not largely understood, nor is the resultant influence upon damage within the composite. While the effect of single and multiple holes in composite laminates have been studied, this has been only to a small degree. Additionally, most existing research does not consider multiple simultaneous effects. This thesis addresses the lack of information in these areas. It is known that the "hole-to-hole proximity effect" and the "edge effect" can occur with the presence of multiple holes, and close proximity to geometric boundaries, respectively. Further, such phenomena can have great influence upon the magnitude of resultant stress concentrations and component strength. As is

the case with most materials, the failure strength depends strongly upon notch sensitivity. These phenomena, in turn, contribute to premature damage initiation within the composite structure.

While composites possess many distinct advantages over traditionally used materials (as mentioned in Section 1.1), they are not without drawbacks. High notch sensitivity is typically associated with brittle materials. In contrast, ductile materials exhibit low notch sensitivity, which lends to their frequent use in structural applications, where holes are often necessary. It has been found that the presence of a notch, hole, cutout, or other discontinuity, in a notch sensitive material significantly reduces its strength. This has also been found to be consistent with the behavior of composites. However, one cannot categorize a composite as either a ductile or a brittle material. Rather, research has demonstrated that the strength of a composite is a function of the size of the notch, or hole. This behavior has been designated the "hole size effect".

Failure within composites is caused by damage accumulation, an understanding of which gives rise to a more pronounced and accurate ability to predict component lifetime. It is critical to make the distinction that composites do not fail catastrophically; their failure is governed by a progressive damage mechanism. Because a composite cannot yield like a ductile material, the energy which would ordinarily be used for the redistribution of stresses is instead used to create damage at locations where allowable stress/strain limits are exceeded. While many types of damage models and criteria exist for composite failure, there is no universally agreed upon "best" model. This is predicated by the fact that since the damage failure mechanism is so complex, no one failure theory can adequately capture the interplay of the many micro-failure modes which contribute to progressive composite damage. However, most, if not all, of the currently available damage theories are capable of modeling damage to an acceptable level.

1.3 Research Problem and Objective

The primary research problem was to understand the effect of multiple holes upon stress concentrations within a quasi-isotropic composite laminate using finite element analysis (FEA). The effects of hole shape, corner radius size, hole edge-to-edge proximity, and hole edge-to-laminate edge proximity upon stress concentrations are taken into consideration.

The second research problem was to gain insight into the damage initiation caused by the stress concentrations due to multiple holes (also using the finite element analysis approach).

Local damage initiation due to the "hole-to-hole proximity effect", hole shape, and the "edge effect" are explored.

The first objective of this study was to investigate the effect of multiple holes on stress concentrations in a continuous fiber reinforced composite laminate, focusing on a quasi-isotropic stacking sequence. Attention was given to multiple holes, which builds upon theory and results from single holes. Additionally, hole shapes and spacings were varied and investigated. It was believed that the influence of the "hole-to-hole proximity effect", hole shape, and the "edge effect" upon stress distribution would elicit increased local stress concentrations at the holes.

The second objective of this study was to understand the influence of the "hole-to-hole proximity effect", hole shape, and the "edge effect" upon consequent local damage initiation. It was believed that the influence of the "hole-to-hole proximity effect", hole shape, and the "edge effect" upon stress distribution and concentrations would dictate the location of damage initiation at the hole periphery, and give rise to an increased amount of local damage. It was thought that the multiple hole configuration with both the "edge effect" and the "hole-to-hole proximity effect" present would produce an increased amount of damage, which would initiate before the multiple hole configuration with only the "hole-to-hole proximity effect" present.

1.4 Outline of Thesis

Past research which is relevant to this study has been reviewed, and can be found in Chapter 2. The phenomena of stress concentration due to single and multiple holes, and their associated stress field analysis methods are presented and discussed, with attention given to research done by Esp. [4] and Kheradiya [5] on multiple circular holes in finite width continuous fiber reinforced composite laminates. The finite element model for a single eccentrically located circular hole in an isotropic plate of finite width subjected to an in-plane uniaxial load is developed and validated against results from Pilkey and Pilkey [6] in Chapter 3. Stress concentrations due to the "edge effect" for a single offset circular hole and a single offset square hole within a finite width continuous fiber reinforced composite laminate are investigated using ANSYS Mechanical APDL 19.1 in Chapter 4. The "edge effect" and the "hole-to-hole proximity effect" in the presence of multiple holes within a continuous fiber reinforced composite laminate are investigated in Chapter 5. A study of damage initiation in a continuous fiber reinforced

composite laminate which contains multiple holes using ANSYS Mechanical APDL 19.1 is given in Chapter 6. Conclusions are presented in Chapter 7.

CHAPTER 2: LITERATURE REVIEW

The phenomena of stress concentration in an isotropic plate with a single circular hole is introduced. A brief exploration of stress distribution in an isotropic plate containing a single centered square hole is then given, followed by a review of stress distribution within laminated composites containing a single hole. The latter discussion is then extended to multiple holes, where emphasis is placed upon work by Esp [4] and Kheradiya [5]. Lastly, a review of the evolution of damage within laminated composites is given.

2.1 Stress Distribution in Homogeneous Isotropic Plates with a Single Circular Hole

The behavior of the stresses in a notched homogeneous isotropic plate has been well understood for many years.[1] The problem of a single circular hole in the center of a wide plate in tension was investigated and solved by Kirsch [7] as early as 1898. In fact, such phenomena have undergone a seemingly exhaustive study, as evidenced by the work from Pilkey and Pilkey [6], and Young *et al.* [8]. There, stress concentrations for various single hole geometries as well as multiple hole geometries and patterns were explored and catalogued. It is important to first understand the concept of stress concentration, as it serves for the foundation of this study.

2.1.1 Infinite-Width Plates

When subjected to external loading, a material prefers to redistribute internal forces throughout its volume such that its maximum strength is retained. For illustration of this concept, consider the simple case of an isotropic plate containing a single centered circular hole under in-plane uniaxial tension. The internal forces can be thought of as force lines which run through the volume of the material parallel to the direction of loading. Upon any removal of volume, the force lines become compressed, as the same amount must now pass through a smaller space on

[1] For potential clarity, the difference here is that homogeneous means the same in all places, whereas isotropic means the same in all directions.

both sides of the hole, causing localization. In effect, the stress field of the body becomes distorted. This can be easily visualized in Fig. 2.1.

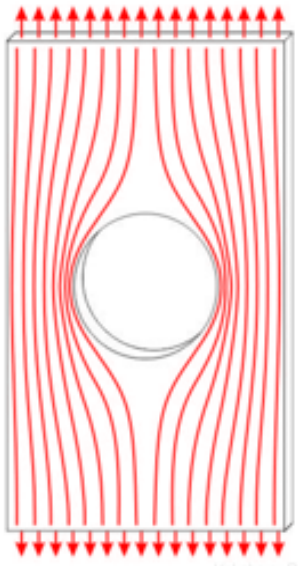

Figure 2.1: The compression of internal force lines in the presence of a single circular hole.

The localization is known as stress concentration, the magnitude of which can be measured with the aid of the stress concentration factor. This factor, K, is defined as the ratio of the maximum stress in the plate (or stress in the perturbed region of interest) to a reference stress (typically the applied remote stress). The distinction between plates of infinite and finite width is worthwhile to make here, as the latter requires a geometrical correction factor. It is noted that in general, a reasonable amount of agreement exists between finite and infinite plate solutions. However, infinite plates remain impractical to model via FEA software, for obvious reasons. It has been suggested that one can mimic infinite plate behavior by simply scaling down the size of the hole; however, there appears to be a practical limit of miniscule hole size beyond which stress field accuracy is lost. For the loading condition shown below in Fig. 2.2, the elastic stress concentration factor (SCF) in a homogeneous isotropic plate of infinite width which contains a single circular hole is given by the well-known equation

$$K_t = \frac{\sigma_{max}}{\sigma_{nom}} \tag{2.1}$$

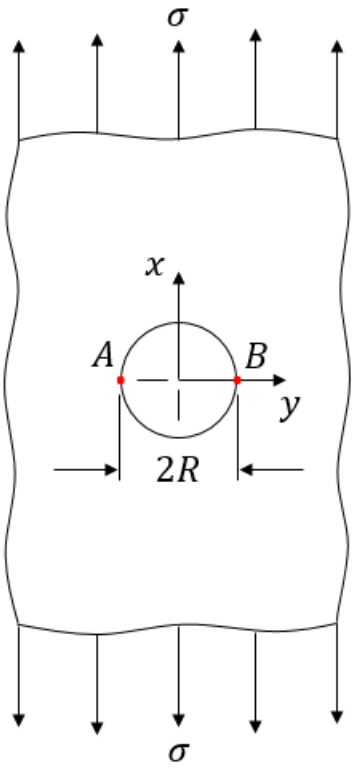

Figure 2.2: A uniaxially loaded infinite width plate with a single circular hole.

where the nominal stress is the applied remote (global) stress, $\sigma_{nom} = \sigma$, and σ_{max} is the local stress at points A and B on the hole periphery[2]. It is important to make the distinction that this relationship applies only to a homogeneous, perfectly elastic body. If desired, the nominal (reference) stress can be calculated based upon either the gross, tw (the remote), or net, $t(w - d)$ (the local), cross-sectional area, where t and w are the thickness and width of the plate, respectively, and d is the diameter of the hole. This choice will result in slightly different values of the stress concentration factor as depicted below in Fig. 2.3, because

$$\sigma_{gross} = \sigma \tag{2.2}$$

and

$$\sigma_{net} = \sigma\left(1 - \frac{d}{w}\right) \tag{2.3}$$

[2] The subscript t stands for theoretical, in that the maximum stress within the plate is based upon the theory of elasticity, or acquired from laboratory experiment.

To further clarify the relationship (and difference) between the stress concentration factors, it can be shown using Eqns. 2.2 and 2.3 that

$$K_{tg} = \frac{\sigma_{max}}{\sigma_{gross}} \tag{2.4}$$

and

$$K_{tn} = \frac{\sigma_{max}}{\sigma_{net}} \tag{2.5}$$

Therefore,

$$K_{tn} = \frac{\sigma_{max}}{\sigma_{gross}} \frac{\sigma_{gross}}{\sigma_{net}} = K_{tg} \frac{1}{1 - \frac{d}{w}} \tag{2.6}$$

so

$$\therefore K_{tg} = K_{tn}\left(1 - \frac{d}{w}\right) \tag{2.7}$$

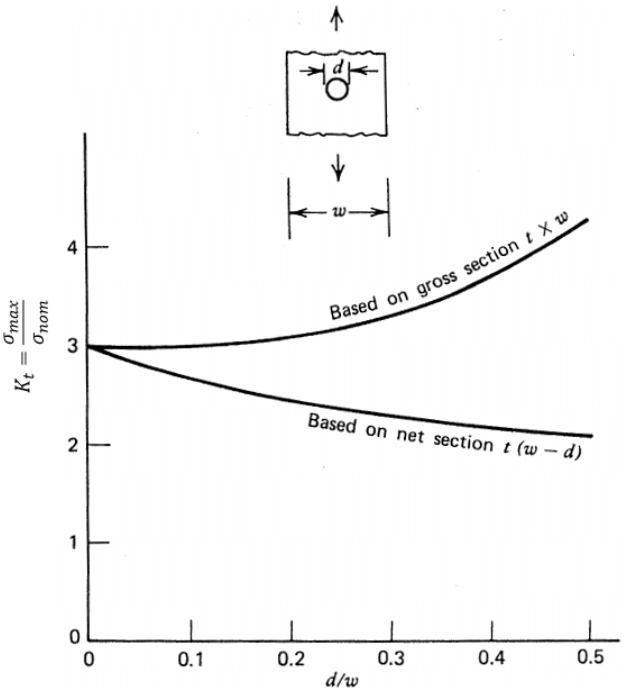

Figure 2.3: Stress concentration factors K_{tg} and K_{tn} for a single centered circular hole in a finite width plate.

It is worth recognizing that the increasing behavior of the top curve in Fig. 2.3 is due to the fact that as the diameter of the hole increases with respect to the fixed width of the plate, less material remains between the hole periphery and the free edge of the plate. Consequently, greater stress localization in that area occurs, as the same amount of force lines must now pass through a smaller volume, thereby causing the stress concentration factor to increase.

Timoshenko and Goodier [9] obtained equations for the stress distribution of an infinite width isotropic plate containing a single circular hole, and when converted from their polar form to cartesian form [10], they are as follows.

$$\frac{\sigma_x}{\bar{\sigma}} = 1 + \frac{1}{2}\left(\frac{R}{y}\right)^2 + \frac{3}{2}\left(\frac{R}{y}\right)^4 \tag{2.8a}$$

$$\frac{\sigma_y}{\bar{\sigma}} = \frac{3}{2}\left(\frac{R}{y}\right)^2 - \frac{3}{2}\left(\frac{R}{y}\right)^4 \tag{2.8b}$$

where $\bar{\sigma}$ is the applied remote stress parallel to the x-axis, and R is the radius of the hole.[3] Interestingly, if the normalized stress is plotted as a function of the distance ahead of the hole $(y - R)$, the stress concentration becomes much more localized in the case of a smaller hole. In effect, hole diameter influences stress concentration. This behavior can be seen below in Fig. 2.4, where Eqn. 2.8a is plotted in terms of $(y - R)$ for two different hole radii.

[3] Throughout this work, S, σ, σ_{nom}, $\bar{\sigma}$, and σ^{∞} are used interchangeably. They mean the same thing; a remote applied stress.

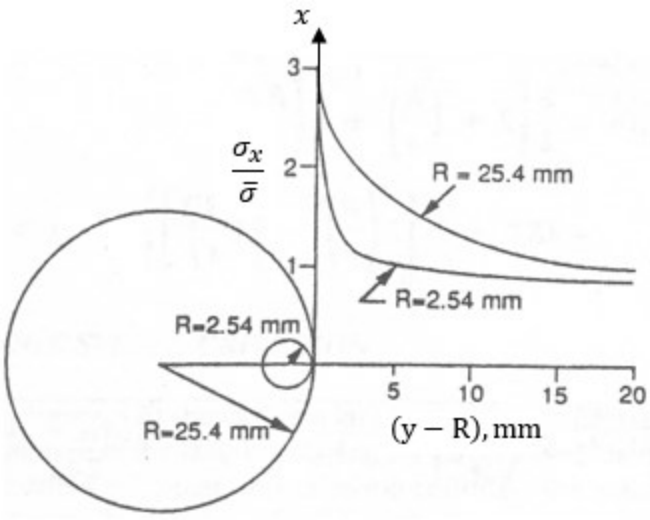

Figure 2.4: Stress distributions for a large and small circular hole in an infinite isotropic plate subjected to uniaxial tension.

Here, one can recognize the relationship between the rate of change of the circumferential curvature and the resulting slope of the stress concentration curve; smaller holes give rise to rapid horizontal asymptotic approach, whereas larger holes demonstrate a slower degree of curvature in the solution graph. The behavior of Eqns. 2.8a and 2.8b can be seen below in Fig. 2.5.

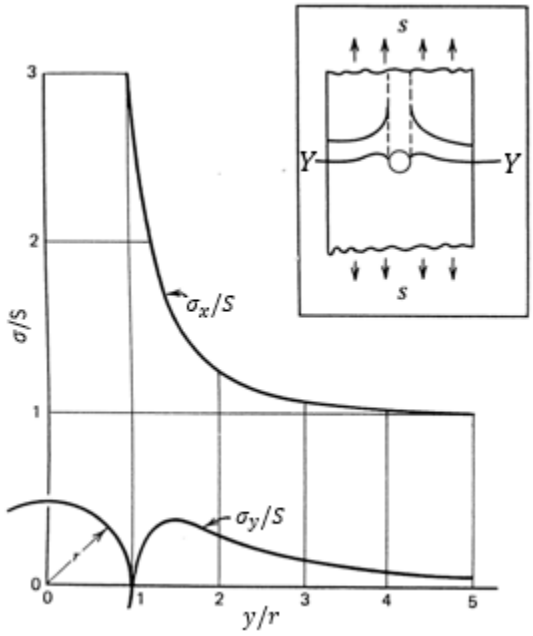

Figure 2.5: Stress distribution along the section Y-Y, in both the x and y-directions.

It is important to note in Fig. 2.5 that $\sigma_y \ll \sigma_x$ for all values of y. At the ends of the horizontal diameter, σ_x reaches the maximum value equal to $K_t S$; however, $\sigma_y = 0$. At a distance $y = 1.414R$, σ_y reaches its maximum value and then starts to decrease with increasing distance. It is also worthwhile to recognize that the magnitude of σ_{max} is dependent upon its proximity to the hole periphery. For an in-plane uniaxially loaded homogeneous isotropic plate, the highest stress is realized directly at the hole edge, and decreases with increasing distance from the hole. This trend is consistent throughout the following sections. To provide a frame of reference, and to illustrate the concept that the stress concentration produced by a given notch, or hole, is not a unique number, the stress concentration factors for a circular hole in a wide plate based upon the type of stress are given below in Table 2.1.

Table 2.1: Stress concentration factors based upon stress type for a single centered circular hole in a wide plate [10].

	In Tension	**In Biaxial Tension**	**In Shear (Max Tension)**	**In Shear (Max Shear)**
K_t	3	2	4	2

For an infinite plate with a single centered circular hole (as seen below in Fig. 2.6), the stress field components in polar coordinates [11] are

$$\sigma_{rr}(r,\theta) = \frac{\sigma}{2}\left[\left(1 - \frac{a^2}{r^2}\right) + \left(1 + 3\frac{a^4}{r^4} - 4\frac{a^2}{r^2}\right)\cos 2\theta\right] \tag{2.9}$$

$$\sigma_{\theta\theta}(r,\theta) = \frac{\sigma}{2}\left[\left(1 + \frac{a^2}{r^2}\right) - \left(1 + 3\frac{a^4}{r^4}\right)\cos 2\theta\right] \tag{2.10}$$

$$\sigma_{r\theta}(r,\theta) = -\frac{\sigma}{2}\left[\left(1 + 3\frac{a^4}{r^4} - 4\frac{a^2}{r^2}\right)\sin 2\theta\right] \tag{2.11}$$

where a is the radius of the hole, r is the radial distance to the point of interest, σ is the remote applied stress in the x-direction, and θ is the angle with respect to the x-axis to the point of interest.

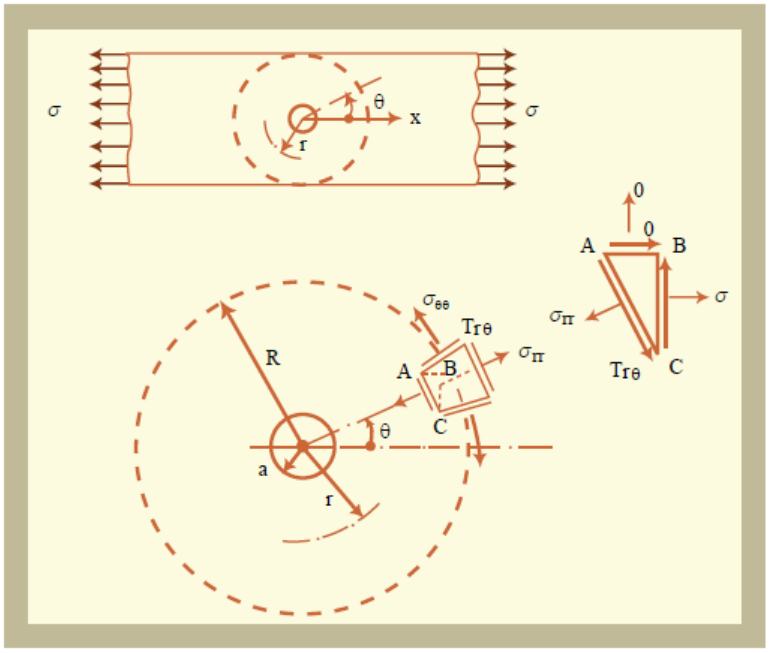

Figure 2.6: Distribution of σ_{rr}, $\sigma_{\theta\theta}$, and τ_{xy} stresses around a circular hole.

At $r = a$, Eqns. 2.9-2.11 become

$$\sigma_{rr}(r = a, \theta) = 0 \tag{2.9a}$$

$$\sigma_{\theta\theta}(r = a, \theta) = \sigma(1 - 2\cos 2\theta) \tag{2.10b}$$

$$\sigma_{r\theta}(r = a, \theta) = 0 \tag{2.11c}$$

The maximum value of the hoop stress $\sigma_{\theta\theta}$ is reached at $\theta = \pi/2$, giving $\sigma_{\theta\theta} = \sigma_{max} = 3\sigma$. Thus, the stress concentration factor, K_t, is 3 for an isotropic plate of infinite width containing a single centered circular hole. This, along with stress field behavior can be seen below in Fig. 2.7.

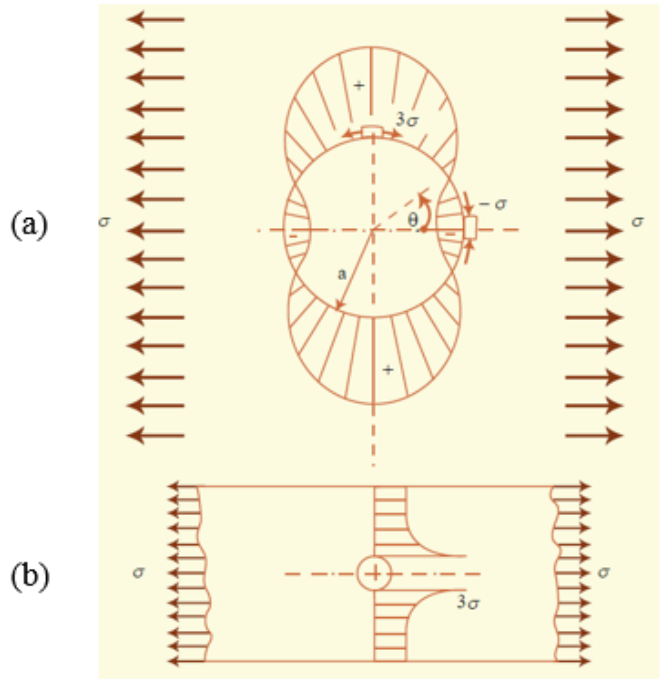

Figure 2.7: Distribution of hoop stress component, $\sigma_{\theta\theta}$: (a) circumferential distribution in a large body, (b) radial distribution for $\theta = \pi/2$.

2.1.2 Finite-Width Plates

Timoshenko and Goodier [9] stated that due to Saint-Venant's principle, for a finite width plate with a single centered circular hole, the change in the stress field is negligible at distances which are large compared to the radius, a, of the hole. Further, he pointed out that a concentric circle of radius b can be drawn about the hole, on which the stresses at the circular boundary are essentially equal to that of a plate with no hole. This is depicted below in Fig. 2.8.

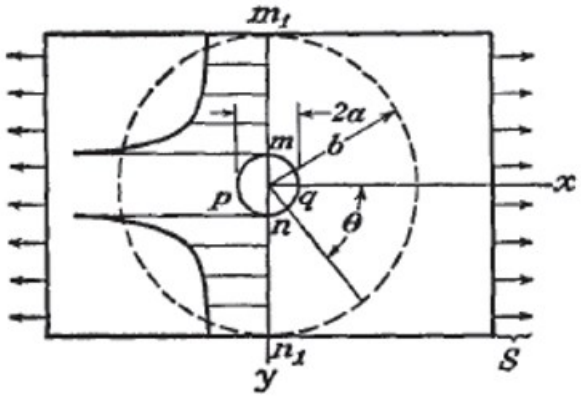

Figure 2.8: Stress distribution and influence of radial distance, b, in a finite width plate with a single centered circular hole of radius, a, subjected to an externally applied in-plane uniform tensile stress, S.

Stress distribution within a finite width plate has been studied using the Heywood equation, which, in terms of the stress concentration factor based on gross area, is given by Pilkey and Pilkey [6] as

$$K_{tg} = \frac{2 + (1 - d/W)^3}{1 - d/W} \tag{2.12}$$

where d is the diameter of the hole, and W is the width of the plate. If desired, the stress concentration factor can be expressed in terms of the net area

$$K_{tn} = 2 + (1 - d/W)^3 \tag{2.13}$$

Pilkey and Pilkey [6] informed that Eqn. 2.13 was found to show good correlation with experimental results from Howland (Heywood [12]) for $d/W < 0.3$, and is only about 1.5% lower at $d/W = 1/2$. Further, Pilkey and Pilkey [6] stated that because most design applications are such that $d/W < 0.3$, Eqn. 2.13 is suitable for use.

2.2 Stress Distribution in Homogeneous Isotropic Plates with a Single Square Hole

The stress field disturbance created by a single square hole in an isotropic plate has been studied to some detail. Young *et al.* [8] listed the following stress concentration factor based on gross area for a rectangular hole with rounded corners in an infinitely wide thin plate subjected to in-plane uniaxial tension.

$$K_{tg} = C_1 + C_2\left(\frac{b}{a}\right) + C_3\left(\frac{b}{a}\right)^2 + C_4\left(\frac{b}{a}\right)^3 \tag{2.14}$$

where

$$C_1 = 14.815 - 15.774\sqrt{\frac{r}{b}} + 8.149\left(\frac{r}{b}\right) \tag{2.15}$$

$$C_2 = -11.201 - 9.750\sqrt{\frac{r}{b}} + 9.600\left(\frac{r}{b}\right) \tag{2.16}$$

$$C_3 = 0.202 + 38.662\sqrt{\frac{r}{b}} - 27.374\left(\frac{r}{b}\right) \tag{2.17}$$

$$C_4 = 3.232 - 23.002\sqrt{\frac{r}{b}} + 15.482\left(\frac{r}{b}\right) \tag{2.18}$$

for

$$0.2 \leq r/b \leq 1.0 \tag{2.19}$$

$$0.3 \leq b/a \leq 1.0 \tag{2.20}$$

where $2a$ is the width of the rectangle, $2b$ is the height of the rectangle, and r is the radius of the corners of the rectangular hole. For the case of a square hole, one simply lets $a = b$. The rectangular hole with rounded corners can be seen below in Fig. 2.9.

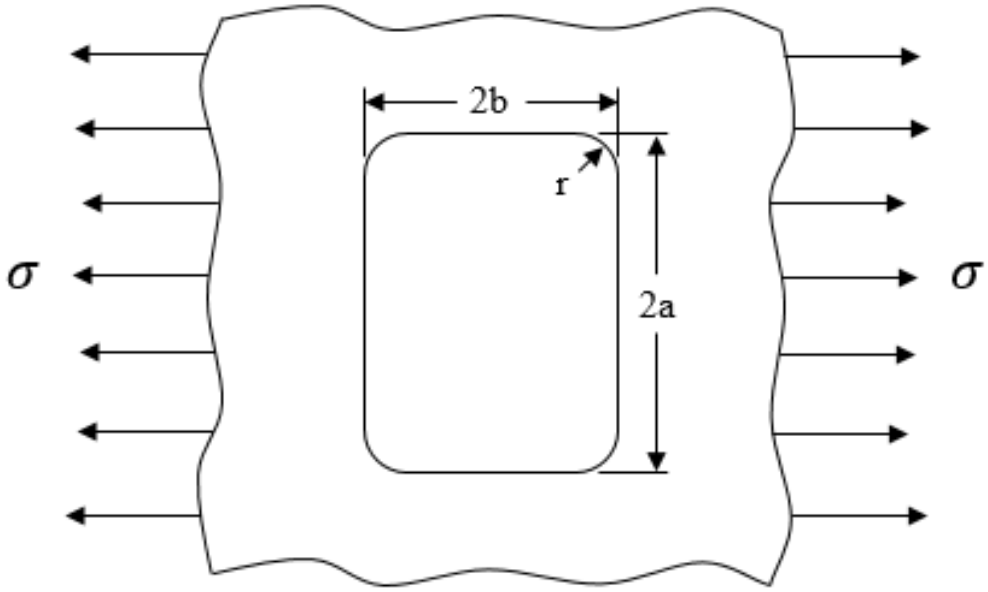

Figure 2.9: Rectangular hole with rounded corners in an infinite plate subjected to an externally applied in-plane uniaxial tensile stress.

2.3 Stress Distribution in Laminated Composites with a Single Hole

The distribution of stresses within symmetric laminated composite plates which contain a hole can be determined in a variety of ways, each of which possessing its own level of accuracy and ease of application. Such methods are listed and discussed in the following subsections. It is important to begin with the recognition of the various aspects which influence stress concentration, as they can dictate the solution approach. These aspects can include the effect of finite geometry, the interaction of multiple holes, degree of anisotropy, hole geometry, and the length of computation time (modeling and solution).

For an infinite symmetric laminated plate containing a circular hole of radius R, the approximate solution for the stress distribution along the axis perpendicular to the loading direction was found by Konish and Whitney, and given by [13] as

$$\frac{\sigma_y(x,0)}{\bar{\sigma}} = \frac{1}{2}\left\{2 + \left(\frac{R}{x}\right)^2 + 3\left(\frac{R}{x}\right)^4 - (K_t^{\infty} - 3)\left[5\left(\frac{R}{x}\right)^6 + 7\left(\frac{R}{x}\right)^8\right]\right\} \quad for \quad x > R \tag{2.21}$$

where

$$K_t^{\infty} = 1 + \sqrt{\frac{2}{A_{22}}\left[\sqrt{A_{11}A_{22}} - A_{12} + \frac{A_{11}A_{22} - A_{12}^2}{2A_{66}}\right]} \tag{2.22}$$

where K_t^{∞} is the stress concentration factor at the edge of the hole, and A_{ij} for i, j = 1, 2, and 6 are the components of the in-plane stiffness matrix with 1 and 2 being parallel and transverse to the loading directions, respectively. Eqn. 2.22 can be expressed in terms of the engineering elastic constants E_x, E_y, G_{xy}, and ν_{xy} as

$$K_t^{\infty} = 1 + \sqrt{2\left(\sqrt{\frac{E_y}{E_x}} - \nu_{xy}\right) + \frac{E_y}{G_{xy}}} \tag{2.23}$$

where E_y and E_x are the laminate moduli in the y-direction (loading) and x-direction respectively, and G_{xy} and ν_{xy} are the laminate shear modulus and Poisson's ratio, respectively. It can be readily seen that by substituting the stress concentration factor for a circular hole in an isotropic plate, $K_t^{\infty} = 3$, in Eqn. 2.21, one recovers Eqn. 2.8a.

It is important to note that, currently, no closed form exact solution for the stress distribution in a finite width composite plate containing a single circular hole has been found. However, Tan [14] was able to approximate the effect of finite width in a closed form solution for an anisotropic material. This, and other similar shortcomings are typically addressed via the use of computer driven numerical analysis, such as finite element analysis. This is discussed in the following section.

2.3.1 Finite Element Analysis

The finite element method (FEM) has been used with some frequency to model and study stress concentrations within fiber reinforced composite laminates. Since the number of closed form solutions for infinite orthotropic composite plates is limited, results from FEA prove useful for comparison and validation. Further, the FEM becomes necessary for problems which are analytically intractable. To simulate infinite geometric conditions within FE computer models, plates are often taken to be some large, but reasonable (≈1000x), value of length, width, and thickness.

Work by Soutis *et al.* [15] sought the hole spacing for which no stress interaction occurs using 2D finite elements. It was found that the hole centers should be spaced at least four diameters apart in order to ensure that no stress field interaction occurs.

Kheradiya [5], whose work focused on using ANSYS to model a composite laminate and analyze the "edge effect", "hole-to-hole proximity effect", and "hole size effect", revealed the correlation between these phenomena and resultant stress concentration. It was demonstrated through a ply-by-ply analysis of a single circular hole in a uniaxially loaded finite width composite laminate, that shear rotation dictates the exact location of maximum stresses in a lamina with fibers which are oriented at some angle, θ, with respect to the loading axis. Additionally, the "edge effect" was shown to greatly influence the stress concentrations at a point on the hole periphery close to the free edge of the laminate. This behavior can be seen below in Fig. 2.10.

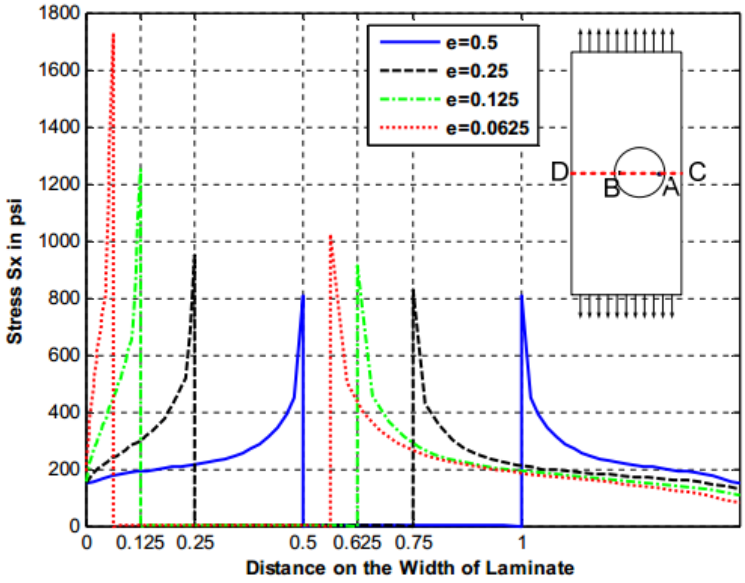

Figure 2.10: Distribution of stress across the width (1.5 inches) of a laminate containing a single offset circular hole, where *e* is the distance in inches from the edge of the hole to the laminate edge [5].

2.3.2 Single Square Hole

The stress concentrations which arise from single square holes have been studied, but to only a limited extent. It is important to note that no rigorous closed-form solution exists for a single square hole in an orthotropic plate (finite width or infinite width), however an approximate expression for the tangential stress on the contour of a square hole does exist, and was found by Lekhnitskii, as informed by Rowlands *et al.* [17].

The stress concentration and strength of uniaxially loaded finite width composite plates containing central square holes with both rough and smooth surfaces was investigated by Rowlands *et al.* [17]. It was discovered that the tensile stress concentration factor increases and strength decreases as the hole diameter-to-plate width ratio increases. This behavior is consistent with conventional metallic materials. Further, it was found that strength decreases with decreasing ratio of laminate thickness-to-hole diameter. Interestingly, it was recommended that if minimum weight is to be placed as a design priority, it may be more advantageous to thicken the plate, rather than increase its width, provided that a specified hole dimension and required gross strength exist. Also, it was found that laminates having a 25.4 mm square hole are slightly stronger than plates with a 25.4 mm diameter circular hole.

Jong [18] studied stress concentrations around square holes with rounded corners using various CFRP composite stacking sequences, and found that square holes with sufficiently

rounded corners do not cause much higher stress concentrations than circular holes. Further, the highest stresses were found to occur mostly in general proximity to the rounded corners.

Cannon [19] studied the effect of stacking sequence and varying radii on a single centered square hole and found that quasi-isotropic laminates possessed lower SCFs than isotropic plates. Additionally, it was found that decreasing the percent of 0° laminas and/or increasing the percent of 45° laminas reduced the SCFs for each hole shape.

2.3.3 Finite-Width Correction Factor

As mentioned previously, composite plates of finite width require a correction factor to obtain the true value of the stress concentration factor. Bakhshandeh *et al.* [20] informed that the finite width correction factor for an isotropic plate is independent of material properties, and can thus be obtained through curve fitting. However, in the case of an orthotropic material, the stress analysis must be employed via elasticity equations or through the FEM. Tan [13] obtained an improved theory for stress concentration prediction in finite width orthotropic plates by implementing a magnification factor into the Heywood formula (Eqn. 2.25). For a single centered circular hole in an orthotropic plate of finite width, the approximate finite width correction factor for gross area is

$$\frac{K_{Tg,O}^{\infty}}{K_{Tg,O}} = \frac{3(1-d/W)}{2+(1-d/W)^3} + \frac{1}{2}\left(\frac{d}{W}M\right)^6 (K_{Tg}^{\infty}-3)\left[1-\left(\frac{d}{W}M\right)^2\right] \tag{2.24}$$

where

$$M^2 = \frac{\sqrt{1-8\left[\frac{3(1-d/W)}{2+(1-d/W)^3}-1\right]}-1}{2(d/W)^2}$$

where $K_{Tg,O}^{\infty}$ is the stress concentration factor in an infinite width orthotropic plate (equal to 3 for a circle), $K_{Tg,O}$ is the stress concentration factor in a finite width orthotropic plate, d is the hole diameter, W is the width of the plate, and M is the magnification factor.

For a quasi-isotropic plate of infinite width containing a single centered circular hole, $K_{Tg}^{\infty} = 3$, and if substituted into Eqn. 2.24, one recovers the Heywood formula for a finite width isotropic plate containing a single centered circular hole,

$$\frac{K_{Tg,O}^{\infty}}{K_{Tg,O}} = \frac{3(1 - d/W)}{2 + (1 - d/W)^3} \tag{2.25}$$

where $K_{Tg,O}^{\infty}$ is the stress concentration factor in an infinite width orthotropic plate (equal to 3 for a circle), $K_{Tg,O}$ is the stress concentration factor in a finite width orthotropic plate, d is the hole diameter, W is the width of the plate, and M is the magnification factor. To make use of Eqn. 2.24, one must obtain $K_{Tg,O}^{\infty}$, which was found by Lekhnitskii [16] and given as

$$\begin{aligned} K_{Tg,O}^{\infty} = \frac{E_\theta}{E_{11}}\{&[-\cos^2\varphi + (k+n)\sin^2\varphi]k\cos^2\theta \\ &+ [(1+n)\cos^2\varphi - k\sin^2\varphi]\sin^2\theta - n(1+k \\ &+ n)\sin\varphi\cos\varphi\sin\theta\cos\theta\} \end{aligned} \tag{2.26}$$

where

$$\frac{1}{E_\theta} = \frac{\sin^4\theta}{E_{11}} + \left(\frac{1}{G_{12}} - \frac{2\nu_{12}}{E_{11}}\right)\sin^2\theta\cos^2\theta + \frac{\cos^4\theta}{E_{22}} \tag{2.27}$$

from which one may obtain

$$\frac{E_\theta}{E_{11}} = \frac{1}{\sin^4\theta + (n^2 - 2k)\sin^2\theta\cos^2\theta + k^2\cos^4\theta} \tag{2.28}$$

$$n = \sqrt{2\left(\sqrt{\frac{E_{11}}{E_{22}}} - \nu_{12} + \frac{E_{11}}{2G_{12}}\right)} \tag{2.29}$$

$$k = \sqrt{E_{11}/E_{22}} \tag{2.30}$$

where E_θ is Young's modulus for directions tangential to the hole periphery, E_{11} and E_{22} are elastic moduli in the principal material direction, G_{12} is the shear modulus, ν_{12} is the major Poisson's ratio, θ is the angle of the point of interest on the periphery of the circular hole measured from the x-axis (principal material direction), and φ is the angle of the applied force, p, with respect to the x-axis. To obtain Eqn. 2.30, simply let $\theta = 0$ in Eqns. 2.27 and 2.28, and substitute the result of Eqn. 2.27 into Eqn. 2.28.

In the case of an infinite width plate with a single centered circular hole subjected to in-plane uniaxial tension, where the direction of the applied force is aligned with the principal material direction, $\varphi = 0°$, and hence $\theta = 0°$ and $90°$ at points A and B, respectively. Substituting these values into Eqns. 2.26 and 2.27, and using Eqn. 2.30 when necessary, one finds

$$K_{Tg,O}^{\infty,1} = -\frac{1}{k} \tag{2.31}$$

$$K_{Tg,O}^{\infty,2} = 1 + n \tag{2.32}$$

where $K_{Tg,O}^{\infty,1}$ and $K_{Tg,O}^{\infty,2}$ are the stress concentration factors at points A and B for an infinite width orthotropic plate, respectively. The infinite width orthotropic plate can be seen below in Fig. 2.11.

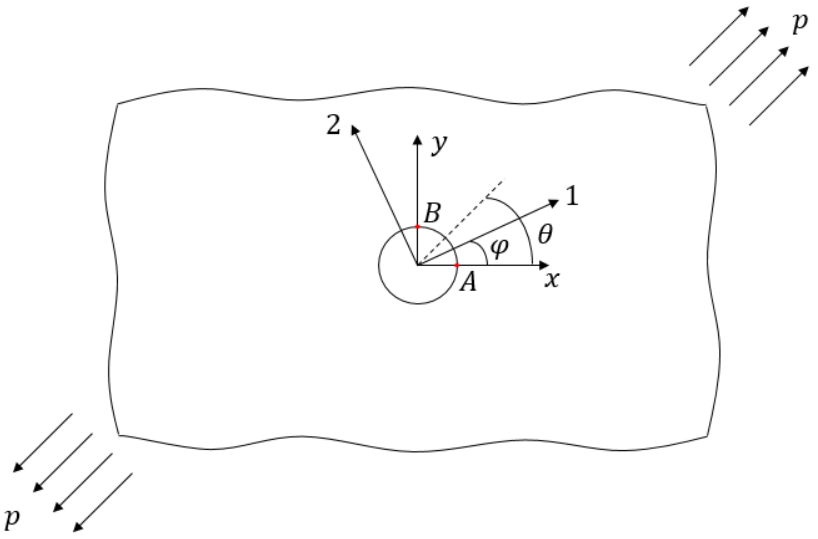

Figure 2.11: An infinite plate containing a single centered circular hole subjected to an externally applied in-plane tensile force, p.

It should be noted that for the case of an isotropic material, where $K_{Tg}^{\infty} = 3$ at point B, if this value is substituted into Eqn. 2.24, one again recovers the Heywood formula for an infinite width isotropic plate with a single centered circular hole, as expected. Finally, one may obtain the stress concentration factors at points A and B for an infinite width isotropic plate with a single centered circular hole by letting $E_{11} = E_{22}$ in Eqns. 2.29 and 2.30, letting $G_{12} = E_{11}/2(1 + \nu_{12})$ in Eqn. 2.29, and then substituting the results into Eqns. 2.31 and 2.32.

2.4 Stress Distribution in Laminated Composites with Multiple Holes

The distribution of stresses within laminated composites which contain multiple circular holes has been investigated using analytical methods and numerical analysis by Esp [4] and Kheradiya [5], respectively. These approaches are addressed in the following sections.

2.4.1 Analytical Methods

Various methods are available for the analysis of stress distribution in orthotropic materials. Research by Esp [4] has led to an understanding of the stress fields surrounding multiple circular holes in an orthotropic composite plate. Esp [4] developed an analytical approach to solving for the stress field due to multiple holes. This is discussed below in Section 2.4.1.1.

2.4.1.1 Least Square Boundary Collocation Method

Esp [4] applied the least square boundary collocation method to internal and external boundaries for two circular holes in an orthotropic material in order to obtain the full field stress solution. Further, Esp [4] was able to demonstrate excellent correlation of circumferential stress, σ_θ, to published solutions from Ling (1942), Fan and Wu (1988), and Lekhnitskii, as well as finite element method solutions.

2.4.2 Finite Element Analysis

As with a single hole, the finite element method has been used to model and study stress concentrations due to multiple holes in fiber reinforced composite laminates. The FEM approach offers great modeling flexibility, as finite geometry, multiple holes, loading and boundary conditions, and material anisotropy are all once complex issues now easily dealt with. Moreover, it is relatively straightforward to tailor FEM models to the problem geometry and conditions at hand, especially since current commercial FEA programs are quite robust with regard to both graphical user interface (GUI) and character user interface (CUI).

Kheradiya [5] studied the effect of multiple circular holes upon stress concentration in an orthotropic $[0_3/\pm45/90]_S$ laminate, and found that for two side-by-side holes transverse to tensile loading, the maximum stress at a point on the hole periphery increases as the distance between the two holes decreases. Additionally, it was found that for three holes in 45° and 60° triangular arrays, the maximum stress of the 0° ply occurs at a point on the outer hole edge. Further, for a given hole array, the maximum stress of the 0° ply increases as the hole size ratio increases.

Doctoral research by Esp [4] used FEA to validate the least square boundary collocation analytic approach, and revealed less than a 1.0% peak difference when used to model two equal diameter holes in close proximity across three different laminate layups. Further, when used to model two unequal sized holes in close proximity, less than a 2.0% peak difference was found. The finite element model used by Esp [4], and its associated stress contour plot and data can be seen below in Figs. 2.12-2.14 and Table 2.2, respectively. Due to symmetry, only half of the plate was modeled.

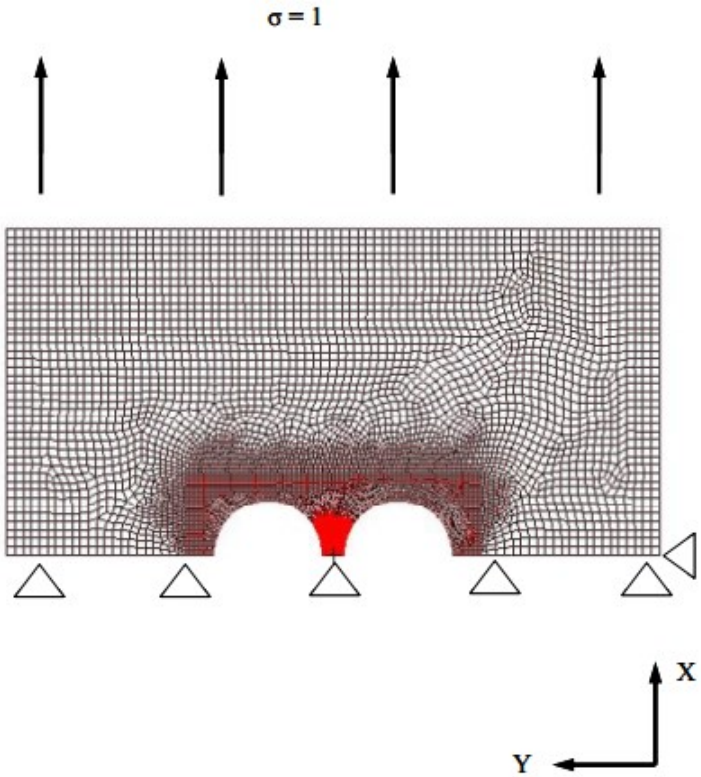

Figure 2.12: Finite element model with two equal diameter circular holes [4].

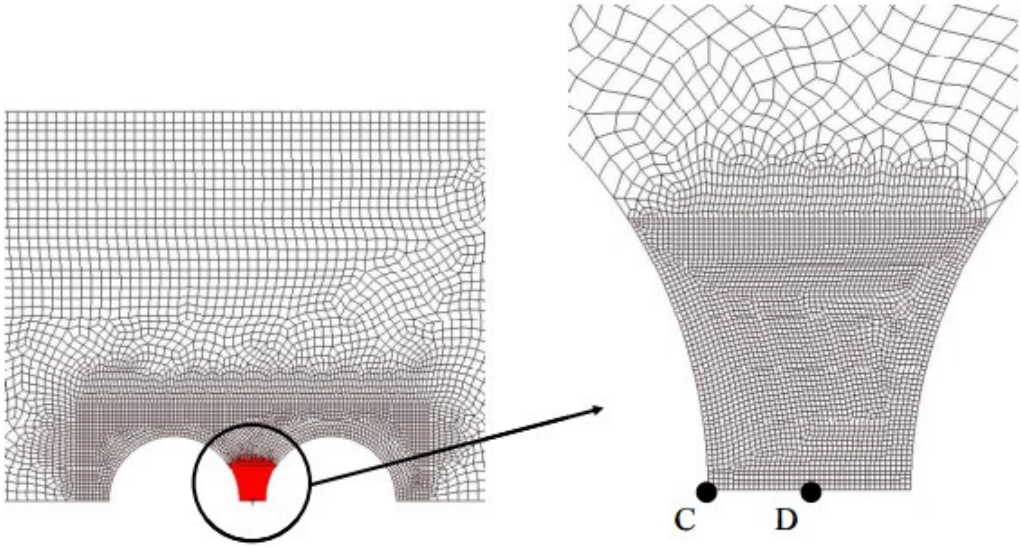

Figure 2.13: Enlarged view of mesh refinement [4].

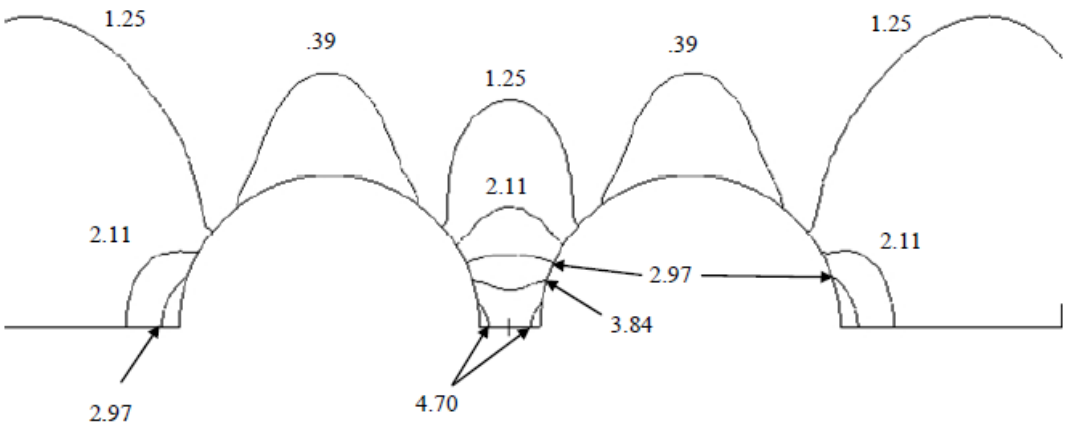

Figure 2.14: Stress field contour plot of σ_x for a quasi-isotropic laminate with equal side-by-side holes [4].

Table 2.2: Comparison between FEM and boundary collocation method for a finite geometry model with equal side-by-side holes [4].

	σ_x (Pt. C) - FEM	σ_x (Pt. C) - B.C.	%Δ	σ_x (Pt. D) - FEM	σ_x (Pt. D) - B.C.	%Δ
Quasi-Isotropic	5.1281	5.1265	0.03	4.3065	4.3082	0.04
Hard Laminate	7.2445	7.2314	0.18	4.2989	4.2900	0.21
Soft Laminate	4.5742	4.5637	0.23	4.4109	4.4304	0.44

2.5 Damage Evolution in Laminated Composites

The understanding of damage initiation and evolution within a composite laminate subjected to external loading is of great importance to a variety of engineering industries. The proper design of a fiber reinforced composite laminate depends greatly on knowledge of its mechanical limitations. It is beneficial to know the magnitude of the applied external loading force that initiates damage, and the rate at which damage accumulates. This allows for a more informed design, where failure is avoided (or at least mitigated) and consequent injury or loss of life does not result. Works by Esp [4] and Kheradiya [5] revealed that hole-to-hole proximity governs local stress concentration. Additionally, the "edge effect" also gives rise to increased local stress concentration, per Kheradiya [5]. It is worth commenting that the inherent complexity of the manufacturing of fiber reinforced composite laminates can also produce defects within the laminate. Such occurrences can lead to premature damage initiation, evolution,

and subsequent failure. The foregoing provides reasons for the motivation to develop this area of knowledge.

The overall mechanism which governs the progressive failure and subsequent damage accumulation of fiber reinforced composite laminates is exceptionally complicated. This is because damage can arise from many different types of individual micro-failure modes, which can occur either singularly or simultaneously, and is typically progressive in nature. Various types of micro-failure modes and their role in damage evolution can be seen below in Fig. 2.15.

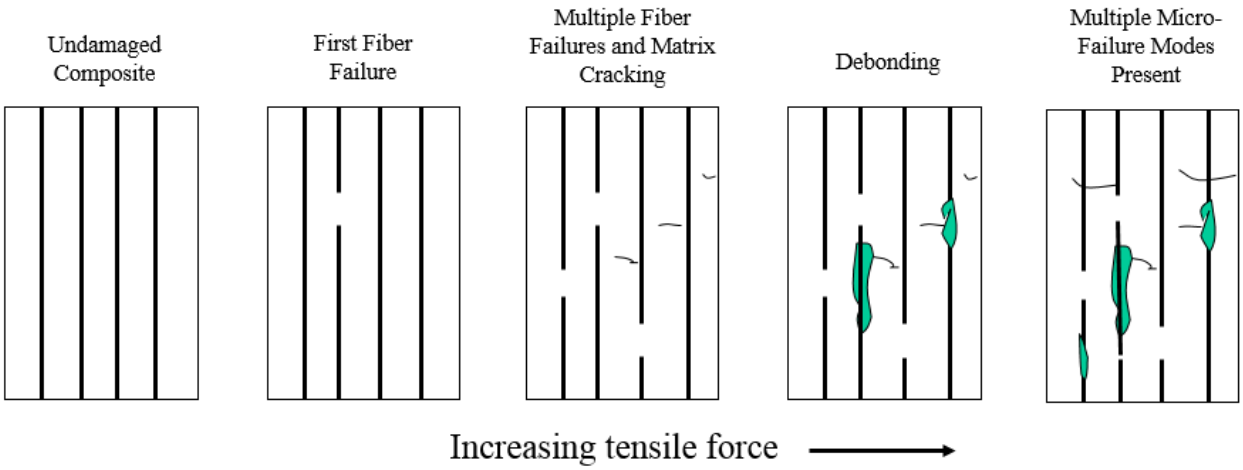

Figure 2.15: Damage evolution in a continuous fiber reinforced composite laminate.

Micro-failure modes can include fiber fracture, fiber buckling, matrix cracking, delamination (common), and fiber-matrix interfacial shear. Owing to such complexities, composite damage problems quickly become analytically intractable. This difficulty can be readily addressed via numerical techniques such as the finite element method.

There are various failure theories which can be used in the analysis of composite damage. Barbero and Shahbazi [21] developed a method to calculate the material parameters required by the progressive damage analysis (PDA) material-model in ANSYS. They found that the ANSYS/PDA predictions of those parameters were dependent upon mesh density, number of elements, and number of nodes, but independent of element type. Further, some of the damage parameters required by PDA (F_{2t}, F_{12}, and G_c) were adjusted, and used to predict damage initiation and evolution in composite laminates with good correlation to available experimental data, in light of certain restrictions.

Investigation by Tan [13] using a progressive failure model comprised of FEMESH and PROFAS revealed that once the number of finite elements in a mesh reaches a certain number, the predicted composite strength approaches a stable value.

El-Sisi *et al.* [22] simulated progressive damage behavior of a composite plate containing a hole using the FEM in ANSYS with a subroutine, USERMAT. They demonstrated through the use of various numerical damage models such as ply discount method (PDM), simple progressive damage model (SPDM), and continuum damage mechanics model (CDMM), that good agreement was found in the SPDM, CDMM, and published experimental results. Additionally, El-Sisi *et al.* [22] used three different damage evolution laws; linear, quadratic, and degradation, and found that no substantial difference in the predicted failure load between them was present.

CHAPTER 3: FINITE ELEMENT MODEL

The composite modeling and analysis capabilities of ANSYS Mechanical APDL 19.1 are discussed, followed by the composite laminate, its properties, and stacking sequence. The hole configurations to be investigated are shown, and the development of the finite element model is then presented. The model is validated against established theory, and convergence is demonstrated.

3.1 ANSYS Mechanical APDL

Because the majority of real-world physical phenomena give rise to nonlinear behavior, computer software is typically implemented as a solution method to problems which are otherwise intractable; be it far too cumbersome and/or time consuming to be solved by hand. ANSYS Mechanical APDL is a commercially available multi-purpose analysis tool frequently used in both academia and industry to model and solve complex engineering problems. The ANSYS finite element program is capable of modeling and solving numerous types of problems which involve composite materials, with various levels of complexities ranging from orthotropic to anisotropic, and static to dynamic. The user has the ability to obtain many types of stress/strain results, as well as create any type of lamina stacking sequence, including using different material properties for each lamina. Additionally, many types of elements may be used, some of which are more suited to composite modeling than others.

3.2 Composite Laminate

The fiber reinforced composite laminate studied in this thesis is manufactured from a glass fiber reinforced epoxy (HyE 9082Af, Fiberite). The choice in material owes to the availability of strength and damage coefficients necessary for composite damage analysis (Chapter 6), and the fact that glass fiber/epoxy lends itself readily to photoelastic study in a laboratory, should future interest arise. A quasi-isotropic layup $[0_3/(\pm 45)_3/90_3]_S$ is considered. In order to correctly model the composite laminate in ANSYS Mechanical APDL 19.1, certain

mechanical properties must be known. In this case, the composite laminate is composed of twenty-four thin laminas, each with a thickness of 0.127 mm and characterized by 6 independent engineering elastic constants (identical for each lamina). Determined in the lamina coordinate system, they are $E_{11}, E_{22}, G_{12}, G_{23}, \nu_{12}$, and ν_{23}. Here, the subscripts 1, 2, and 3 are parallel to the fiber direction, perpendicular to the fiber direction in the plane of the lamina, and normal to the lamina surface, respectively. This can be seen below in Fig. 3.1.

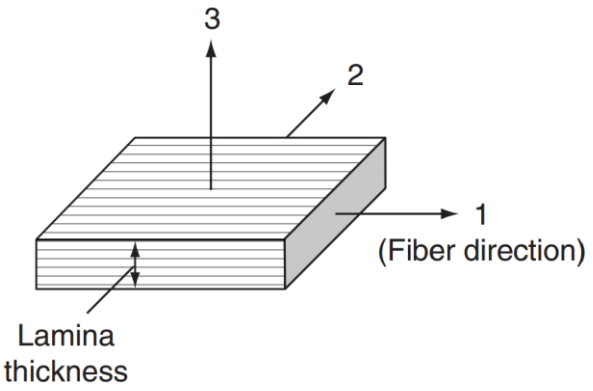

Figure 3.1: Unidirectional lamina coordinate system.

The elastic constants for the unidirectional fiber reinforced composite laminas can be found below in Table 3.1.

Table 3.1: Unidirectional lamina elastic constants [21, 23].

Glass Fiber/Epoxy (HyE 9082Af, Fiberite)		
E_{11} **(MPa)**	E_{22} **(MPa)**	E_{33} **(MPa)**
44700	12700	12700
G_{12} **(MPa)**	G_{23} **(MPa)**	G_{13} **(MPa)**
5800	4500	5800
ν_{12}	ν_{23}	ν_{13}
0.297	0.4111	0.297

The overall dimensions for the composite laminate used in this study are given below in Table 3.2. The length (L) and width (W) of the laminate were selected to follow the modeling guidelines that $L \geq 2W$ for stress field study. When measuring stress with the intent of ascertaining resultant stress concentration factors, the laminate must be sufficiently long such

that the ends of the laminate in the length direction do not influence the stress fields at the hole (or holes). This is why theory considers plates of infinite dimensions; in order to obtain the true behavior of the stress fields, without any influence from the boundaries.

Table 3.2: Composite laminate dimensions.

Stacking Sequence	Width, W (mm)	Length, L (mm)	Number of Laminas, N	Lamina Thickness, t (mm)	Laminate Thickness, H (mm)
$[0_3/(\pm45)_3/90_3]_S$	38.1	127	24	0.127	3.048

3.2.1 Quasi-Isotropic Laminate

To obtain a quasi-isotropic laminate, the individual laminas must be oriented such that the extensional stiffness matrix, $[A]$, becomes isotropic. In this manner, extension and shear become decoupled ($A_{16} = A_{26} = 0$), and the components of $[A]$ become independent of the lamina orientation. For a quasi-isotropic laminate [3],

$$[A] = \begin{bmatrix} A_{11} & A_{12} & 0 \\ A_{12} & A_{22} = A_{11} & 0 \\ 0 & 0 & A_{66} = \dfrac{A_{11} - A_{12}}{2} \end{bmatrix} \tag{3.1}$$

The above conditions for isotropic behavior apply only to the $[A]$ matrix; the $[B]$ and $[D]$ matrices may or may not be completely populated, and bending-twisting coupling is still possible. Staab [24] pointed out that for a laminate to be considered quasi-isotropic, the following conditions shall be met:

1. The total number of layers, $N \geq 3$
2. All layers shall possess identical orthotropic elastic constants (i.e. they shall be the same material) and identical thickness.
3. The orientation of the kth layer of an N-layer laminate shall be

$$\theta_k = \frac{\pi(k-1)}{N} \tag{3.2}$$

For further clarity, top views of various quasi-isotropic fiber orientations are shown below in Fig. 3.2.

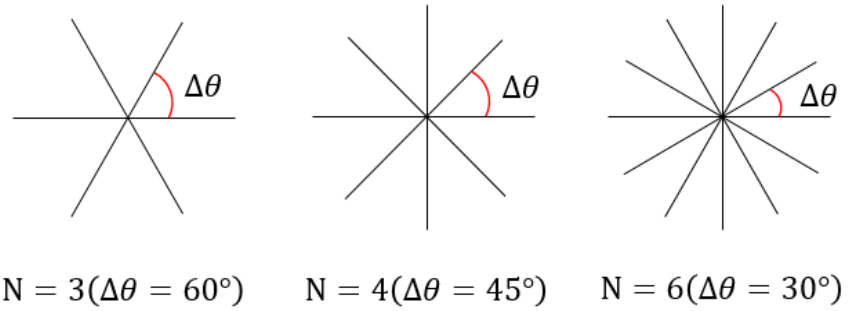

Figure 3.2: Top view of common examples of quasi-isotropic fiber orientations.

It is worth noting that an example of the general form of a quasi-isotropic stacking sequence for N=4 is $[0_n/(\pm 45)_n/90_n]_S$, where n is the number of laminas for each fiber orientation. The number of laminas, n, must be the same for the various fiber orientation angles in each general form example, in order to ensure that Eqns. 3.1 and 3.2 are satisfied.

Additionally, Mallick [3] informed that for a quasi-isotropic laminate, the elastic constants at the laminate level may be obtained via

$$E_{xx} = E_{yy} = \frac{A_{11}^2 - A_{12}^2}{hA_{11}} \tag{3.3}$$

$$\nu_{xy} = \frac{A_{12}}{A_{11}} \tag{3.4}$$

$$G_{xy} = \frac{A_{11} - A_{12}}{2h} \tag{3.5}$$

where h is the laminate thickness (equal to H in this study).

3.2.2 Laminate Stacking Sequence

The stacking sequence is chosen to reflect the quasi-isotropic construction that is commonly used in design. Balanced and symmetric stacking sequences avoid the bending-

twisting coupling. For additional clarity, the stacking sequence of the laminate used in this study is shown below in Figs. 3.3 and 3.4.[4]

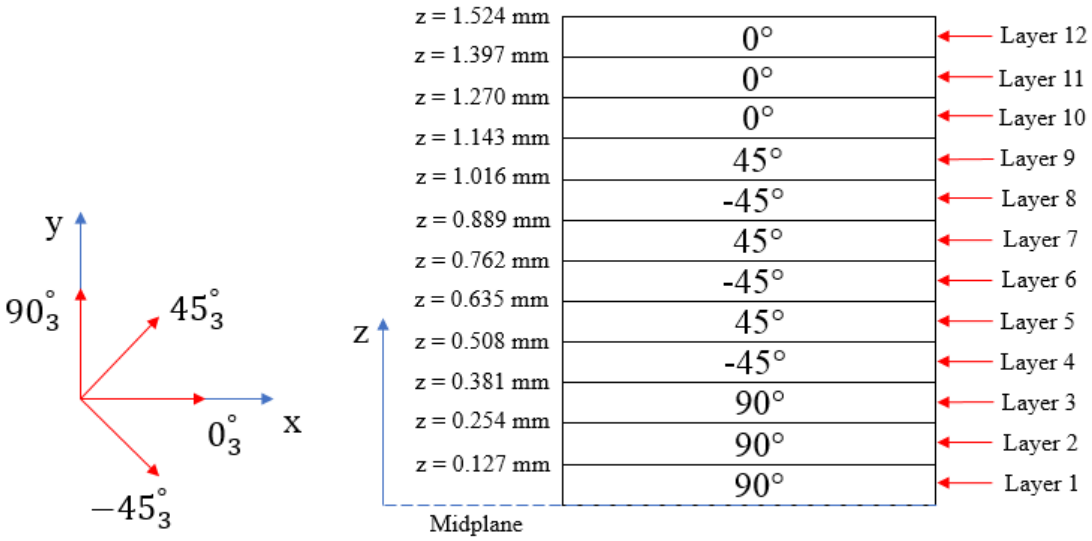

Figure 3.3: Stacking sequence for the top half of the $[0_3/(\pm45)_3/90_3]_S$ laminate.

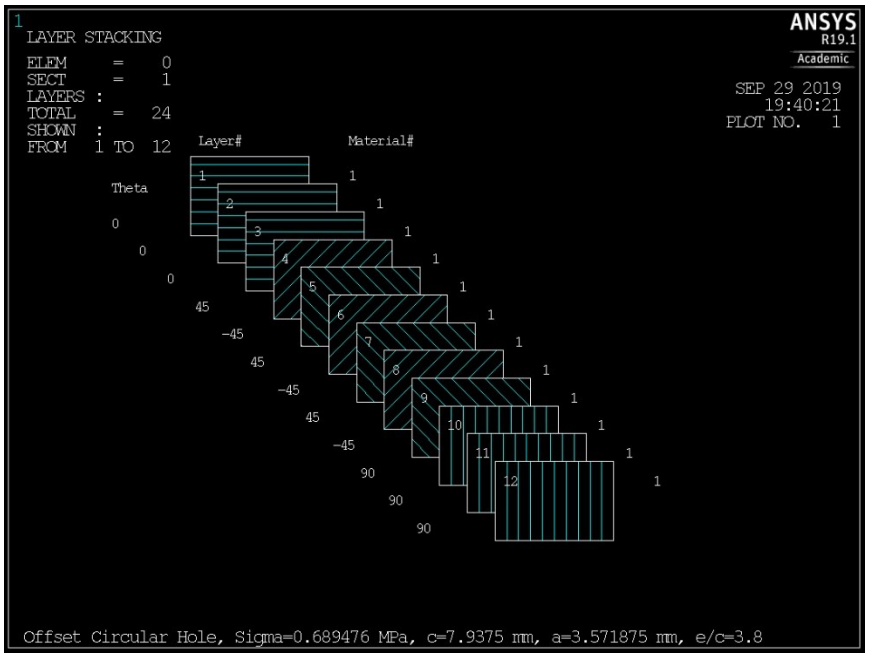

Figure 3.4: ANSYS Mechanical APDL 19.1 lamina stacking sequence for the top half of the $[0_3/(\pm45)_3/90_3]_S$ laminate.

[4] ANSYS Mechanical APDL 19.1 will only display 20 layers at a time, therefore only half of the laminate (12 layers) is shown in Fig. 3.4.

3.3 Composite Laminate Hole Configurations

The configuration for the various hole patterns and their associated dimensions are shown below in Fig. 3.5. There, d is the diameter of the circular hole (constant), d_e is the distance of the hole edge to the free edge of the laminate, d_h is the distance between the two holes, h is the height of the square hole (constant), L is the length of the laminate, r_c is the radius of the rounded corners for Hole 1 and Hole 2, and W is the width of the laminate.

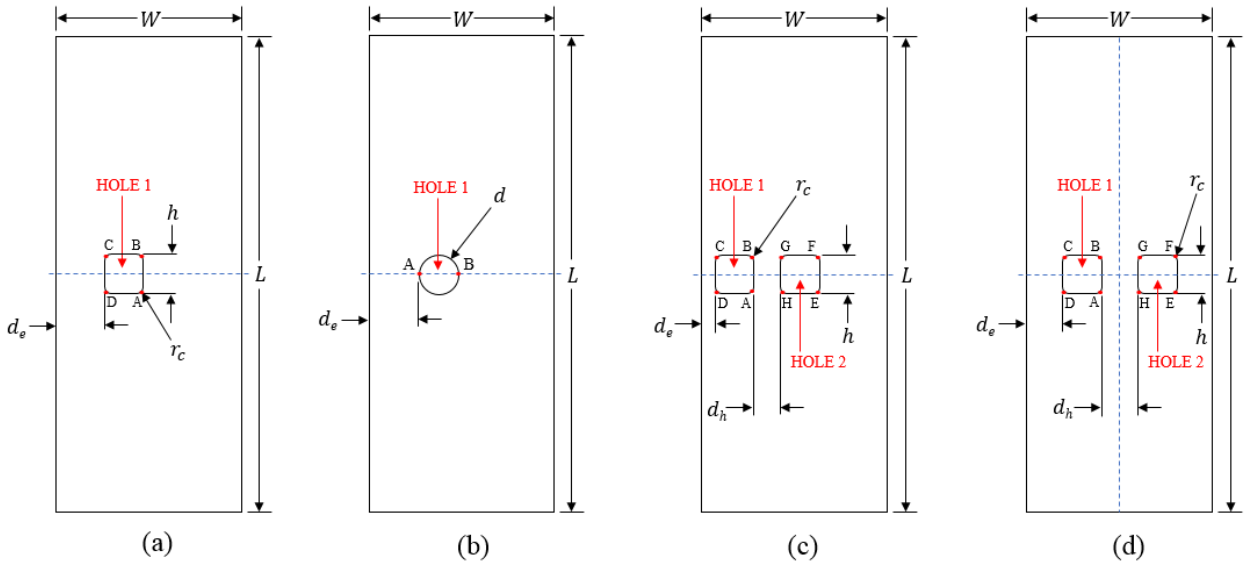

Figure 3.5: Laminate hole configurations: (a) eccentrically located single square hole with rounded corners, (b) eccentrically located single circular hole, (c) two asymmetric square holes with rounded corners, (d) two axisymmetric square holes with rounded corners.

The variables which are of particular interest to this study are d_e, d_h, and r_c. The remaining laminate geometry variables, L and W, are held constant. The laminate thickness, H, which is not shown in Fig. 3.5 is also constant. The points around the periphery of the hole or holes can range from A to H, and are points of interest where the magnitude of local stress fields is measured and recorded.

3.4 Finite Element Model Development

The finite element model is constructed via ANSYS Mechanical APDL 19.1, an industry standard analysis software. It is then validated against results from Pilkey and Pilkey [6], to ensure the integrity of the model, as discussed in Section 3.6. The Batch Mode method is used to

create the finite element model, which involves the use of an input file written in ANSYS Parametric Design Language (APDL). In this manner, the geometry and features of the model are easily controlled and modified, and the troubleshooting process becomes relatively straightforward. Because finite element problems (especially complex ones) cannot be readily solved with a model that lacks sufficient integrity, much effort has been taken to ensure that the modeling process (geometry, discretization, mesh refinement, convergence, etc.) has been followed correctly. Because this work addresses problems for which no rigorously established theoretical closed form solutions exist, it is imperative that a robust finite element model is created and used for study.

3.4.1 Element Types

The selection of element types is critical to the formulation and solution of any FE model. Some elements are better suited to model certain types of problems than others. Depending upon the problem, an element with more nodes and integration points will yield more accurate numerical results and response. However, it should be noted that while using elements with more nodes than is necessary may yield slightly more accurate results, computation time and cost of analysis will often suffer. The finite element model was constructed using two different element type approaches: 1) Using PLANE183 and SOLID186 elements, 2) Using SHELL281 elements. Although both approaches are acceptable, this was done in order to ascertain the most accurate and appropriate type of element for this study.

3.4.1.1 SOLID186 Element

The finite element model makes use of two different types of elements, due to the method in which it is constructed. Initially, an individual lamina is meshed using 2D structural elements called PLANE183, which is a solid quadrilateral containing 8 nodes. Using a loop within the user code, the lamina is copied N times and then extruded to create the laminate volume which contains N layers. The 3D continuum element SOLID186 is a hexahedron containing 20 nodes, with each node having three translational degrees of freedom: u_x, u_y, and u_z. This rectangular solid element, sometimes referred to as a “brick” element, is then used for the laminate volume. The element sizes are selected such that their aspect ratio remains under 20, as to avoid element

shape warning messages from ANSYS, and subsequent convergence issues. The PLANE183 and SOLID186 elements are shown below in Fig. 3.6.

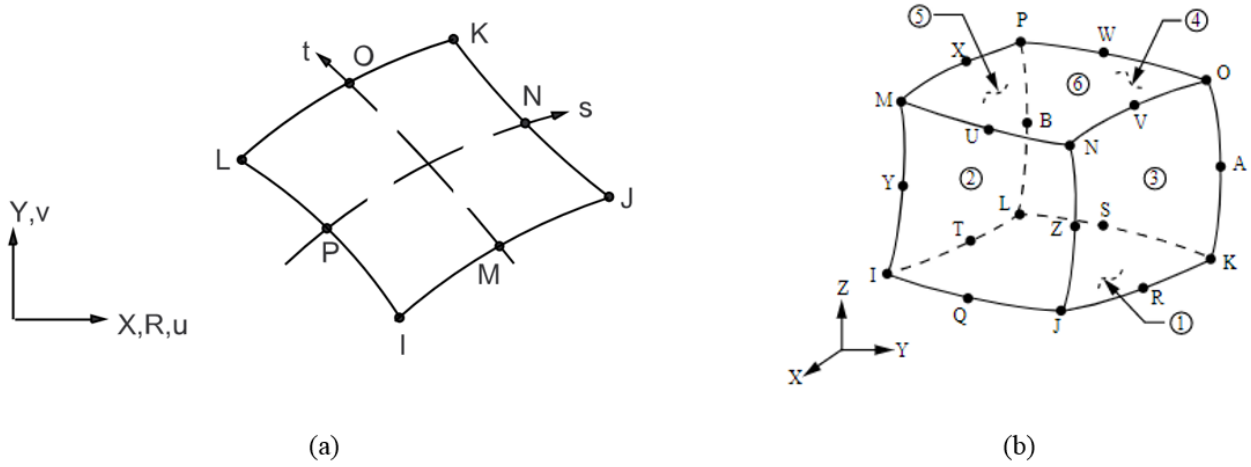

Figure 3.6: ANSYS FEA elements considered: (a) PLANE183 element (8 node quadrilateral), (b) SOLID186 element (20 node hexahedron).

3.4.1.2 SHELL281 Element

The finite element model is now constructed using the SHELL281 element, which is a structural shell quadrilateral element in 3D space. The use of shell elements in the modeling of composites is a common practice, as they tend to yield more accurate results. In fact, ANSYS Mechanical APDL user documentation recommends using shell elements (either SHELL181 or SHELL281) when modeling composites. Further, it is relatively straightforward to employ shell elements when writing the batch file, as they do not require the use of loops to generate the laminate volume. Perhaps the only drawback to using shell elements is that the graphical display of the results shows only one 2D lamina at a time, whereas with solid elements the 3D laminate can be viewed with all the contour information of every lamina present at once. The SHELL281 element contains 8 nodes with each node having six degrees of freedom (three translational: u_x, u_y, and u_z, and three rotational: θ_x, θ_y, and θ_z), and either 1, 3, 5, 7, or 9 through-thickness integration points. For this study, 5 integration points were used in all laminate configurations. It was discovered that if one intends to model surfaces which contain curvature, the presence of the three rotational degrees of freedom are both desirable, and necessary; they are not for this study. The inclusion of the rotational degrees of freedom lead to data which did not consistently obey

expected trends, nor was convergence in the FEA model possible. Consequently, additional code was implemented to eliminate the rotational degrees of freedom. The SHELL281 element allows the user to obtain stress results at three different locations in the through-thickness direction, from the top, middle, or bottom sections of the element. This can be especially useful, as the top and bottom stress results of the SHELL281 element will differ if through-thickness bending is present; it is not for this study. All stress field data were taken from the middle layer for the sake of consistency; however, all layers will yield the same results. The SHELL281 element, and its different stress result layers can be seen below in Fig. 3.7.

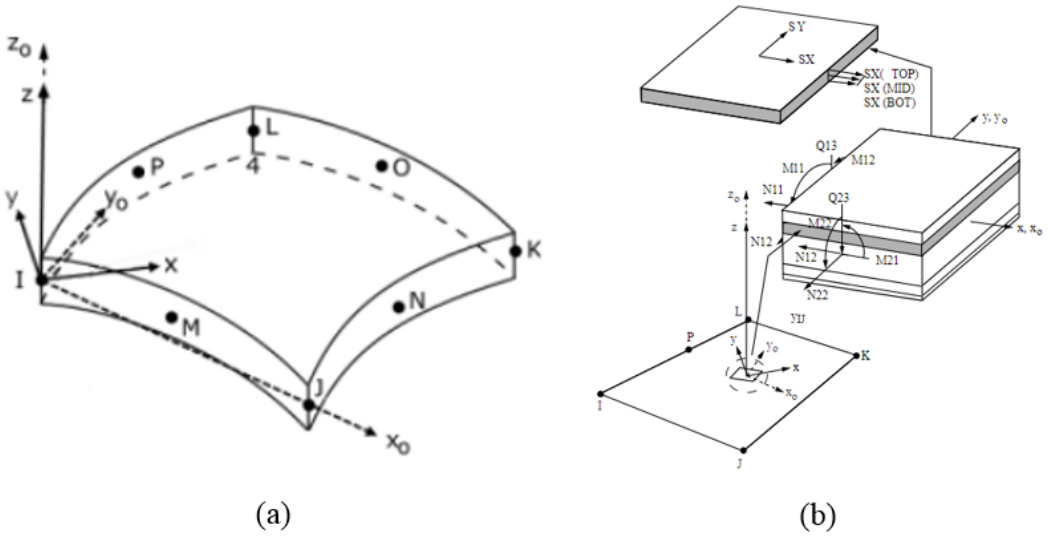

Figure 3.7: SHELL281 element: (a) SHELL281 element (8 node quadrilateral), (b) SHELL281 element layers (TOP, MID, and BOTTOM) for stress results.

3.4.2 Modeling and Mesh Generation

The methodology used in the creation of the finite element model for the composite laminate ensures that an efficient and accurate 3D model is created. As mentioned in Section 2.4.2, ANSYS has both a GUI and a CUI. Here, the latter is utilized to create the model (the GUI is used to acquire all numerical data, and stress contour plots). A bottom-up approach is used in the creation of the finite element model, and is accomplished through the use of a batch file containing user written code. While the subsequent sections detail the process for the creation of the finite element model geometry used for single hole validation, the methodology remains the same for multiple hole configurations.

3.4.2.1 Keypoints

The modeling process begins with the creation of the keypoints. Each keypoint is defined by (x, y, z) coordinates with respect to the working plane. The keypoints are then connected by lines to form areas, which will then be discretized by the mesh. The numbered keypoints are shown below in Fig. 3.8.

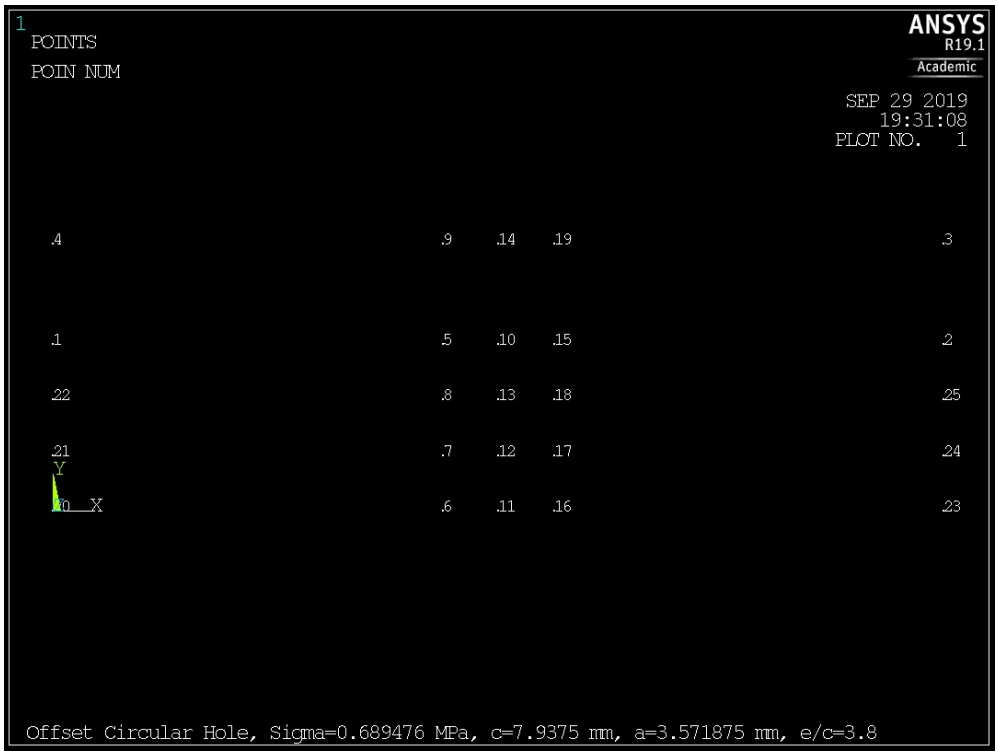

Figure 3.8: Numbered keypoints.

3.4.2.2 Areas

The areas are created by specifying the keypoints at each corner of the intended area. A Boolean subtraction is then performed to create the circular hole. Once the numbered areas have been established, they are discretized by the meshing approach specified by the user. This is described in greater detail in Section 3.6.1. The numbered areas can be seen below in Fig. 3.9.

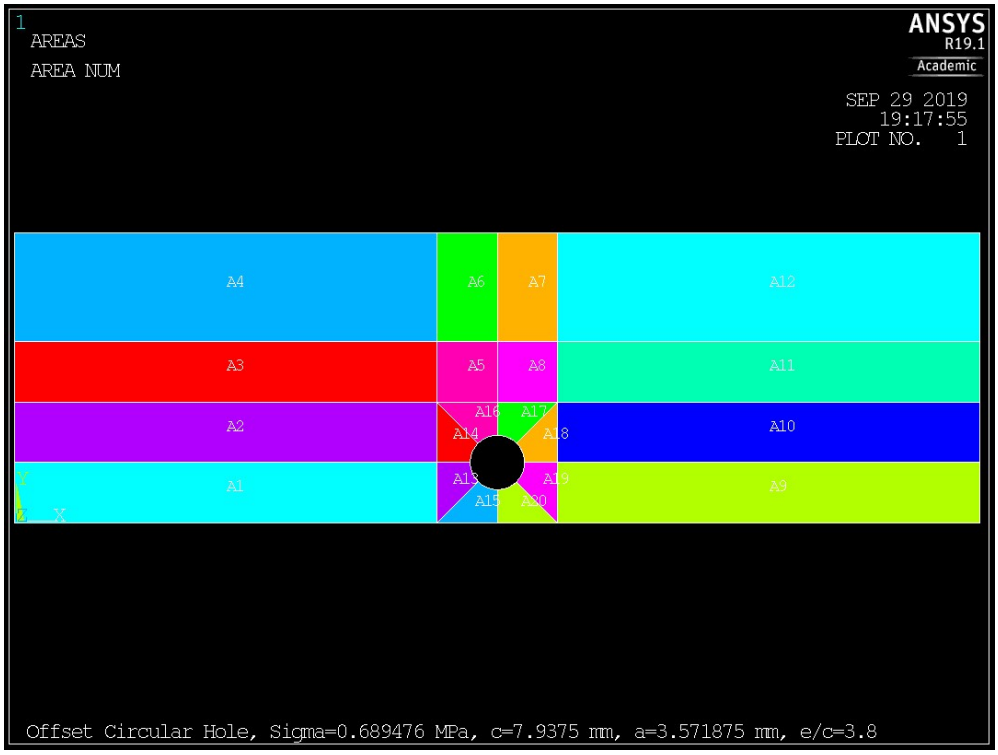

Figure 3.9: Numbered areas.

3.4.2.3 Laminate

For the case of the SOLID186 element, the laminate is generated by copying and extruding the meshed area of a lamina, as described above in Section 3.4.1.1. A completed half-laminate which will be used solely for validation, and an enlarged view depicting its 12 individual laminas are shown below in Figs. 3.10 and 3.11, respectively.

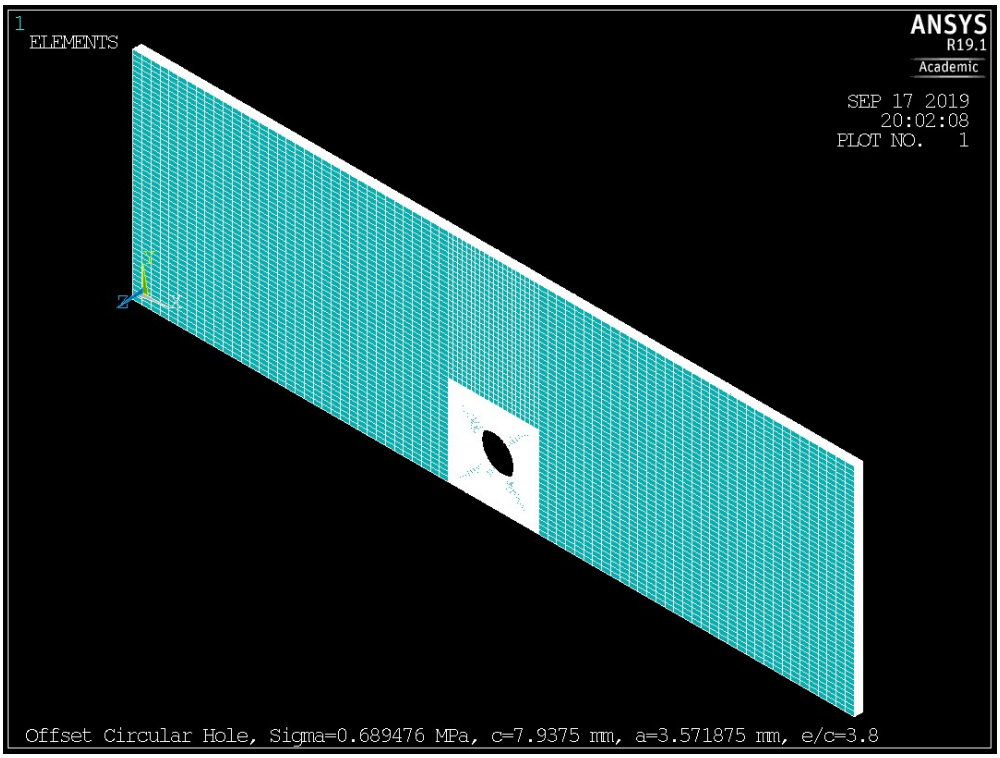

Figure 3.10: Completed half-laminate using SOLID186 elements.

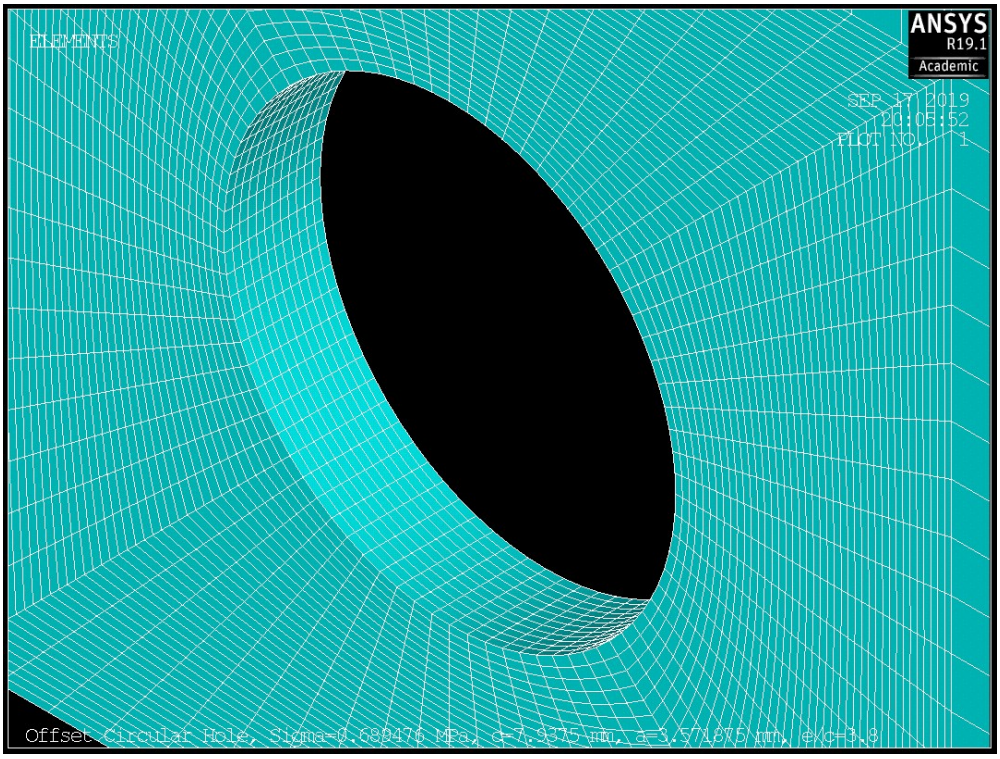

Figure 3.11: Enlarged view of the 12 laminas in the completed half-laminate using SOLID186 elements.

For the case of the SHELL281 element, the laminate is generated by specifying the number of layers and their respective fiber orientation. The laminate is represented by a sheet, which contains the laminas specified by the user. In order to view stress field contour results, the user simply specifies the layer and coordinate system to be displayed. A completed laminate which will be used solely for validation, and an enlarged view are shown below in Figs. 3.12 and 3.13, respectively.

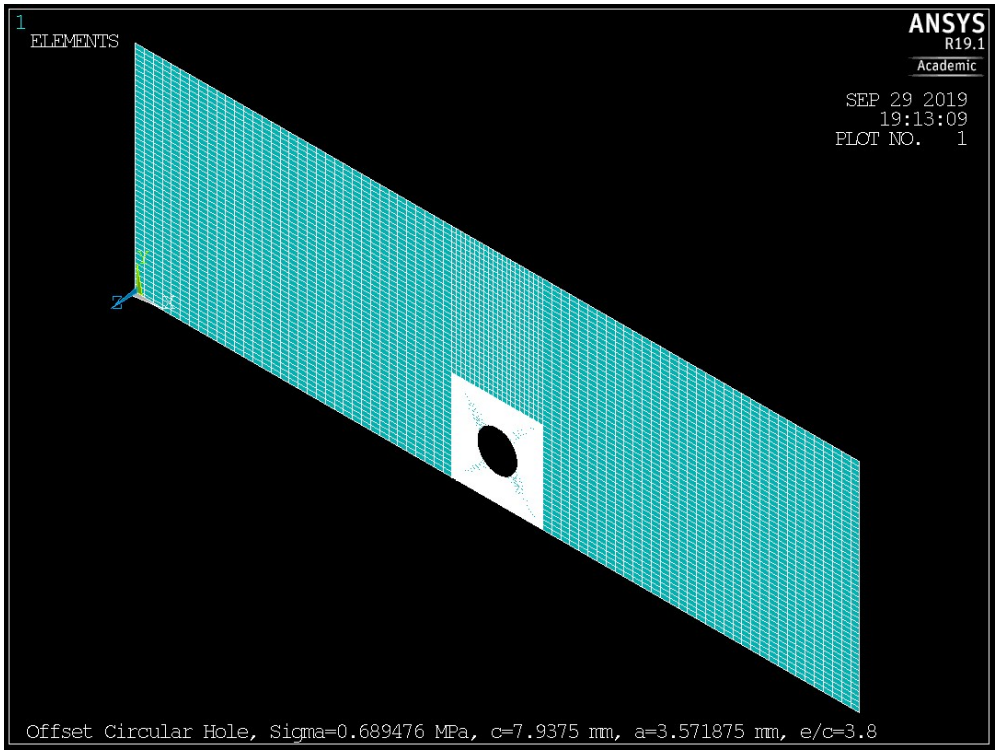

Figure 3.12: Completed laminate using SHELL281 elements.

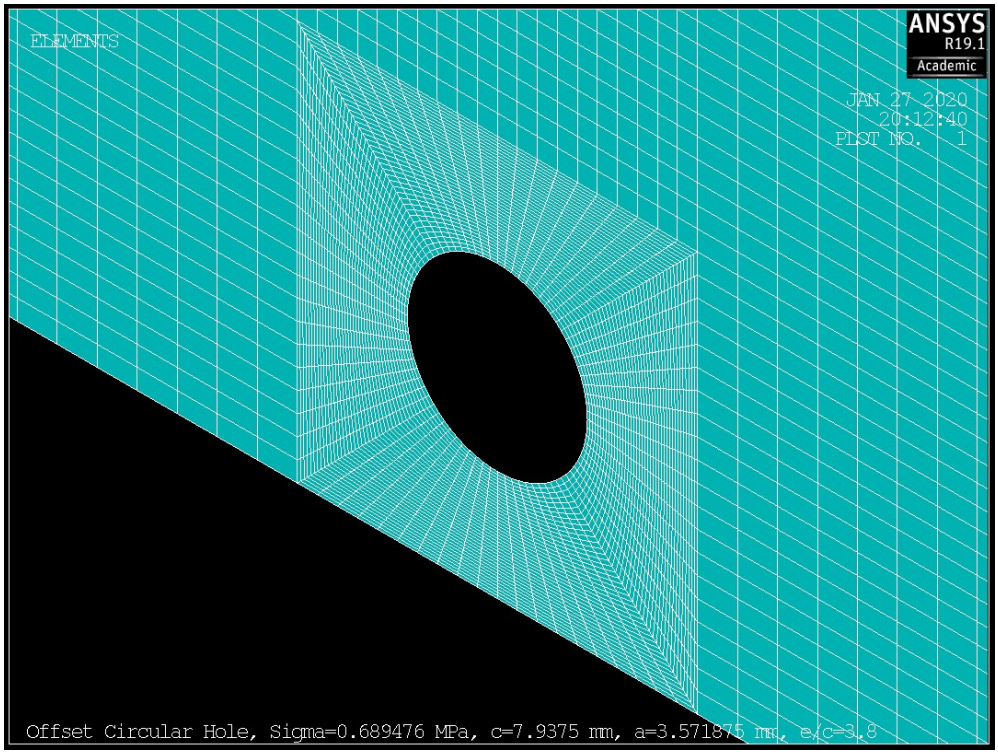

Figure 3.13: Enlarged view of the completed laminate using SHELL281 elements.

Since the general behavior of stress concentration within a notched material is known *a priori* (localization at the cutout), the finite element model can be broken into two distinct regions; areas in which stress localization is expected, and areas in which it is not. In the interest of keeping the total number of finite elements in the model at a level which does not exceed what is truly necessary, the global mesh is optimized for local analysis and overall computational efficiency. Because an accurate value of the stress gradients immediately surrounding the cutout is required for study, this region of the mesh must be sufficiently refined. To this end, square areas are defined around the holes, which serve as local regions for mesh refinement. This is addressed in Section 3.6. For the case of validation, only a single hole exists in the laminate, and thus only one square area of the mesh needs to be refined. This can be seen below in Fig. 3.14.

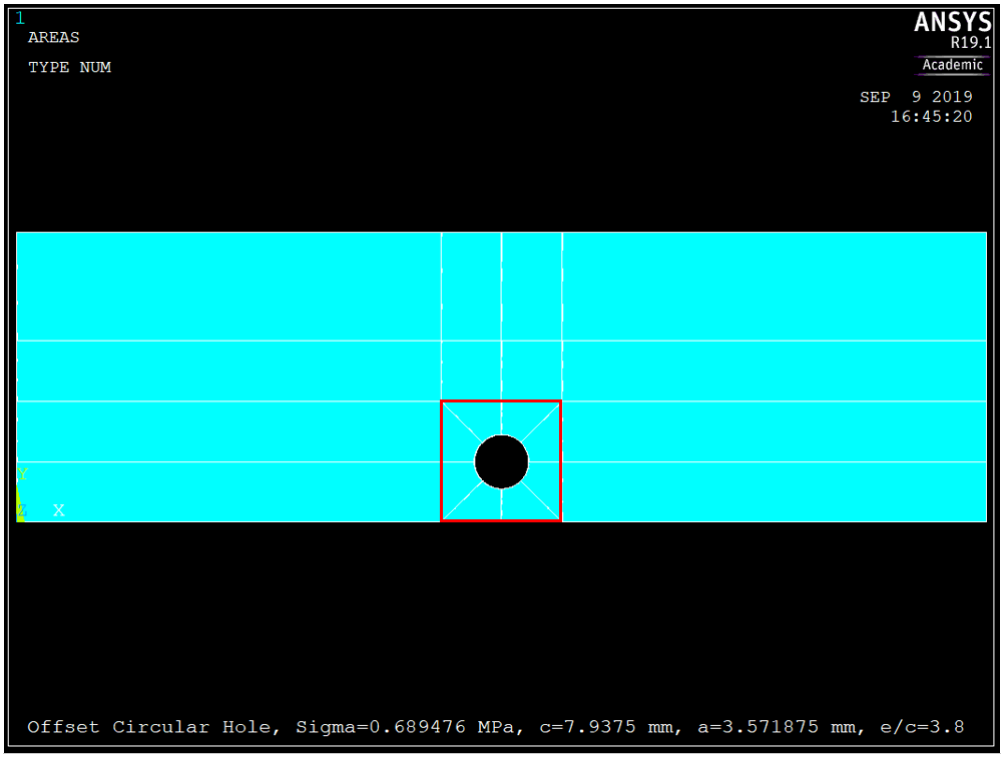

Figure 3.14: Square region (outlined in red) for local mesh refinement.

3.4.3 Boundary Conditions

The appropriate boundary conditions must be applied to the finite element model in order to ensure results which are consistent with the problem intent. It is important to make sure that the model is not overconstrained, as this would distort the stress field and produce incorrect results. In the case of the SHELL281 element, and for this particular study, only the three translational degrees of freedom must be fixed, at particular points and boundaries. User code has been implemented to remove the three rotational degrees of freedom from the SHELL281 elements. This is due to the fact that the laminate is modeled as a flat plate, thereby eliminating any curvature in the surfaces, and any consequent need for rotational degrees of freedom to capture such an effect. Further, immobilizing all six degrees of freedom explicitly would result in an overconstrained model, thereby inducing artificial stiffness, leading to inaccurate results. To eliminate the coupling effects of tension and shear and well as bending and torsion, the fiber reinforced composite laminates used in this study are all balanced, and symmetric about the midplane. Consequently, because of the lamina stacking sequence symmetry, and for the case of the PLANE183 and SOLID186 element modeling approach, only laminas which are above the

midplane need to modeled. Thus, the translational degree of freedom in the z-plane is fixed, such that all nodes with coordinates of $z = 0$ experience zero displacement ($U_z = 0$). The composite laminate is assumed to be fixed along the surface of its yz face in the longitudinal direction (x-direction) at one end ($x = L$), such that zero translational displacement occurs ($U_x = 0$). Lastly, all the nodes along a vertical center line (y-direction) are constrained such that no displacement occurs ($U_y = 0$). The nodal boundary conditions can be seen below in Fig. 3.15.

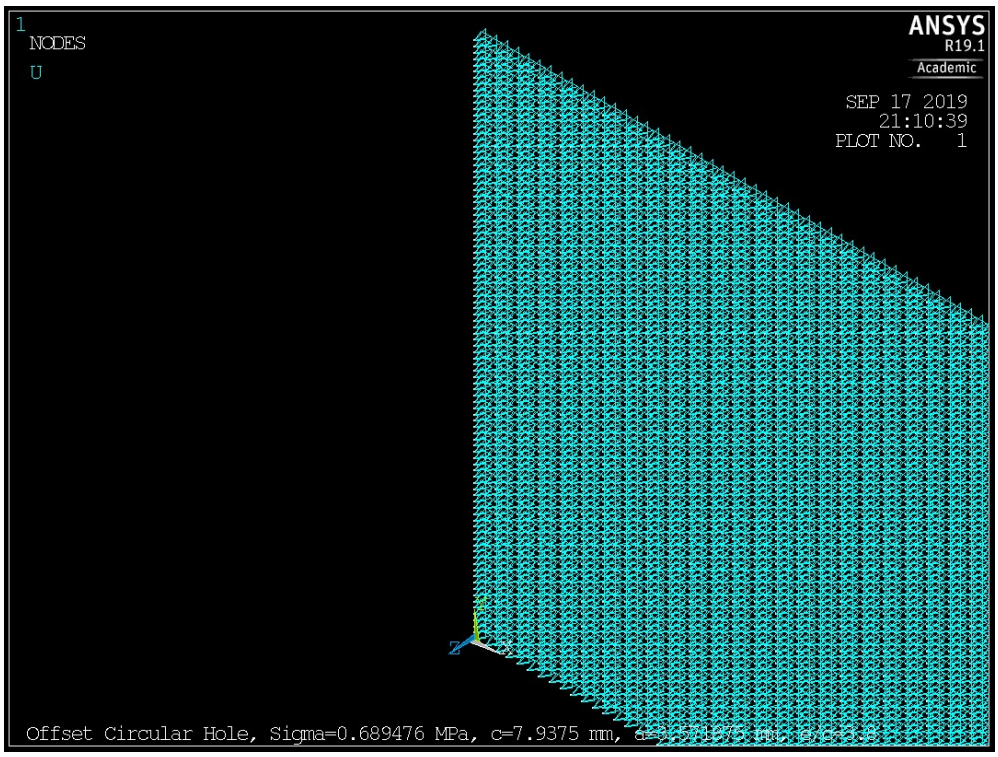

Figure 3.15: Fixed nodal boundary conditions.

3.4.4 Loading Condition

The fiber reinforced composite laminate is considered to be under a static state of in-plane uniaxial tension. In effect, the FEA simulation seeks to mimic a laboratory tension test. However, it must be noted that this is *not* a tension test. When measuring stress and resultant stress concentration factors, one needs only apply enough load such that the general behavior of the stress field is captured. This is to avoid damaging the laminas, which would influence the local stress field and will not then provide the accurate measure of the stress concentration factors. Thompson and Thompson [25] recognized that due to the round off error (≈1e-20 units)

which is present in all computer driven FEA simulations, it becomes necessary to consider all problems which would ordinarily have equal and opposite forces applied to maintain static equilibrium, as constrained on one side and loaded on the other. Such an approach is considered here; a nominal in-plane uniaxial tensile stress, σ, is applied to the yz face of the composite laminate which is not constrained ($x = 0$). ANSYS only allows a distributed force to be applied as a pressure. Because pressure is considered to act at an inward normal direction with respect to the body upon which it is applied, it must be negated in order to act as a tensile stress. For the case of the SHELL281 elements, the laminate is loaded using a force acting over a line, rather than over an area. Therefore, the applied in-plane nominal tensile stress is $\sigma = 100$ psi $= 0.689476$ MPa. Since $\sigma = F/A = F/(NtW) = N_{xx}/(Nt)$, the applied uniform line load (or normal force resultant) is $N_{xx} = \sigma Nt$. Consequently, the linear load that must be applied to the $[0_3/(\pm 45)_3/90_3]_S$ laminate in ANSYS, is $N_{xx} = 0.689476$ MPa $*$ 24 layers $*$ 0.127 mm/layer $=$ 2.10152 N/mm. The loading condition (vertical red line) along with the individual nodes (white dots) for the $[0_3/(\pm 45)_3/90_3]_S$ laminate using the SHELL281 element can be seen below in Fig. 3.16.

Figure 3.16: Applied negative uniform linear load at $x = 0$, for the SHELL281 laminate.

For the case of the laminate model which uses SOLID186 elements, the applied in-plane nominal tensile stress is the same, $\sigma = 100$ psi $= 0.689476$ MPa, however the stress is applied over the unconstrained *surface* of the laminate at $x = 0$, as opposed to using a uniform linear force in the case of the SHELL281 model. This can be seen below in Fig. 3.17.

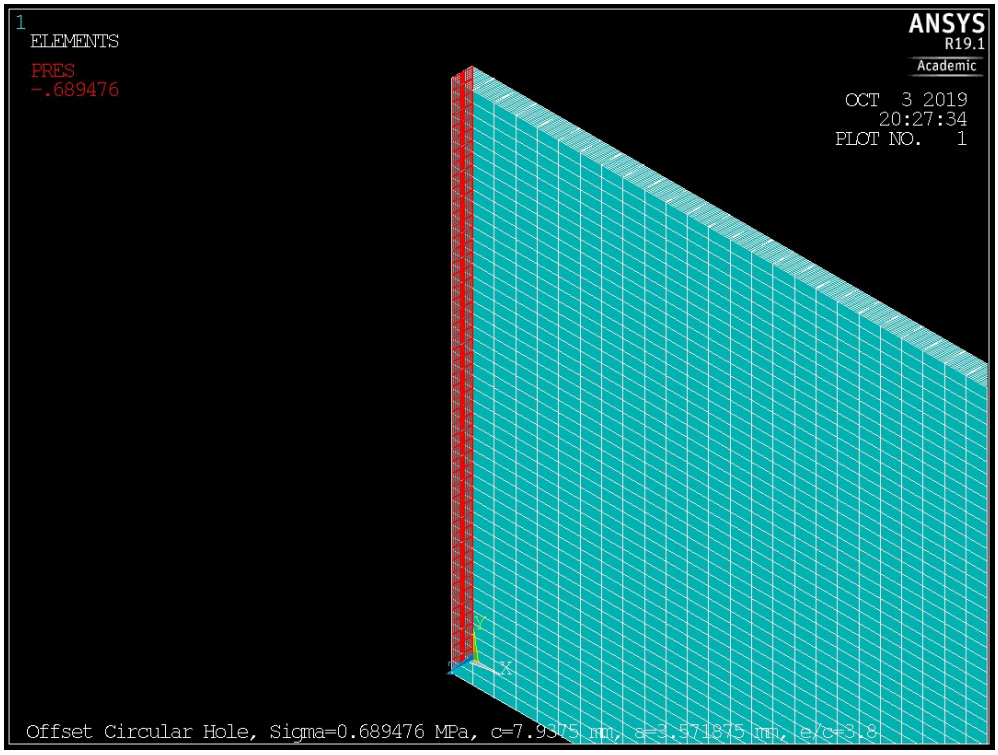

Figure 3.17: Applied negative uniform surface pressure at $x = 0$, for the SOLID186 half-laminate.

3.4.5 Reaction Forces

The reaction forces should reflect the proper constraint of the laminate based upon the applied loading. These include nodal forces (NFOR) and reaction forces (RFOR). Their locations and directions are as expected, based upon the applied external loading and constraint. The nodal forces (pink arrows) and reaction forces (purple arrows) can be seen below in Fig. 3.18.

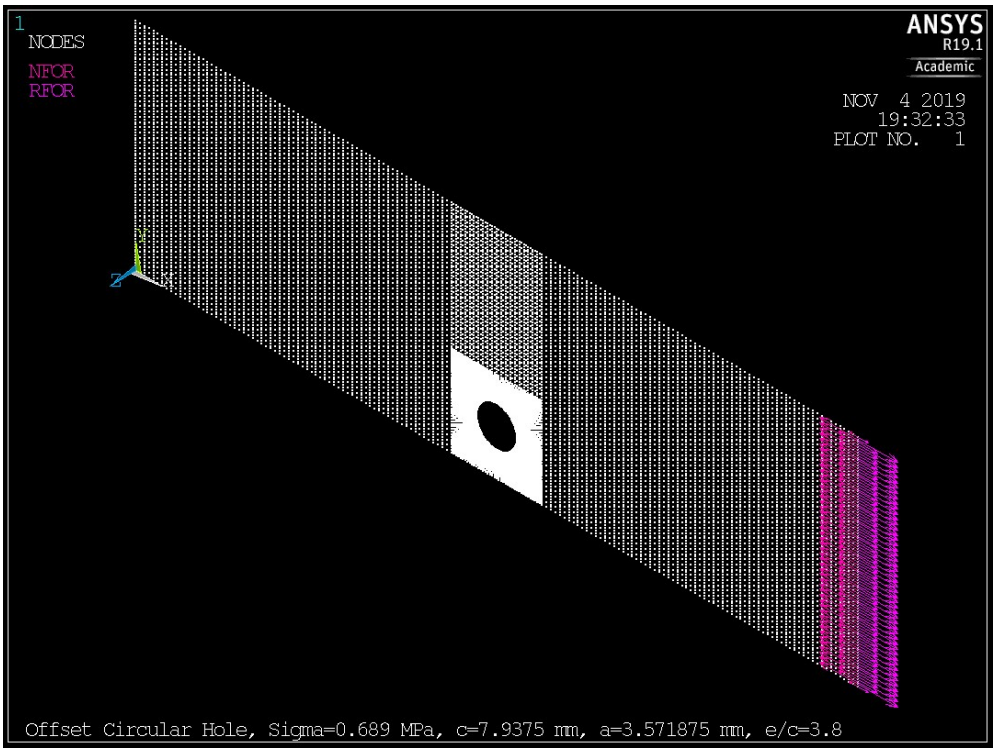

Figure 3.18: Nodal forces and reaction forces at the constrained edge $x = L$ (the right edge).

3.5 Validation

It is critical to validate the finite element model against previous research results which are well defined, and universally accepted. This ensures accuracy of the modeling technique, and brings confidence to the results developed in later sections. Consequently, the ANSYS model is compared to the results obtained from Pilkey and Pilkey [6]. There, the "edge effect" for an eccentrically located single circular hole in an isotropic plate of finite width subjected to a remotely applied in-plane uniaxial tensile stress was investigated. In the interest of a thorough comparison, both gross and net stress concentration factors are explored. The closed form solution for the stress concentration factor based upon gross area is

$$K_{tg} = C_1 + C_2\left(\frac{a}{c}\right) + C_3\left(\frac{a}{c}\right)^2 + C_4\left(\frac{a}{c}\right)^3 \tag{3.6}$$

where

$$C_1 = 2.9969 - 0.0090\left(\frac{c}{e}\right) + 0.01338\left(\frac{c}{e}\right)^2 \tag{3.7}$$

$$C_2 = 0.1217 + 0.5180\left(\frac{c}{e}\right) - 0.5297\left(\frac{c}{e}\right)^2 \tag{3.8}$$

$$C_3 = 0.5565 + 0.7215\left(\frac{c}{e}\right) + 0.6153\left(\frac{c}{e}\right)^2 \tag{3.9}$$

$$C_4 = 4.082 + 6.0146\left(\frac{c}{e}\right) - 3.9815\left(\frac{c}{e}\right)^2 \tag{3.10}$$

where a is the hole radius, c is the distance from the close edge of the plate to the center of the circular hole, and e is the distance from the far edge of the plate to the center of the circular hole. The maximum stress at point B is then simply

$$\sigma_{max} = \sigma_B = K_{tg}\sigma \tag{3.11}$$

The closed form solution for the stress concentration factor based upon net area is

$$K_{tn} = C_1 + C_2\left(\frac{a}{c}\right) + C_3\left(\frac{a}{c}\right)^2 \tag{3.12}$$

where

$$C_1 = 2.989 - 0.0064\left(\frac{c}{e}\right) \tag{3.13}$$

$$C_2 = -2.872 + 0.095\left(\frac{c}{e}\right) \tag{3.14}$$

$$C_3 = 2.348 + 0.196\left(\frac{c}{e}\right) \tag{3.15}$$

where all variables are as defined above. The maximum stress at point B is then

$$\sigma_{max} = \sigma_B = K_{tn}\sigma_{nom} \tag{3.16}$$

where

$$\sigma_{nom} = \frac{\sigma\sqrt{1-(a/c)^2}}{1-(a/c)} \frac{1-(c/H)}{1-(c/H)\left[2-\sqrt{1-(a/c)^2}\right]} \tag{3.17}$$

where H is the width of the plate, and all other variables are as defined above. The corresponding stress concentration factors chart from Pilkey and Pilkey (p. 272) [6] can be seen below in Fig. 3.19.

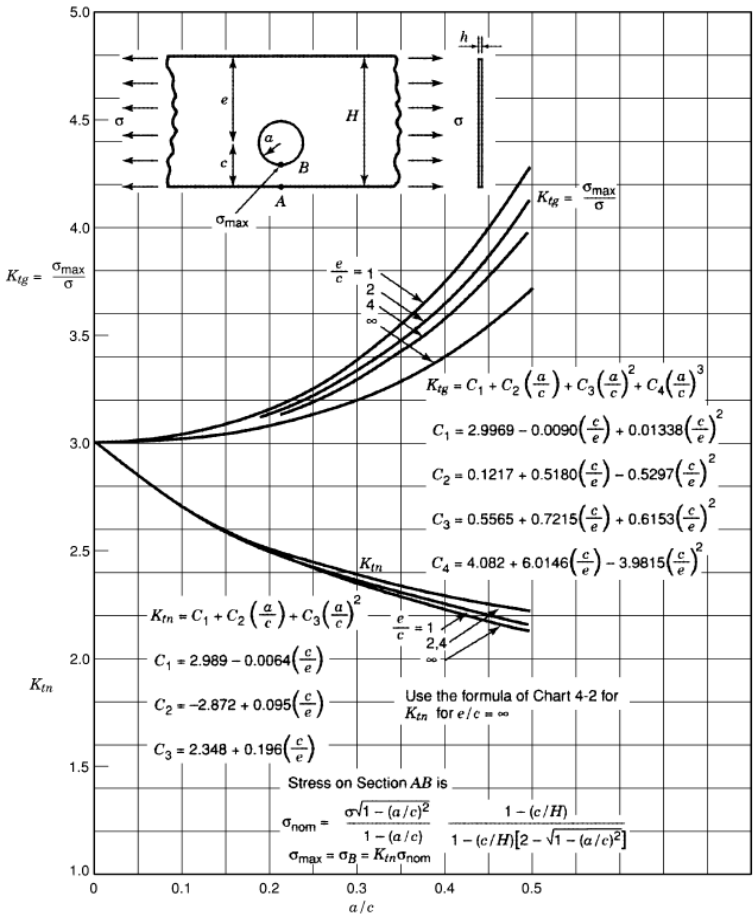

Figure 3.19: Stress concentration factors for a finite width isotropic plate in uniaxial tension with an eccentrically located single circular hole (based upon mathematical analysis of Sjöström 1950) [6].

Since the above results from Pilkey and Pilkey [6] are for that of a homogeneous isotropic plate, the validation was conducted with an isotropic material, namely A36 steel. To change the ANSYS composite model, one may simply alter the material properties in the code to that of A36 steel in the following manner:

$$E_{11} = E_{22} = E_{33} \tag{3.18}$$

$$G_{12} = G_{13} = G_{23} = \frac{E_{11}}{2(1+\nu_{12})} \tag{3.19}$$

$$\nu_{12} = \nu_{13} = \nu_{23} \tag{3.20}$$

The above properties of A36 steel are given below in Table 3.3.

Table 3.3: Material properties for A36 steel [26].

Young's Modulus, E_{11} (GPa)	Shear Modulus, G_{12} (MPa)	Poisson's Ratio, ν_{12}
200	79365.1	0.26

3.6 Convergence

Perhaps one of the most important steps in the proper use of finite element software to solve problems is the test for convergence. In the sections below, the mesh is refined until the number of elements used no longer significantly affects the results provided by ANSYS. The initial instinct is typically that "more is better", however, computer models with vast amounts of elements can take many hours to solve, which can be time consuming and expensive. Therefore, an initial test for convergence avoids unnecessary effort, and serves to validate both the model and the approach. In the interest of a simple comparison to the theoretical results, Sections 3.6.1-3.6.3 consider the above from Pilkey and Pilkey [6]. It is important to recall that the finite element method (FEM) obtains only *approximate* solutions. However, these are often within 1%-5% of the theoretical solution, provided the mesh is sufficiently refined and the problem is accurately modeled. This is discussed and demonstrated in the following sections.

3.6.1 Mesh Sensitivity

Since the approximate location of the stress concentration is known, only the meshed areas immediately surrounding the hole need to be refined, as this is where stress field data will be acquired. To demonstrate convergence, this square area is discretized into a progressively increasing number of elements, which is shown in Sections 3.6.1.1-3.6.1.4. Throughout this study a mapped meshing approach is used. This allows for greater control over discretization; element size, shape, aspect ratio, and number of elements can all be controlled with relative ease. Further, meshes generated using this approach are more regular and geometrically structured. Consequently, a mapped mesh is more computationally well-behaved. In order to ensure that a sufficient amount of the stress field surrounding the hole is accurately captured, the width and height of the square area for local mesh refinement is taken to be equal to half of the laminate width, or $w = h = W/2 = 38.1 \text{ mm}/2 = 19.05 \text{ mm}$. It should be noted for the cases of offset holes and multiple holes, this square area must shrink as the hole approaches the edge of the laminate, or becomes within proximity of another hole. It is important to recognize that the introduction of discretization into the problem brings inherent approximation error. However, this can be mitigated by increasing the number of elements in the mesh. This is perhaps somewhat at odds with previous statements regarding the unnecessary use of large numbers of elements. The progression from a coarse mesh to a very fine mesh serves to illustrate the correlation between the number of finite elements used in the mesh and the accuracy of the simulated stress results. In effect, this is an analysis of mesh sensitivity. The accuracy of the solution, namely the stress gradient results, will depend upon the mesh density. As expected, a finer mesh will yield a more accurate solution due to a greater number of nodes being used in computation. It is important to note that all stress data acquired in this study is from the *nodal* solution provided by ANSYS. The nodal stress solution, as opposed to the elemental stress solution, is an average of the stresses at the nodes. This averaged nodal solution results in a stress field contour which is continuous across the elements. Such results are achieved through nodal integration, as opposed to Gauss point integration used in the elemental solution. Ultimately, the mesh must be refined to a degree such that the stress/strain gradients are captured at a level which most accurately reflects reality. Once an acceptable amount of error is achieved, the addition of more elements serves only to hinder the CPU effort, subsequent computational time, and cost of FEA simulation.

3.6.1.1 Coarse Mesh

The test for convergence begins with a finite element model which possesses a coarse mesh. The level of mesh refinement is very low, and consequently, the accuracy of the expected stress results is also very low. It is important to note the number of elements in the square area surrounding the hole. As the convergence process evolves, this area will become more refined, and hence increase in its number of elements. The coarse mesh can be seen below in Fig. 3.20.

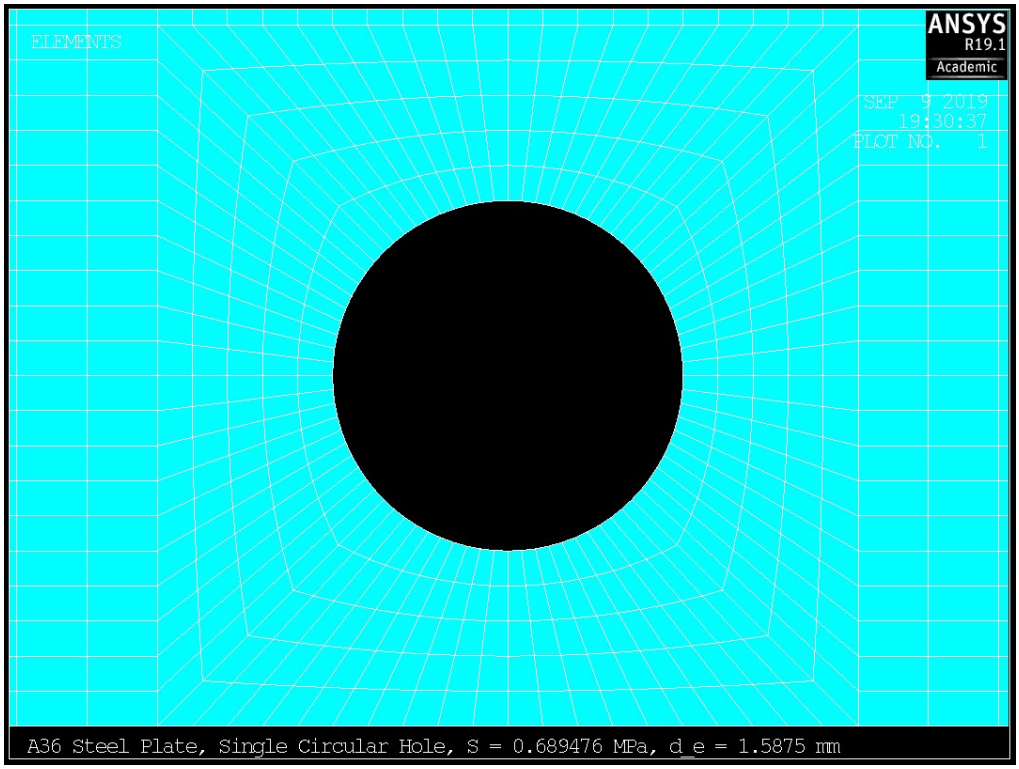

Figure 3.20: Coarse mesh.

The number of elements within the square area which surrounds the hole is directly related to the accuracy of the stress results. In Fig. 3.20 above, the number of circular division lines in the square area is equal to four, and the number of radial division lines is 80. The element count for the square area is given below in Table 3.4.

Table 3.4: Number of elements in square area for coarse mesh.

Circular Division Lines	Radial Division Lines	Number of Elements
4	80	400

3.6.1.2 Medium Mesh

Here the degree of mesh refinement is slightly greater than before, but the expected accuracy of the stress results is still very low. It is anticipated that the mesh will still need to be refined two more times before mesh sensitivity is sufficiently eliminated. The medium mesh can be seen below in Fig. 3.21.

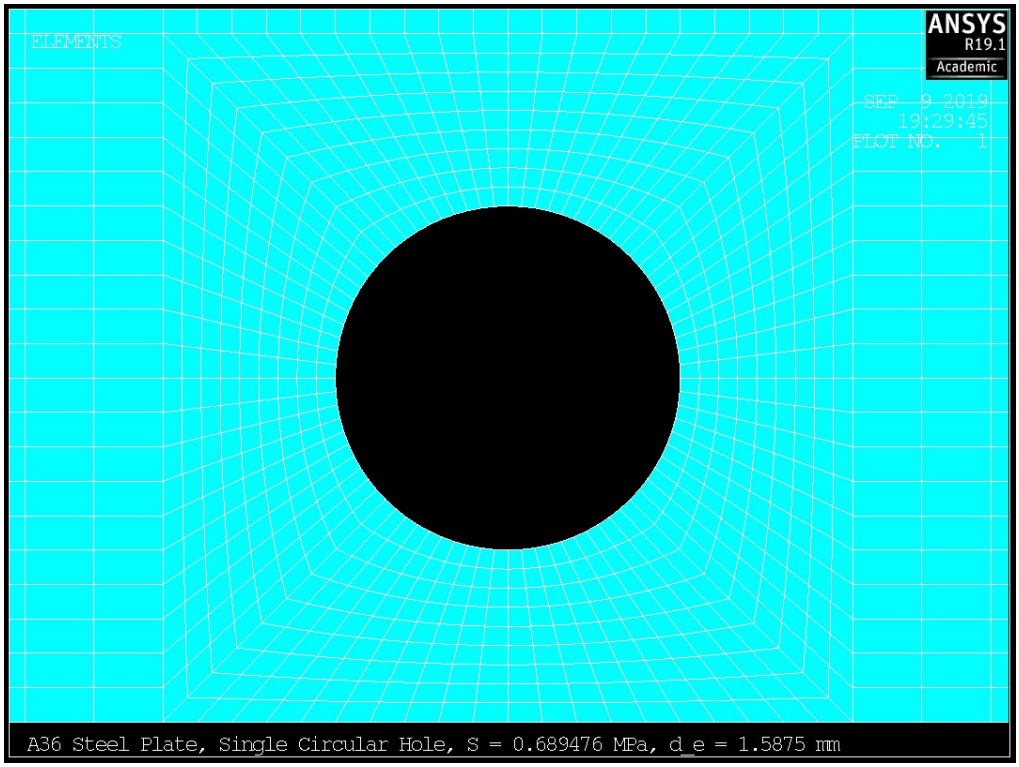

Figure 3.21: Medium mesh.

Now the number of circular division lines in the square area has increased to eight. The number of radial division lines remains 80. The element count for the square area is given below in Table 3.5. It can be seen that the number of elements in the medium mesh is now almost double that of the coarse mesh.

Table 3.5: Number of elements in square area for medium mesh.

Circular Division Lines	Radial Division Lines	Number of Elements
8	80	720

3.6.1.3 Fine Mesh

The third mesh refinement step will yield much better results than the previous two, yet still retains a degree of sensitivity. The fine mesh can be seen below in Fig. 3.22.

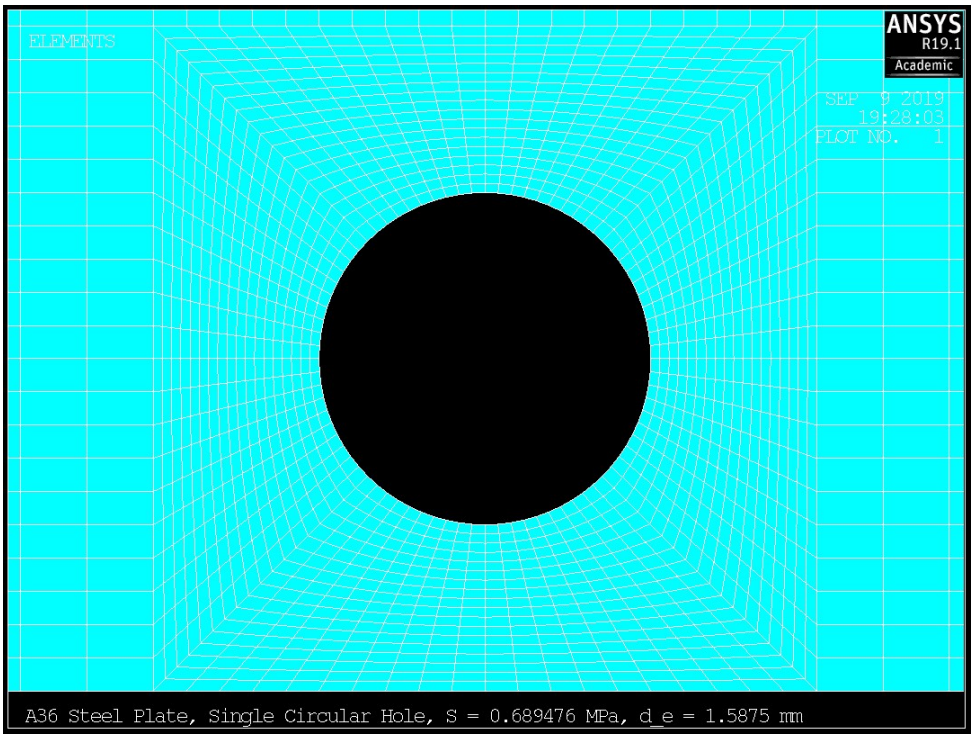

Figure 3.22: Fine mesh.

At this stage of mesh refinement, the number of circular division lines in the square area has increased to 17. The number of radial division lines is again 80. The element count for the square area is given below in Table 3.6.

Table 3.6: Number of elements in square area for fine mesh.

Circular Division Lines	Radial Division Lines	Number of Elements
17	80	1440

3.6.1.4 Very Fine Mesh

Following a number of mesh refinement iterations, the mesh sensitivity has been almost completely eliminated, and is sufficiently refined. The resulting stress field behavior can now be captured with a high level of accuracy, and the very fine mesh can be seen below in Fig. 3.23.

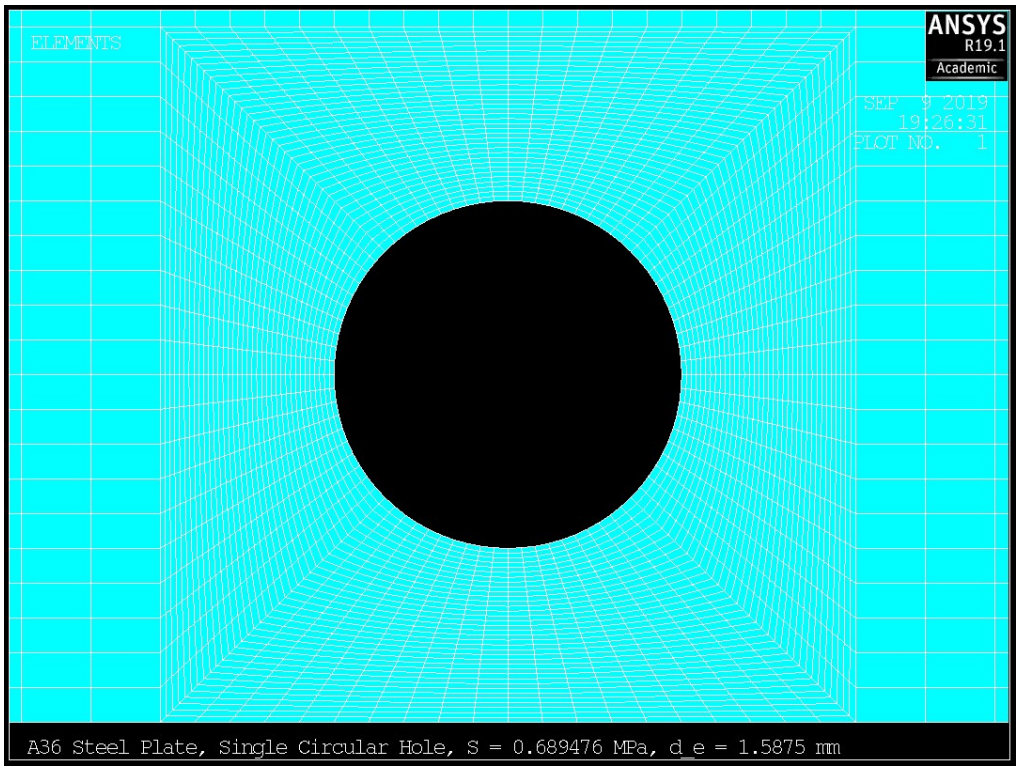

Figure 3.23: Very fine mesh.

In the final level of local mesh refinement, the number of circular division lines in the square area has increased to 35. The number of radial division lines remains unchanged at 80. The element count for the square area is given below in Table 3.7.

Table 3.7: Number of elements in square area for very fine mesh.

Circular Division Lines	Radial Division Lines	Number of Elements
35	80	2880

3.6.2 Theoretical Results

By using Eqns. 3.6-3.17, and plotting the result on the stress chart below in Fig. 3.24 for the circular hole, at point B, with $a/c = 0.45$, and $e/c = 3.8$, the stress concentration factor based upon gross area and net area, is $K_{tg} = 3.7459$ and $K_{tn} = 2.2933$, respectively. Therefore, since the local stress at section AB, σ_{nom} , can be calculated based upon the applied stress, σ, the maximum stress at point B for gross and net area are $\sigma_{max} = 3.7459\sigma$, and $\sigma_{max} = 2.2933\sigma_{nom}$, respectively.

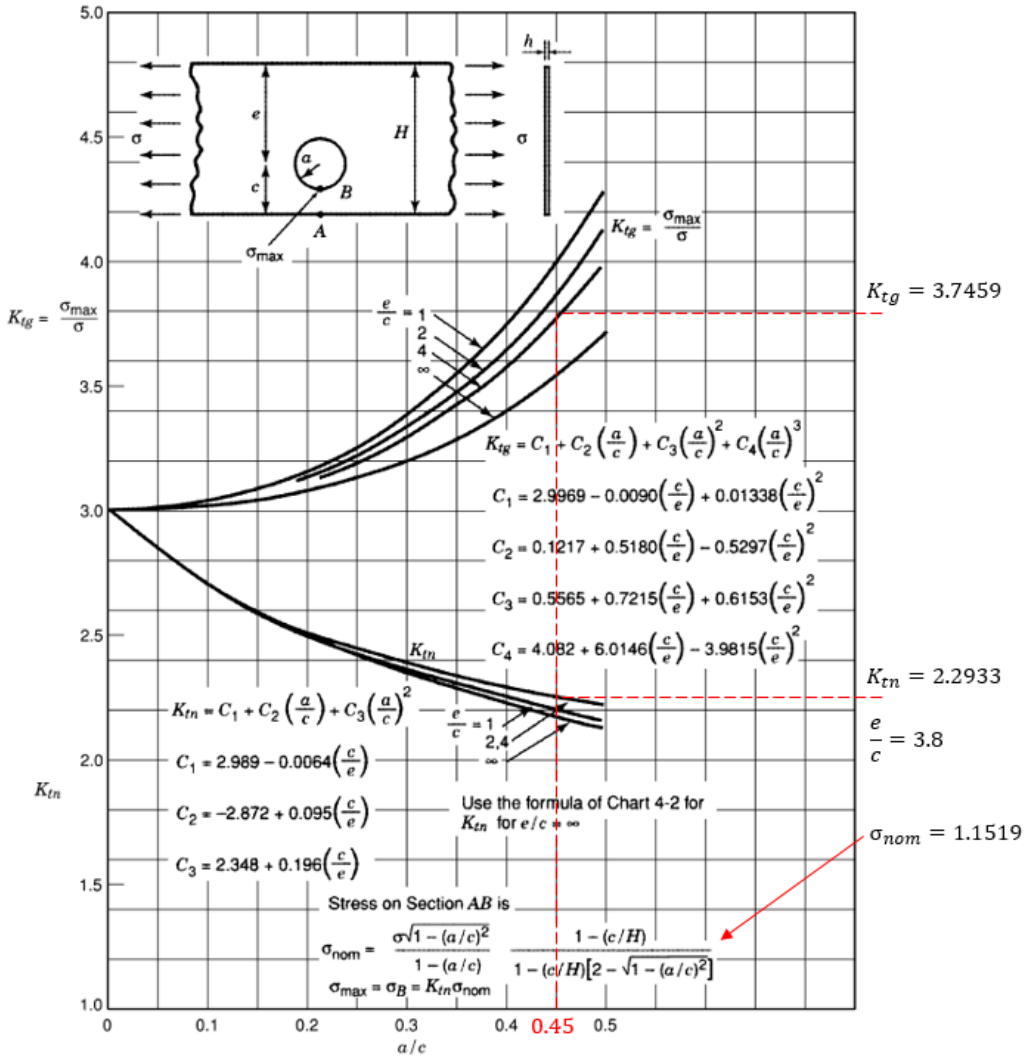

Figure 3.24: Stress concentration factors for gross and net area [6].

3.6.3 Convergence Results

The final step in the convergence process is to summarize the information, and calculate the error between the FEA and experimental results for the two types of element approaches, such that the accuracy of the ANSYS finite element model may be understood. A comparison is also made between the acquired stress data, and the theoretical stress based upon the two types of stress concentration factors, K_{tg} and K_{tn}. The ANSYS mesh sensitivity results for the two different element modeling approaches, SOLID186 and SHELL281, are shown in Figs. 3.25 and 3.26, respectively. Data regarding the validation and calculated error for both the SOLID186 and SHELL281 models can be found below in Tables 3.8 and 3.9, respectively.

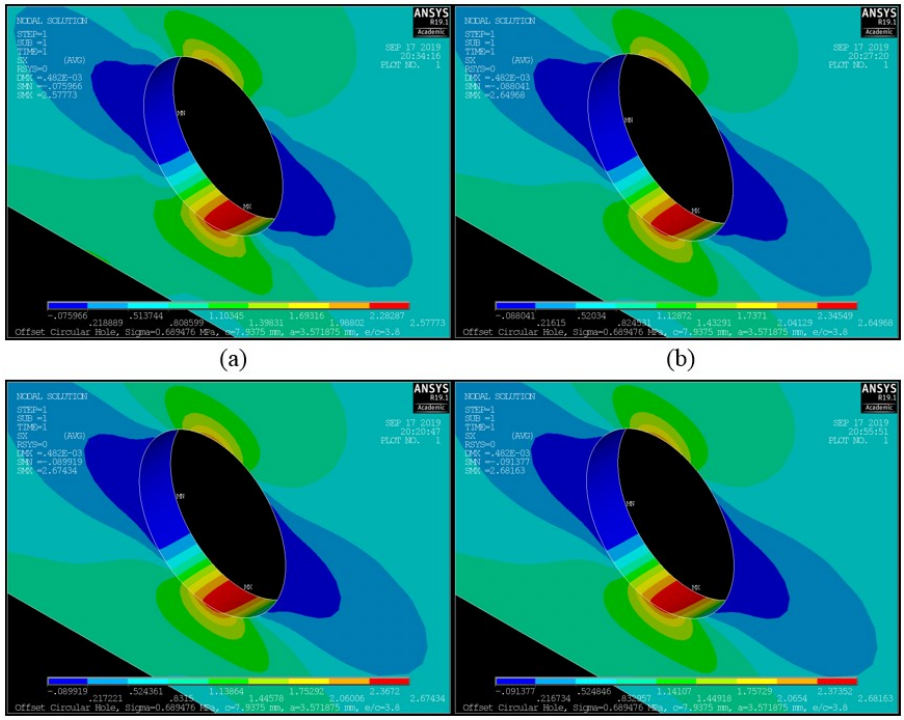

Figure 3.25: SOLID186 mesh results: (a) coarse, (b) medium, (c) fine, (d) very fine.

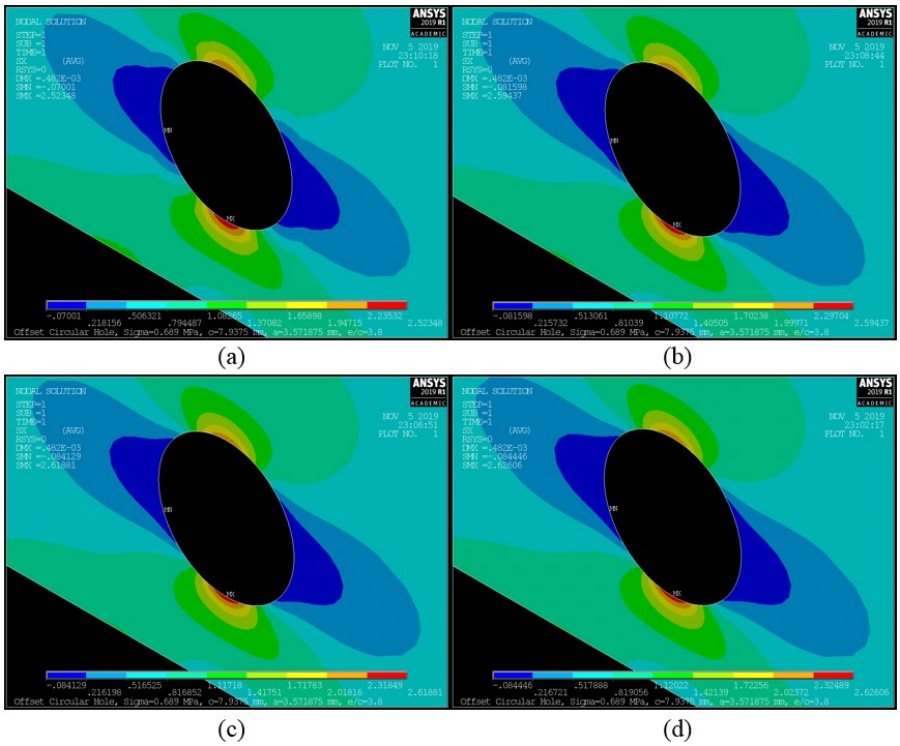

Figure 3.26: SHELL281 mesh results: (a) coarse, (b) medium, (c) fine, (d) very fine.

Table 3.8: Correlation between number of elements to SOLID186 FEA stress result accuracy.

Local Mesh Refinement	Total Number of SOLID186 Elements	Total Number of SOLID186 Nodes	SOLID186 FEA Stress, $\sigma_{x,max}$ (MPa)	Theoretical Stress, $\sigma_{x,max}$ (MPa) Based on K_{tg}	FEA $\sigma_{x,max}$ versus K_{tg} Theoretical $\sigma_{x,max}$ % Error	Theoretical Stress, $\sigma_{x,max}$ (MPa) Based on K_{tn}	FEA $\sigma_{x,max}$ versus K_{tn} Theoretical $\sigma_{x,max}$ % Error	ANSYS Runtime
Coarse	51840	373560	2.5777	2.5827	0.193	2.6417	2.423	2 min 38 sec
Medium	56640	407160	2.6497		2.593		0.301	3 min 2 sec
Fine	66240	474360	2.6743		3.548		1.234	4 min 33 sec
Very Fine	85440	608760	2.6816		3.830		1.510	6 min 57 sec

Table 3.9: Correlation between number of elements to SHELL281 FEA stress result accuracy.

Local Mesh Refinement	Total Number of SHELL281 Elements	Total Number of SHELL281 Nodes	SHELL281 FEA Stress, $\sigma_{x,max}$ (MPa)	Theoretical Stress, $\sigma_{x,max}$ (MPa) Based on K_{tg}	FEA $\sigma_{x,max}$ versus K_{tg} Theoretical $\sigma_{x,max}$ % Error	Theoretical Stress, $\sigma_{x,max}$ (MPa) Based on K_{tn}	FEA $\sigma_{x,max}$ versus K_{tn} Theoretical $\sigma_{x,max}$ % Error	ANSYS Runtime
Coarse	4320	13316	2.5235	2.5827	2.293	2.6417	4.476	2 sec
Medium	4720	14516	2.5944		0.451		1.793	2 sec
Fine	5520	16916	2.6188		1.398		0.868	3 sec
Very Fine	7120	21716	2.6261		1.678		0.593	3 sec

The trend between the number of elements in the finite element model and their relationship to the maximum stress in the x-direction, $\sigma_{x,max}$, as calculated by ANSYS for the SOLID186 and SHELL281 elements are shown below in Fig. 3.27 and 3.28, respectively.

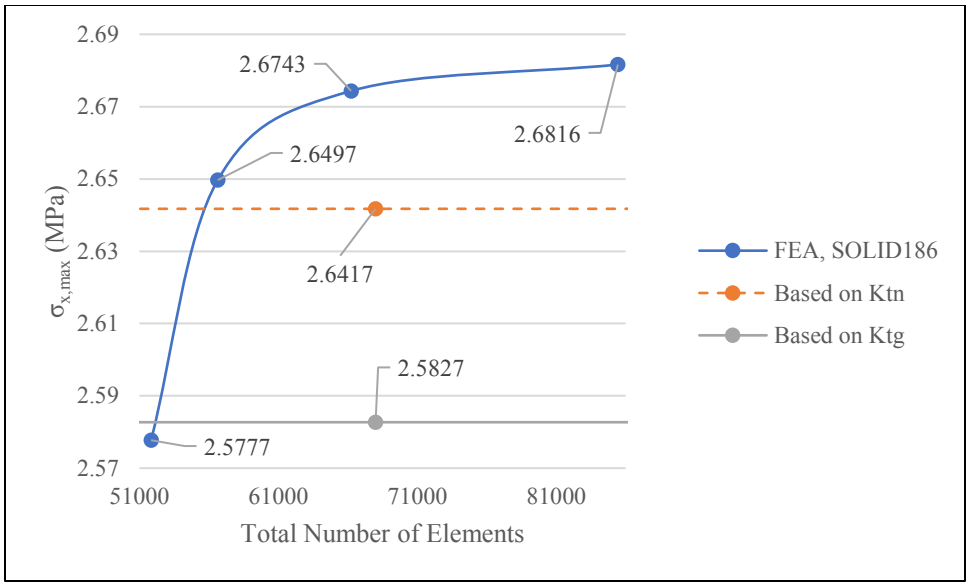

Figure 3.27: FEA max stress versus the total number of SOLID186 elements.

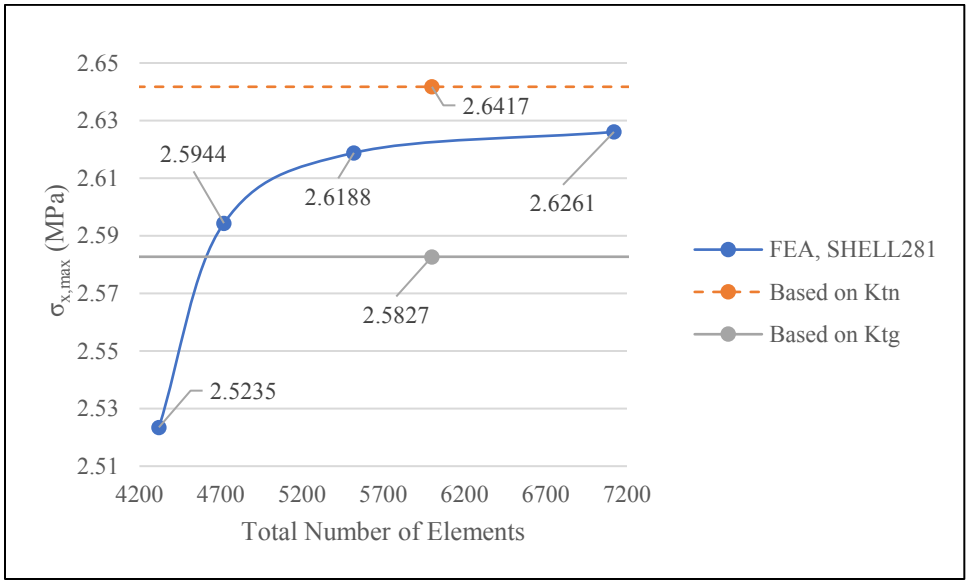

Figure 3.28: FEA max stress versus the total number of SHELL281 elements.

In the case of the SOLID186 elements, the finite element model converges to a value above that which is predicted by theory for both the gross and net area stress concentration factors. This value is only slightly above the theoretical value for the net area stress concentration factor, and is thought to be due to truncation error within ANSYS. Also, there may exist some practical limit of ply thinness that can be modeled using SOLID186 elements which

has been reached or exceeded. Even so, the model yields results which are still very close to values which are predicted by theory. The results from the SHELL281 finite element model slightly exceed what is predicted by K_{tg}, but then converge below the value of K_{tn}, which is desirable. Therefore, the proposed SHELL281 meshing yields data which are consistent with the published results, and within a small amount of error (≈1.68% and ≈0.59% for K_{tg} and K_{tn}, respectively). It is thought that both models surpass the K_{tg} stress concentration factor due to error introduced by defining the remote stress at a large distance from the local stress point of interest. This can be seen in the complexity of Eqns. 3.6-3.10 versus Eqns. 3.12-3.15. Additionally, the use of SHELL281 elements saves greatly on computation time, as the high number of elements present in the SOLID186 finite element model due to the presence of half of the layers (12 laminas) in the laminate gives rise to an exceedingly large number (>1,000,000 for the case of the very fine mesh) of partial differential equations to solve. Based upon the above results, it is concluded that SHELL281 elements with a very fine mesh size should be used.

CHAPTER 4: LAMINATE WITH A SINGLE HOLE

Stress distributions, maximum stress locations, and stress concentrations due to the "edge effect" for a single offset square hole with rounded corners transverse to an externally applied in-plane uniaxial tensile stress in a finite width laminate are studied. Additionally, this phenomenon is also explored for a single offset circular hole transverse to an externally applied in-plane uniaxial tensile stress. Stress concentration factors for both hole geometries are then investigated, which is followed by a conclusion.

4.1 Single Square Hole Transverse to Applied Load

Stress distributions and maximum stress locations due to a single offset square hole with rounded corners subjected to an in-plane uniaxial tensile stress in a finite width laminate are explored here. In order to investigate the "edge effect", four different cases are considered. To begin with, the square hole is located at the center of the laminate width, with each subsequent case becoming closer to the laminate edge by a factor of one-half. In the interest of contrast, these results will be compared to that of a single offset circular hole in Section 4.2. The initial study of a single square hole with rounded corners is to provide a baseline for the extension to two holes in Chapter 5.

4.1.1 Geometry and Loading

The geometry and loading configuration for the single square hole with rounded corners is shown below in Fig. 4.1. The hole dimension, h, is 6.35 mm and the plate width, W, is 38.1 mm, so that the h/W ratio is 0.17. The plate thickness, H, is 3.048 mm. The hole edge-to-laminate edge distance, d_e, is varied, along with the corner radius, r_c, which ranges over four different values for each case; $r_c = 0.25, 1, 2,$ and 3 mm. The height (and thus, the width) of the square hole, h, is held constant for all cases. For all values of d_e, the center of the square hole is located at the mid-length of the laminate, at $x = L/2$. Lastly, A through D are the points of interest at the hole corners where stress field measurements are taken.

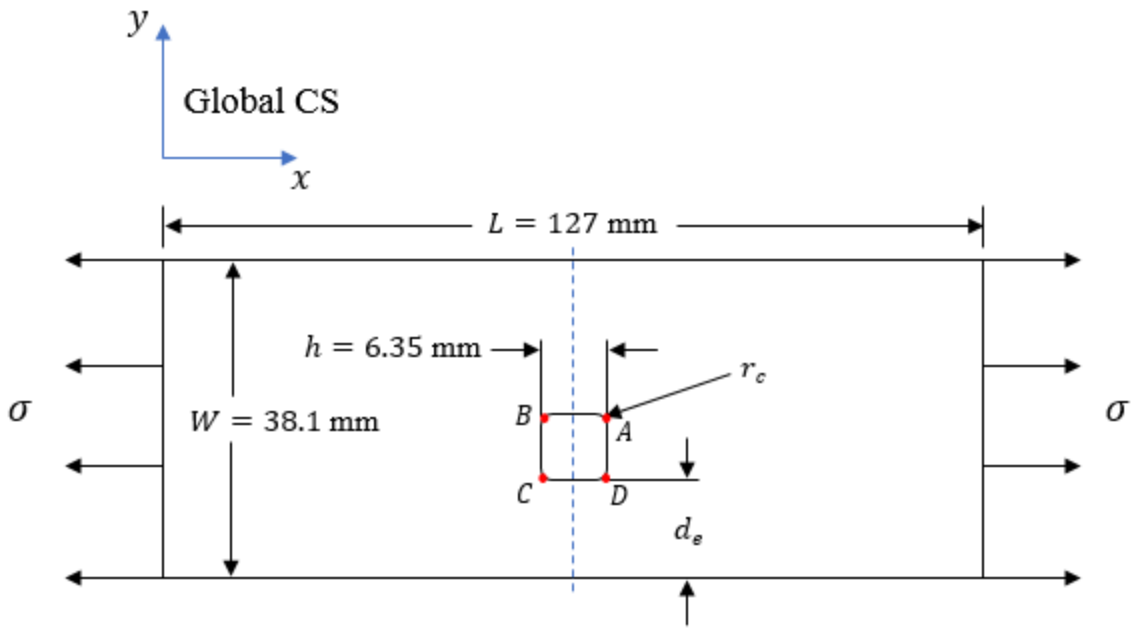

Figure 4.1: Geometry and loading condition for the single offset square hole with rounded corners.

The various cases for the spacing of the single offset square hole with rounded corners are given below in Table 4.1.

Table 4.1: Cases for the single offset square hole with rounded corners.

Case	Hole Edge-to-Laminate Edge Distance, d_e (mm)	Square Hole Height, h (mm)
1	15.875 (Centered)	6.35
2	7.938	
3	3.969	
4	1.984	

4.1.2 Meshing

The mesh is obtained using the same approach as in Chapter 3. Keypoints are established and used to generate areas, which are then meshed and refined locally in the square area surrounding the square hole. In order to ensure a high degree of accuracy, the number of elements in the square area surrounding the hole was refined and compared against results from Eqns. 2.14-2.20 until good agreement for the various corner radii values was obtained for an isotropic plate (A36 steel). The isotropic elastic constants in ANSYS were then changed to the values in Table 3.1 to reflect the quasi-isotropic laminate. Additionally, the number of elements

in the square area (3840) is kept constant for all corner radius sizes, r_c, and hole edge-to-laminate edge distances, d_e. It should be noted that this study omits the case of a square hole with sharp corners. Due to the stress singularities at the sharp corners, refining the mesh serves only to increase the maximum stress value. In theory, the stress at the corners is infinite in magnitude, because the area over which the force acts shrinks to an infinitesimal point. Since stress is defined as $\sigma = F/A$, where F is the applied force, and A is the area over which the force acts, dividing by such a small number would result in infinity. Conversely, for the case of the rounded corners, the singularity is eliminated by the smooth curvature of the corner radius. Thus, some finite value of maximum stress at the neighborhood of the hole corners can now be converged upon. The meshing for the single offset square hole with a corner radius of $r_c = 2$ mm can be seen below in Fig. 4.2.

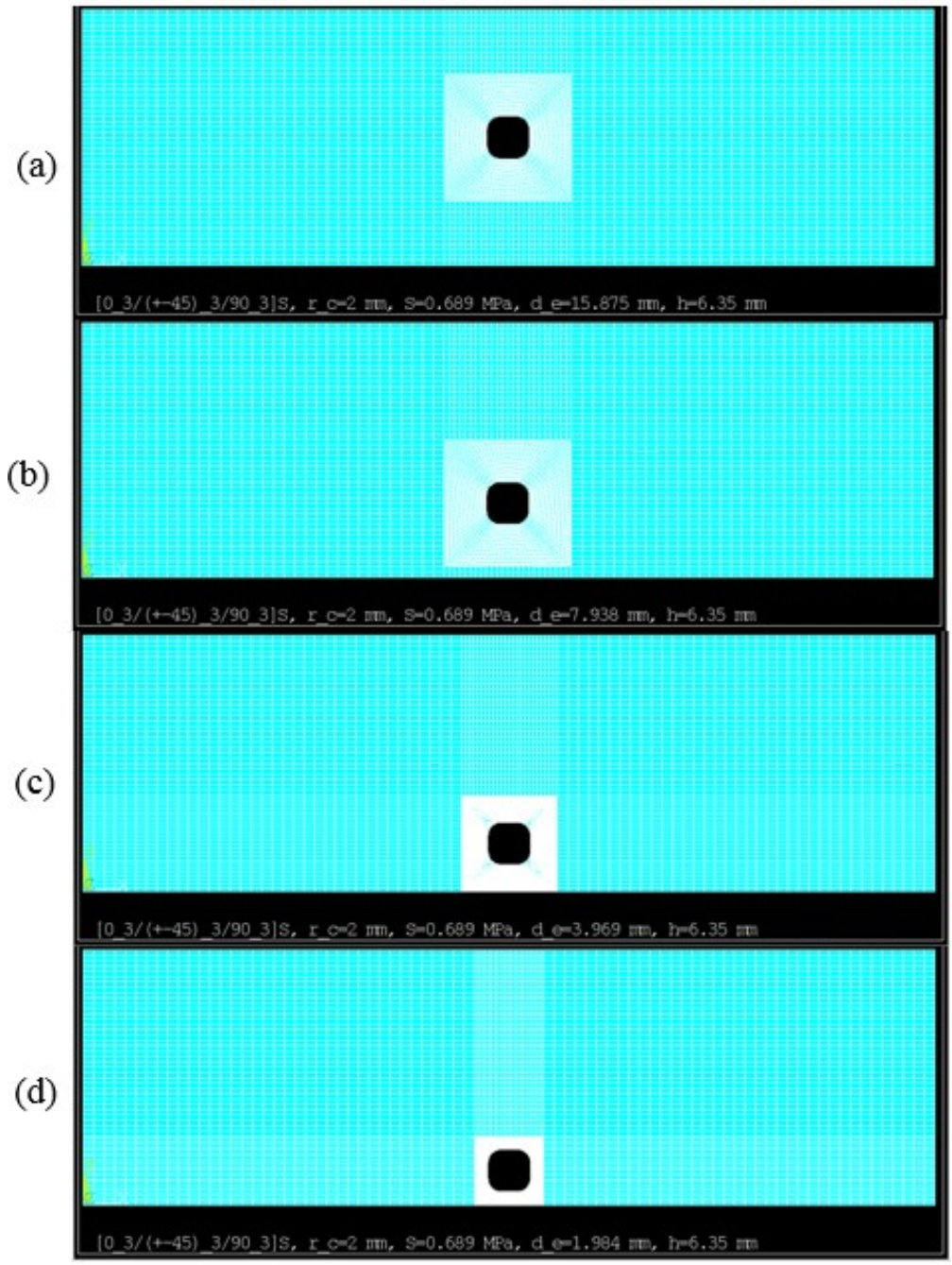

Figure 4.2: Mapped meshing for the single offset square hole for $r_c = 2$ mm: (a) $d_e = 15.875$ mm, (b) $d_e = 7.938$ mm, (c) $d_e = 3.969$ mm, (d) $d_e = 1.984$ mm.

4.1.3 Stress Distribution

It should be mentioned that ANSYS APDL allows the user to select stress results in a variety of ways. The SHELL281 element model contains elements in each lamina which possess local coordinate systems that are aligned with the specified fiber angle for that lamina. As such,

the user can select σ_x stress results from ANSYS which are in the global coordinate system (laminate level; σ_x, σ_y, and τ_{xy}), or the local coordinate system of the fiber orientation (lamina level; σ_{11}, σ_{22}, and τ_{12}). Using the local fiber coordinate system gives different stress results (in most cases much higher) than when using the global coordinate system, provided the fibers are oriented at some angle with respect to the loading direction. In effect, the maximum stress results obtained using the local fiber coordinate system represent the peak lamina stress which the fibers must withstand for a particular lamina. It is important to recall that laminate strength and failure are governed by the maximum stress and its location within each lamina. Therefore, all stress data acquired in this study are taken from the local coordinate system in each lamina. For clarity, the global and local coordinate systems for each lamina, along with the fiber orientation, are shown below in Fig. 4.3.

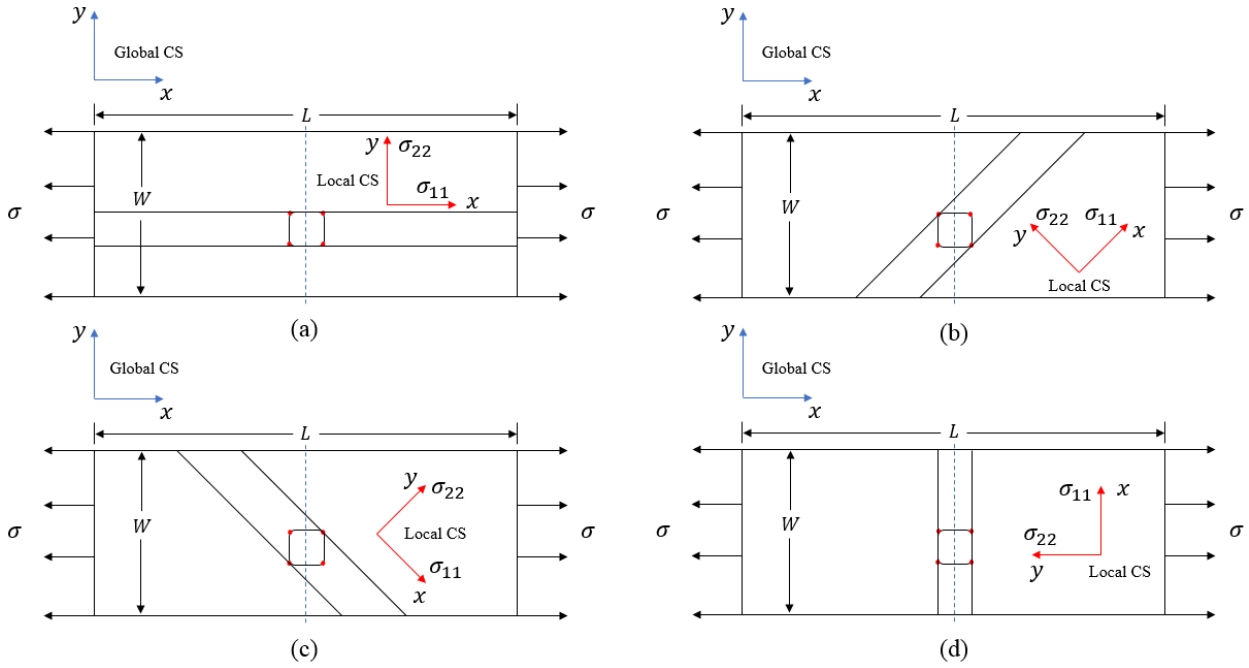

Figure 4.3: Global and local coordinate systems for the laminas: (a) 0° lamina, (b) 45° lamina, (c) -45° lamina, (d) 90° lamina.

It is interesting to note that using Eqns. 2.14-2.20 for the case of an infinite isotropic plate with a single centered square hole with rounded corners yields a result close to that which is obtained using the finite width FEM model. It is not expected that these two results will coincide exactly; however, Timoshenko and Goodier [9] revealed that finite width versus infinite width

isotropic plate solutions for a circular hole are usually within roughly 6% of one another, provided the width of the plate is not less than four times the diameter of the hole. Here, the width of the plate is six times the width of the square hole. The comparison can be seen below, in Table 4.2. It is worth recognizing that as the corner radius increases to the point of transforming the square to a circle, both the FEA and the theoretical SCFs approach 3, the value of a single centered circular hole in an infinite isotropic plate. In Eqn. 2.19, the value for the corner radius is only allowed to shrink to ≈ 0.65 mm before the governing equations become invalid. It should be noted that because of this, substantial confidence is not present in the quantitative accuracy of data acquired for the composite laminate with $r_c = 0.25$ mm; it is shown merely to illustrate the high stresses encountered as one approaches a singularity, and the general qualitative behavior of the stress fields and SCF. Such effort may be predominately academic. Further, such a small radius is impractical from both a design and machining standpoint; the probability that such a small radius would be necessary for a component is relatively low. It can be seen in Table 4.2 that the percent error between the SCFs based on FEA and theory converges to -1.721% as the square hole transitions into a circular hole. The higher error in the case of the 3 mm corner radius is attributed primarily to the number of elements used in the local meshing surrounding the square hole, and secondly to a comparison between finite width results and infinite width plate solutions. It is also important to be aware that Eqns. 2.14-2.20 are the result of a curve fit to experimental data, and are within 5% error of that data per [8]. Further, Eqns. 2.14-2.20 were used to calculate the theoretical K_{tg} found below in Table 4.2.

Table 4.2: Theoretical infinite width SCFs versus FEA finite width SCFs for a single centered square hole with rounded corners in an isotropic plate.

Applied Remote Stress, σ (MPa)	**Corner Radius, r_c (mm)**	**FEA Max Stress, $\sigma_{x,max}$ (MPa)**	**FEA K_{tg}, Finite Isotropic Plate (A36 Steel)**	**Theory K_{tg}, Infinite Isotropic Plate**	**K_{tg} % Error**
0.689	1	2.308	3.347	3.357	-0.284
	2	1.999	2.899	2.909	-0.334
	3	2.029	2.942	2.994	-1.721

The σ_{11} stress field contours for each of the laminas in the single square hole with $r_c = 2$ mm can be seen below in Figs. 4.4-4.7.

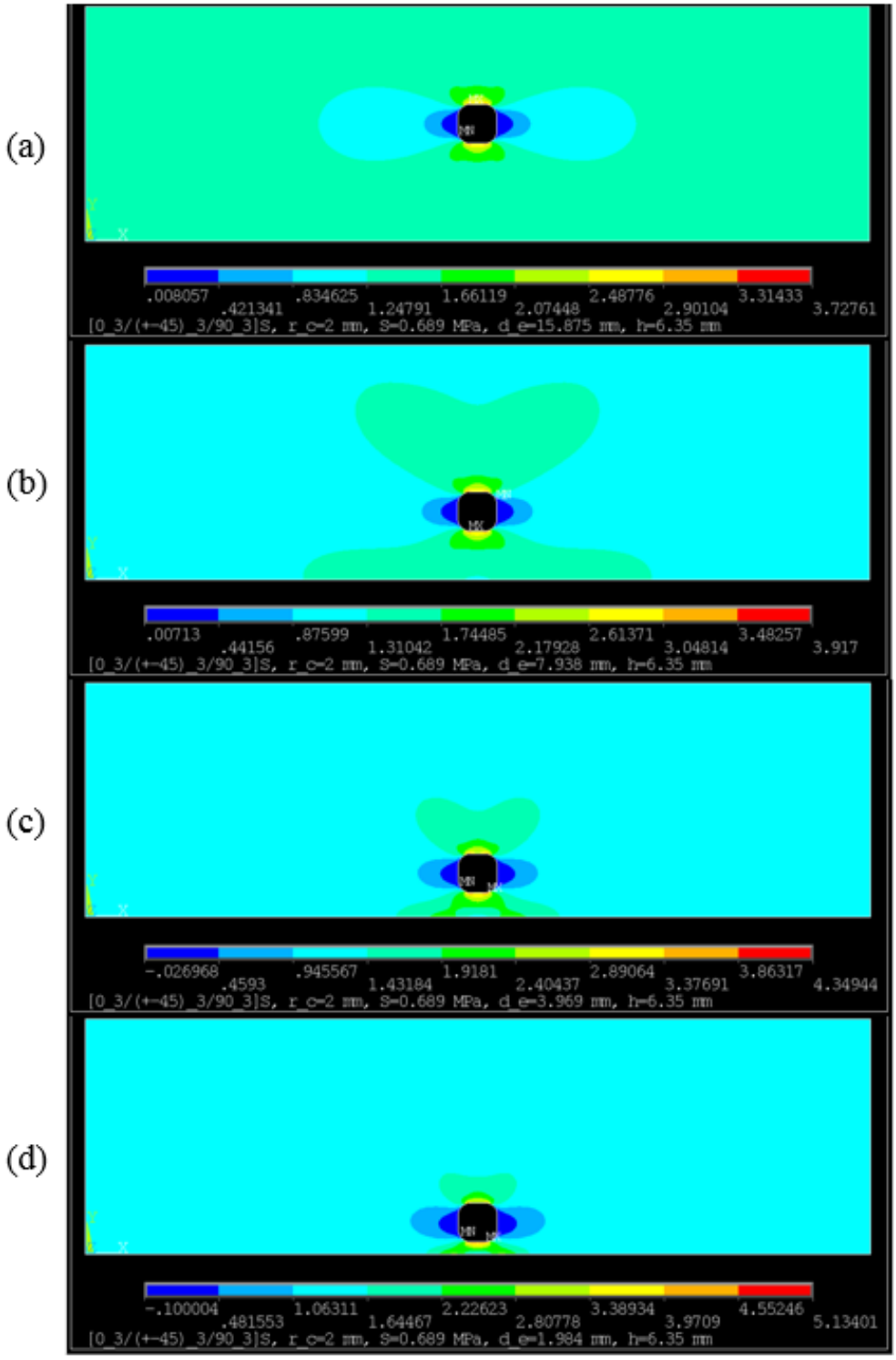

Figure 4.4: σ_{11} stress field contours in the 0° lamina for the single offset square hole with $r_c = 2$ mm: (a) $d_e = 15.875$ mm, (b) $d_e = 7.938$ mm, (c) $d_e = 3.969$ mm, (d) $d_e = 1.984$ mm.

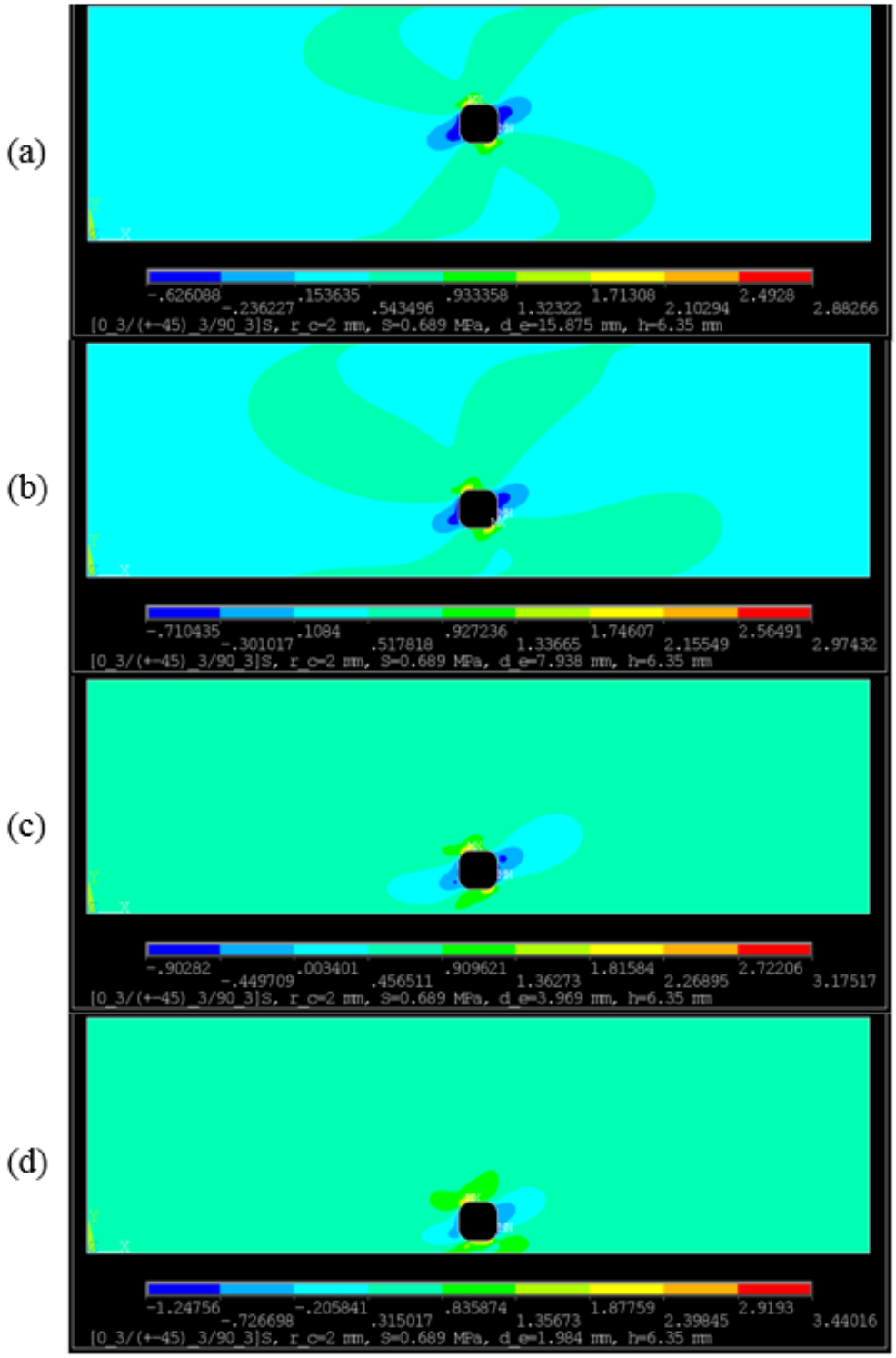

Figure 4.5: σ_{11} stress field contours in the 45° lamina for the single offset square hole with $r_c = 2$ mm: (a) $d_e = 15.875$ mm, (b) $d_e = 7.938$ mm, (c) $d_e = 3.969$ mm, (d) $d_e = 1.984$ mm.

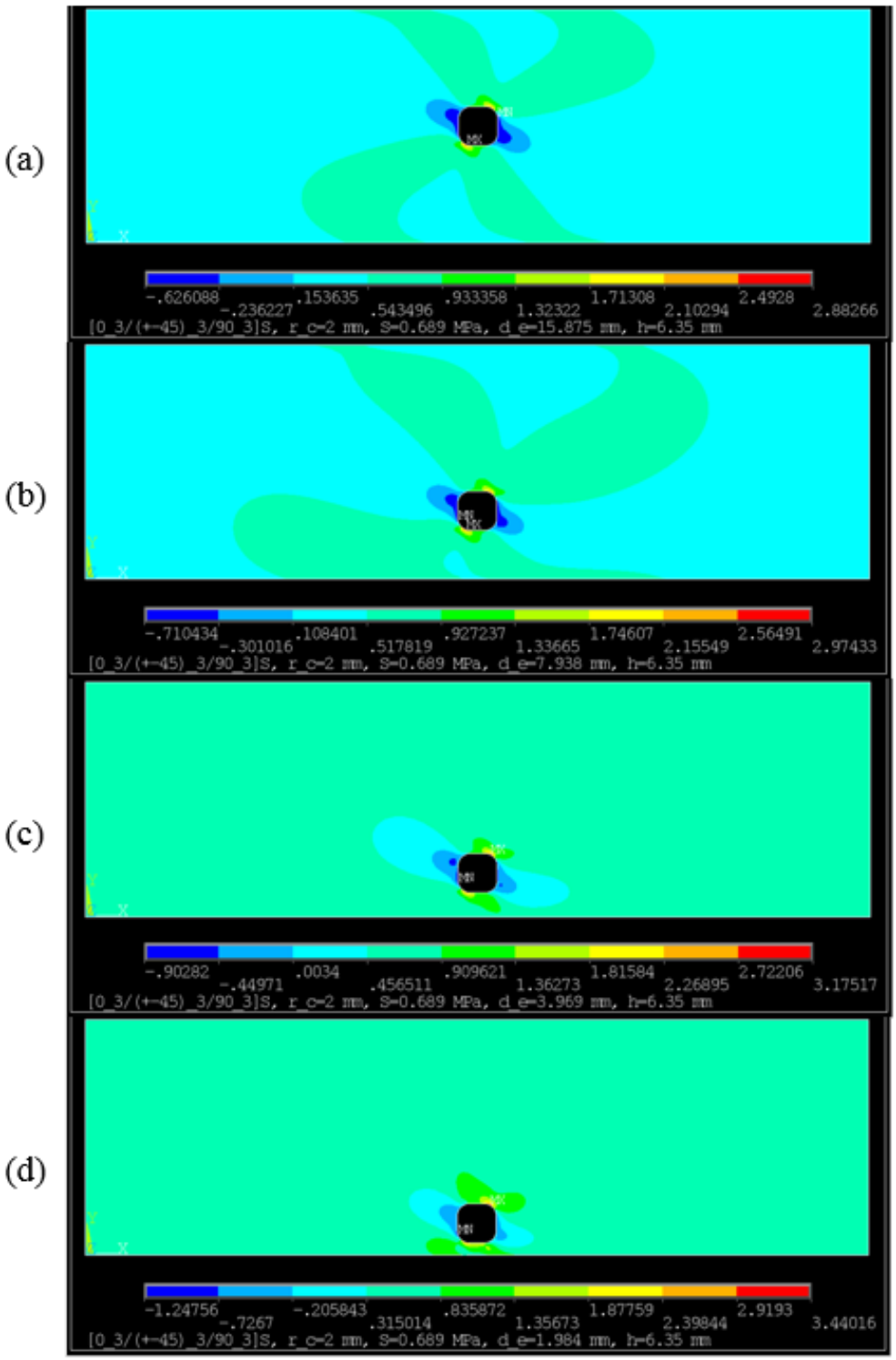

Figure 4.6: σ_{11} stress field contours in the -45° lamina for the single offset square hole with $r_c = 2$ mm: (a) $d_e = 15.875$ mm, (b) $d_e = 7.938$ mm, (c) $d_e = 3.969$ mm, (d) $d_e = 1.984$ mm.

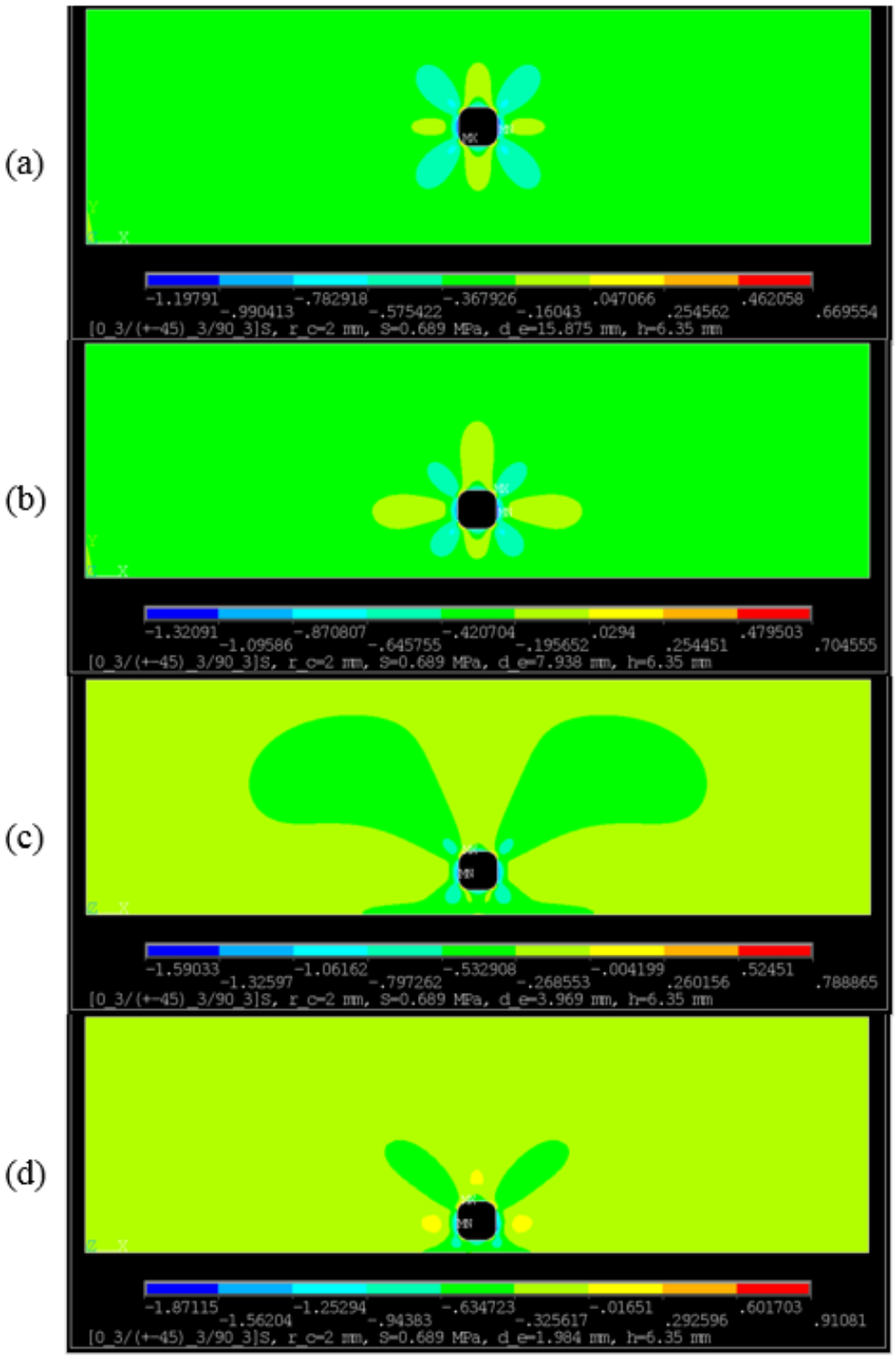

Figure 4.7: σ_{11} stress field contours in the 90° lamina for the single offset square hole with $r_c = 2$ mm: (a) $d_e = 15.875$ mm, (b) $d_e = 7.938$ mm, (c) $d_e = 3.969$ mm, (d) $d_e = 1.984$ mm.

4.1.4 Location of Maximum Stresses

The behavior of the σ_{11} stress field for the single square hole changes based upon the presence of the corner radii, their size, as well as the distance of the square hole from the central axis of the laminate. The incremental enlargement of the corner radius changes the magnitude and location of the maximum stress within the laminas. The location of the greatest σ_{11} stress in the laminate for any given d_e and r_c occurs in the 0° laminas, specifically, in the vicinity of the transition from the horizontal straight edge (parallel to the central axis of the laminate) of the hole to the curvature of the corner radius. This is consistent with results from Jong [18], in that the location of the highest stress is found in the neighborhood of the rounded corner. Such behavior can be seen below in Fig. 4.8 for $r_c = 0.25$ mm. It must be noted that ANSYS displays only one maximum stress location, however, due to symmetry conditions explained in Section 4.3.1, there can exist more than one location of maximum σ_{11} stress on the hole periphery.

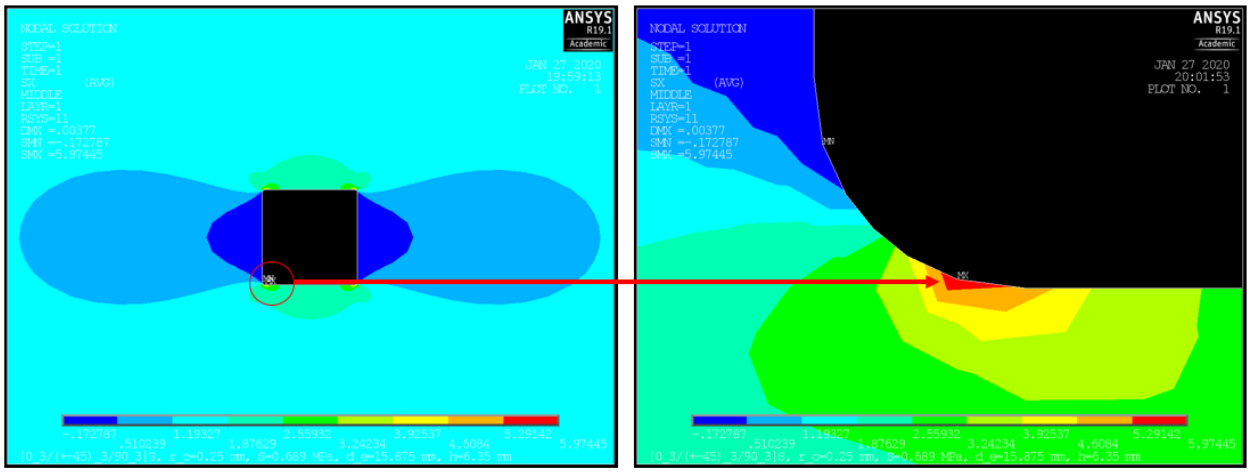

(a) (b)

Figure 4.8: (a) Maximum σ_{11} stress location in the 0° lamina for $d_e = 15.875$ mm, and $r_c = 0.25$ mm, (b) enlarged view.

By way of simple trigonometric relationships, one can determine the clocking angle of the maximum σ_{11} stress locations (A' and B') in the single square hole with rounded corners. This can be seen below in Fig. 4.9, where a and b are the vertical and horizontal legs of the triangle under investigation, respectively.

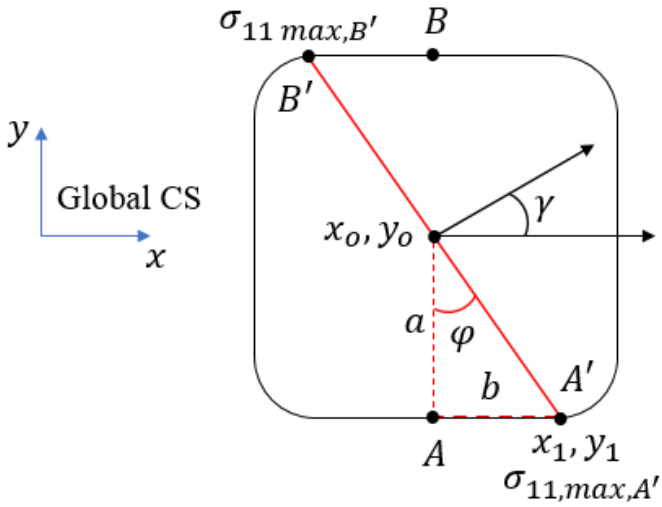

Figure 4.9: Diagram for the locations of maximum σ_{11} stresses in the 0° lamina for the single centered square hole with rounded corners.

Using the inverse tangent function, the angle with respect to the vertical axis of the center of the square is

$$\varphi = tan^{-1}\frac{b}{a} = tan^{-1}\frac{x_1 - x_0}{y_o - y_1} \tag{4.1}$$

where x_o and y_o are the coordinates of the center of the hole (known), and x_1 and y_1 are the coordinates of one of the maximum σ_{11} stress nodes (obtained using ANSYS) at the end point of the line $A'B'$. The locations of the maximum σ_{11} stress in the 0° lamina with respect to the horizontal loading direction, x, are now simply

$$\gamma_{A'} = \varphi - 90° \tag{4.2}$$

$$\gamma_{B'} = \varphi + 90° \tag{4.3}$$

For the case of the single centered square hole with rounded corners, the magnitude of the σ_{11} stress in the 0° lamina is the same at each corner due to symmetry about the central axis, as well as the fiber orientation. This relationship is lost as soon as the hole moves away from the central

axis of the laminate. The clocking angle for the maximum stress at points A' and B' for the single centered square hole with varying radii are calculated and given below in Table 4.3.

Table 4.3: Clocking angle for the maximum σ_{11} stress locations in the 0° lamina for a single centered square hole with rounded corners.

Hole Edge-to-Laminate Edge Distance, d_e (mm)	Corner Radius, r_c (mm)	$\gamma_{A'}$ (°)	$\gamma_{B'}$ (°)
15.875 (Centered)	0.25	-46.54	133.46
	1	-53.56	126.44
	2	-64.55	115.45
	3	-82.41	97.59

The angular change in the location of the maximum σ_{11} stress for the case of the single centered square hole with rounded corners can be seen below in Fig. 4.10. For this case, the locations of the maximum σ_{11} stress in the 0° lamina are always found in the neighborhood of points A through D (a consequence of symmetry, see Fig. 4.24a) on the hole periphery.

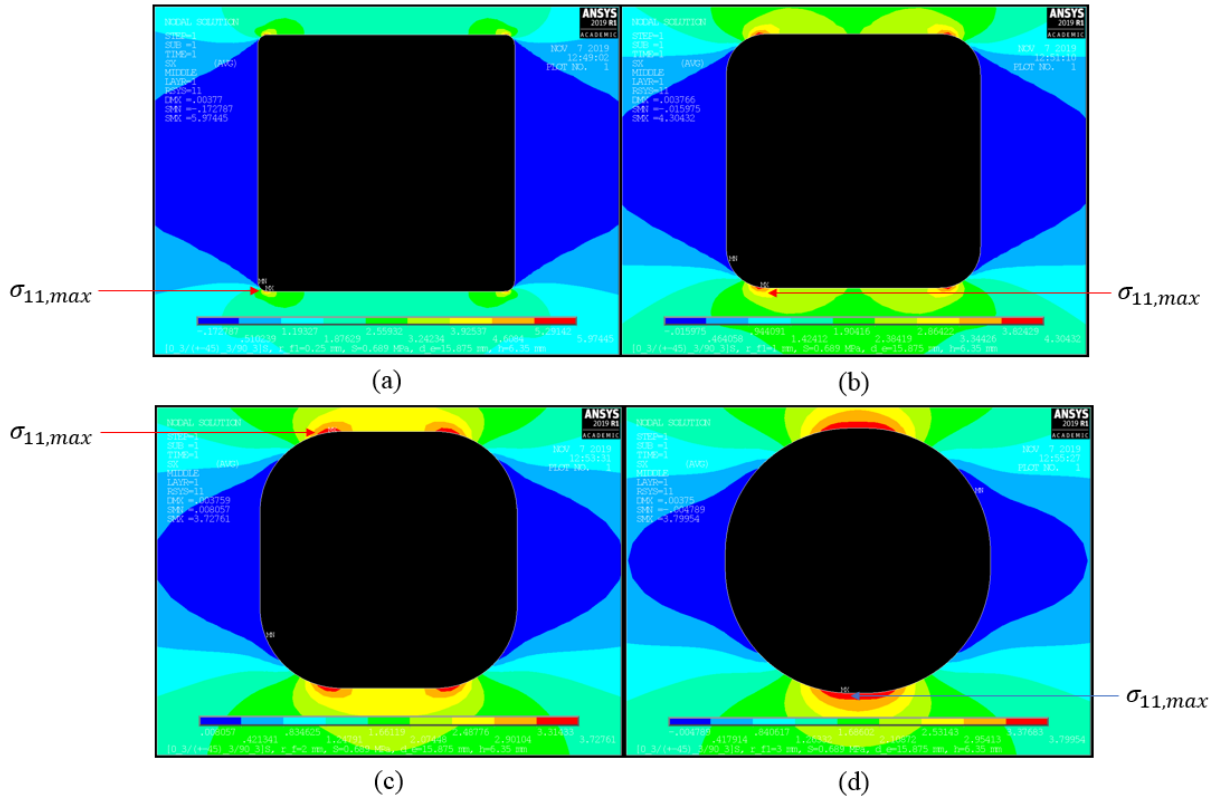

Figure 4.10: Location of maximum σ_{11} stress in the 0° lamina with $d_e = 15.875$ mm for: (a) $r_c = 0.25$ mm, (b) $r_c = 1$ mm, (c) $r_c = 2$ mm, (d) $r_c = 3$ mm.

For the single offset square hole with rounded corners, the maximum σ_{11} stress always occurs in the 0° lamina. This is because the fibers in the 0° ply are parallel to the loading axis, and therefore carry most of the load applied to the laminate. These findings are consistent with results for a single square hole with rounded corners from Cannon [19]. Also, for a given hole offset distance in the 0° lamina, the magnitude of the stress drops for increasing r_c, provided $0.25 \text{ mm} < r_c < 2 \text{ mm}$, but then increases for $r_c > 2$ mm. This decreasing-increasing behavior is consistent with earlier results for an isotropic plate in Table 4.2, and is also consistent with results from Cannon [19] (discussed in Section 4.3.2). Additionally, the magnitude of the stress in the ±45° laminas is equivalent, as is expected. The maximum σ_{11} stress for each lamina is given below in Table 4.4.

Table 4.4: Maximum σ_{11} stress in each lamina for the single offset square hole with rounded corners.

Single Offset Square Hole					
Corner Radius, r_c (mm)	**Hole Edge-to-Laminate Edge Distance, d_e (mm)**	**$\sigma_{11,max}$ (MPa)**			
		0° Lamina	**45° Lamina**	**-45° Lamina**	**90° Lamina**
0.25	15.875 (Centered)	5.974	5.663	5.663	2.138
	7.938	6.198	5.907	5.907	2.273
	3.969	6.771	6.483	6.483	2.602
	1.984	7.515	7.291	7.291	3.115
1	15.875 (Centered)	4.304	3.512	3.512	0.971
	7.938	4.464	3.644	3.644	1.021
	3.969	4.833	3.948	3.948	1.147
	1.984	5.219	4.355	4.355	1.374
2	15.875 (Centered)	3.728	2.883	2.883	0.670
	7.938	3.917	2.974	2.974	0.705
	3.969	4.349	3.175	3.175	0.789
	1.984	5.134	3.440	3.440	0.911
3	15.875 (Centered)	3.800	2.660	2.660	0.530
	7.938	4.019	2.766	2.766	0.552
	3.969	4.594	2.989	2.989	0.612
	1.984	5.664	3.345	3.345	0.702

4.2 Single Circular Hole Transverse to Applied Load

Stress distributions and maximum stress locations due to a single offset circular hole subjected to an in-plane uniaxial tensile stress in a finite width laminate are investigated in this section. As in Section 4.1, the hole edge-to-laminate edge distance is varied in the interest of studying the "edge effect", and comparing it to the results from the previous section.

4.2.1 Geometry and Loading

The geometry and loading configuration for the single circular hole is shown below in Fig. 4.11. The hole edge-to-laminate edge distance, d_e, is varied, while the diameter of the hole, d, is held constant at 6.35 mm. This circular hole geometry is equivalent to a square hole with rounded corners, when $r_c = 3.175$ mm. For all values of d_e, the center of the circular hole is located at the mid-length of the laminate, at $x = L/2$. Lastly, A and B are points of interest where stress field measurements will be taken.

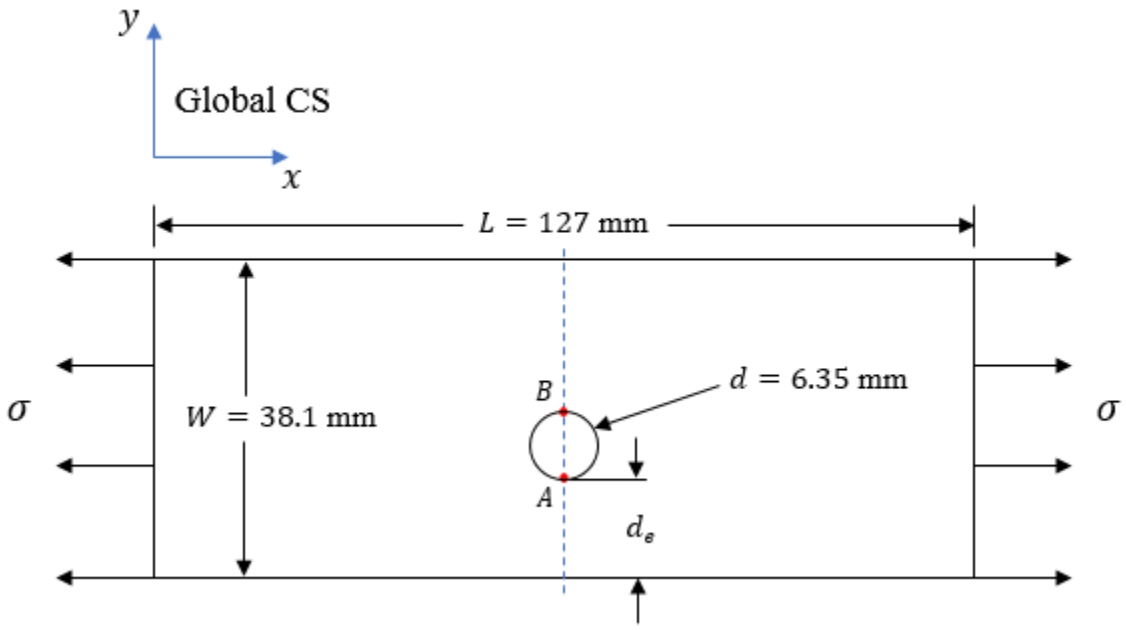

Figure 4.11: Geometry and loading condition for the single offset circular hole.

The various cases for the spacing of the single offset circular hole are given below in Table 4.5.

Table 4.5: Cases for the single offset circular hole.

Case	Hole Edge-to-Laminate Edge Distance, d_e (mm)	Hole Diameter, d (mm)
1	15.875 (Centered)	6.35
2	7.938	
3	3.969	
4	1.984	

4.2.2 Meshing

The mesh is obtained using the same approach as in Chapter 3. The keypoints are established and used to generate areas, which are then meshed and refined locally in each square area surrounding the circular hole. As in Section 4.1.2, the number of elements in the square area surrounding the hole is held constant at 3840 for each offset distance. The meshing for the single offset circular hole can be seen below in Fig. 4.12.

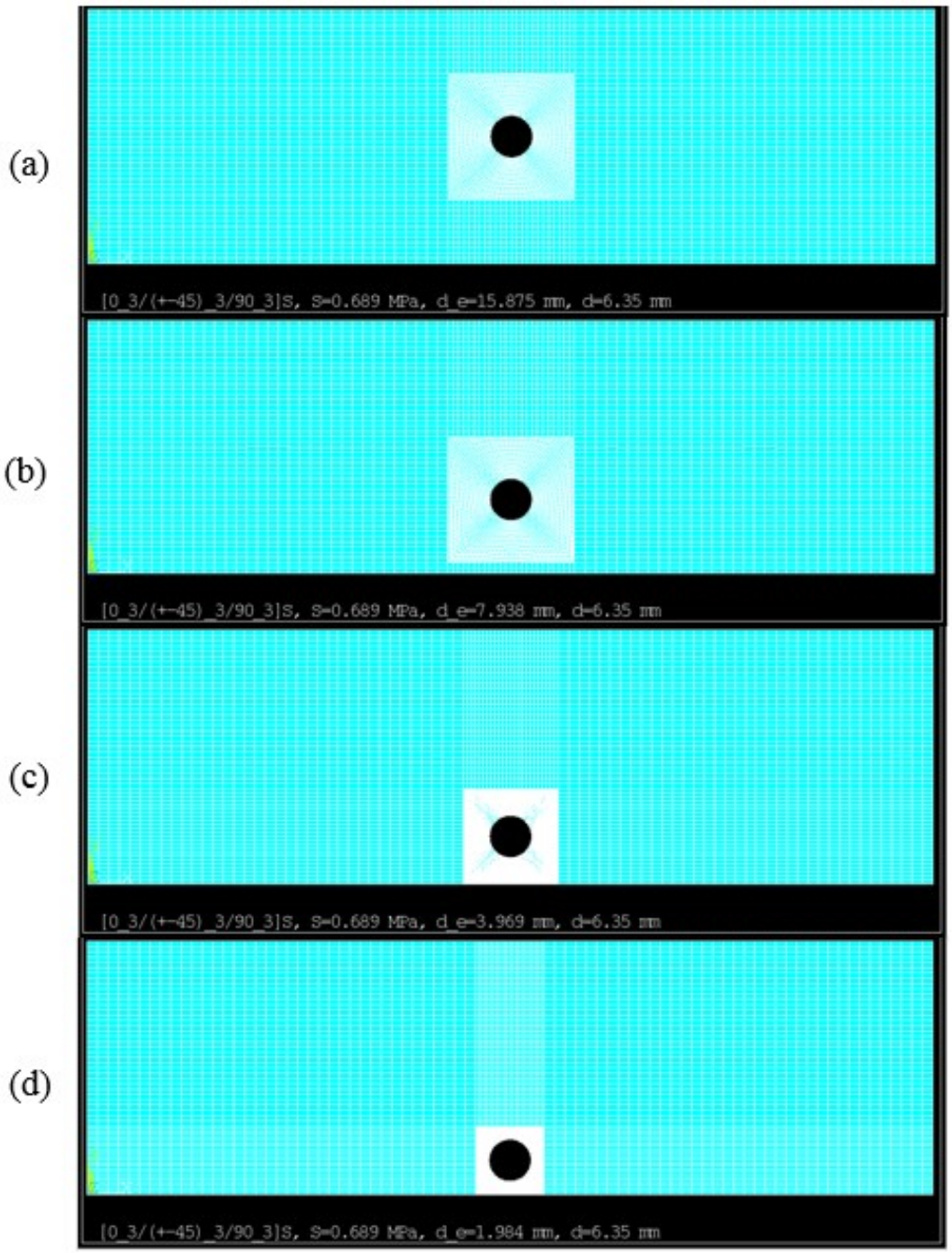

Figure 4.12: Mapped meshing for the single offset circular hole: (a) $d_e = 15.875$ mm, (b) $d_e = 7.938$ mm, (c) $d_e = 3.969$ mm, (d) $d_e = 1.984$ mm.

4.2.3 Stress Distribution

The σ_{11} stress field contours for each of the laminas in the single offset circular hole can be seen below in Figs. 4.13-4.16.

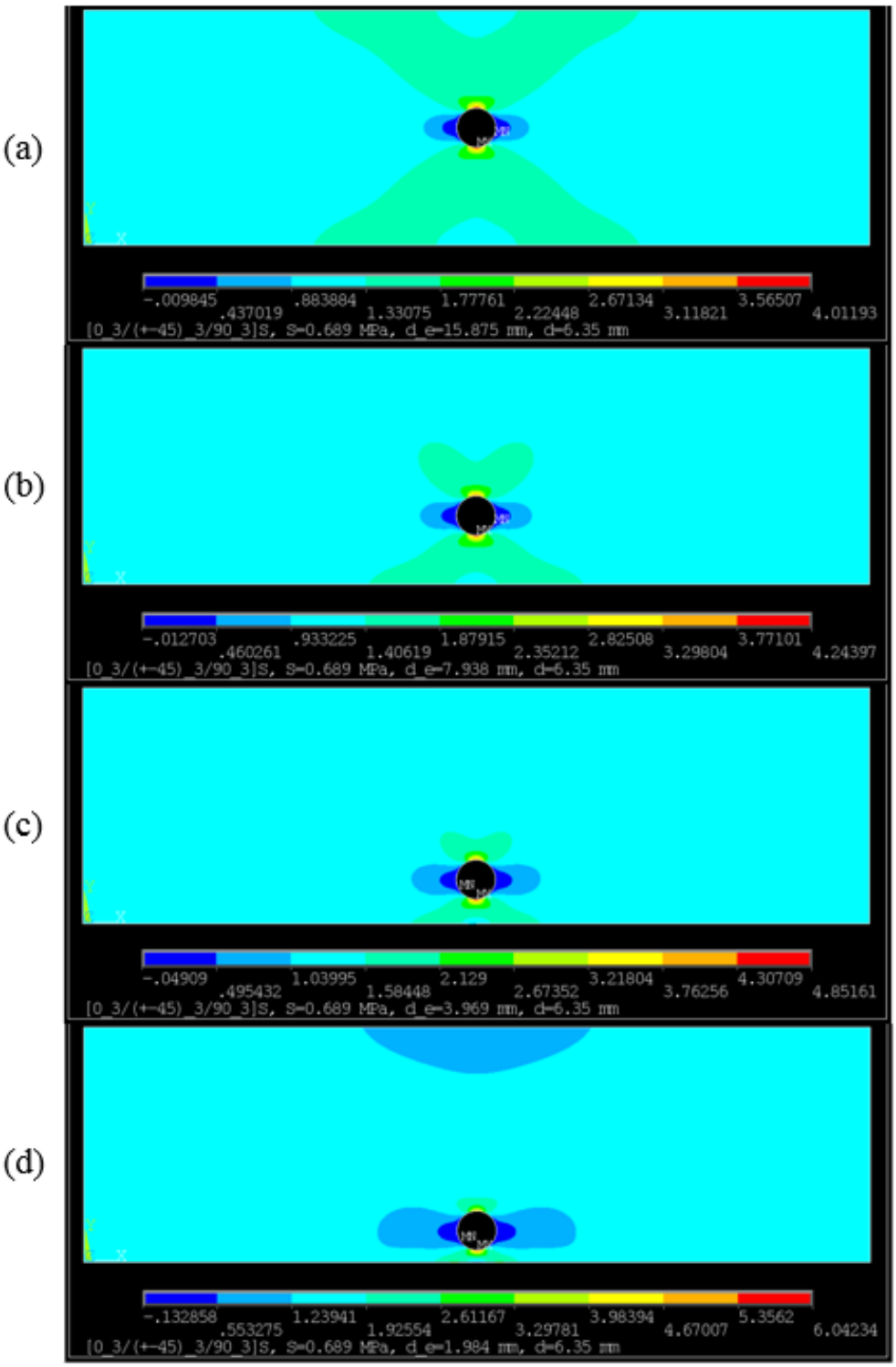

Figure 4.13: σ_{11} stress field contours in the 0° lamina for the single offset circular hole: (a) $d_e = 15.875$ mm, (b) $d_e = 7.938$ mm, (c) $d_e = 3.969$ mm, (d) $d_e = 1.984$ mm.

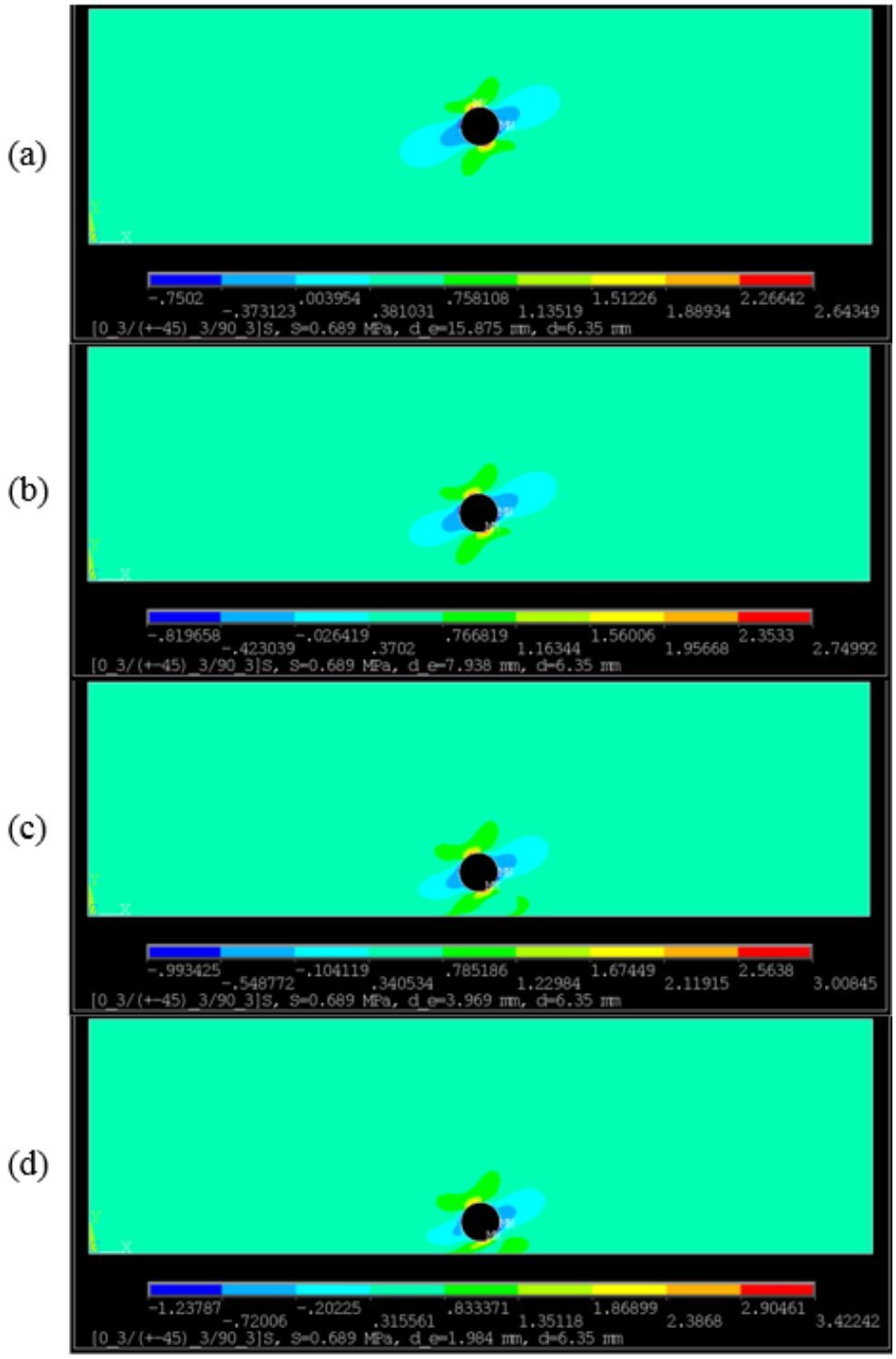

Figure 4.14: σ_{11} stress field contours in the 45° lamina for the single offset circular hole: (a) $d_e = 15.875$ mm, (b) $d_e = 7.938$ mm, (c) $d_e = 3.969$ mm, (d) $d_e = 1.984$ mm.

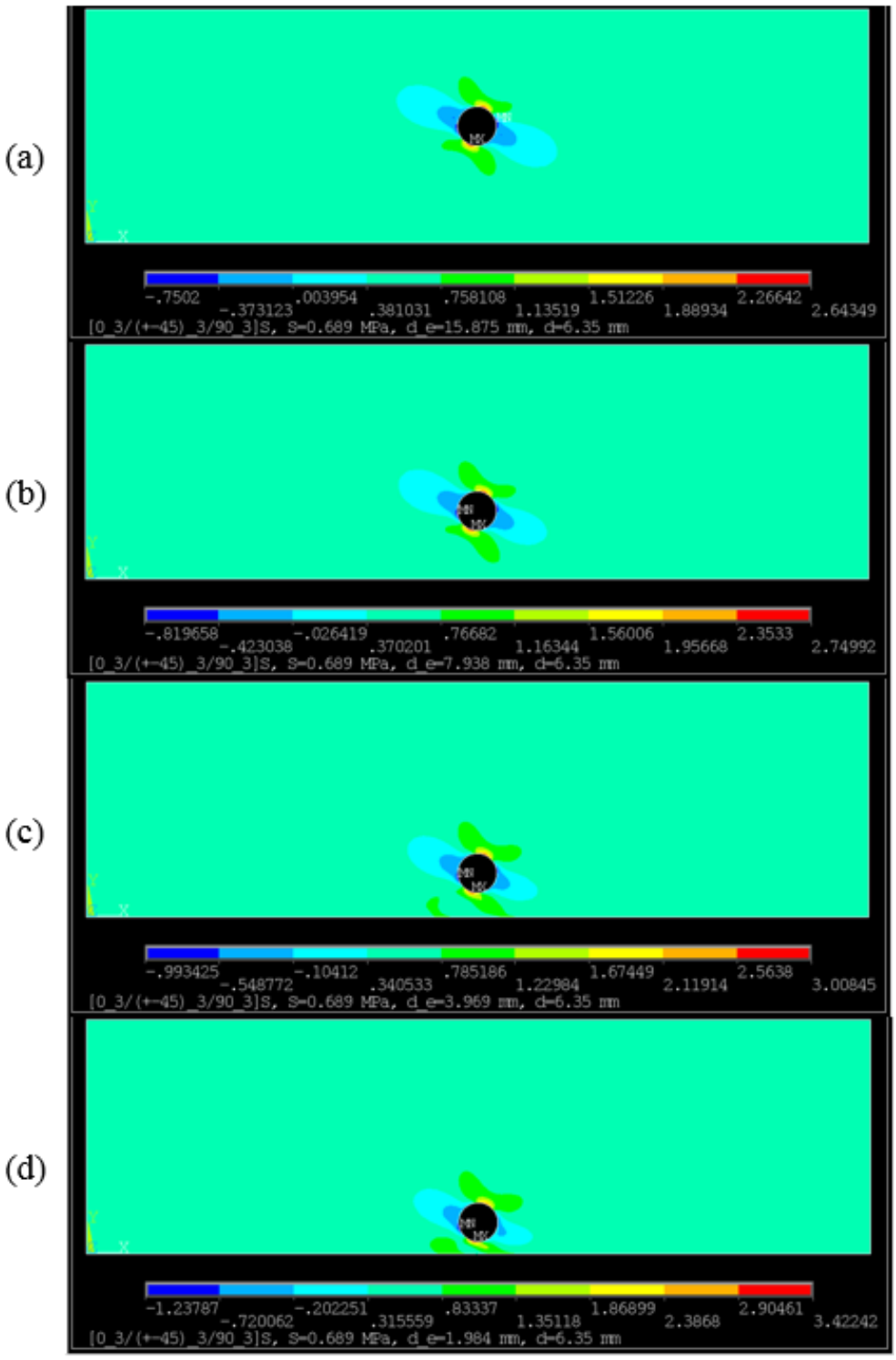

Figure 4.15: σ_{11} stress field contours in the -45° lamina for the single offset circular hole: (a) $d_e = 15.875$ mm, (b) $d_e = 7.938$ mm, (c) $d_e = 3.969$ mm, (d) $d_e = 1.984$ mm.

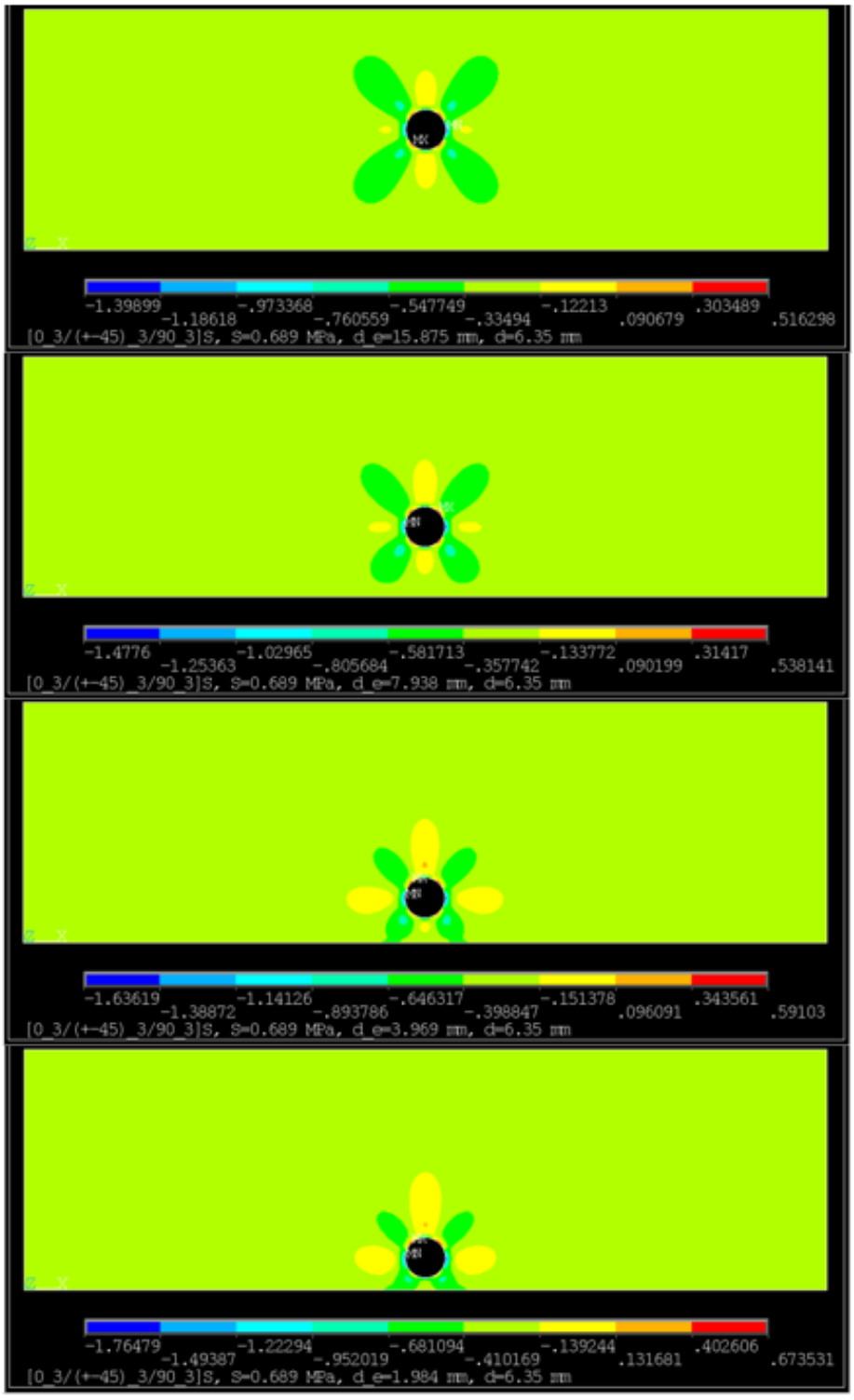

Figure 4.16: σ_{11} stress field contours in the 90° lamina for the single offset circular hole: (a) $d_e = 15.875$ mm, (b) $d_e = 7.938$ mm, (c) $d_e = 3.969$ mm, (d) $d_e = 1.984$ mm.

4.2.4 Location of Maximum Stresses

The locations of the maximum σ_{11} stress on the periphery of the single centered circular hole change depending upon the lamina. Due to symmetry conditions for single centered circular hole, one might initially expect points A and B to be of the same magnitude and location, regardless of lamina. It has been shown by Kheradiya [5] that for a single centered circular hole, the maximum σ_{11} stress in the 0° lamina occurs at points A and B. It may be thought (erroneously) that the location of the maximum σ_{11} stresses in the 45° lamina are simply at the tangent points (C and D) of the fibers and circular hole periphery, as below in Fig. 4.17.

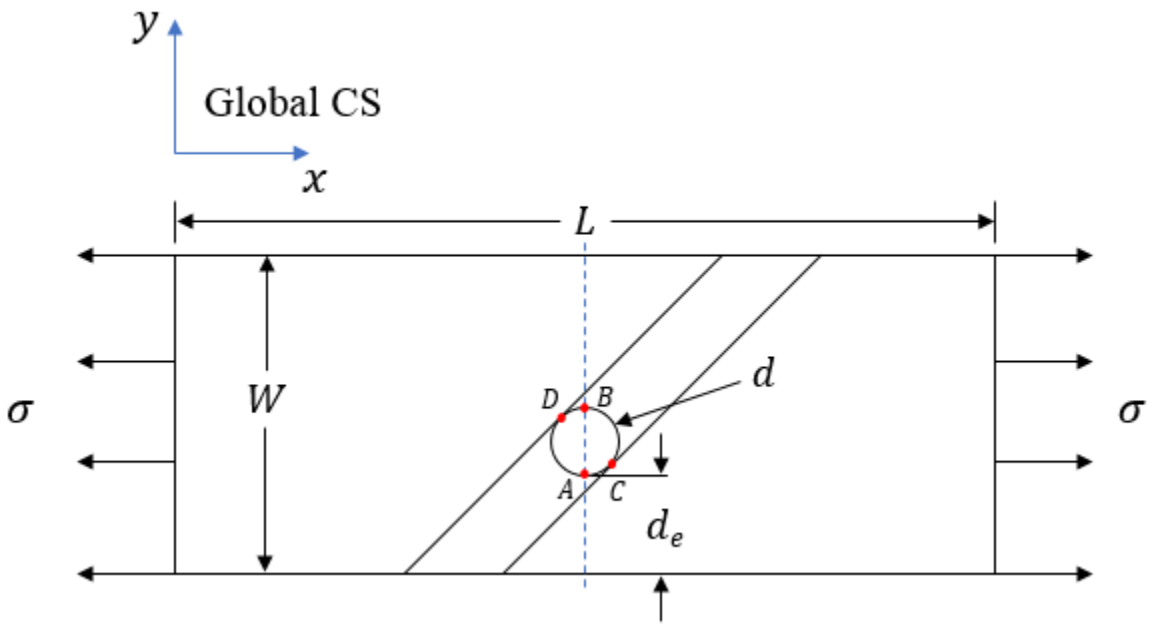

Figure 4.17: Tangent point locations (C and D) of the fibers and circular hole periphery in the 45° lamina.

However, due to the angle of inclination (or declination) of the fibers in the ±45° lamina, as well as the effect of shear rotation, the locations of the maximum σ_{11} stress (C and D) are rotated at some angle other than ±45° with respect to the vertical axis of the hole center. The effect of shear rotation on the locations of the maximum σ_{11} stress in the 45° lamina can be seen below in Fig. 4.18.

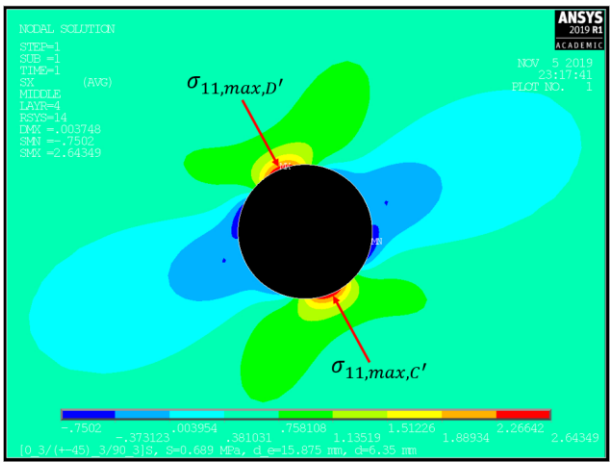

Figure 4.18: Maximum σ_{11} stress locations in the 45° lamina for the single centered circular hole.

One can use the same approach found in Section 4.1.4 to determine the clocking angle of the maximum σ_{11} stress locations for the single offset circular hole, as shown below in Fig. 4.19.

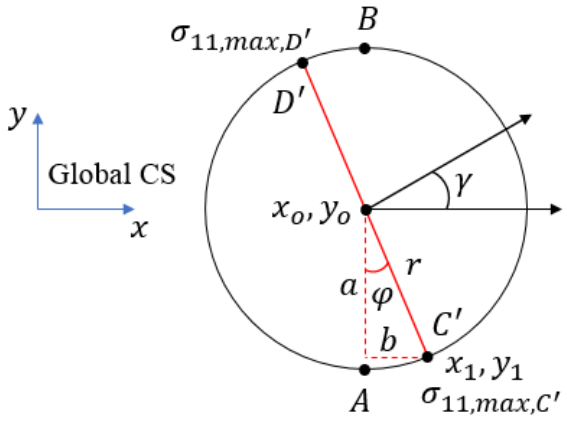

Figure 4.19: Diagram for the locations of maximum σ_{11} stresses in the 45° lamina for the single offset circular hole.

Evaluating Eqns. 4.1-4.3, one finds the angles listed below in Table 4.6 for points C' and D' for the 45° laminas. For the -45° laminas, the values of $\gamma_{C'}$ and $\gamma_{D'}$ are simply reversed from the 45° lamina results. This table also shows that the centered circular hole results are consistent with results from Kheradiya [5]. It is interesting to note that there is no change in the location of the maximum σ_{11} stress from $d_e = 7.938$ mm to $d_e = 3.969$ mm. For the case of the single centered circular hole, the magnitude of the σ_{11} stress in the 45° lamina is the same at points C'

and D' due to symmetry about the central axis, as well as the fiber orientation. This relationship is lost as soon as the hole moves away from the central axis of the laminate.

Table 4.6: Clocking angle for the maximum σ_{11} stress locations in the 45° lamina for the single offset circular hole.

Hole Edge-to-Laminate Edge Distance, d_e (mm)	$\gamma_{C'}$ (°)	$\gamma_{C'}$ (°), [5]	$\gamma_{D'}$ (°)	$\gamma_{D'}$ (°), [5]
15.875 (Centered)	-67.50	-67.50	112.50	112.50
7.938	-71.25	N/A	108.75	N/A
3.969	-71.25		108.75	
1.984	-75.00		105.00	

The maximum σ_{11} stress for each lamina and offset distance, d_e is given below in Table 4.7. It can readily be seen that the maximum σ_{11} stress increases with decreasing offset distance, regardless of fiber orientation. Additionally, the ±45° laminas share the same maximum σ_{11} stress value for all offset distances, as expected. Remark is due here, in that the agreement between the results for this study and the results from Kheradiya [5] (where $d = 12.7$ mm) would seem to indicate that for a centered circular hole, the locations of the maximum stress are the same in the ±45° laminas, irrespective of the hole diameter, layup sequence, and material, provided that the external applied stress, laminate length, and laminate width are equivalent.

Table 4.7: Maximum σ_{11} stress in each lamina for the single offset circular hole.

Single Offset Circular Hole			
Hole Edge-to-Laminate Edge Distance, d_e (mm)	**Fiber Orientation Angle, θ (°)**	**$\sigma_{11,max}$ (MPa)**	**%Δ wrt Centered Hole**
15.875 (Centered)	0	4.012	-
	45	2.643	
	-45	2.643	
	90	0.516	
7.938	0	4.244	5.62
	45	2.750	3.95
	-45	2.750	3.95
	90	0.538	4.14
3.969	0	4.852	18.95
	45	3.008	12.91
	-45	3.008	12.91
	90	0.591	13.50
1.984	0	6.042	40.39
	45	3.422	25.68
	-45	3.422	25.68
	90	0.674	26.43

4.3 Stress Concentration Factors

To obtain the stress concentration factor for each lamina, the applied stress in each lamina with no hole present must first be calculated. The following approach is taken, as there exist no closed form solutions for the SCF of a lamina which contains a single (or multiple) square hole with rounded corners. Further, this methodology is consistent with that found in work by Kheradiya [5] and Cannon [19]. Using classical laminate analysis equations for a balanced symmetric laminate from Mallick [3], and with no bending moment present (i.e. $k_{xx} = k_{yy} = k_{xy} = 0$), the applied stresses in the j[th] lamina with no hole are simply

$$\begin{bmatrix} \sigma_{xx,No\ Hole} \\ \sigma_{yy,No\ Hole} \\ \tau_{xy,No\ Hole} \end{bmatrix}_j = [\bar{Q}_{mn}]_j \begin{bmatrix} \overset{\circ}{\varepsilon}_{xx} \\ \overset{\circ}{\varepsilon}_{yy} \\ \overset{\circ}{\gamma}_{xy} \end{bmatrix}_j = [\bar{Q}_{mn}]_j \frac{1}{A_{11}A_{22} - A_{12}^2} \begin{bmatrix} A_{22} & -A_{12} & 0 \\ -A_{12} & A_{11} & 0 \\ 0 & 0 & \dfrac{A_{11}A_{22} - A_{12}^2}{A_{66}} \end{bmatrix} \begin{bmatrix} N_{xx} \\ N_{yy} \\ N_{xy} \end{bmatrix} \qquad (4.4)$$

where $[\bar{Q}_{mn}]_j$ is the stiffness matrix for the j[th] lamina, and N_{xx}, N_{yy}, and N_{xy} are the applied force resultants per unit width on the edges of the laminate. For this study, $N_{yy} = N_{xy} = 0$. The applied stresses for each lamina with no hole are calculated and shown below in Table 4.8. Excellent agreement between the ANSYS FEA simulation and closed form theoretical equations was obtained.

Table 4.8: Applied lamina stresses $\sigma_{xx,No\ Hole}$, $\sigma_{yy,No\ Hole}$, and $\tau_{xy,No\ Hole}$ for the $[0_3/(\pm45)_3/90_3]_S$ laminate with no hole.

Lamina	Global CS, ANSYS Stress, $\sigma_{xx,No\ Hole}$ (MPa)	Global CS, ANSYS Stress, $\sigma_{yy,No\ Hole}$ (MPa)	Global CS, ANSYS Stress, $\tau_{xy,No\ Hole}$ (MPa)	Theoretical Stress, $\sigma_{xx,No\ Hole}$ (MPa)	Theoretical Stress, $\sigma_{yy,No\ Hole}$ (MPa)	Theoretical Stress, $\tau_{xy,No\ Hole}$ (MPa)	ANSYS versus Theoretical $\sigma_{xx,No\ Hole}$ % Error
0°	1.29333	0.005002	0	1.29341	0.004987	0	-0.0062
45°	0.559916	0.12956	0.169864	0.559863	0.129466	0.169951	0.0095
-45°	0.559916	0.12956	-0.169864	0.559863	0.129466	-0.169951	0.0095
90°	0.344746	-0.264123	0	0.344852	-0.264179	0	-0.0307

Having obtained the applied lamina stresses, $\sigma_{xx,No\ Hole}$, $\sigma_{yy,No\ Hole}$, and $\tau_{xy,No\ Hole}$, one is now able to calculate the stress in each lamina based upon the fiber coordinate system (local). Appealing to the stress transformation equations for a thin lamina under plane stress listed by Mallick [3], one finds

$$\sigma_{11,No\ Hole} = \sigma_{xx,No\ Hole}\cos^2\theta + \sigma_{yy,No\ Hole}\sin^2\theta + 2\tau_{xy,No\ Hole}\cos\theta\sin\theta$$
$$\sigma_{22,No\ Hole} = \sigma_{xx,No\ Hole}\sin^2\theta + \sigma_{yy,No\ Hole}\cos^2\theta - 2\tau_{xy,No\ Hole}\cos\theta\sin\theta \quad (4.5)$$
$$\tau_{12,No\ Hole} = (-\sigma_{xx,No\ Hole} + \sigma_{yy,No\ Hole})\sin\theta\cos\theta + \tau_{xy,No\ Hole}(\cos^2\theta - \sin^2\theta)$$

where θ is the fiber orientation angle with respect to the laminate (global) x-axis. For any given lamina, Eqn. 4.5 represents the stresses in the laminas due to the applied lamina stresses. These are thought to be the equations used by ANSYS to calculate the stresses in the lamina using the local coordinate systems, from which all data in this study is acquired. It is important to recall that for any given unidirectional continuous fiber lamina, the matrix carries a much smaller fraction of the applied load in relation to the fibers. In fact, the contribution from the elastic modulus of the matrix, E_m, is often neglected when considering the elastic modulus of the lamina in the 11-direction, E_{11}, such that it becomes a function of the fiber stress, σ_f. The lamina stresses for each lamina with no hole are calculated and shown below in Table 4.9. Again, excellent agreement between the ANSYS FEA simulation and closed form theoretical equations was found.

Table 4.9: Lamina stresses $\sigma_{11,No\ Hole}$, $\sigma_{22,No\ Hole}$, and $\tau_{12,No\ Hole}$ for the $[0_3/(\pm45)_3/90_3]_S$ laminate with no hole.

Lamina	Local CS, ANSYS Stress, $\sigma_{11,No\ Hole}$ (MPa)	Local CS, ANSYS Stress, $\sigma_{22,No\ Hole}$ (MPa)	Local CS, ANSYS Stress, $\tau_{12,No\ Hole}$ (MPa)	Theoretical Stress, $\sigma_{11,No\ Hole}$ (MPa)	Theoretical Stress, $\sigma_{22,No\ Hole}$ (MPa)	Theoretical Stress, $\tau_{12,No\ Hole}$ (MPa)	ANSYS versus Theoretical $\sigma_{11,No\ Hole}$ % Error
0°	1.29333	0.005002	0	1.29341	0.004987	0	-0.0062
45°	0.514602	0.174874	-0.215178	0.514616	0.174714	-0.215199	-0.0027
-45°	0.514602	0.174874	0.215178	0.514616	0.174714	0.215199	-0.0027
90°	-0.264123	0.344746	0	-0.264179	0.344852	0	-0.0212

To fully illustrate the need for the lamina stress with no hole, one may return to the concept of force lines, as briefly discussed in Section 2.1.1. At the laminate level, the SCF for gross area, K_{tg}, is obtained by dividing the stress present at the location of interest in the laminate by the applied remote stress, analogous to Eqn. 2.1. However, for the case of an individual lamina, the stress at the location of interest in the lamina with a hole must be divided

by the applied stress present in the lamina without a hole. The presence of the hole creates a disturbance in the constant force lines, thus creating a localization, and consequent increase in local stress. This concept is analogous to fluid flow, wherein the force lines would be considered streamlines. Such behavior can be seen below in Fig. 4.20.

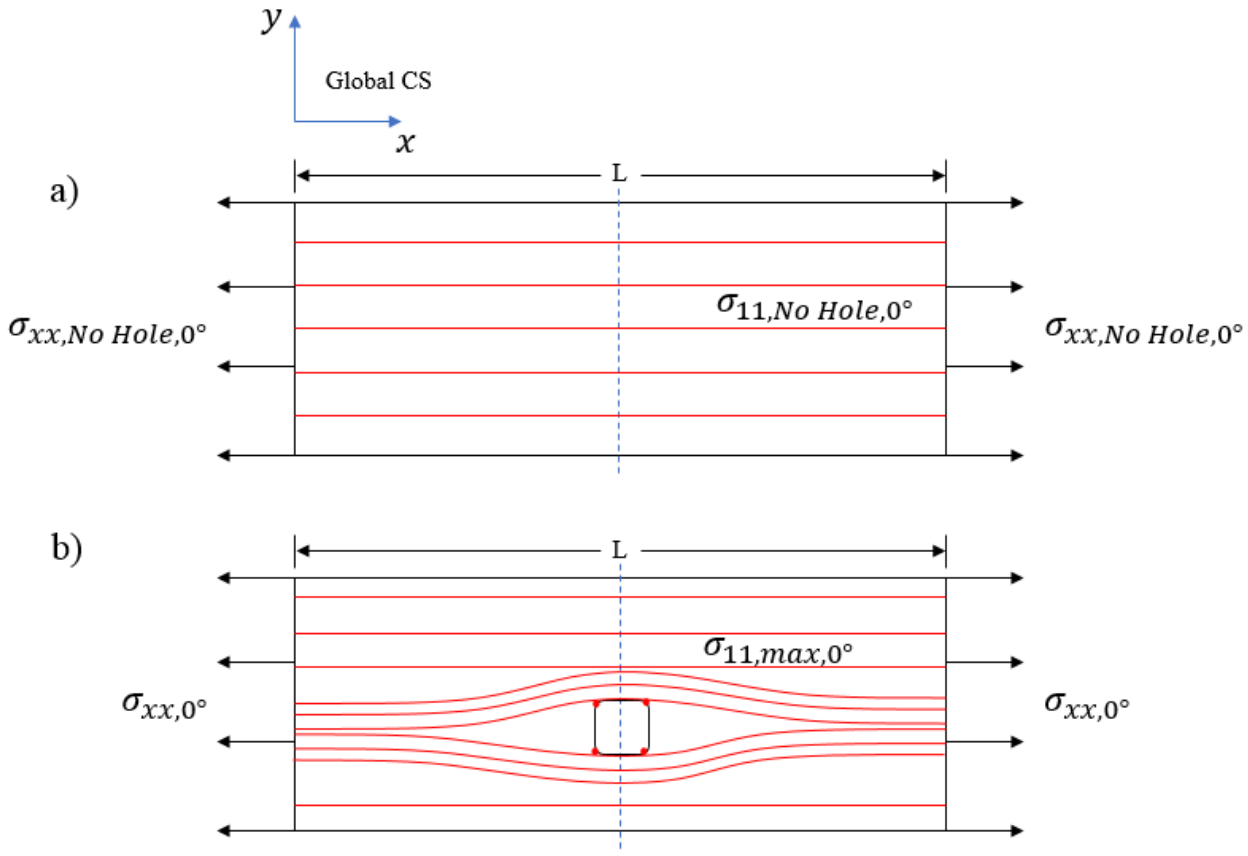

Figure 4.20: Constant force lines in the 0° lamina for the composite laminate: (a) with no hole, (b) with a single square hole with rounded corners.

In order to calculate the stress concentration factor for each individual lamina, the peak lamina $\sigma_{11,max}$ stress (local CS) is divided by the applied $\sigma_{xx,No\ Hole}$ stress (global CS) in each lamina with no hole, conceptually analogous to Eqn. 2.1, and given below in Eqn. 4.6.

$$K_{t,\theta} = \sigma_{11,max,\theta} / \sigma_{xx,No\ Hole,\theta} \tag{4.6}$$

4.3.1 Effect of Edge Distance

The lamina stress concentration factors, $K_{t,\theta}$, are calculated using Eqn. 4.6 and the values from Tables 4.4, 4.7, and 4.8, and summarized below in Table 4.10. The highest SCFs are always found in the ±45° laminas, due to division by the lower value of $\sigma_{xx,No\ Hole}$ stress found in the ±45° lamina values from Table 4.8.

Table 4.10: Lamina SCFs for the single offset square hole with rounded corners and the single offset circular hole.

Corner Radius, r_c (mm)	**Hole Edge-to-Laminate Edge, d_e (mm)**	**Single Offset Square Hole: $K_{t,\theta}$**			
		$\theta = 0°$	**$\theta = 45°$**	**$\theta = -45°$**	**$\theta = 90°$**
0.25	15.875 (Centered)	4.619	10.113	10.113	6.201
	7.938	4.792	10.550	10.550	6.594
	3.969	5.235	11.579	11.579	7.549
	1.984	5.811	13.022	13.022	9.035
1	15.875 (Centered)	3.328	6.273	6.273	2.815
	7.938	3.452	6.509	6.509	2.963
	3.969	3.737	7.052	7.052	3.327
	1.984	4.035	7.777	7.777	3.987
2	15.875 (Centered)	2.882	5.148	5.148	1.942
	7.938	3.029	5.312	5.312	2.044
	3.969	3.363	5.671	5.671	2.288
	1.984	3.970	6.144	6.144	2.642
3	15.875 (Centered)	2.938	4.750	4.750	1.536
	7.938	3.108	4.940	4.940	1.602
	3.969	3.552	5.337	5.337	1.775
	1.984	4.379	5.975	5.975	2.036
Single Offset Circular Hole: $K_{t,\theta}$					
3.175 (Circle)	15.875 (Centered)	3.102	4.721	4.721	1.498
	7.938	3.281	4.911	4.911	1.561
	3.969	3.751	5.373	5.373	1.714
	1.984	4.672	6.112	6.112	1.954

The SCFs for each lamina as a function of distance from the hole edge to the laminate edge are shown below in Figs. 4.21-4.23. It can readily be seen that as the square hole edges become more rounded, the SCF curves approach the behavior of a circular hole, as expected.

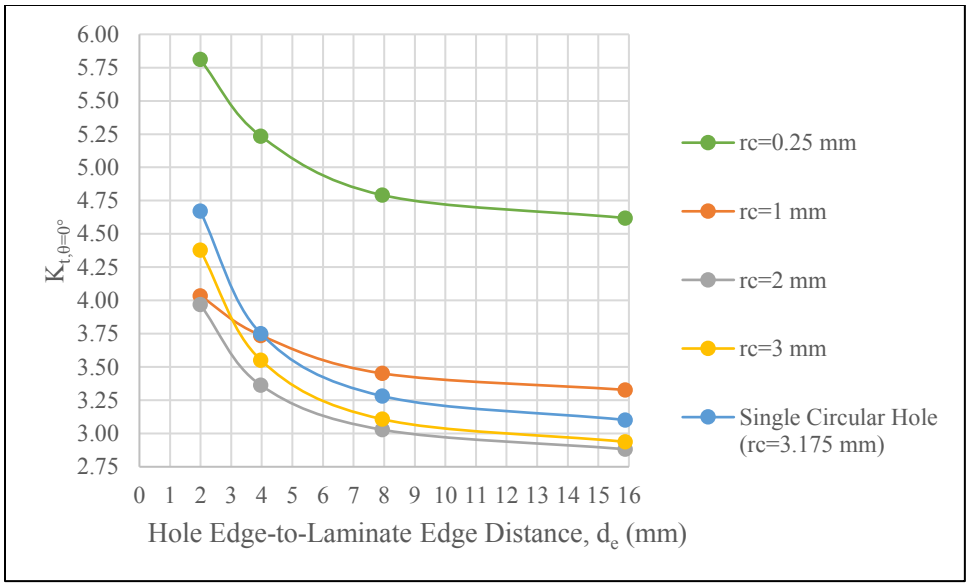

Figure 4.21: SCFs for 0° lamina versus single square hole edge-to-laminate edge distance.

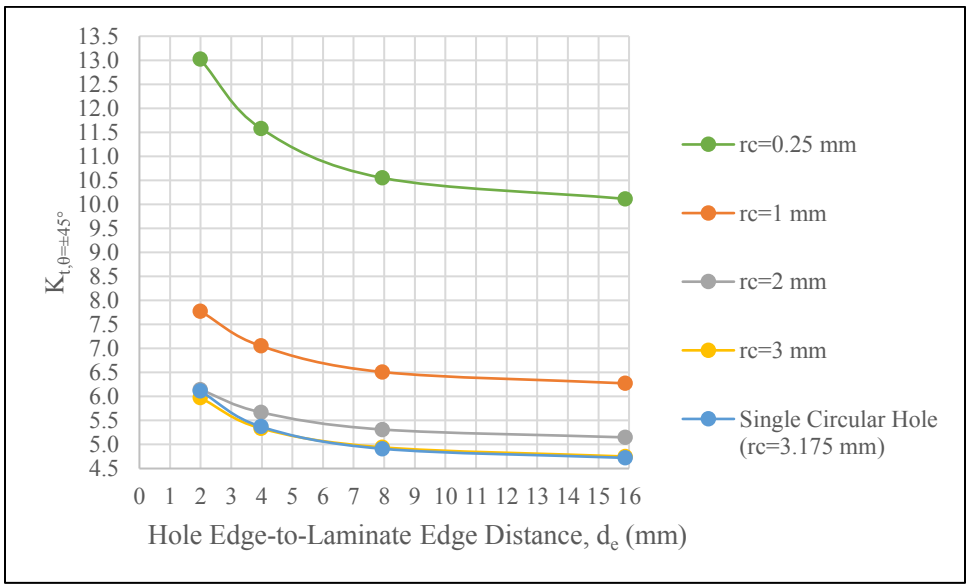

Figure 4.22: SCFs for ±45° lamina versus single square hole edge-to-laminate edge distance.

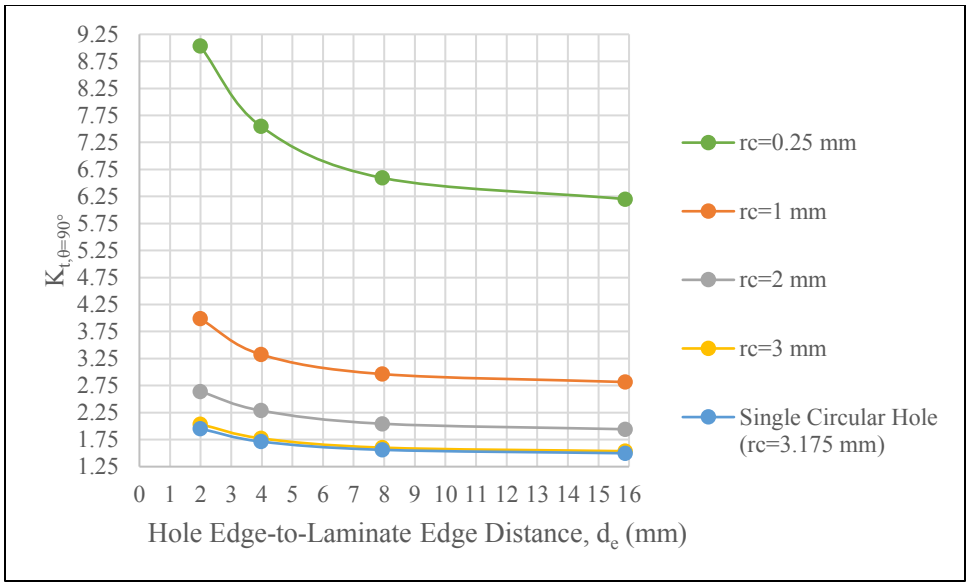

Figure 4.23: SCFs for 90° lamina versus single square hole edge-to-laminate edge distance.

It is worthwhile to recognize that due to symmetry created by the fiber orientation angle, certain stress field values at each of the four corners of the square hole are expected to be equivalent. However, this is only encountered for single centered square hole. Once the hole moves away from the central axis, some symmetry relationships are lost due to influence from the "edge effect". The symmetry equivalencies for a single centered square hole can be seen below in Fig. 4.24, where the dashed lines passing through each hole represent the fibers. The symmetry conditions for a single centered square hole with rounded corners are consistent with those found by Cannon [19].

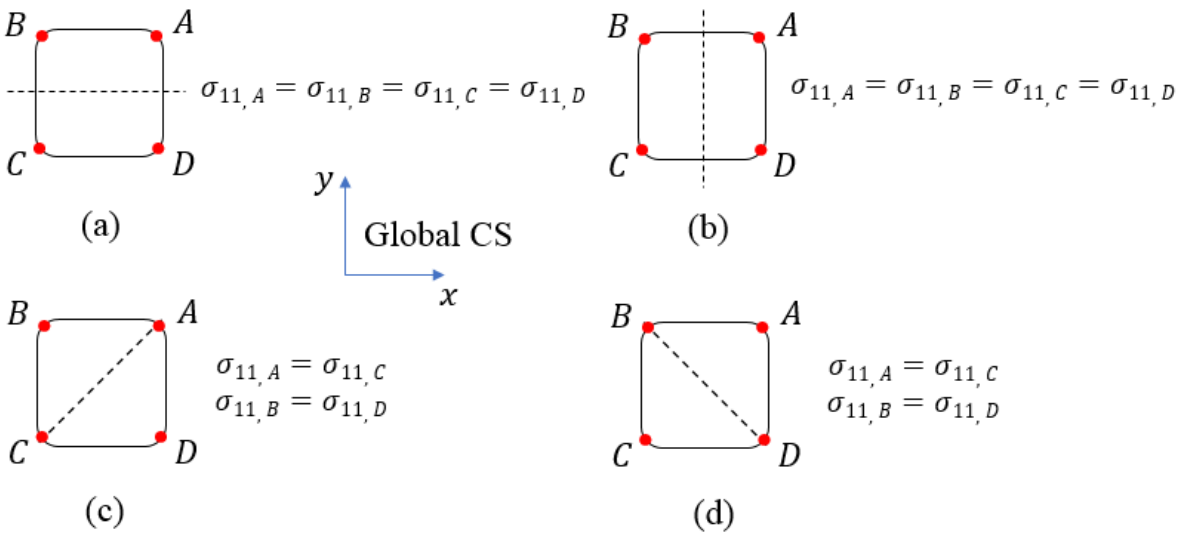

Figure 4.24: Stress symmetry conditions based on fiber orientation directions for a single centered square hole: (a) 0° fiber, (b) 90° fiber, (c) 45° fiber, (d) -45° fiber.

To illustrate symmetry and the "edge effect", the normalized 0° lamina σ_{11} stress for the various single offset square hole cases with $r_c = 2$ mm are plotted below in Fig. 4.25.

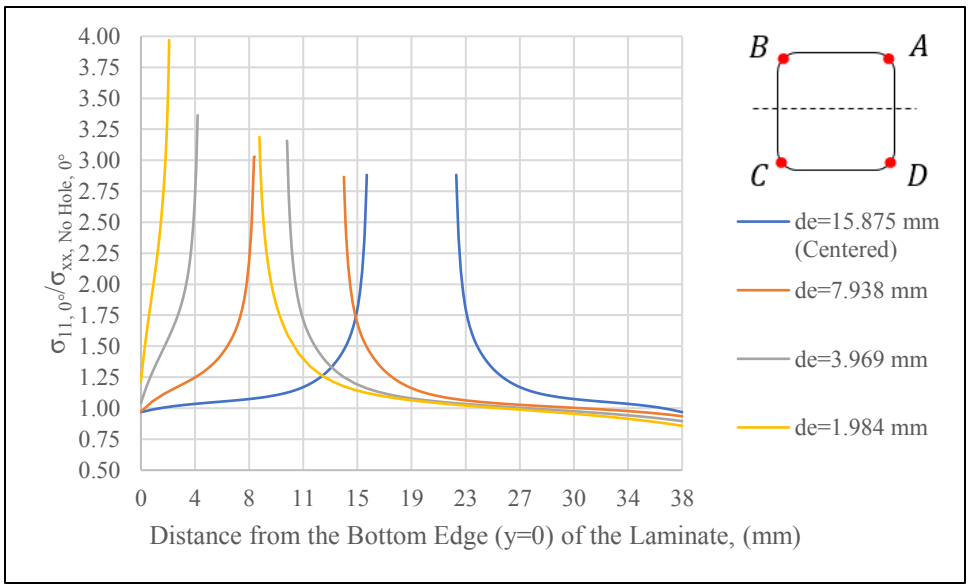

Figure 4.25: Normalized 0° lamina σ_{11} stress for the single offset square hole cases with $r_c = 2$ mm.

It should be noted that the maximum σ_{11} stress in the 0° lamina is found at points C or D for the offset cases. These points are closer to the laminate edge, and thus one expects a higher stress at

these locations. The σ_{11} stress is lower at points A and B, which are on the opposite side of the square hole, closer to the central axis of the laminate.

Further, symmetry is present in the 0° laminas for all offset cases for select corner points. Specifically, $\sigma_{11,A} = \sigma_{11,B}$ and $\sigma_{11,C} = \sigma_{11,D}$. Once the center of the single square hole moves away from the central axis of the laminate (i.e. $d_e < 15.875$ mm), symmetry about the central axis is lost due to influence from the "edge effect", and secondary bending. As such, the σ_{11} stress at all four corner points will no longer be equal. This behavior can be seen below in Fig. 4.26, and Table 4.11. It is worth noting that the "splitting" of the normalized σ_{11} stress curve due to the "edge effect" is consistent with results from Kheradiya [5]. The remaining study will focus only on a corner radius of $r_c = 2$ mm, which is more of a practical application.

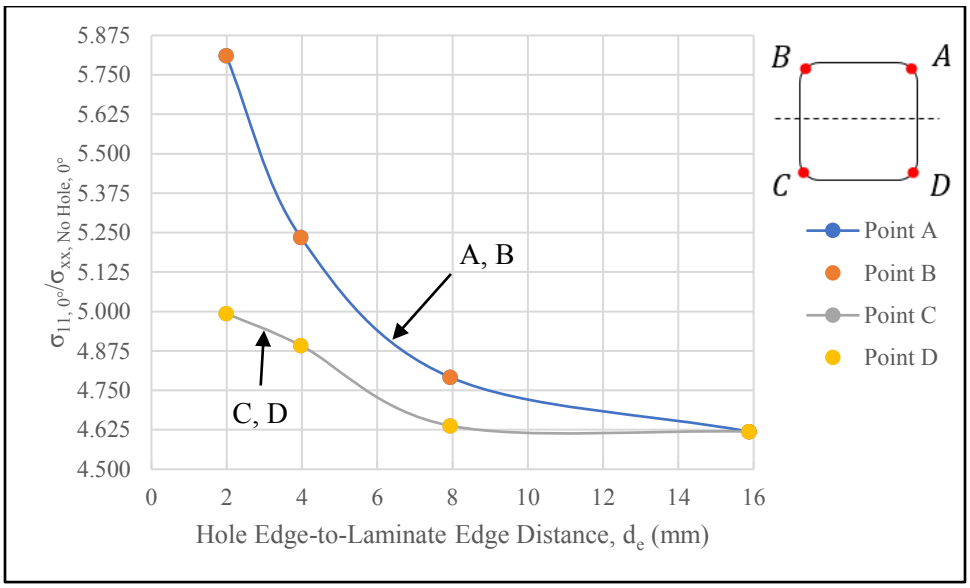

Figure 4.26: Normalized 0° lamina σ_{11} stress at points A through D for $r_c = 0.25$ mm.

Table 4.11: Normalized σ_{11} stress at the single offset square hole corner points for the 0° lamina with $r_c = 0.25$ mm.

Hole Edge-to-Laminate Edge Distance, d_e (mm)	$\sigma_{11,0°}/\sigma_{xx,No\ Hole,0°}$			
	A	***B***	***C***	***D***
15.875 (Centered)	4.619	4.619	4.619	4.619
7.938	4.792	4.792	4.638	4.638
3.969	5.235	5.235	4.892	4.892
1.984	5.811	5.811	4.994	4.994

The σ_{11} stress values at each of the four corners of the single offset square hole with $r_c = 2$ mm are given below in Table 4.12.

Table 4.12: σ_{11} stress at points A through D for the single offset square hole with $r_c = 2$ mm.

Hole Edge-to-Laminate Edge Distance, d_e (mm)	**Fiber Orientation Angle, θ (°)**	**σ_{11} (MPa)**			
		A	***B***	***C***	***D***
15.875 (Centered)	0	3.728	3.728	3.728	3.728
7.938		3.822	3.822	3.917	3.917
3.969		4.061	4.061	4.349	4.349
1.984		4.192	4.192	5.134	5.134
15.875 (Centered)	45	-0.064	2.883	-0.064	2.883
7.938		-0.066	2.970	-0.059	2.974
3.969		-0.079	3.175	-0.077	3.130
1.984		-0.394	3.440	-0.314	2.710
15.875 (Centered)	-45	2.883	-0.064	2.883	-0.064
7.938		2.970	-0.066	2.974	-0.059
3.969		3.175	-0.079	3.130	-0.077
1.984		3.440	-0.394	2.710	-0.314
15.875 (Centered)	90	0.670	0.670	0.670	0.670
7.938		0.705	0.705	0.629	0.629
3.969		0.789	0.789	0.545	0.545
1.984		0.911	0.911	0.276	0.276

The σ_{11} stress values at points A through D for the single square hole with rounded corners ($r_c = 2$ mm) from Table 4.12 are normalized and shown below in Figs. 4.27-4.29.

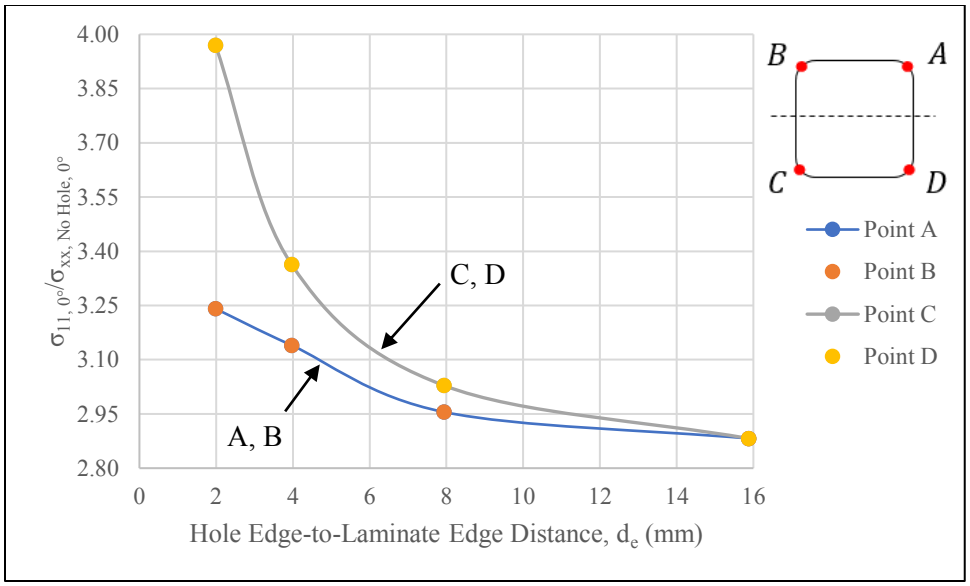

Figure 4.27: Normalized 0° lamina σ_{11} stress at points A through D for $r_c = 2$ mm.

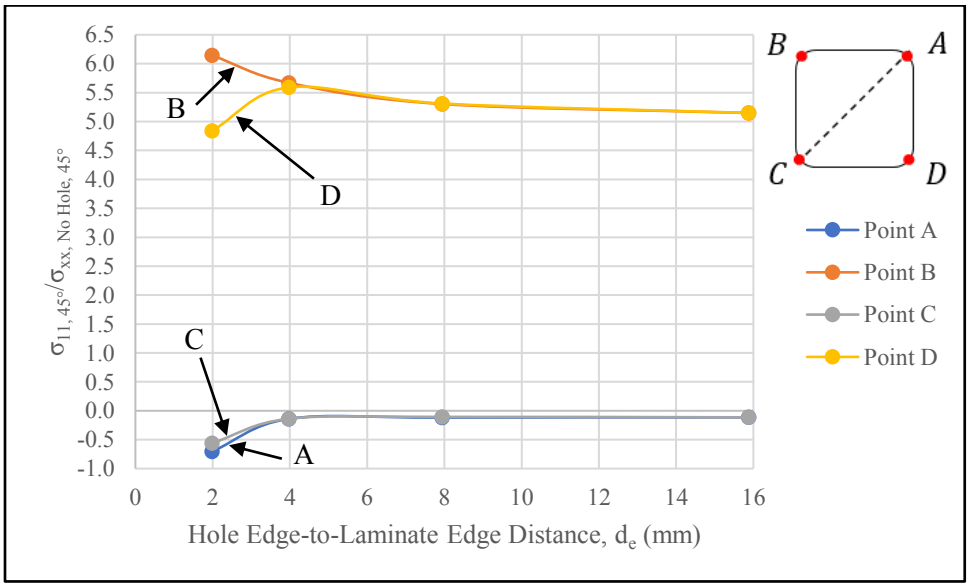

Figure 4.28: Normalized 45° lamina σ_{11} stress at points A through D for $r_c = 2$ mm.

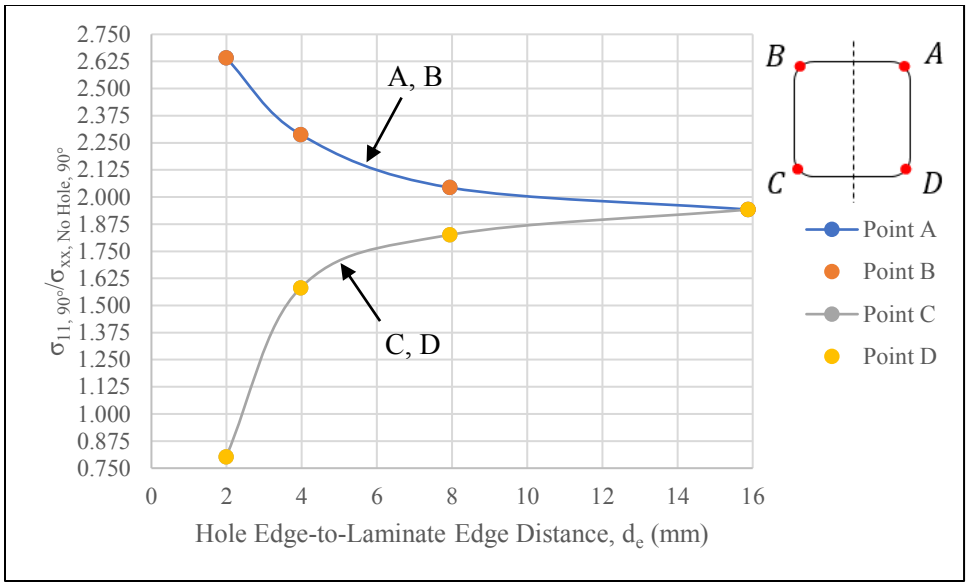

Figure 4.29: Normalized 90° lamina σ_{11} stress at points A through D for $r_c = 2$ mm.

The loss of equivalency in the stress values at the various points around the square hole with rounded corners is due to the eccentricity of the load path. Secondary bending is introduced once the hole moves away from the central axis, which serves to increase the stress at both the top and bottom of the hole. This origin of this effect is shown in the free body diagrams below in Fig. 4.30. There, the loading for the laminate can be transformed by using equivalent forces in order to arrive at the loading case which gives rise to secondary bending (Step 4).

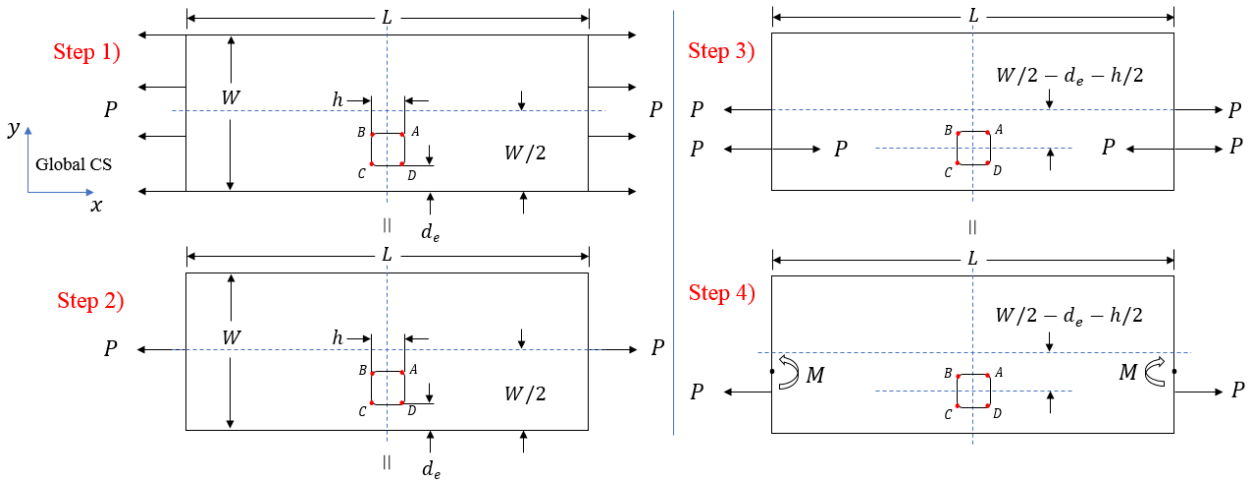

Figure 4.30: Laminate free body diagrams illustrating secondary bending.

The stresses which act at the four points of the square hole (or holes) can be understood using the same concept. The equivalent stress due to the applied load can be split into the stresses found at each point; those due to the applied force, P, and those due to the moment, M, induced by the offset force. Fundamentally, this can also be thought of as the addition of stresses due to an applied force and moment as seen below in Fig 4.31. Free body diagrams depicting the application of the concept to this study can be seen below in Fig. 4.32.

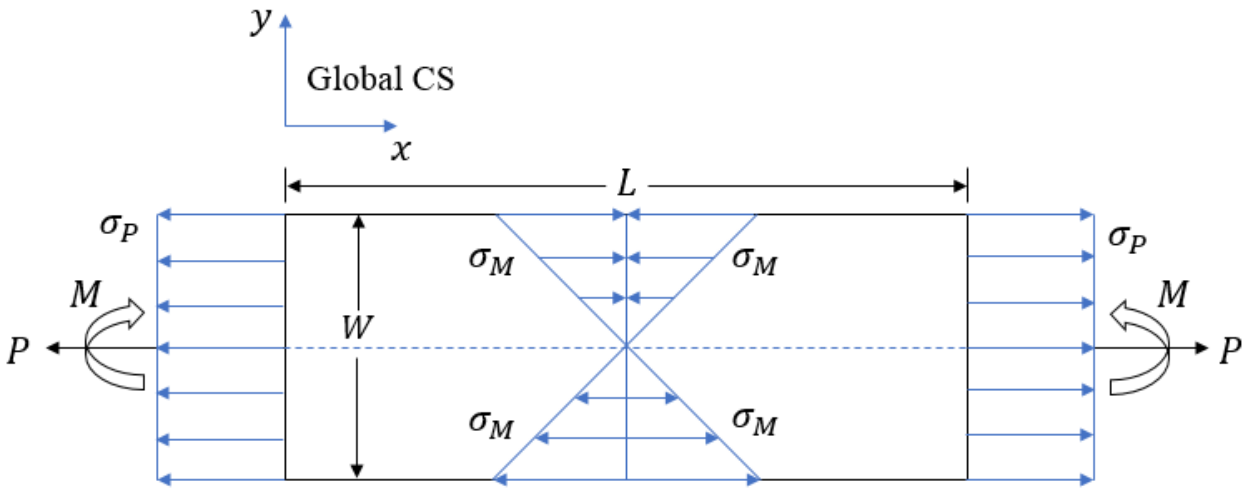

Figure 4.31: General free body diagram illustrating the directional contribution of distributed σ_P and σ_M stresses due to P and M, respectively.

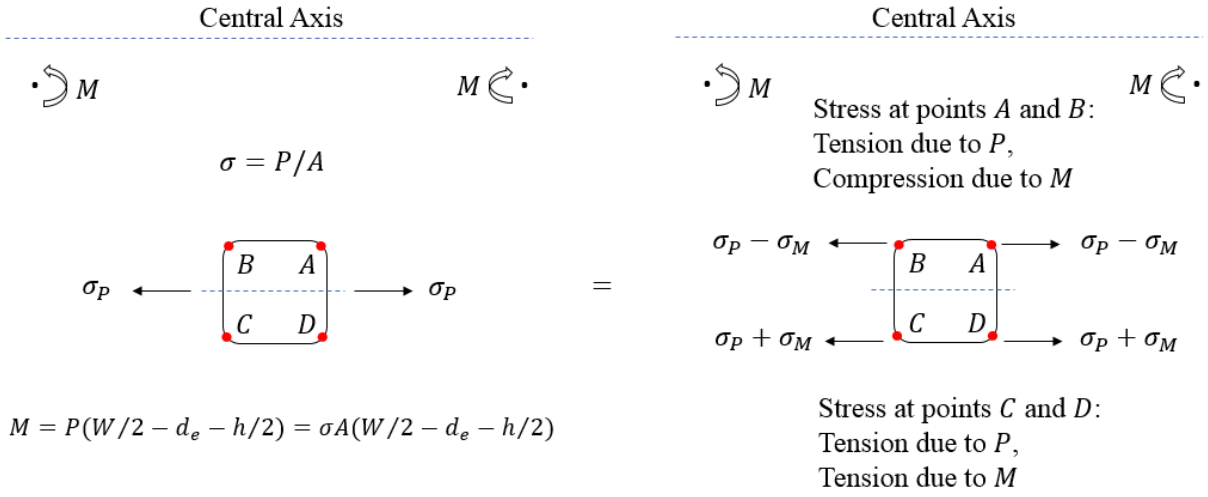

Figure 4.32: Offset square hole free body diagrams illustrating secondary bending effects.

To further illustrate the effects of secondary bending, the σ_{11} stress field contours for the single centered square hole ($d_e = 15.875$ mm) and the single offset square hole ($d_e = 1.984$ mm) with $r_c = 2$ mm are shown below in Figs. 4.33 and 4.34. An enlarged view of Fig. 4.34 is provided below in Fig. 4.35. The undeformed laminate (solid white lines) is also shown to provide context in Figs. 4.33-4.35. Further, the effect of extension and bending are greatly exaggerated by ANSYS, with an auto calculated scale factor of ≈ 1689. Additionally, the Poisson effect can also be seen below in Fig. 4.35.

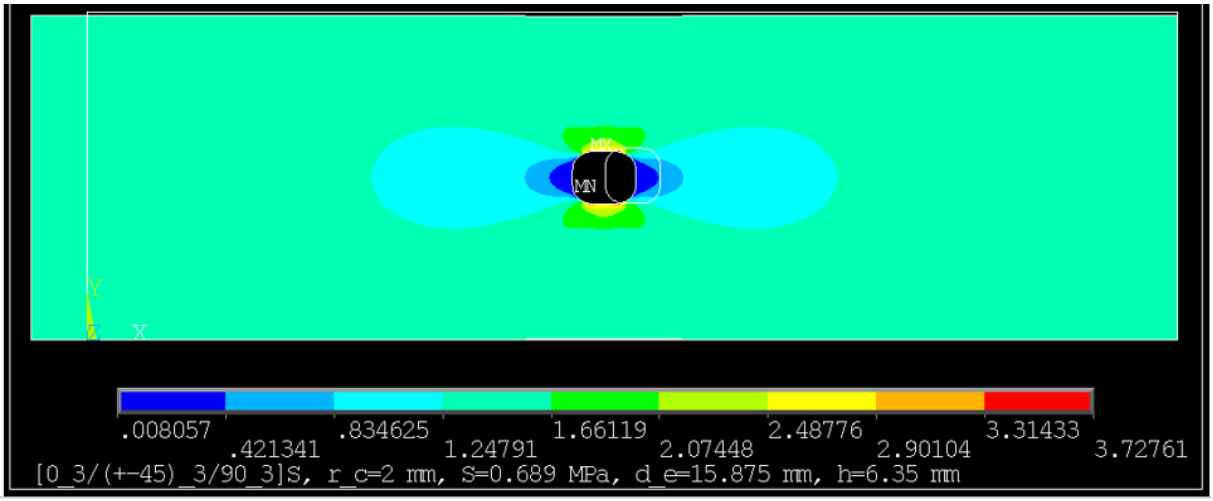

Figure 4.33: Single centered square hole ($d_e = 15.875$) with rounded corners ($r_c = 2$ mm), with no secondary bending and x-direction extension only.

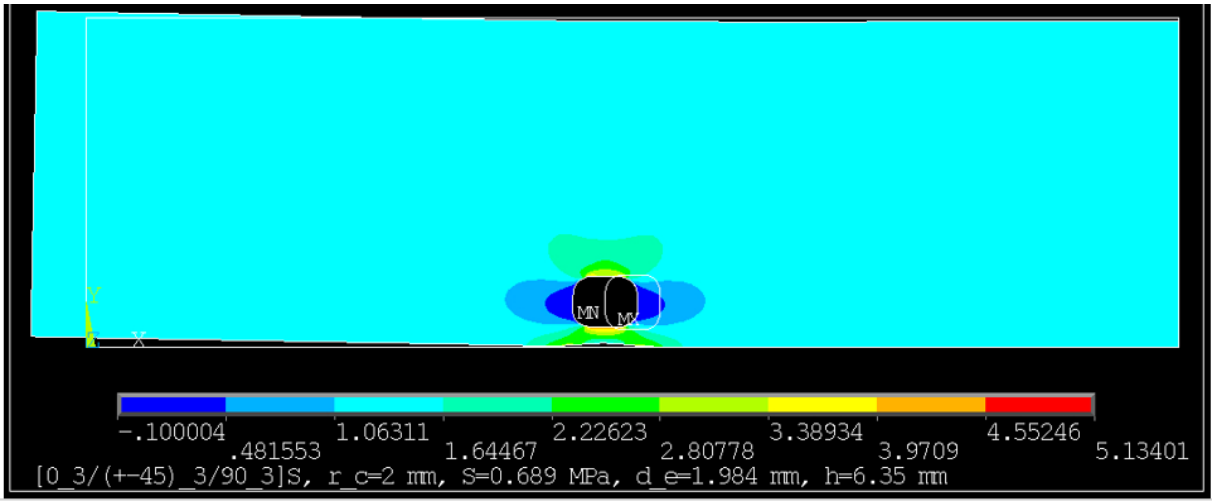

Figure 4.34: Single offset square hole ($d_e = 1.984$ mm) with rounded corners ($r_c = 2$ mm), with secondary bending and x-direction extension present.

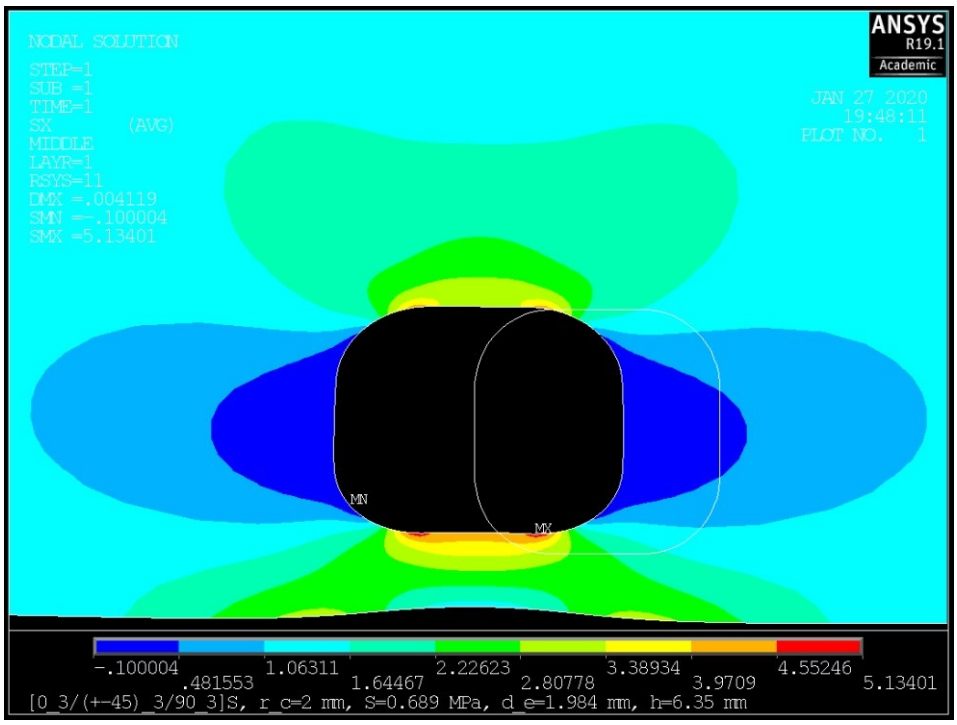

Figure 4.35: Enlarged view of single offset square hole ($d_e = 1.984$ mm) with rounded corners ($r_c = 2$ mm), with secondary bending and x-direction extension present.

To fully understand the distribution of σ_{11} stress found in the laminas, as well as the influence of the "edge effect" for the single circular hole, it is worthwhile to plot the normalized σ_{11} stress. Because the greatest σ_{11} stress in the laminate is found in the 0° lamina, this layer is of particular interest. The normalized σ_{11} stress field results for the 0° laminas at the four different hole edge-to-laminate edge distances can be seen below in Fig. 4.36.

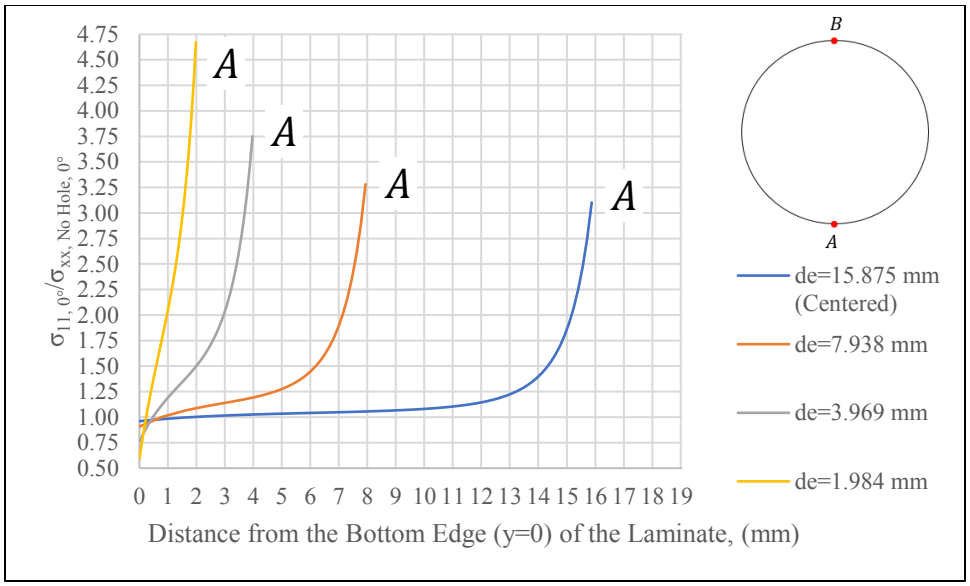

Figure 4.36: Normalized 0° lamina σ_{11} stress for the single offset circular hole cases.

For the single circular hole, the effect of edge distance upon the normalized maximum σ_{11} stress found in each layer can be seen below in Fig. 4.37. It is noted that the 45° and -45° laminas should possess the same stress values, and there was consistent agreement up to the fifth decimal place, which is the maximum that ANSYS displayed.

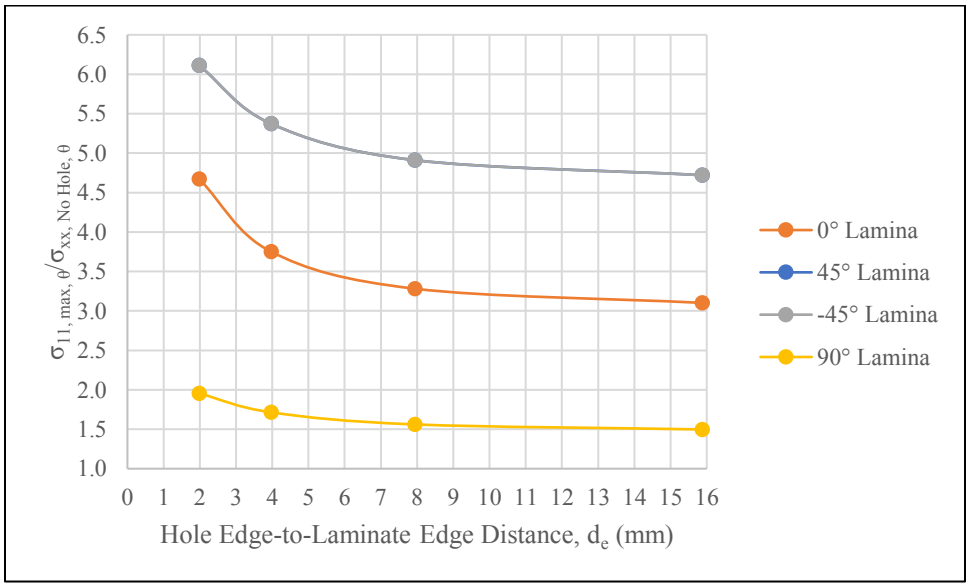

Figure 4.37: Normalized maximum σ_{11} stress in the laminas for the single offset circular hole cases.

The normalized σ_{11} stress in the 0° lamina around the periphery of the circular hole as a function of the angle about the center of the hole, γ, has been determined for the various offset distances and is shown below in Fig. 4.38.

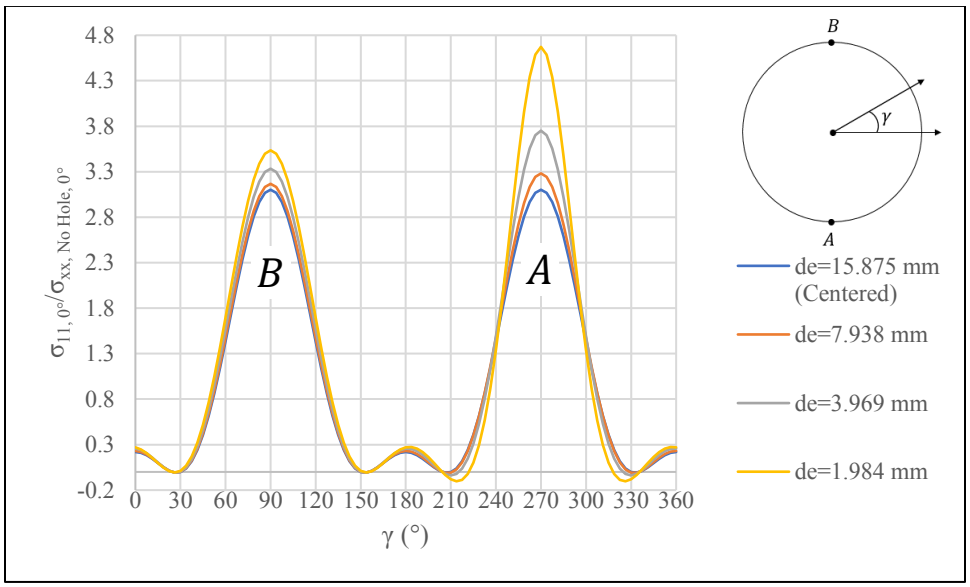

Figure 4.38: Normalized 0° lamina σ_{11} periphery stress for the single offset circular hole cases.

The maximum σ_{11} stress in the single offset circular hole in all cases is always found in the 0° laminas. As the hole becomes closer to the edge of the laminate, the "edge effect" begins to have a greater influence on the maximum σ_{11} stress found at point A, which is expected.

4.3.2 Effect of Corner Radius

The normalized σ_{11} stress from the edge of the laminate to the hole center for the 0° lamina is plotted below in Figs. 4.39 and 4.40. There, the behavior of the σ_{11} stress concentration as the square hole with rounded corners transitions to a circular hole can be readily understood.

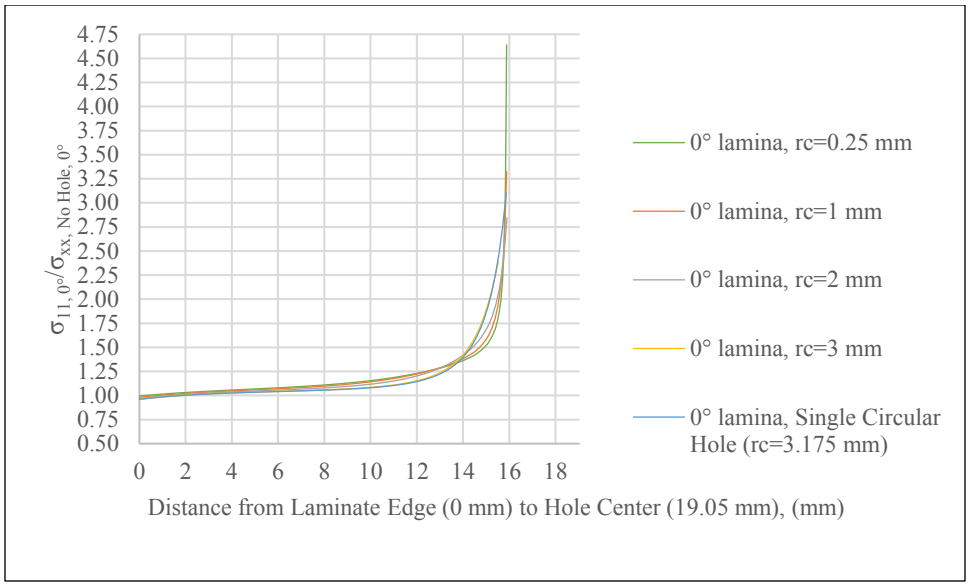

Figure 4.39: Normalized 0° lamina σ_{11} stress versus hole edge-to-laminate edge distance for the single centered square hole with rounded corners and the single centered circular hole.

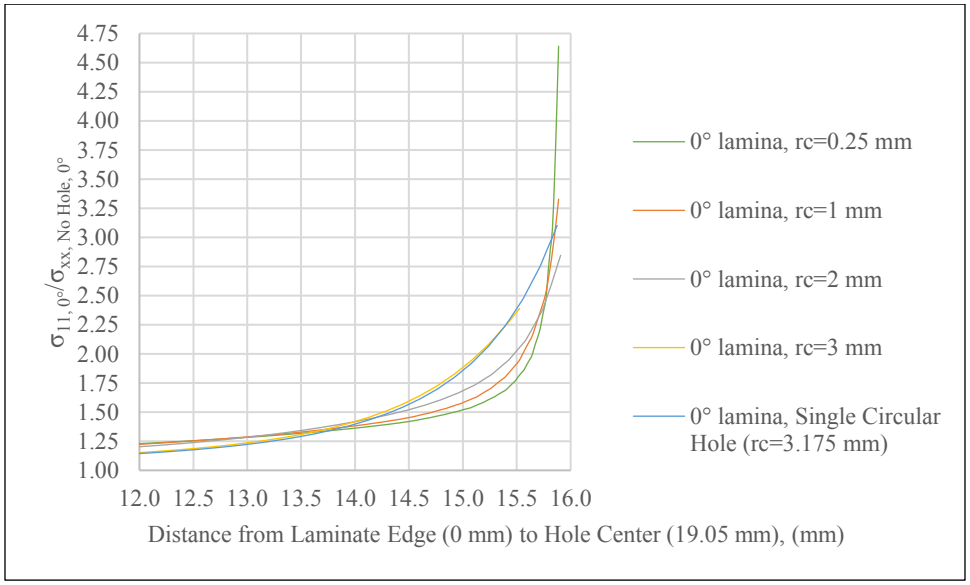

Figure 4.40: Enlarged view of the normalized 0° lamina σ_{11} stress versus hole edge-to-laminate edge distance for the single centered square hole with rounded corners and the single centered circular hole.

It is interesting to note that as the size of the corner radius increases, the square hole approaches the geometry of a circular hole. Accordingly, the σ_{11} stress fields begin to behave as if a circular hole was present, and at $r_c = 3$ mm, one recovers the normalized σ_{11} stress values of the circular hole within -0.139% in the 0° lamina, as seen above in Fig. 4.40. It can also be seen

that the normalized σ_{11} stress in each curve approaches an average value of ≈ 0.975 at the edge of the laminate (zero on the global y-axis). While this value is slowly decreasing, it is certainly not equal to the normalized applied laminate stress, $\sigma/\sigma_{xx,No\ Hole,0°}$, of 0.533. This is to be expected, as the plate is of finite width. If the plate were of infinite width, one would recover the value of the applied stress (or normalized stress), at some large distance from the center of the hole.

It is worthwhile to compare the results from the single square hole to the single circular hole, in the interest of identifying stress field behavior trends. Stress concentration factors in each lamina for both the single centered circular hole and the single centered square hole with varying corner radii are presented below in Fig. 4.41, where the laminate thickness increases from left to right, with the midplane (vertical dashed line) being located in the center of the two 90° laminas. The ±45° and 90° lamina clusters have been reduced from three to one on each side of the midplane in order to condense the size of the graph. It can readily be seen that the stress concentration factors in each lamina approach those of a circular hole, upon increasing corner radius size.

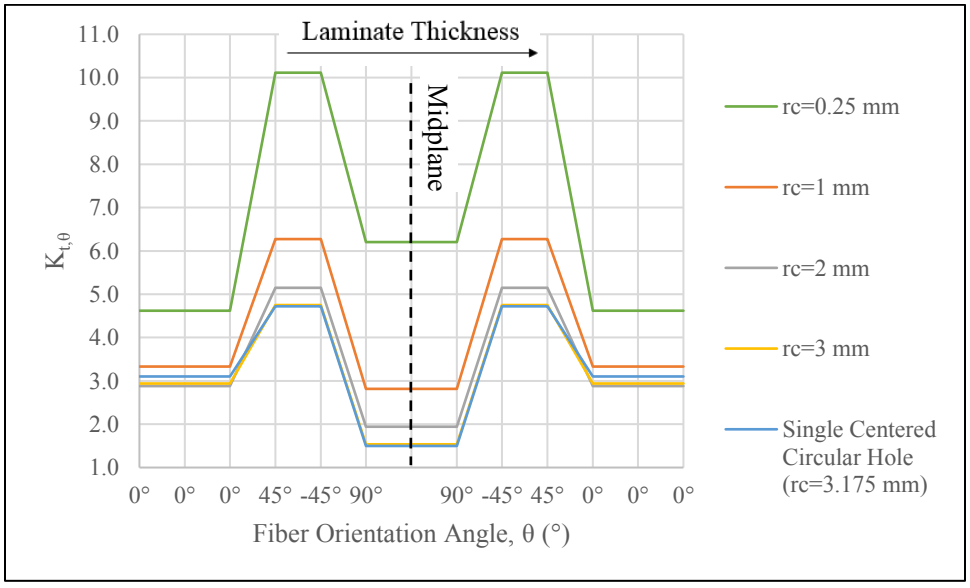

Figure 4.41: Stress concentration factor for each lamina in a single centered square hole with varying corner radii laminate and in a single centered circular hole laminate.

To illustrate the effect of the corner radius on the surrounding σ_{11} stress field in the 0° and 45° laminas, the corresponding stress concentration factors from Table 4.10 are summarized

below in Table 4.13. The SCF for the square hole with rounded corners approaches the SCF for a circle in both the 0° and 45° laminas as the corner radius increases.

Table 4.13: Lamina SCFs for the 0° and ±45° laminas.

Fiber Orientation Angle, θ (°)	Hole Edge-to-Laminate Edge Distance, d_e (mm)	Single Square Hole: $K_{t,\theta}$				Single Circular Hole: $K_{t,\theta}$
		$r_c = 0.25$ mm	$r_c = 1$ mm	$r_c = 2$ mm	$r_c = 3$ mm	Hole Diameter, $d = 6.35$ mm ($r_c = 3.175$ mm)
0	15.875 (Centered)	4.619	3.328	2.882	2.938	3.102
±45		10.113	6.273	5.148	4.750	4.721

Transformation of the σ_{11} stress field can be seen in the 0° lamina with increasing corner radius. The four maximum σ_{11} stress points at each corner of the square hole travel inward to converge at a single point, mimicking the σ_{11} stress field behavior seen in the circular hole. This is depicted below in Fig. 4.42.

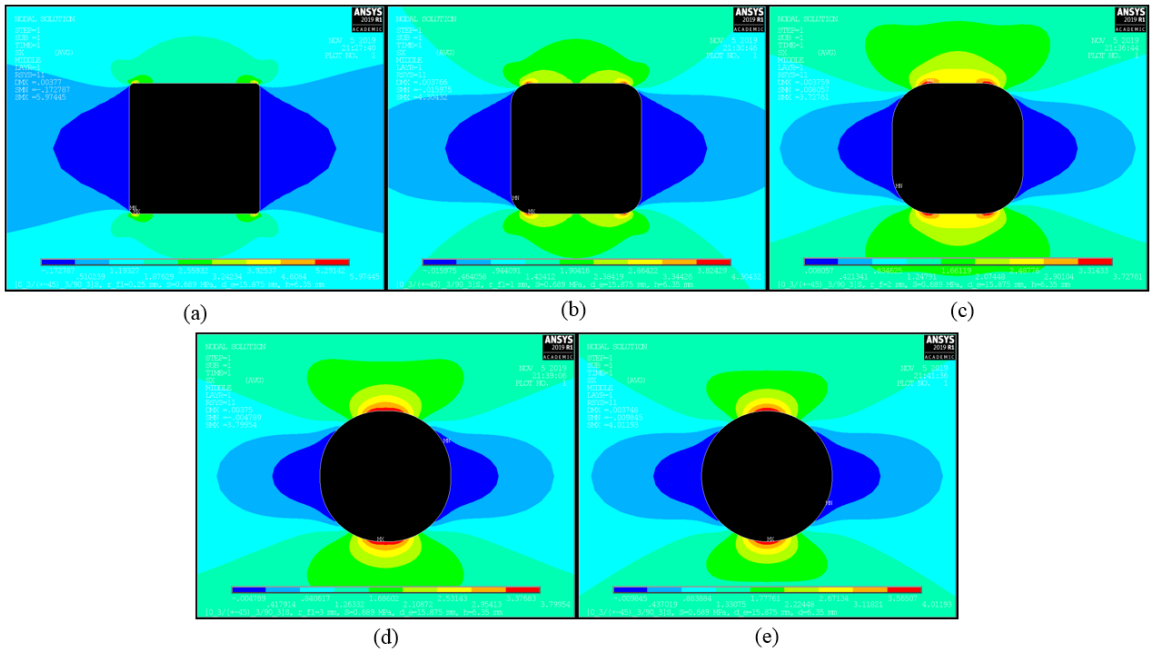

Figure 4.42: 0° lamina σ_{11} stress field transformation: (a) central square hole with $r_c = 0.25$ mm, (b) central square hole with $r_c = 1$ mm, (c) central square hole with $r_c = 2$ mm, (d) central square hole with $r_c = 3$ mm, (e) central circular hole ($r_c = 3.175$ mm).

Transformation of the σ_{11} stress field can also be seen in the 45° lamina. It should be noted that the location of the maximum σ_{11} stress begins to travel clockwise as the corner radius is increased. This can be seen below in Fig. 4.43.

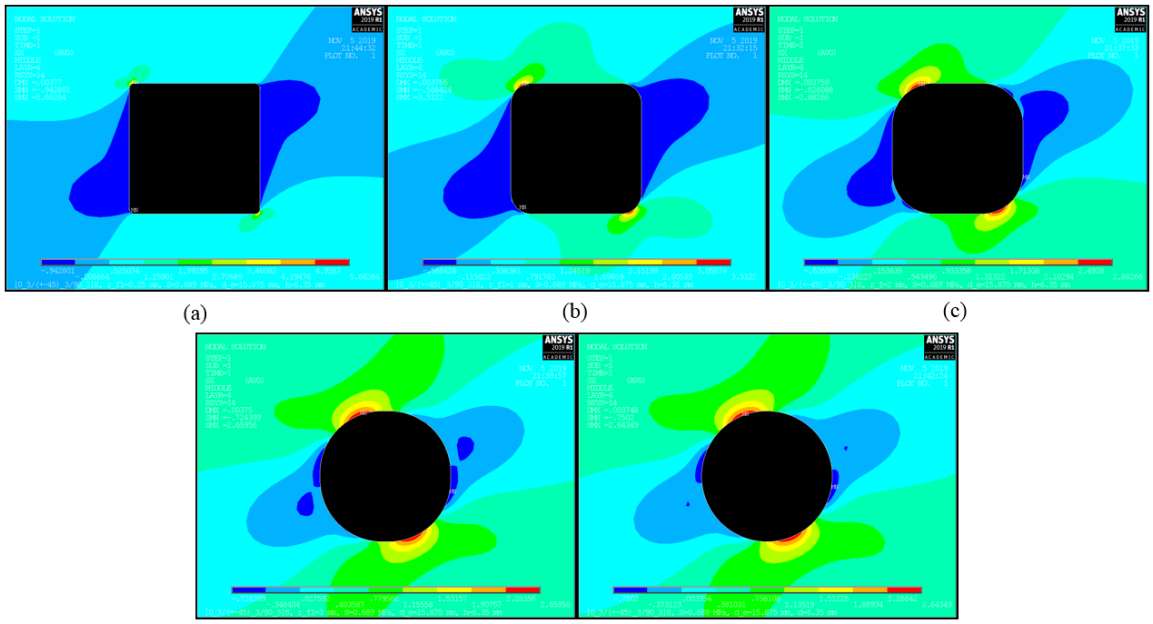

Figure 4.43: 45° lamina σ_{11} stress field transformation: (a) central square hole with $r_c = 0.25$ mm, (b) central square hole with $r_c = 1$ mm, (c) central square hole with $r_c = 2$ mm, (d) central square hole with $r_c = 3$ mm, (e) central circular hole ($r_c = 3.175$ mm).

The SCFs for the transition of a single centered square hole with rounded corners to a single centered circular hole are graphed below in Fig. 4.44, along with a fourth order polynomial trendline. It is worth recognizing that a minimum exists at the inflection point in the $K_{t,\theta=0°}$ curve found in Fig. 4.44. The SCF for the 0° lamina decreases with increasing corner radius until the minimum value is reached, at which point the SCF increases for increasing corner radius, until the corresponding SCF for a circle is attained. This behavior is consistent with results from Cannon [19], which can be seen further below in Fig. 4.45. By fitting a trendline to the curve in Fig. 4.44, one can easily see that a minimum corner radius actually exists at some value of r_c for 2.3 mm $\leq r_c \leq$ 2.8 mm, and not at a point found on the original $K_{t,\theta=0°}$ curve, as one may be initially lead to believe. That point is the $\min(y)$, and a more accurate approximation of that value can be determined simply by first letting

$$\frac{dy}{dx} = \frac{d}{dx}(0.1381x^4 - 1.0373x^3 + 3.0211x^2 - 4.3202x + 5.5263) = 0 \tag{4.7}$$

$$\frac{dy}{dx} = 0.5524x^3 - 3.1119x^2 + 6.0422x - 4.3202 = 0 \tag{4.8}$$

Solving Eqn. 4.8 for the independent variable gives $x = 2.537$ mm, indicating that the minimum SCF for the 0° lamina is obtained when the corner radius is $r_c = 2.537$ mm. This would be more readily apparent in the $K_{t,\theta=0°}$ curve, had data been taken for additional values of r_c. Similarly, this is also the case for results from Cannon [19] in Fig. 4.45 below.

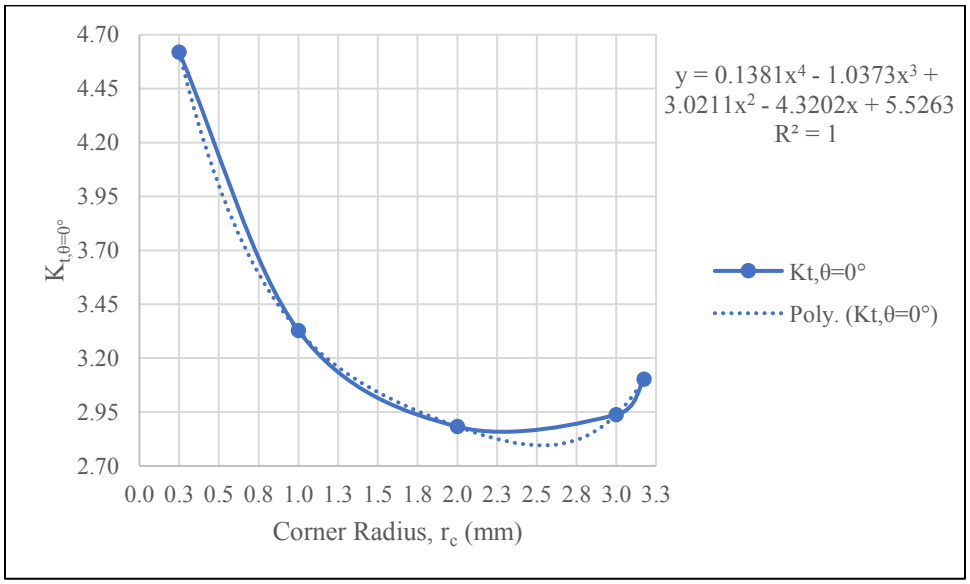

Figure 4.44: SCFs and trendline for the 0° lamina with a single centered square hole.

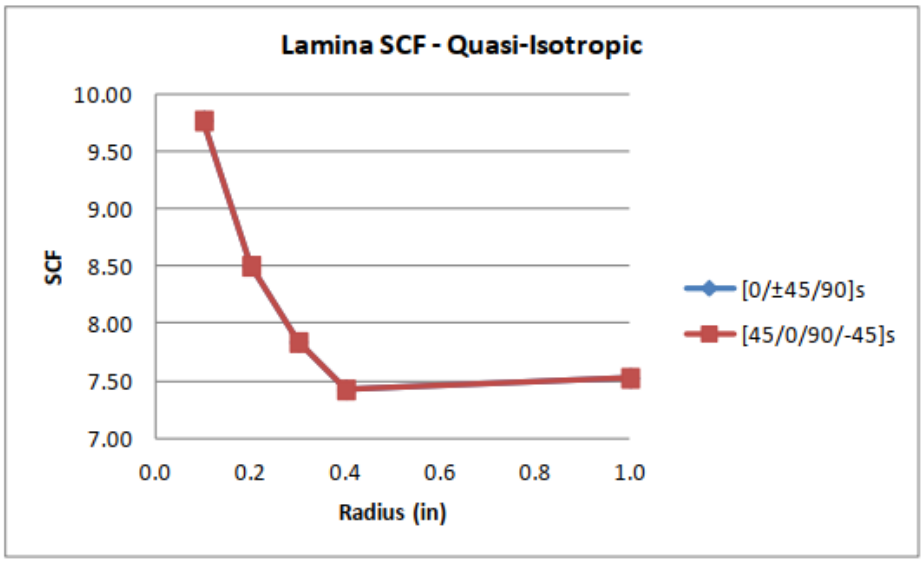

Figure 4.45: SCF for laminas in quasi-isotropic laminates [19].

To validate the results from Eqn. 4.8, the single square hole with $r_c = 2.537$ mm was created and the SCF results are plotted below in Fig. 4.46. Fitting a fourth order polynomial again gives an R^2 value of 0.9996 which is very close to unity, indicating an excellent correlation between the revised data and the new curve fit. The data for Fig. 4.46 is given below in Table 4.14, where one can easily see that $r_c = 2.537$ mm does indeed yield a minimum value for the SCF $K_{t,\theta=0°}$.

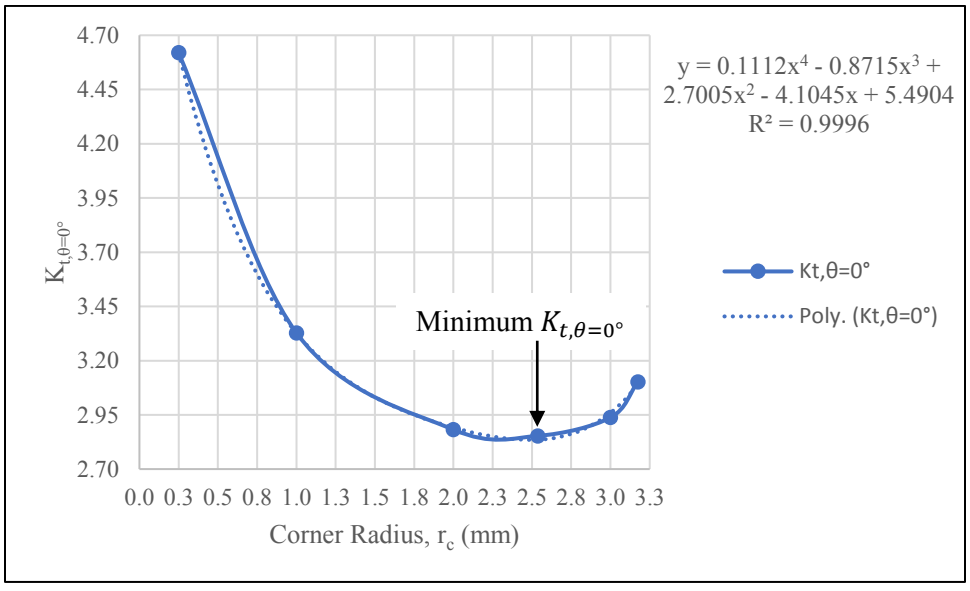

Figure 4.46: Addition of $r_c = 2.537$ mm data point and updated trendline for the 0° lamina.

Table 4.14: SCFs for the 0° laminas in Fig. 4.46.

Corner Radius, r_c (mm)	$K_{t,\theta=0°}$
0.250	4.619
1.000	3.328
2.000	2.882
2.537	2.853
3.000	2.938
3.175 (Circle)	3.102

4.3.3 Laminate Stress Concentration

Using classical laminate analysis equations from Mallick [3], the extensional stiffness matrix, $[A]$, for the $[0_3/(\pm45)_3/90_3]_S$ laminate is found to be

$$[A] = \begin{bmatrix} 79.08 & 22.44 & 0 \\ 22.44 & 79.08 & 0 \\ 0 & 0 & 28.32 \end{bmatrix} \tag{4.9}$$

The elastic constants for the laminate are calculated using Eqns. 3.3-3.5 as below in Table 4.15.

Table 4.15: Elastic constants for the quasi-isotropic laminate.

E_x (MPa)	E_y (MPa)	G_{xy} (MPa)	ν_{xy}
23857.10	23857.10	9292.22	0.28

It is worth remarking that if one uses the above values for $[A]$ in Eqn. 2.22, and the values from Table 4.15 in Eqn. 2.23, one finds that $K_t = 3$ in both instances, thus recovering the stress concentration factor for a single centered circular hole in an infinitely wide isotropic plate subjected to an in-plane uniaxial tensile stress. In effect, this validates the fact that the quasi-isotropic laminate behaves (in the xy-plane only) as an isotropic material. This is shown below in Table 4.16.

Table 4.16: Laminate theoretical stress concentration factors for a single centered circular hole.

SCF Orthotropic Plate Central Circular Hole Using [A] Values	SCF Orthotropic Plate Central Circular Hole Using Laminate Elastic Constants
3	3

The maximum stress in the laminate can be obtained by using the values from Table 4.15 as the elastic constants for the laminate. In this way, the composite is modeled as an isotropic material using its own laminate-level elastic constants. This approach is taken, as there exist no closed form solutions for laminate-level SCFs for single (or multiple) square holes with rounded corners. The elastic constants used in ANSYS to obtain the global laminate stress, σ_x, and SCFs are given below in Table 4.17.

Table 4.17: Elastic constants for an isotropic laminate.

E-Glass Fiber/Epoxy		
E_{11} **(MPa)**	E_{22} **(MPa)**	E_{33} **(MPa)**
23857.10	23857.10	23857.10
G_{12} **(MPa)**	G_{23} **(MPa)**	G_{13} **(MPa)**
9292.22	9292.22	9292.22
ν_{12}	ν_{23}	ν_{13}
0.28	0.28	0.28

The maximum laminate σ_x stress for all cases of both the single square hole with rounded corners and the single circular hole are given below in Table 4.18.

Table 4.18: Maximum laminate σ_x stress using laminate elastic constants.

Corner Radius, r_c (mm)	**Hole Edge-to-Laminate Edge Distance, d_e (mm)**	**Single Square Hole: $\sigma_{x,max}$ (MPa)**
0.25	15.875 (Centered)	3.254
	7.938	3.375
	3.969	3.681
	1.984	4.079
1	15.875 (Centered)	2.310
	7.938	2.397
	3.969	2.591
	1.984	2.796
2	15.875 (Centered)	2.000
	7.938	2.103
	3.969	2.333
	1.984	2.740
3	15.875 (Centered)	2.030
	7.938	2.148
	3.969	2.454
	1.984	3.025
		Single Circular Hole: $\sigma_{x,max}$ (MPa)
3.175 (Circle)	15.875 (Centered)	2.141
	7.938	2.264
	3.969	2.588
	1.984	3.223

In order to calculate the SCFs for the laminate, one can make use of the following equation

$$K_{tg} = \sigma_{x,max,laminate}/\sigma \tag{4.10}$$

The SCFs for the laminate with the single square hole and the various corner radii along with the laminate containing the single circular hole are calculated using Eqn. 4.10 above, and shown below in Table 4.19. Additionally, correlation to published results from Jong [18] has been identified, in that square holes with sufficiently rounded corners do not cause much higher stress concentrations than circular holes.

Table 4.19: SCFs based on the gross area of the laminate.

Corner Radius, r_c (mm)	Hole Edge-to-Laminate Edge Distance, d_e (mm)	Single Square Hole: K_{tg}
0.25	15.875 (Centered)	4.719
	7.938	4.896
	3.969	5.339
	1.984	5.915
1	15.875 (Centered)	3.350
	7.938	3.477
	3.969	3.758
	1.984	4.055
2	15.875 (Centered)	2.901
	7.938	3.049
	3.969	3.384
	1.984	3.974
3	15.875 (Centered)	2.945
	7.938	3.115
	3.969	3.559
	1.984	4.388
		Single Circular Hole: K_{tg}
3.175 (Circle)	15.875 (Centered)	3.105
	7.938	3.284
	3.969	3.754
	1.984	4.675

The laminate SCFs for the various corner radii for a single square hole, and single circular hole are plotted below in Fig. 4.47.

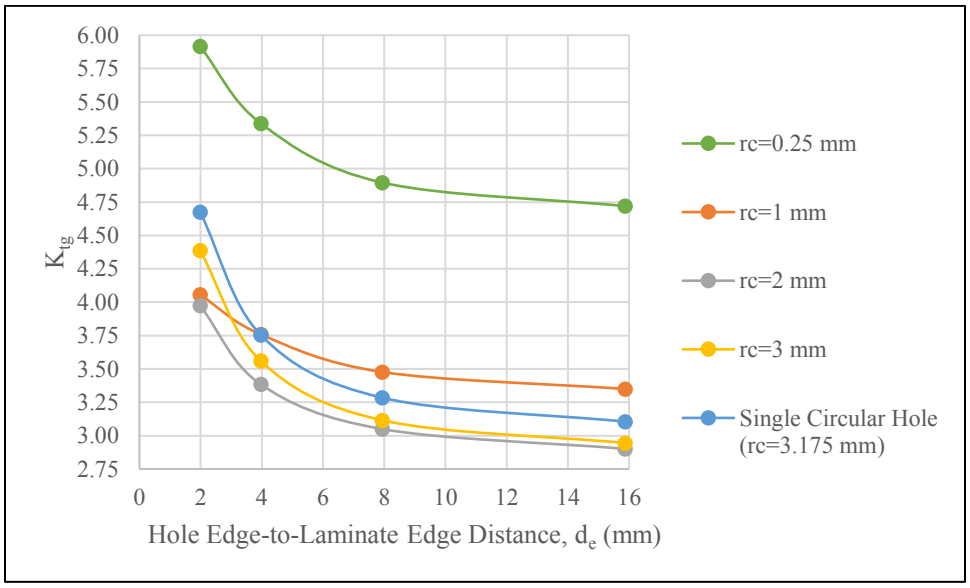

Figure 4.47: Laminate SCFs for the single square hole with rounded corners and the single circular hole.

To illustrate the similarity in behavior between the quasi-isotropic laminate and the isotropic A36 steel plate, the SCF values from Table 4.2. are plotted against the laminate SCF values for 1 mm $\leq r_c \leq$ 3 mm. It is expected that the steel plate and laminate perform identically, and this can be seen below in Fig. 4.48 and Table 4.20. As explained in the beginning of this chapter, the slight difference between the data points at $r_c = 3$ mm for the FEA and theoretical results is attributed to the number of elements present in the local meshing surrounding the square hole (constant for all values of r_c), and also the fact that the FEA simulation uses a plate of finite width, whereas theory considers a plate of infinite width. This variance begins to emerge slightly before $r_c = 2$ mm, and becomes more pronounced as the corner radius approaches $r_c = 3$ mm.

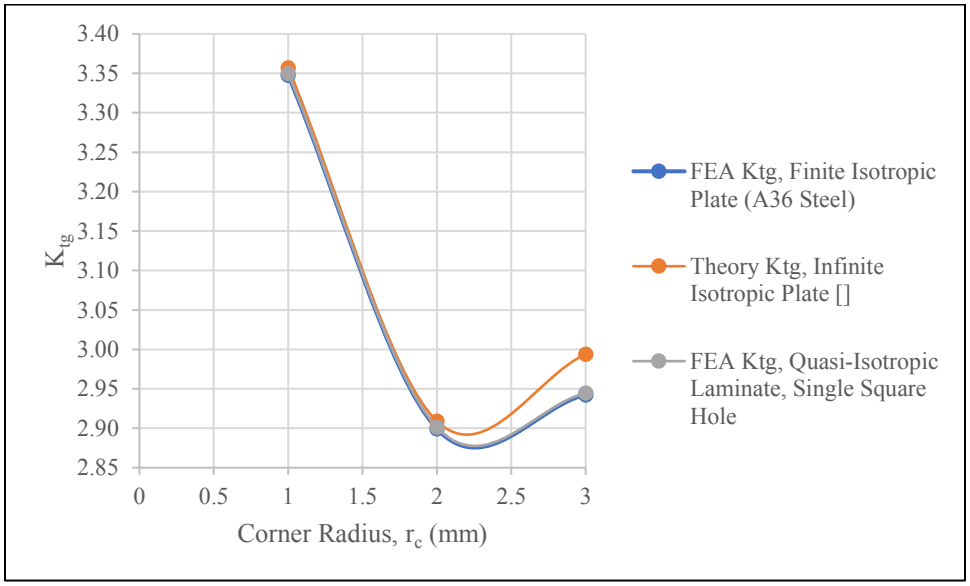

Figure 4.48: SCF based on the gross area for an isotropic plate and quasi-isotropic laminate containing a single centered square hole with rounded corners.

Table 4.20: A36 steel plate and laminate SCF comparisons for a single centered square hole with rounded corners.

Applied Remote Stress, σ (MPa)	**Corner Radius, r_c (mm)**	**FEA K_{tg}, Isotropic Plate (A36 Steel)**	**Theory K_{tg}, Isotropic Plate**	**%Error, Isotropic Plate K_{tg} versus Theory K_{tg}**	**Quasi-Isotropic Laminate K_{tg}**	**%Error, Quasi-Isotropic Laminate K_{tg} versus FEA Isotropic Plate K_{tg}**
0.689	1	3.347	3.357	-0.284	3.350	-0.067
	2	2.899	2.909	-0.334	2.901	-0.069
	3	2.942	2.994	-1.721	2.945	-0.071

For a single centered circular hole in a finite width isotropic plate, the Heywood formula (Eqn. 2.12) yields $K_{tg} = 3.094$. This value is within 0.341% error of the SCF for the finite width laminate containing a single centered circular hole from Table 4.19 (further above), $K_{tg} = 3.105$. Interestingly, if one uses the square hole equations to model a circular hole (let $a = b = r$ in Eqns. 2.14-2.20), one obtains $K_{tg} = 3.041$, which has a $\approx -1.713\%$ error when compared to results from the Heywood formula. The SCF for the quasi-isotropic laminate containing a single centered square hole with varying corner radius is shown below in Fig. 4.49.

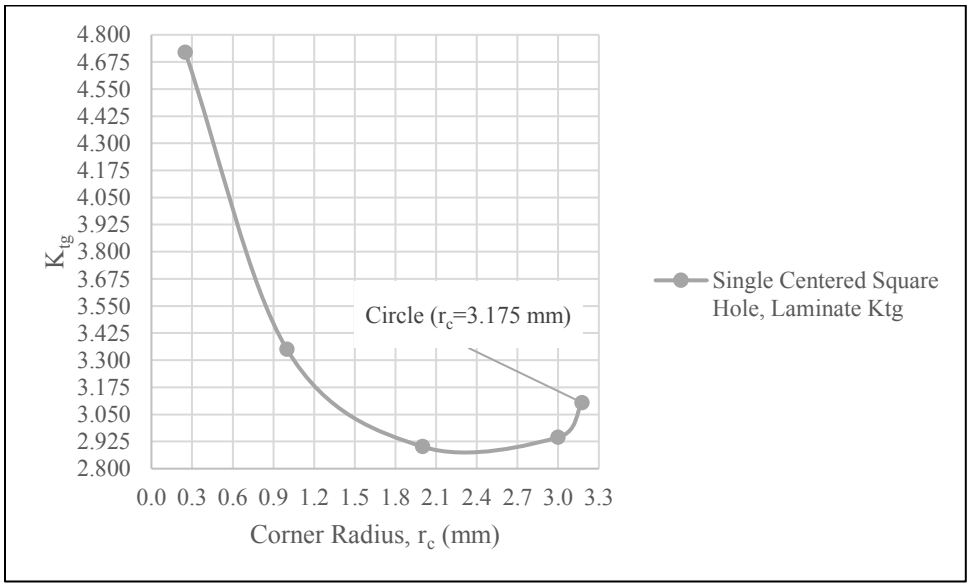

Figure 4.49: Laminate SCFs for the quasi-isotropic laminate containing a single centered square hole with rounded corners, with $d_e = 15.875$ mm.

It should be noted that a minimum exists at the inflection point in the curve found in Fig. 4.49. The SCF for the laminate decreases with increasing corner radius, until the minimum value is reached, at which point the SCF for the laminate increases for increasing corner radius, until the corresponding SCF for a circle is attained. This behavior is consistent with results for an isotropic plate, from Cannon [19], which can be seen below in Fig. 4.50. It is thought that had more corner radii data points been taken for the quasi-isotropic laminates in the study by Cannon [19], the same trend as seen in the isotropic curve would emerge.

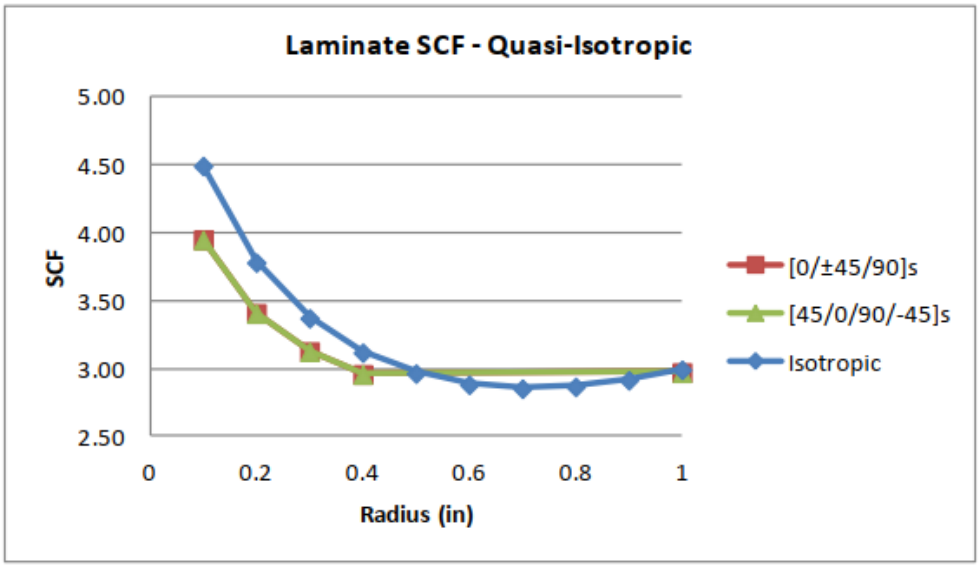

Figure 4.50. SCF for quasi-isotropic laminates and an isotropic plate [19].

The difference in curvature between Figs. 4.49 and 4.50 is thought to be due to the dimensions of the square hole (hole size effect), and corner radii. Because of the smaller square hole and corner radii used in this study, the curve must bend more severely (fishhook) to approach the SCF of a circle, versus the gradual slope change seen above in Fig. 4.50. Also, the laminate width to square hole height ratio used by Cannon [19] is 15, whereas the ratio used in this study is 6, meaning that Cannon [19] has modeled conditions which more closely represent an infinite width laminate. This could also be the cause for a smoother, more gradual change in the 0° lamina and laminate SCF curves, as well as the SCF equal to 3 at a radius value of unity.

4.4 Conclusions

The maximum σ_{11} stress tables for both the single offset square hole with rounded corners and the single offset circular hole reveal a steadily increasing trend in the σ_{11} stress in all laminas as the hole edge-to-laminate edge distance, d_e, decreases. This behavior is expected, as the contribution from the "edge effect" and secondary bending serve to increase the stress found at all points on the periphery of the square hole and circular hole.

The maximum σ_{11} stress in the laminate is always found in the 0° lamina, regardless of hole edge-to-laminate edge distance and corner radius, r_c, size. This is expected, as the 0° lamina

contains fibers which are parallel to the direction of the externally applied remote stress, σ, and thus are the predominate load bearing material in the laminate.

The location of the maximum σ_{11} stress always occurs in the vicinity of the rounded corner transition which is parallel to the central axis of the laminate, regardless of hole edge-to-laminate edge distance and corner radius size.

In terms of σ_{11} stress concentration, a square hole with sufficiently rounded corners ($r_c > 0.25$ mm) located at the laminate edge $d_e = 1.984$ mm elicits a lower SCF than a circular hole. Also, due to decreasing-increasing σ_{11} stress behavior found in the 0° lamina for a single square hole with rounded corners, an associated minimum SCF exists.

In terms of the laminate SCF, a single centered square hole with rounded corners elicits a lower gross SCF than a single centered circular hole, provided ≈ 1.5 mm $< r_c < 3.175$ mm. Further, a minimum laminate gross SCF for all d_e for a single square hole with rounded corners exists due to decreasing-increasing σ_x stress behavior.

In general, square holes with sufficiently rounded corners evoke lower SCFs than a circle of equal width. This is consistent with observations from Pilkey & Pilkey [6], in that an isotropic plate containing a square hole with rounded corners equal to about one-third of its width ($r_c = 2.117$ mm for this study) has a lower SCF than a circular hole of the same diameter.

CHAPTER 5: LAMINATE WITH TWO HOLES

Stress distributions, maximum stress locations, and stress concentrations due to the "edge effect" and the "hole-to-hole proximity effect" for two asymmetric square holes with rounded corners transverse to an externally applied in-plane uniaxial tensile stress are studied. Additionally, these phenomena are also explored for two symmetric square holes with rounded corners transverse to an externally applied in-plane uniaxial tensile stress. For both the asymmetric and symmetric two-hole configurations, two circular holes are also investigated. A comparison of the results between the different two-hole configurations is made, which is then followed by a conclusion.

5.1 Two Asymmetric Square Holes Transverse to Applied Load

Stress distributions, maximum stress locations, and stress concentrations due to two asymmetric square holes with rounded corners subjected to an in-plane uniaxial tensile stress in a finite width composite laminate are explored here. In order to investigate the "edge effect" and the "hole-to-hole proximity effect" simultaneously, three different cases are considered. To begin with, a square hole (Hole 2 in Fig. 5.1) is located at the center of the laminate width, while another square hole (Hole 1) is held at a constant distance from the edge. Both holes have the same dimensions, 6.35 mm x 6.35 mm. Each subsequent case moves Hole 2 closer toward Hole 1 by a factor of one-half.

5.1.1 Geometry and Loading

The geometry and loading configuration for the two asymmetric square holes with rounded corners are shown below in Fig. 5.1. The inside hole edge-to-edge distance, d_h, is varied, along with the corner radius, r_c, which ranges over four different values for each case; $r_c = 0.25, 1, 2,$ and 3 mm. The Hole 1 edge-to-laminate edge distance, d_e, and the square hole height for both holes, h, are each held constant. In addition, two asymmetric circular holes with a diameter of 3.175 mm are also considered, where the d_e and d_h values are the same as those

used for two asymmetric square holes. For all values of d_h, the centers of the holes are located at the mid-length of the laminate, at $x = L/2$. Lastly, A through H are the points of interest at the hole corners where stress field measurements are taken.

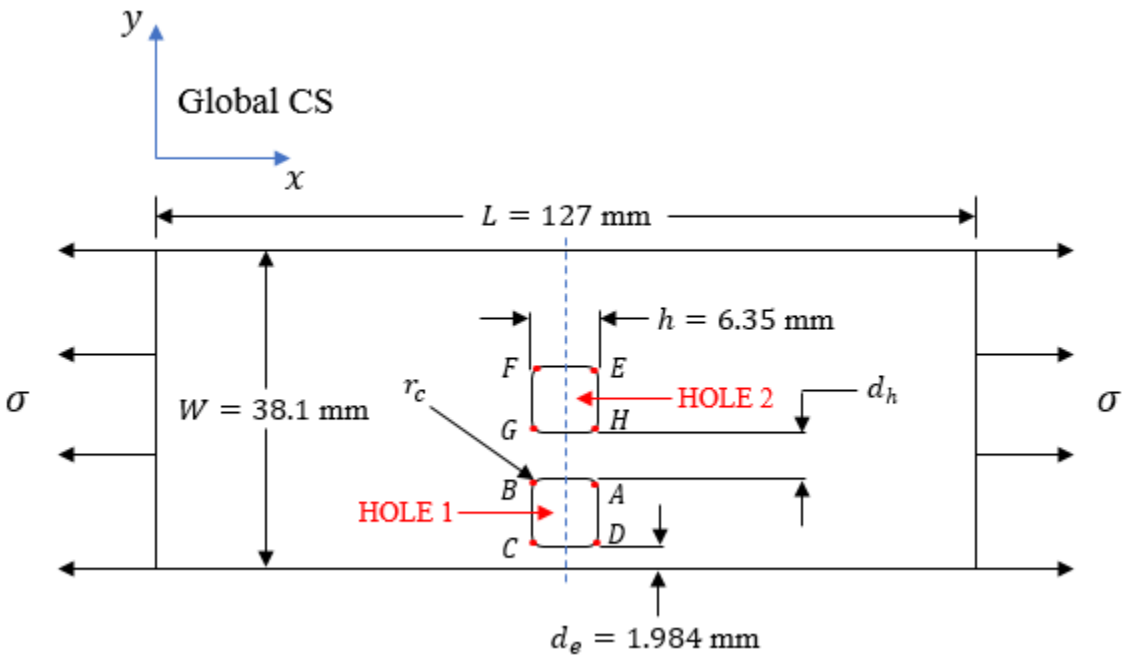

Figure 5.1: Geometry and loading condition for two asymmetric square holes with rounded corners.

The various cases for the spacing of the two asymmetric square holes with rounded corners are given below in Table 5.1.

Table 5.1: Cases for the two asymmetric square holes with rounded corners.

Case	Hole 1 Edge-to-Laminate Edge Distance, d_e (mm)	Hole Edge-to-Edge Distance, d_h (mm)	Square Hole Height, h (mm)
1	1.984	7.541 (Hole 2 Centered)	6.35
2		3.770	
3		1.885	

5.1.2 Meshing

The mesh is obtained using the same approach as in Chapter 3. The keypoints are established and used to generate areas, which are then meshed and refined locally in each square area surrounding the two square holes. The number of elements in the square area surrounding

each hole is kept constant at 5760. This number was increased from the 3840 used in the single hole cases in order to avoid aspect ratio warnings from ANSYS. The meshing for two square holes with a corner radius of $r_c = 2$ mm can be seen below in Fig. 5.2. It is worth mentioning that the horizontal solid white lines seen in Fig. 5.2a and 5.2c are areas of high element count. This was done to ensure stress field accuracy for the "hole-to-hole proximity effect" and the "edge effect" seen in Fig. 5.2a and 5.2c, respectively. The extension of the solid white lines beyond the immediate area of stress field interest (the two square areas surrounding the square holes with rounded corners) is an unintended consequence of the discretization method used by ANSYS.

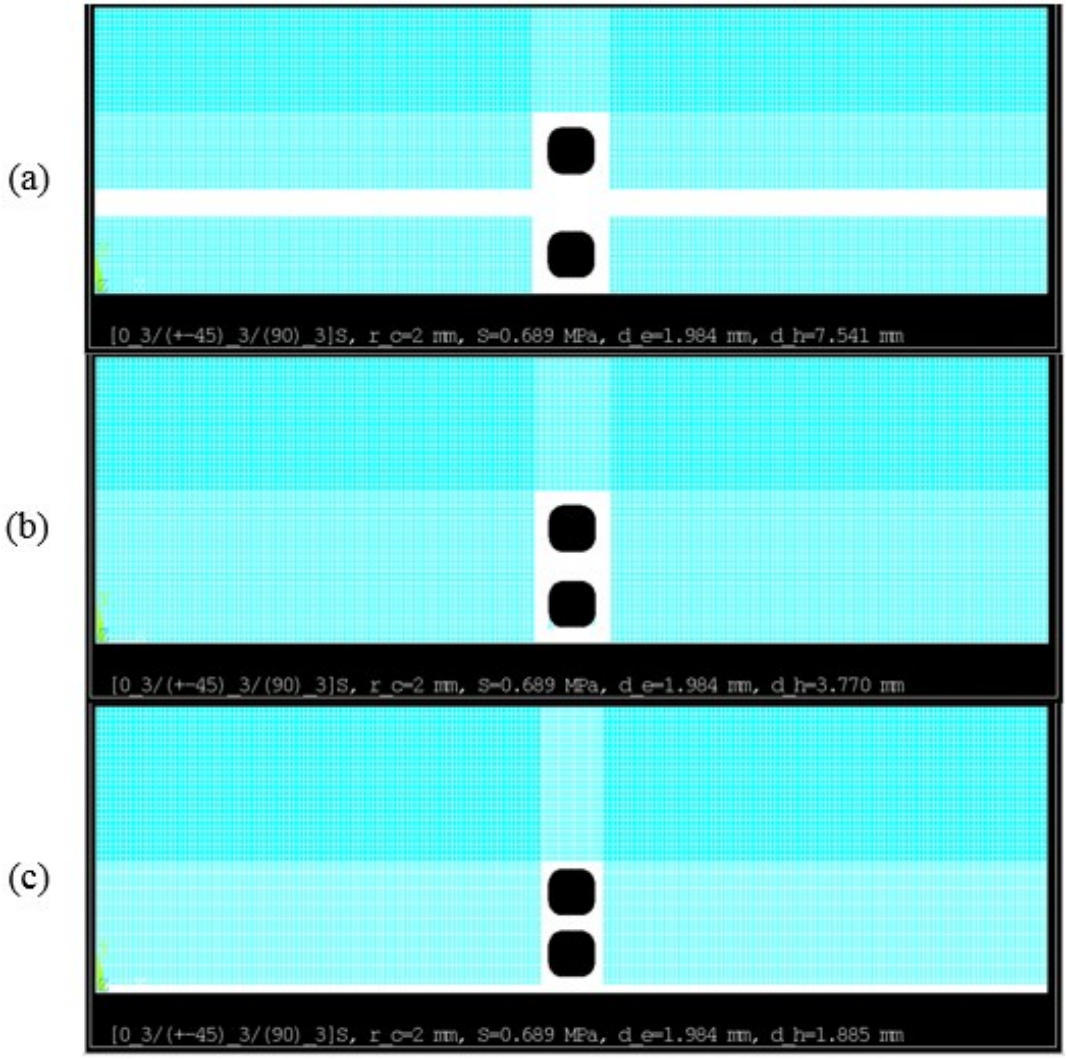

Figure 5.2: Mapped meshing for two asymmetric square holes with $r_c = 2$ mm and $d_e = 1.984$ mm: (a) $d_h = 7.541$ mm (Hole 2 centered), (b) $d_h = 3.770$ mm, (c) $d_h = 1.885$ mm.

5.1.3 Stress Distribution

The σ_{11} stress field contour plots for the two asymmetric square holes with rounded corners can be seen below in Figs. 5.3-5.6. It can be seen in all laminas that as Hole 2 approaches Hole 1, the stress field between the two holes increases in magnitude, as does the maximum σ_{11} stress in the lamina. Such behavior is due to the "hole-to-hole proximity effect".

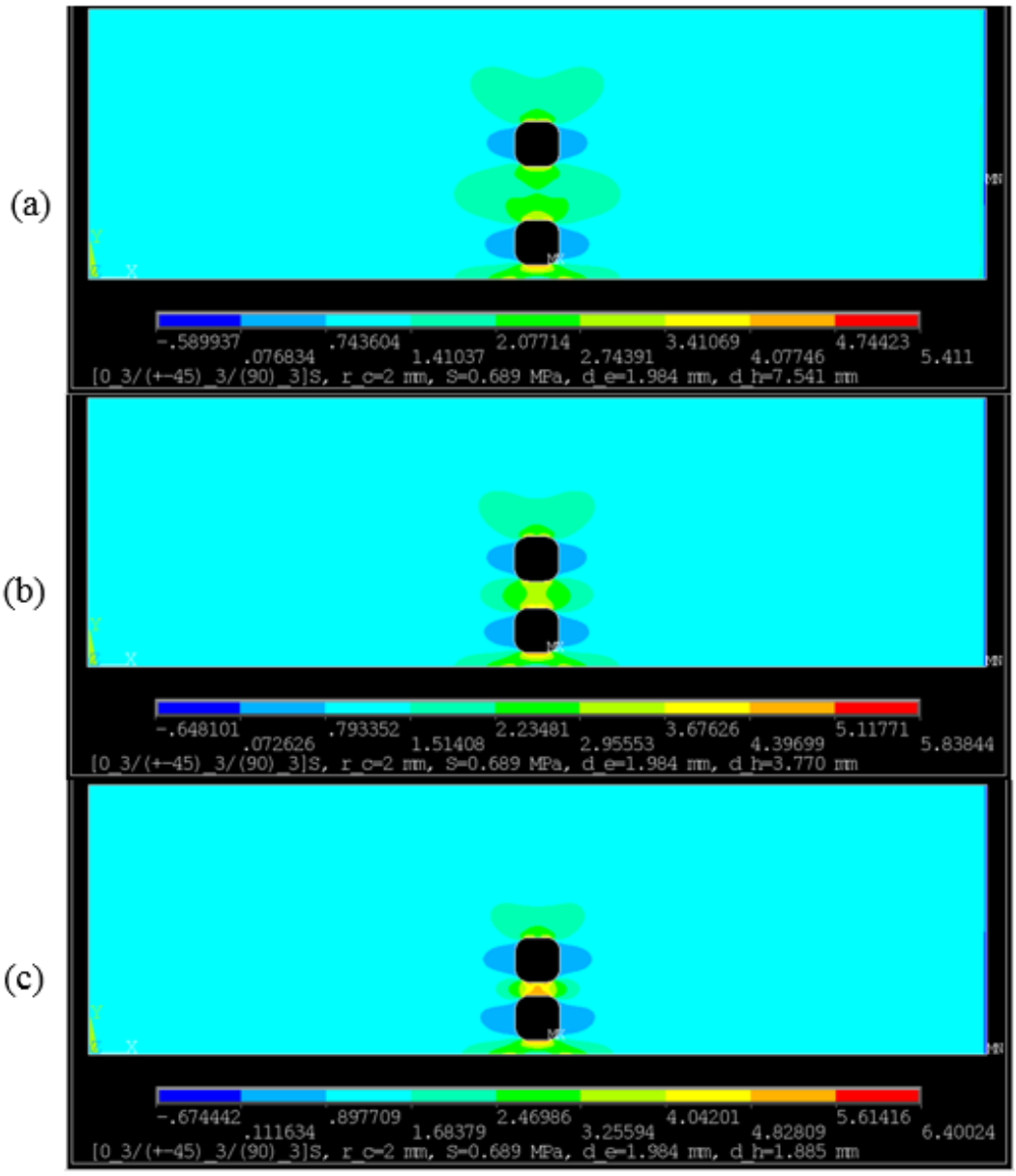

Figure 5.3: σ_{11} stress field contours in the 0° lamina for two asymmetric square holes with $r_c = 2$ mm and $d_e = 1.984$ mm: (a) $d_h = 7.541$ mm (Hole 2 centered), (b) $d_h = 3.770$ mm, (c) $d_h = 1.885$ mm.

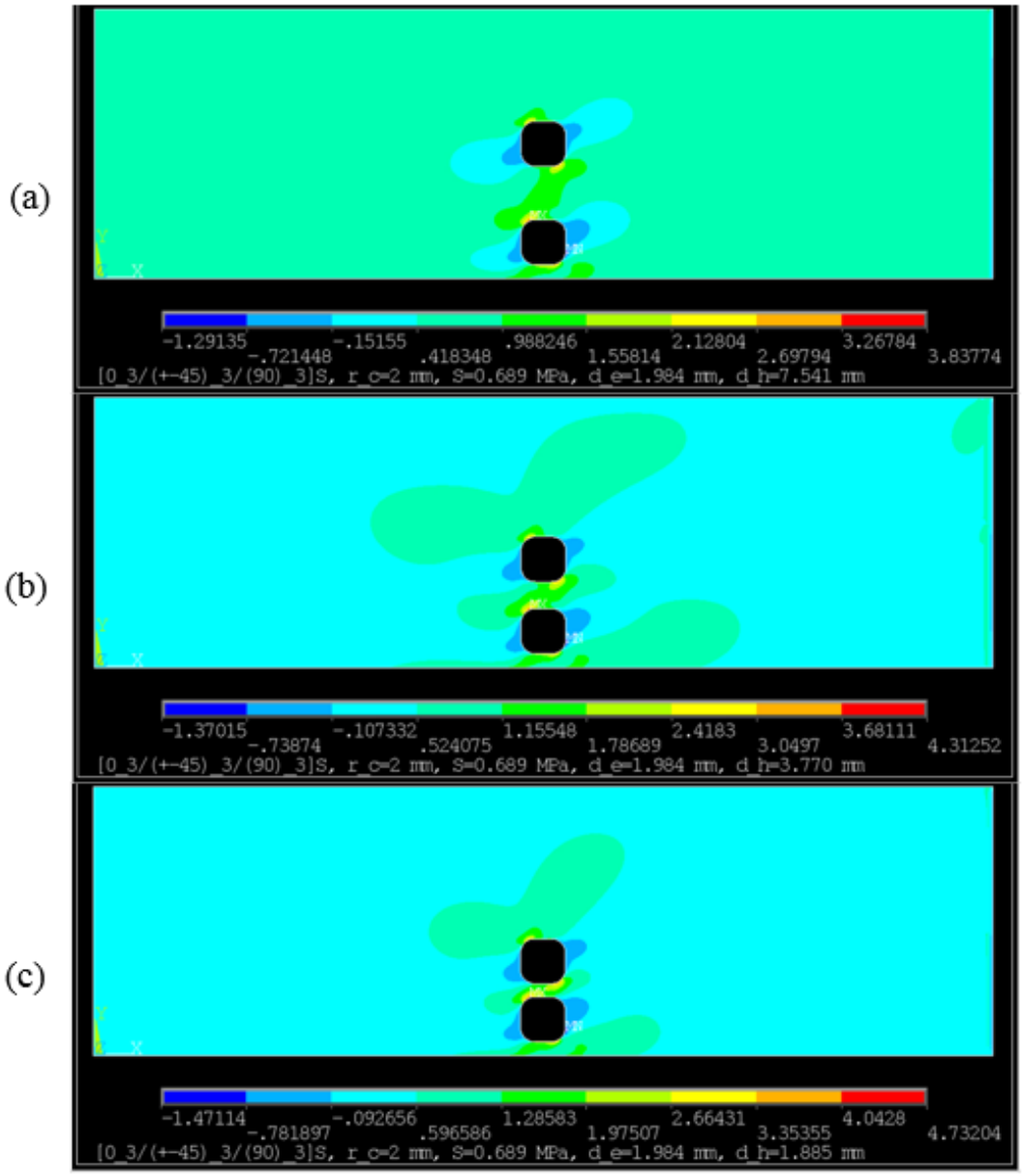

Figure 5.4: σ_{11} stress field contours in the 45° lamina for two asymmetric square holes with $r_c = 2$ mm and $d_e = 1.984$ mm: (a) $d_h = 7.541$ mm (Hole 2 centered), (b) $d_h = 3.770$ mm, (c) $d_h = 1.885$ mm.

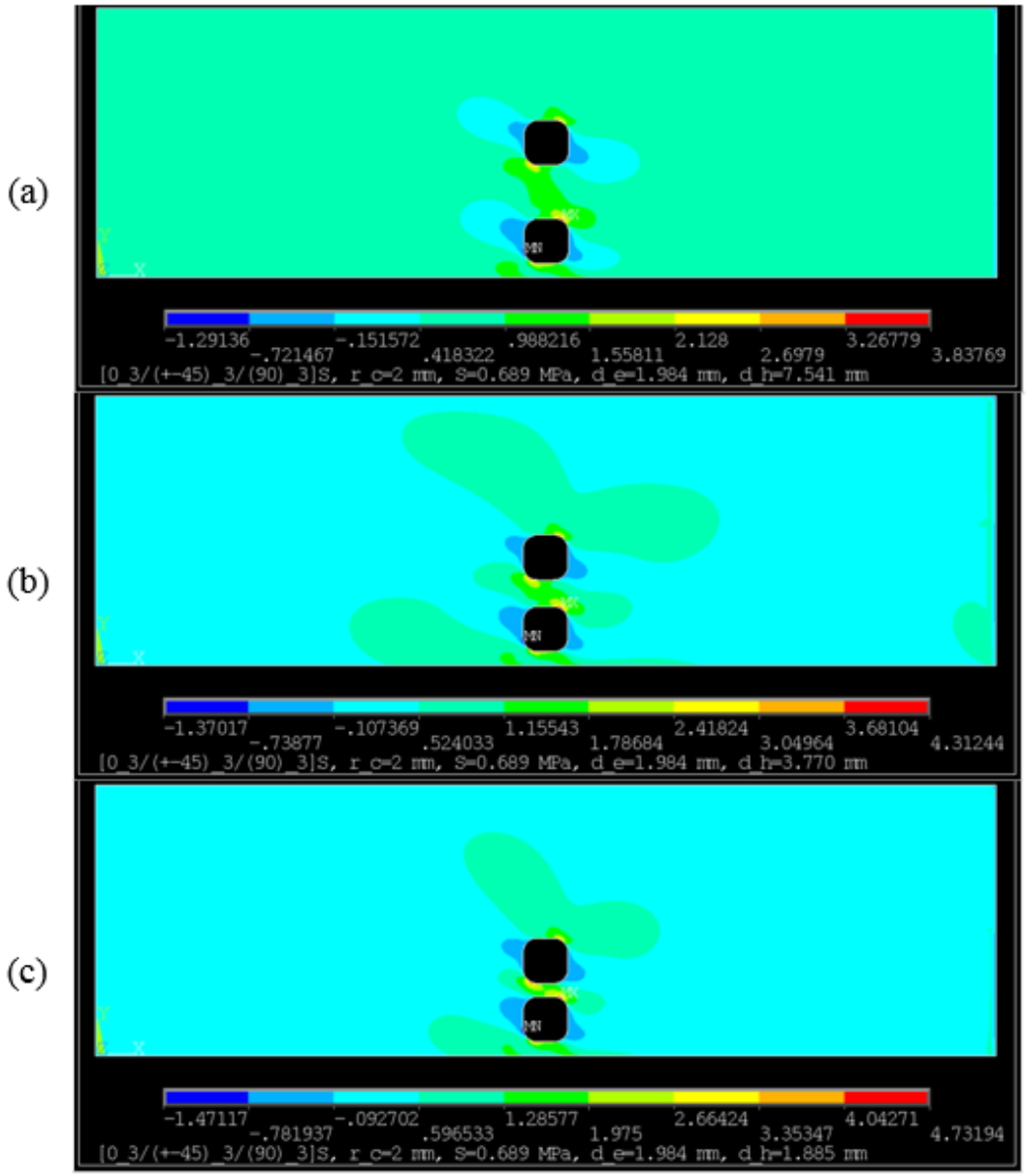

Figure 5.5: σ_{11} stress field contours in the -45° lamina for two asymmetric square holes with $r_c = 2$ mm and $d_e = 1.984$ mm: (a) $d_h = 7.541$ mm (Hole 2 centered), (b) $d_h = 3.770$ mm, (c) $d_h = 1.885$ mm.

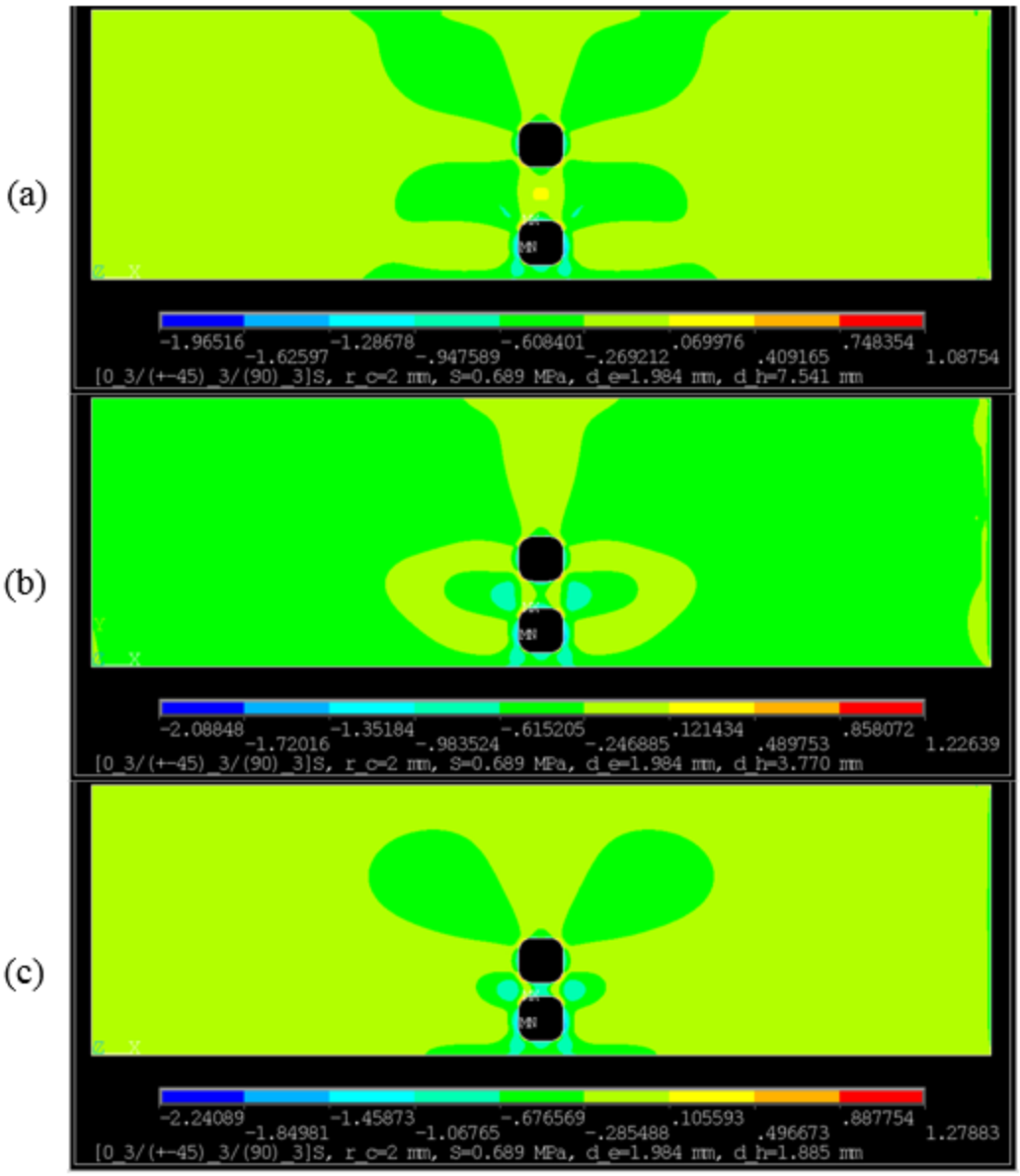

Figure 5.6: σ_{11} stress field contours in the 90° lamina for two asymmetric square holes with $r_c = 2$ mm and $d_e = 1.984$ mm: (a) $d_h = 7.541$ mm (Hole 2 centered), (b) $d_h = 3.770$ mm, (c) $d_h = 1.885$ mm.

5.1.4 Location of Maximum Stresses

It is interesting to note the progression of the "hole-to-hole proximity effect" present in the 0° lamina. As Hole 2 approaches Hole 1, the σ_{11} stress fields between the two holes coalesce and intensify. Also, the location of the maximum σ_{11} stress is always found in the neighborhood of points C and D (a consequence of symmetry, see Fig. 5.11a) on Hole 1 at the edge of the laminate, regardless of hole edge-to-edge distance. This would suggest that the "edge effect" has

a greater influence than the "hole-to-hole proximity effect", even in light of $d_h < d_e$ for Case 3. Further, because the location of the maximum σ_{11} stress does not change, but increases with decreasing d_h, it would seem that the "hole-to-hole proximity effect" exacerbates the "edge effect". This is depicted below in Fig. 5.7, and Table 5.2. Using $d_h = 7.541$ mm as a baseline for comparison, it can be seen that for a 50% reduction in d_h, there exists a 7.89% increase in maximum σ_{11} stress, and for a 75% reduction in d_h, there exists a 18.28% increase in maximum σ_{11} stress. As before, ANSYS displays only one maximum stress location, however, due to symmetry conditions explained in Section 5.1.5, there can exist more than one location of maximum σ_{11} stress on the hole periphery.

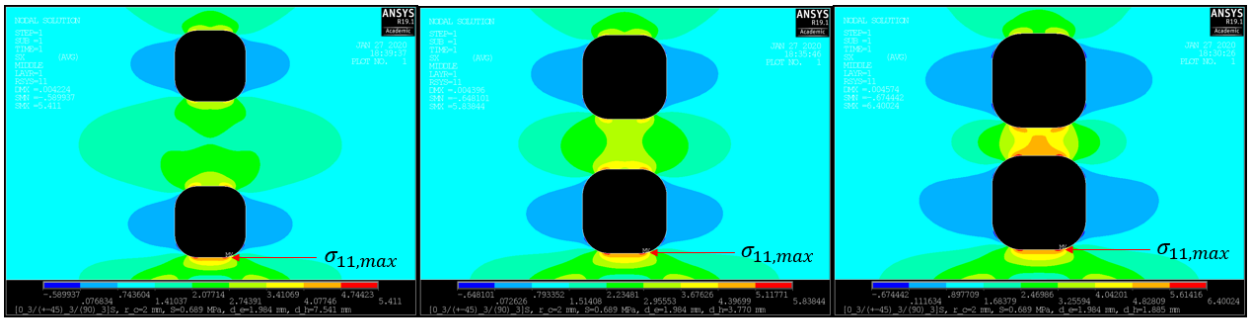

(a) (b) (c)

Figure 5.7: Effect of hole-to-hole proximity on σ_{11} stress fields for two asymmetric square holes with $r_c = 2$ mm and $d_e = 1.984$ mm: (a) $d_h = 7.541$ mm (Hole 2 centered), (b) $d_h = 3.770$ mm, (c) $d_h = 1.885$ mm.

Table 5.2: Effect of hole-to hole-proximity on hole edge-to-laminate edge maximum σ_{11} stress for two asymmetric square holes with $r_c = 2$ mm.

Hole Edge-to-Edge Distance, d_h (mm)	**Hole 1 Edge-to-Laminate Edge Distance, d_e (mm)**	**$\sigma_{11,max}$ (MPa)**
7.541 (Hole 2 Centered)	1.984	5.411
3.770		5.838
1.885		6.400

The maximum σ_{11} stress for each lamina is given below in Table 5.3. For comparison, two circular holes, each with a 6.35 mm diameter, were also modeled. It can be seen that for both types of holes, the maximum σ_{11} stress always occurs in the 0° lamina. As in the case of single holes, this is because the fibers in the 0° lamina are parallel to the loading direction, and therefore carry the majority of the load applied to the laminate. For each lamina and all values of r_c, the maximum σ_{11} stress increases with decreasing hole edge-to-edge distance, d_h. This is

anticipated and is a result of the "hole-to-hole proximity effect". Consistent with results seen in Chapter 4, there is a decreasing-increasing behavior in the σ_{11} stress for increasing corner radius, suggesting a minimum r_c. Finally, the σ_{11} stresses in the +45° and -45° laminas are equivalent up to three decimal places for most cases.

Table 5.3: Maximum σ_{11} stress in each lamina for two asymmetric square holes with rounded corners and two asymmetric circular holes.

Corner Radius, r_c (mm)	**Hole 1 Edge-to-Laminate Edge Distance, d_e (mm)**	**Hole Edge-to-Edge Distance, d_h (mm)**	**Two Asymmetric Square Holes: $\sigma_{11,max}$ (MPa)**			
			0° Lamina	**45° Lamina**	**-45° Lamina**	**90° Lamina**
0.25	1.984	7.541 (Hole 2 Centered)	8.439	8.227	8.226	3.599
		3.770	9.360	9.054	9.053	3.908
		1.885	10.201	9.665	9.665	4.094
1	1.984	7.541 (Hole 2 Centered)	5.612	4.924	4.924	1.653
		3.770	6.314	5.474	5.474	1.823
		1.885	7.081	5.901	5.901	1.905
2	1.984	7.541 (Hole 2 Centered)	5.411	3.838	3.838	1.088
		3.770	5.838	4.313	4.312	1.226
		1.885	6.400	4.732	4.732	1.279
3	1.984	7.541 (Hole 2 Centered)	5.916	3.485	3.485	0.825
		3.770	6.314	3.738	3.738	0.951
		1.885	6.823	4.258	4.258	1.017
			Two Asymmetric Circular Holes: $\sigma_{11,max}$ (MPa)			
3.175 (Circle)	1.984	7.541 (Hole 2 Centered)	6.257	3.545	3.545	0.791
		3.770	6.663	3.772	3.772	0.914
		1.885	7.171	4.200	4.200	0.983

5.1.5 Stress Concentration Factors

It is important to note that due to the asymmetrically offset square holes, secondary bending is present, and therefore a contribution from this is found in the maximum σ_{11} stress and resulting SCF. This behavior can be seen below in Fig. 5.8.

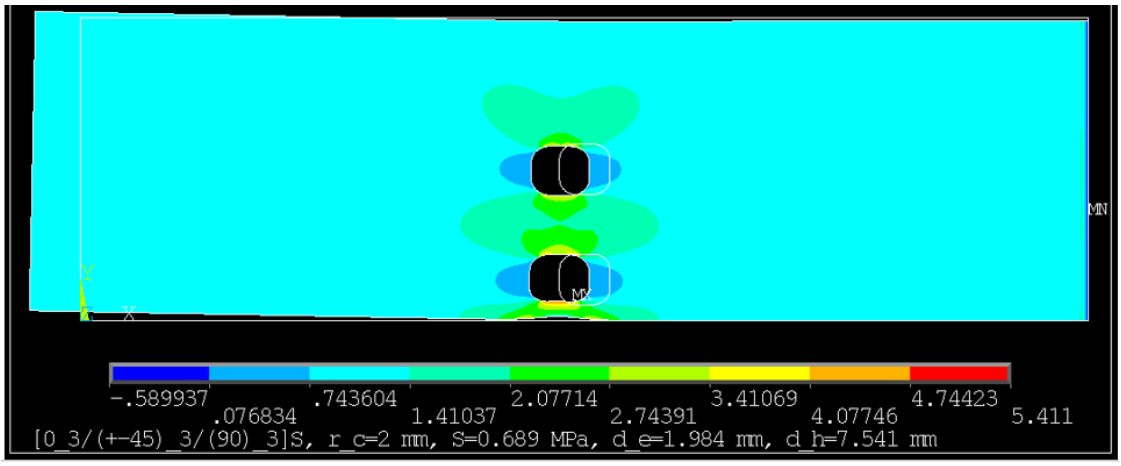

Figure 5.8: Two asymmetric square holes with $d_e = 1.984$ mm, $d_h = 7.541$ mm (Hole 2 centered), and $r_c = 2$ mm, with secondary bending and x-direction extension present.

The normalized σ_{11} stress in the 0° lamina due to the "hole-to-hole proximity effect" and the "edge effect" between the two asymmetric square holes for the various cases can be represented graphically, and is shown below in Figs. 5.9 and 5.10. For a given d_h, it can be seen that the maximum normalized σ_{11} stress always occurs at the side of the hole closest to the edge of the laminate (Hole 1), and that the normalized stress decreases with increasing distance from the bottom laminate edge ($y = 0$). Moreover, the maximum (and overall) normalized σ_{11} stress decreases with increasing d_h.

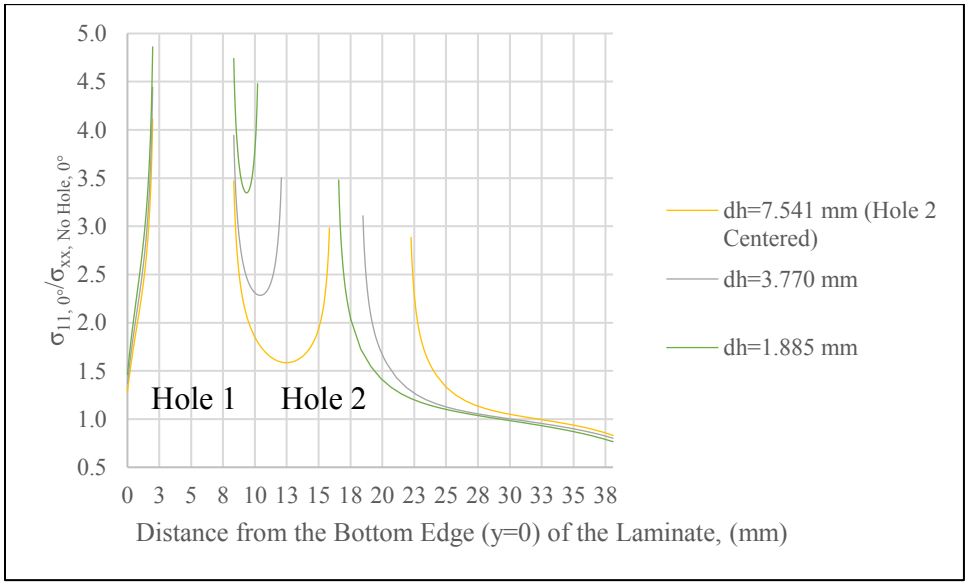

Figure 5.9: Normalized 0° lamina σ_{11} stress for two asymmetric square holes with $d_e = 1.984$ mm and $r_c = 2$ mm.

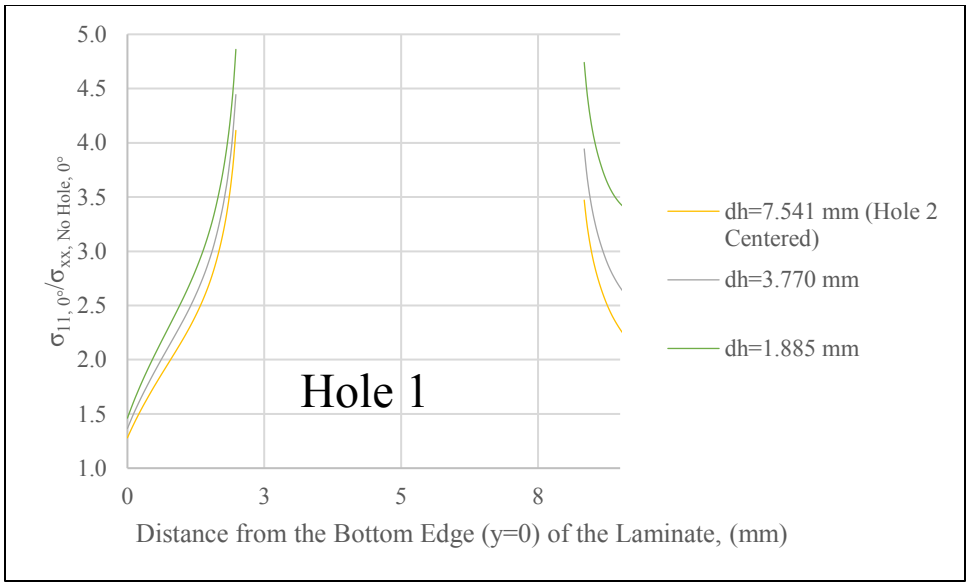

Figure 5.10: Enlarged view of the normalized 0° lamina σ_{11} stress for two asymmetric square holes with $d_e = 1.984$ mm and $r_c = 2$ mm.

The conditions for symmetry in the σ_{11} stress field behavior for the two asymmetric square holes with rounded corners are slightly different than the conditions found for a single square hole with rounded corners. Here, only the 0° and 90° laminas exhibit such behavior. The symmetry equivalencies and the σ_{11} stress values at each of the four corners for the two asymmetric square holes can be seen below in Fig. 5.11, and Table 5.4, respectively. The solid line below Hole 1 in Fig. 5.11 represents the laminate edge ($y = 0$).

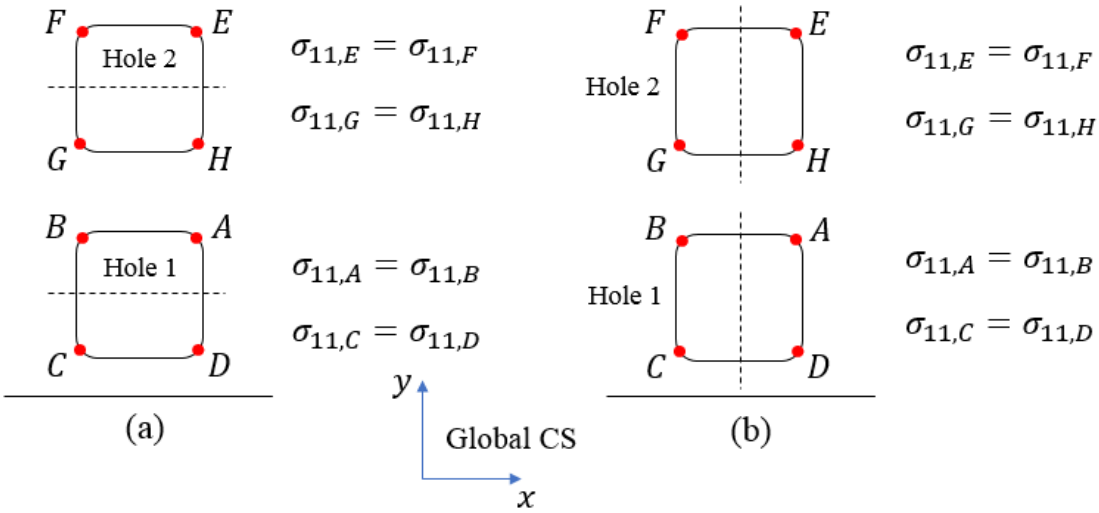

Figure 5.11: σ_{11} stress symmetry conditions based on fiber orientation directions for two asymmetric square holes with rounded corners: (a) 0° lamina, (b) 90° lamina.

Table 5.4: σ_{11} stress at points A through H for two asymmetric square holes with rounded corners, for $d_e = 1.984$ mm and $r_c = 2$ mm.

Two Asymmetric Square Holes									
Hole Edge-to-Edge Distance, d_h (mm)	**Fiber Orientation Angle, θ (°)**	**σ_{11} (MPa)**							
		Hole 1				**Hole 2**			
		A	***B***	***C***	***D***	***E***	***F***	***G***	***H***
7.541 (Hole 2 Centered)	0	4.601	4.601	5.411	5.411	3.914	3.914	4.041	4.041
3.770		5.223	5.223	5.838	5.838	4.209	4.209	4.749	4.749
1.885		6.277	6.277	6.400	6.400	4.579	4.579	5.919	5.919
7.541 (Hole 2 Centered)	45	-0.334	3.838	-0.263	3.024	-0.267	3.073	-0.295	3.392
3.770		-0.375	4.313	-0.269	3.253	-0.292	3.356	-0.346	3.978
1.885		-0.415	4.732	-0.317	3.588	-0.324	3.703	-0.397	4.526
7.541 (Hole 2 Centered)	-45	3.838	-0.334	3.024	-0.263	3.073	-0.267	3.392	-0.295
3.770		4.312	-0.375	3.252	-0.269	3.356	-0.292	3.978	-0.346
1.885		4.732	-0.415	3.588	-0.317	3.703	-0.324	4.526	-0.397
7.541 (Hole 2 Centered)	90	1.088	1.088	0.127	0.127	0.751	0.751	0.963	0.963
3.770		1.226	1.226	0.122	0.122	0.871	0.871	1.151	1.151
1.885		1.279	1.279	0.171	0.171	1.015	1.015	1.244	1.244

The behavior of the symmetry found at the various points of the two asymmetric square holes with rounded corners using the normalized σ_{11} stress values can be easily understood in graphical form, which is shown below in Figs. 5.12-5.15.

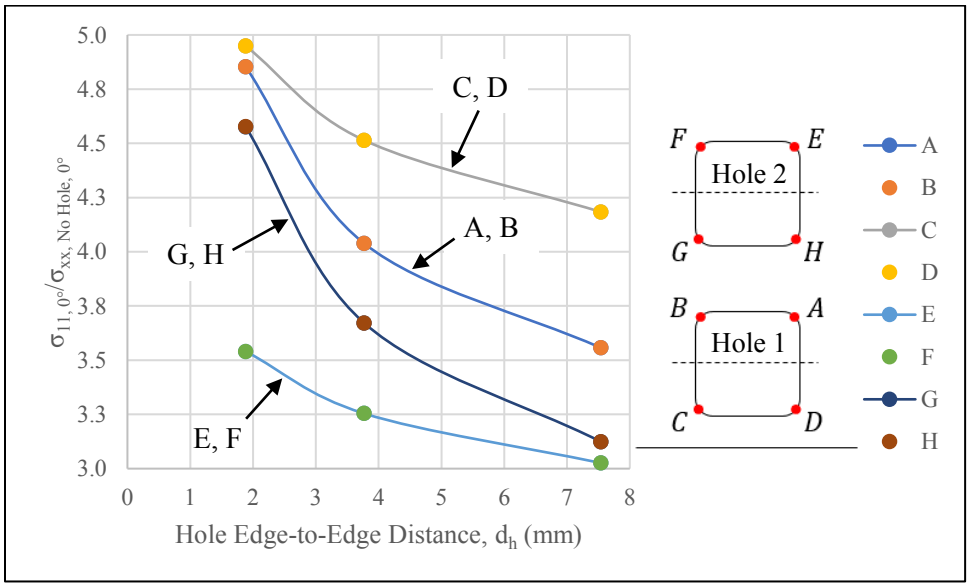

Figure 5.12: Normalized 0° lamina σ_{11} stress at points A through H for two asymmetric square holes with rounded corners with $d_e = 1.984$ mm and $r_c = 2$ mm.

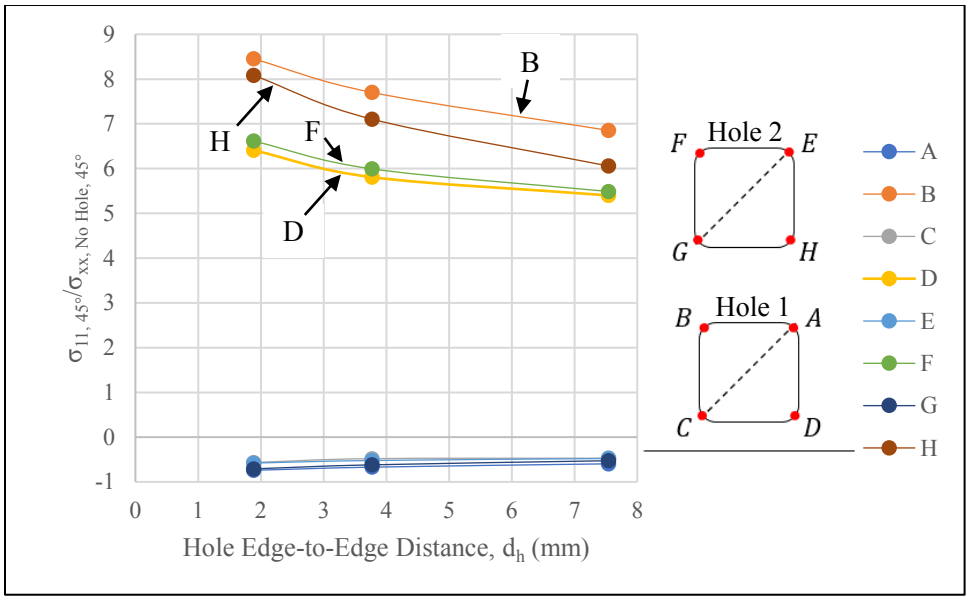

Figure 5.13: Normalized 45° lamina σ_{11} stress at points A through H for two asymmetric square holes with rounded corners with $d_e = 1.984$ mm and $r_c = 2$ mm.

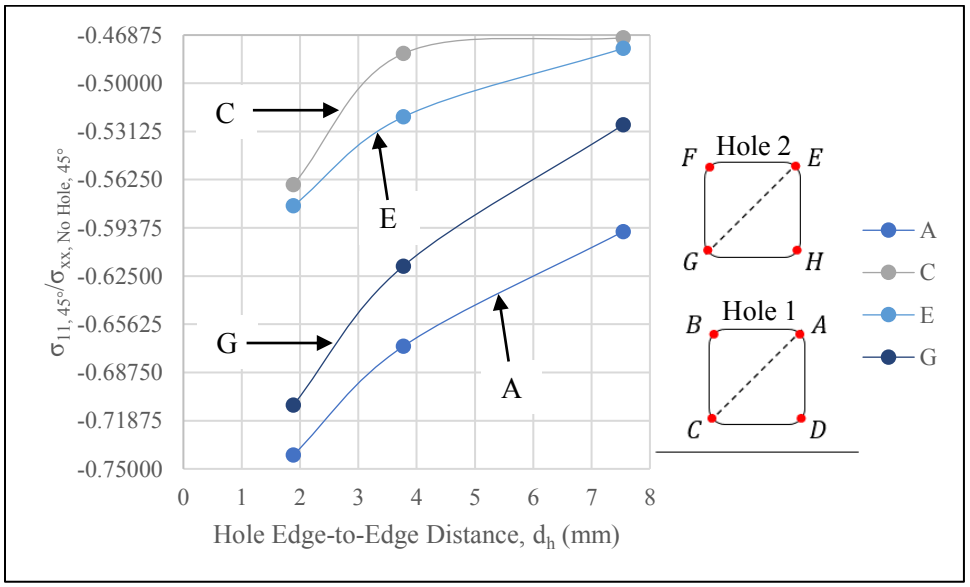

Figure 5.14: Enlarged view of the normalized 45° lamina σ_{11} stress at points A, C, E, and G, for two asymmetric square holes with rounded corners with $d_e = 1.984$ mm and $r_c = 2$ mm.

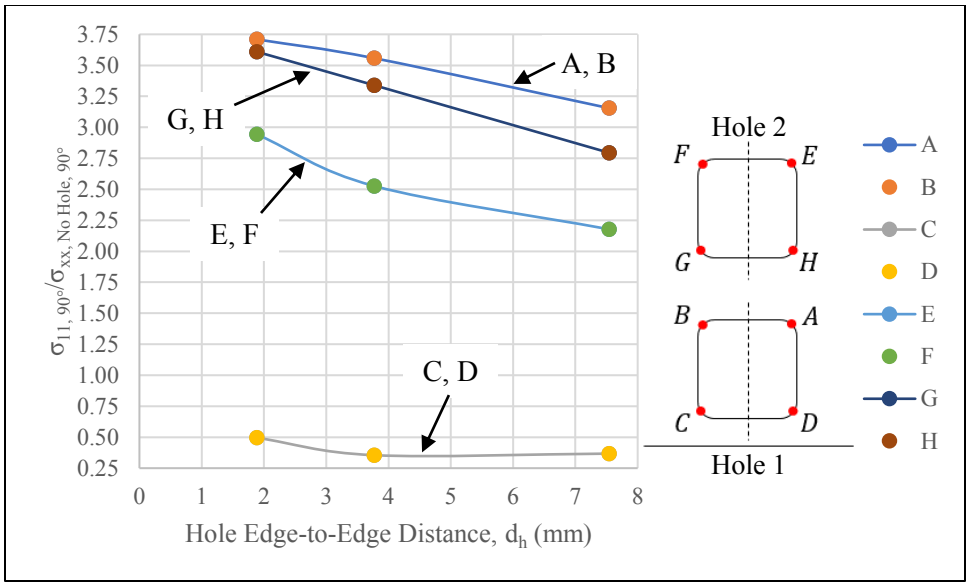

Figure 5.15: Normalized 90° lamina σ_{11} stress at points A through H for two asymmetric square holes with rounded corners with $d_e = 1.984$ mm and $r_c = 2$ mm.

As in Section 4.3, the SCFs for the laminas found in the two asymmetric square holes with rounded corners configuration are obtained using Eqn. 4.6 and the values in Table 5.3, and given below in Table 5.5.

Table 5.5: Lamina SCFs for two asymmetric square holes with rounded corners and two asymmetric circular holes.

Corner Radius, r_c (mm)	**Hole 1 Edge-to-Laminate Edge Distance, d_e (mm)**	**Hole Edge-to-Edge Distance, d_h (mm)**	**Two Asymmetric Square Holes: $K_{t,\theta}$**			
			$\theta = 0°$	**$\theta = 45°$**	**$\theta = -45°$**	**$\theta = 90°$**
0.25	1.984	7.541 (Hole 2 Centered)	6.525	14.693	14.692	10.438
		3.770	7.237	16.169	16.169	11.335
		1.885	7.887	17.262	17.261	11.875
1	1.984	7.541 (Hole 2 Centered)	4.339	8.794	8.794	4.794
		3.770	4.882	9.777	9.777	5.289
		1.885	5.475	10.539	10.539	5.526
2	1.984	7.541 (Hole 2 Centered)	4.184	6.854	6.854	3.155
		3.770	4.514	7.702	7.702	3.557
		1.885	4.949	8.451	8.451	3.709
3	1.984	7.541 (Hole 2 Centered)	4.574	6.225	6.224	2.394
		3.770	4.882	6.675	6.675	2.758
		1.885	5.275	7.605	7.605	2.950
			Two Asymmetric Circular Holes: $K_{t,\theta}$			
3.175 (Circle)	1.984	7.541 (Hole 2 Centered)	4.838	6.331	6.331	2.294
		3.770	5.152	6.737	6.737	2.652
		1.885	5.545	7.501	7.501	2.853

The normalized maximum σ_{11} stress in each lamina as a function of hole edge-to-edge distance has been plotted below in Figs. 5.16-5.18. These graphs are equivalent to the lamina SCF, $K_{t,\theta}$.

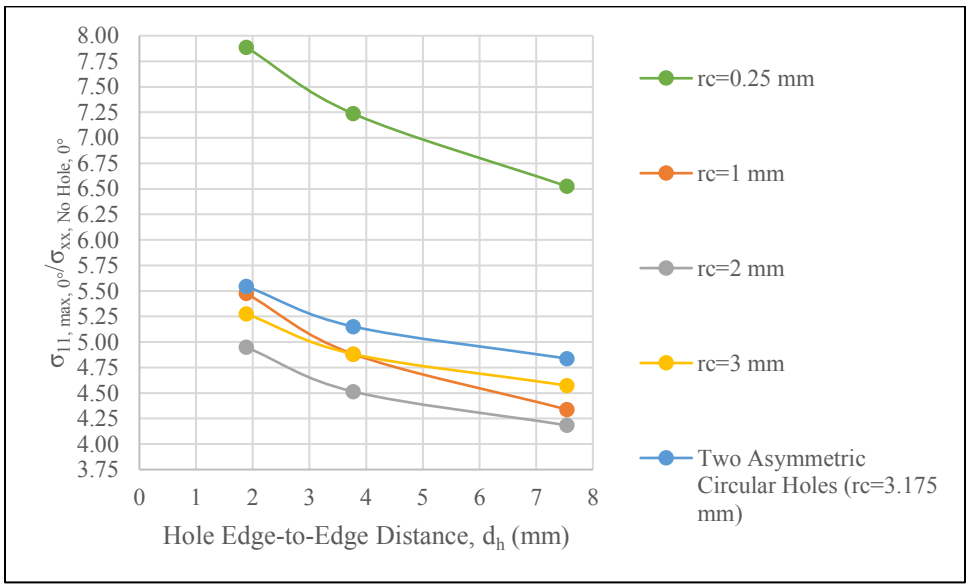

Figure 5.16: Normalized maximum 0° lamina σ_{11} stress for two asymmetric square holes with rounded corners and two asymmetric circular holes.

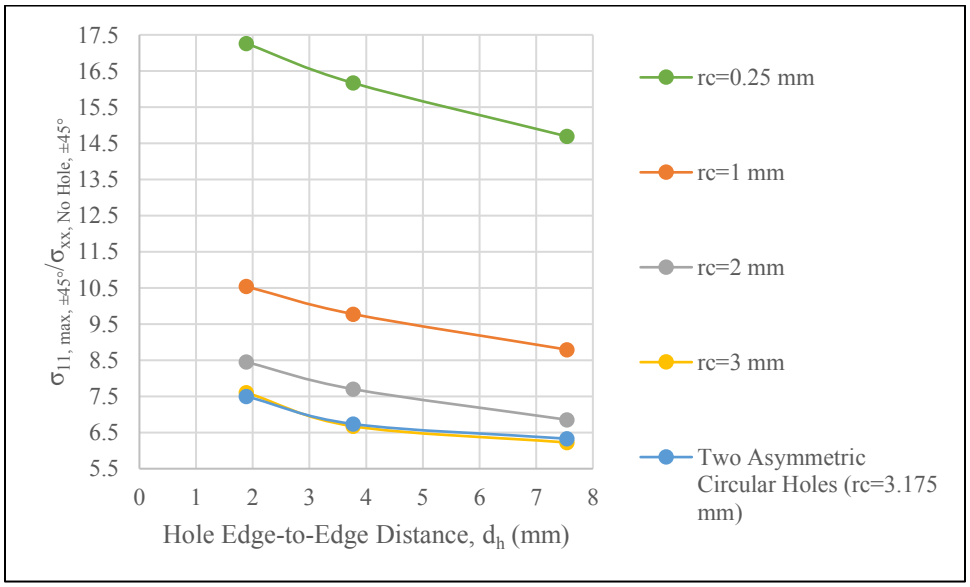

Figure 5.17: Normalized maximum ±45° lamina σ_{11} stress for two asymmetric square holes with rounded corners and two asymmetric circular holes.

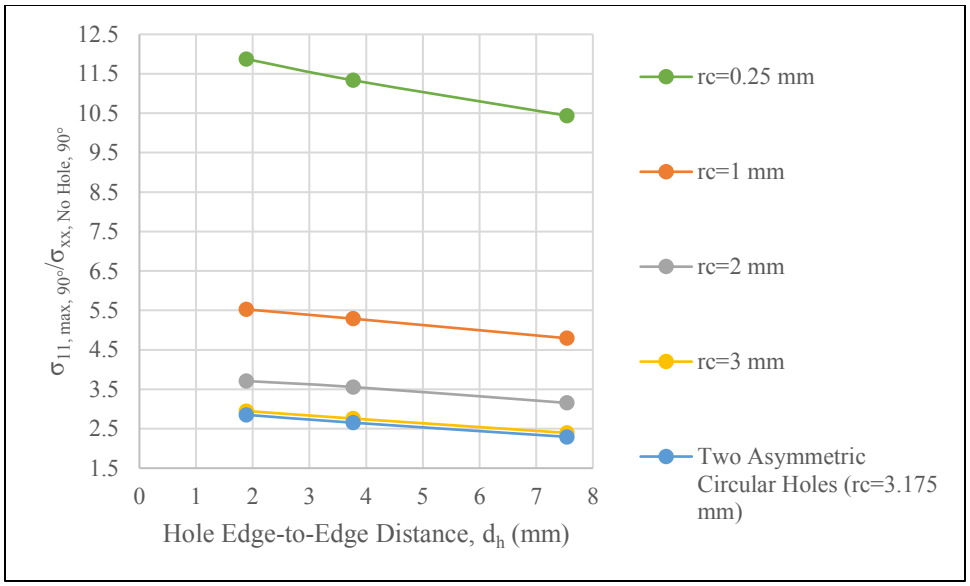

Figure 5.18: Normalized maximum 90° lamina σ_{11} stress for two asymmetric square holes with rounded corners and two asymmetric circular holes.

As before, the maximum σ_x stress in the laminate can be obtained by using the values from Table 4.17 as the elastic constants for the laminate, in order to model it as an isotropic material. The maximum laminate σ_x stress for all cases of both the two asymmetric square holes with rounded corners and the two asymmetric circular holes are given below in Table 5.6. The laminate SCFs are calculated as in Section 4.3.3, via Eqn. 4.10, and are also given below in Table 5.6. This approach is taken, as there exist no closed form solutions for the laminate level SCFs for multiple square holes with rounded corners, or for multiple circular holes.

Table 5.6: Maximum laminate σ_x stress using laminate elastic constants, and SCFs based on the gross area of the laminate.

Corner Radius, r_c (mm)	Hole Edge-to-Edge Distance, d_h (mm)	Two Asymmetric Square Holes: $\sigma_{x,max}$ (MPa)	Two Asymmetric Square Holes: K_{tg}
0.25	7.541 (Hole 2 Centered)	4.576	6.636
	3.770	5.074	7.359
	1.885	5.523	8.011
1	7.541 (Hole 2 Centered)	3.007	4.361
	3.770	3.383	4.907
	1.885	3.793	5.501
2	7.541 (Hole 2 Centered)	2.890	4.192
	3.770	3.119	4.524
	1.885	3.418	4.958
3	7.541 (Hole 2 Centered)	3.157	4.579
	3.770	3.369	4.887
	1.885	3.640	5.280
		Two Asymmetric Circular Holes: $\sigma_{x,max}$ (MPa)	**Two Asymmetric Circular Holes: K_{tg}**
3.175 (Circle)	7.541 (Hole 2 Centered)	3.338	4.841
	3.770	3.555	5.155
	1.885	3.826	5.549

The SCFs for the laminate are also shown graphically, which can be seen below in Fig. 5.19.

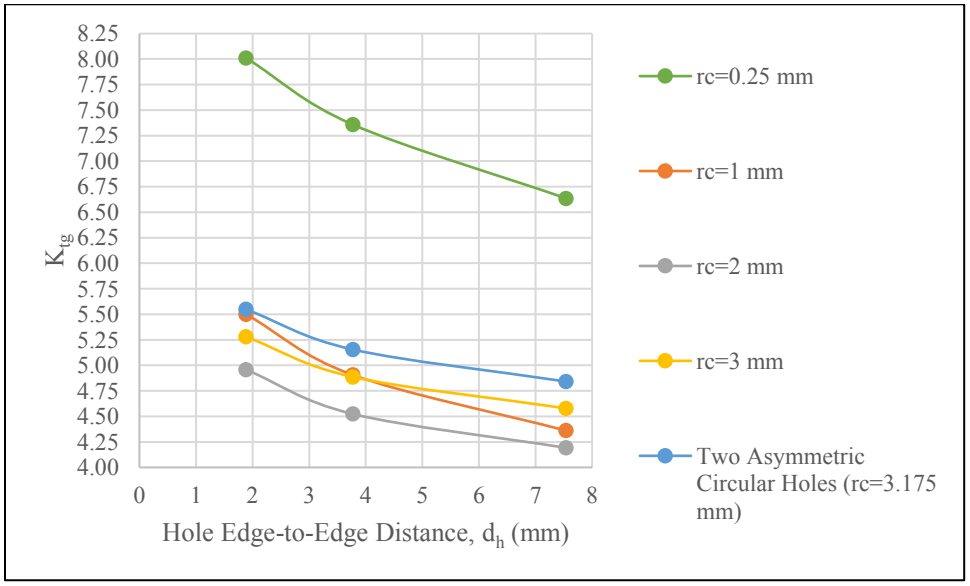

Figure 5.19: Laminate SCFs for two asymmetric square holes with rounded corners and two asymmetric circular holes.

5.2 Two Axisymmetric Square Holes Transverse to Applied Load

Stress distributions, maximum stress locations, and stress concentrations due to two axisymmetric square holes with rounded corners subjected to a transversely applied in-plane uniaxial tensile stress in a finite width laminate are investigated here. The locations of Hole 1 and Hole 2 are varied equally about the central axis of the laminate, at four different hole-to-hole distances, in order to investigate the "hole-to-hole proximity effect".

5.2.1 Geometry and Loading

The geometry and loading configuration for the two axisymmetric square holes with rounded corners are shown below in Fig. 5.20. The Hole 1 edge-to-laminate edge distance, d_e, the hole edge-to-edge distance, d_h, and the corner radius, r_c, are all varied. The corner radius ranges over four different values; $r_c = 0.25, 1, 2,$ and 3 mm. In addition, two axisymmetric circular holes with a diameter of 3.175 mm are also considered, where the d_e and d_h values are the same as those used for two axisymmetric square holes. For all values of d_e and d_h, the centers of the holes are located at the mid-length of the laminate, at $x = L/2$. Again, A through H are the points of interest at the hole corners where stress field measurements are taken.

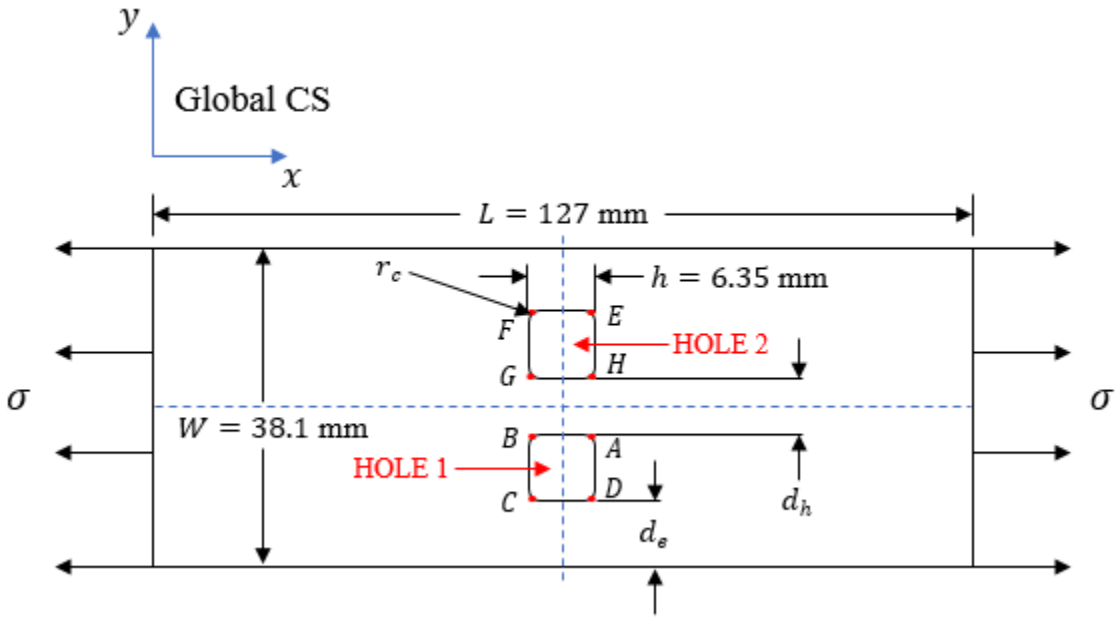

Figure 5.20: Geometry and loading condition for two axisymmetric square holes with rounded corners.

The various cases for the spacing of the two axisymmetric square holes with rounded corners are given below in Table 5.7.

Table 5.7: Cases for the two axisymmetric square holes with rounded corners.

Case	Hole Edge-to-Edge Distance, d_h (mm)	Hole 1 Edge-to-Laminate Edge Distance, d_e (mm)	Square Hole Height, h (mm)
1	8.467 (Equidistant)	8.467 (Equidistant)	6.35
2	7.541	8.930	
3	3.770	10.815	
4	1.885	11.757	

5.2.2 Meshing

The mesh is obtained using the same approach as in Chapter 3. The keypoints are established and used to generate areas, which are then meshed and refined locally in each square area surrounding the two square holes. The number of elements in the square area surrounding the holes was 576 for $d_h = 8.467$ mm, and kept constant at 3840 for $d_h = 7.541$ mm and 3.770 mm. To avoid an element aspect ratio warning for $d_h = 1.885$ mm, this number was increased to 5760. The meshing for two axisymmetric square holes with a corner radius $r_c = 2$ mm can be seen below in Fig. 5.21.

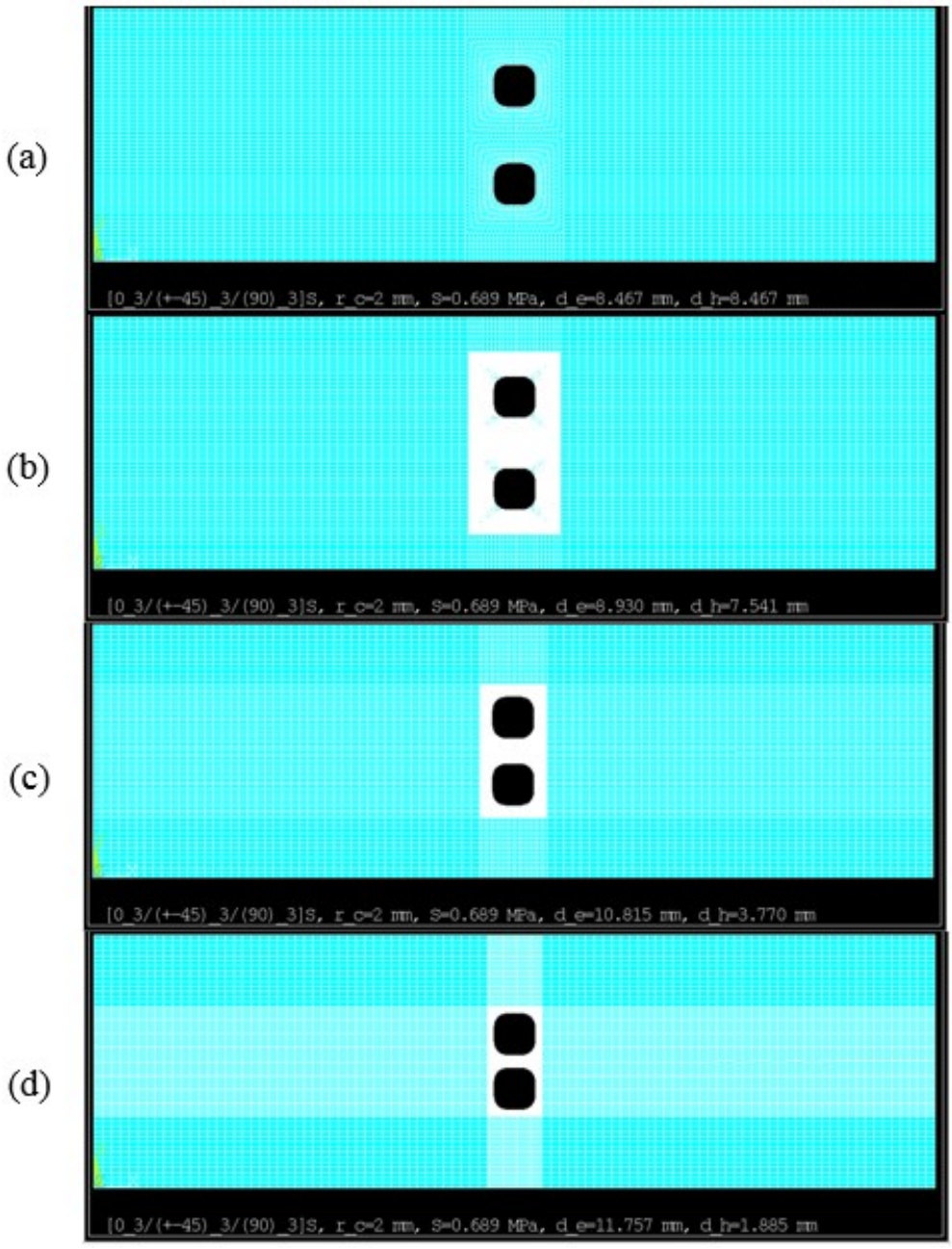

Figure 5.21: Mapped meshing for two axisymmetric square holes with $r_c = 2$ mm: (a) $d_h = 8.467$ mm (equidistant), (b) $d_h = 7.541$ mm, (c) $d_h = 3.770$ mm, (d) $d_h = 1.885$ mm.

5.2.3 Stress Distribution

The σ_{11} stress field contour plots for the two axisymmetric square holes with rounded corners are shown below in Figs. 5.22-5.25. It can be seen that as the two holes approach one another, the magnitude of the σ_{11} stress between the holes increases, as does the maximum value of the σ_{11} stress in each lamina.

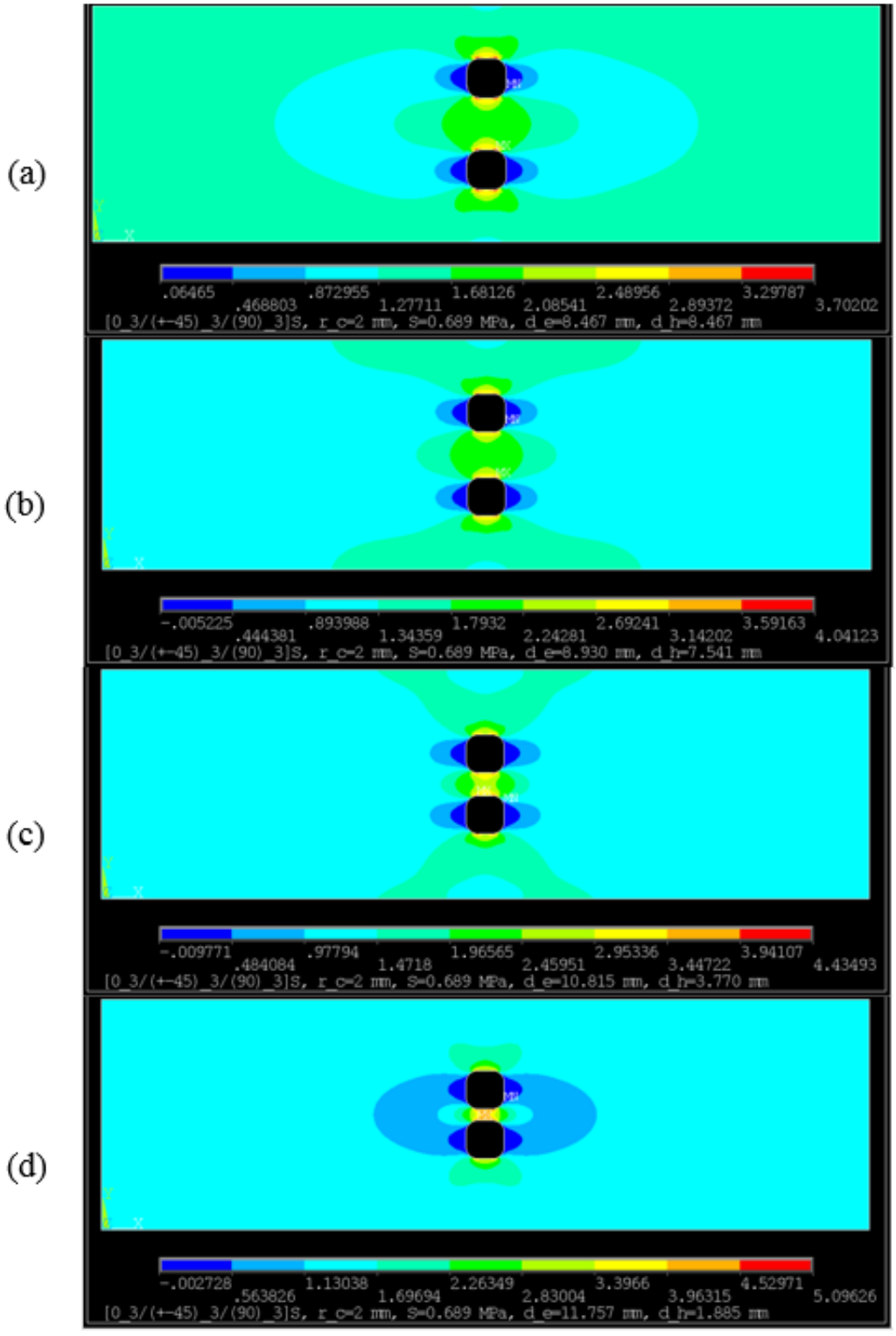

Figure 5.22: σ_{11} stress field contours in the 0° lamina for two axisymmetric square holes with $r_c = 2$ mm: (a) $d_h = 8.467$ mm (equidistant), (b) $d_h = 7.541$ mm, (c) $d_h = 3.770$ mm, (d) $d_h = 1.885$ mm.

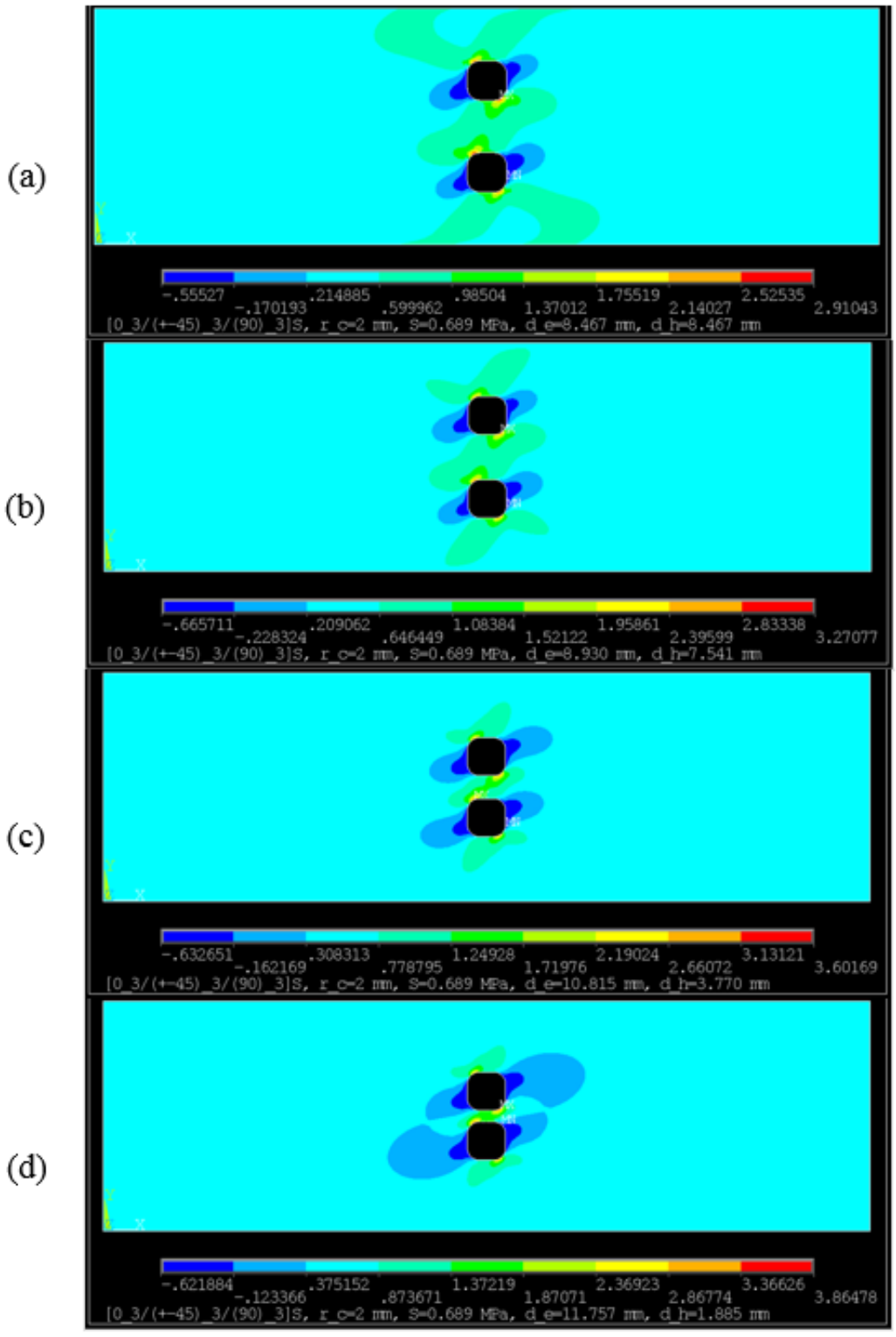

Figure 5.23: σ_{11} stress field contours in the 45° lamina for two axisymmetric square holes with $r_c = 2$ mm: (a) $d_h = 8.467$ mm (equidistant), (b) $d_h = 7.541$ mm, (c) $d_h = 3.770$ mm, (d) $d_h = 1.885$ mm.

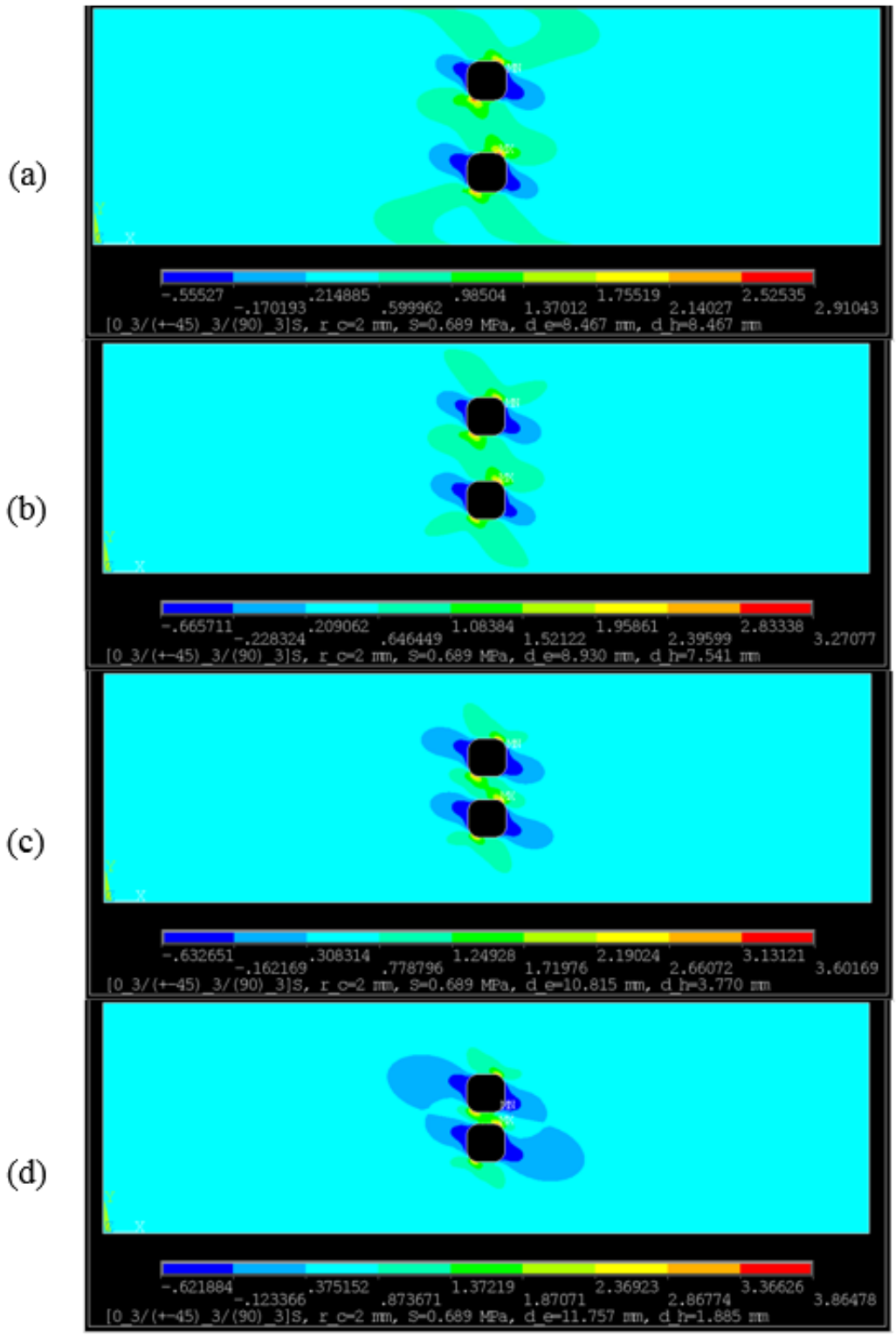

Figure 5.24: σ_{11} stress field contours in the -45° lamina for two axisymmetric square holes with $r_c = 2$ mm: (a) $d_h = 8.467$ mm (equidistant), (b) $d_h = 7.541$ mm, (c) $d_h = 3.770$ mm, (d) $d_h = 1.885$ mm.

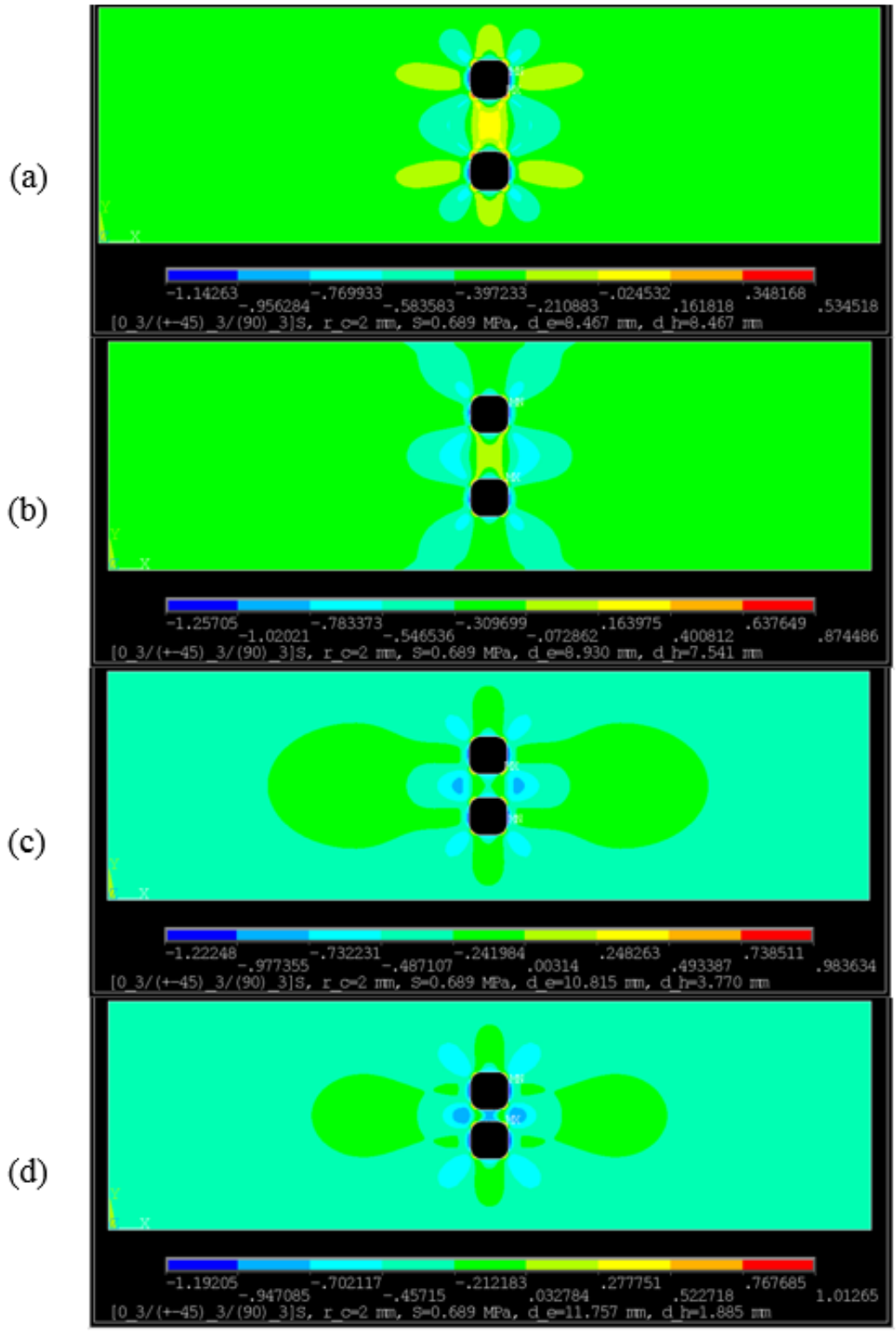

Figure 5.25: σ_{11} stress field contours in the 90° lamina for two axisymmetric square holes with $r_c = 2$ mm: (a) $d_h = 8.467$ mm (equidistant), (b) $d_h = 7.541$ mm, (c) $d_h = 3.770$ mm, (d) $d_h = 1.885$ mm.

5.2.4 Location of Maximum Stresses

The locations and magnitude of the maximum σ_{11} stress in the 0° laminas for the two axisymmetric square holes with rounded corners, can be seen below in Fig. 5.26 and Table 5.8, respectively. The location of the maximum σ_{11} stress is always found in the neighborhood of points A, B, G and H (a consequence of symmetry, see Fig. 5.33a) on Hole 1 and Hole 2. As before, ANSYS displays only one maximum stress location, however, due to symmetry conditions explained in Section 5.2.5, there can exist more than one location of maximum σ_{11} stress on the hole periphery. The σ_{11} stress field interaction due to the "hole-to-hole proximity effect" can also be seen in Fig. 5.26.

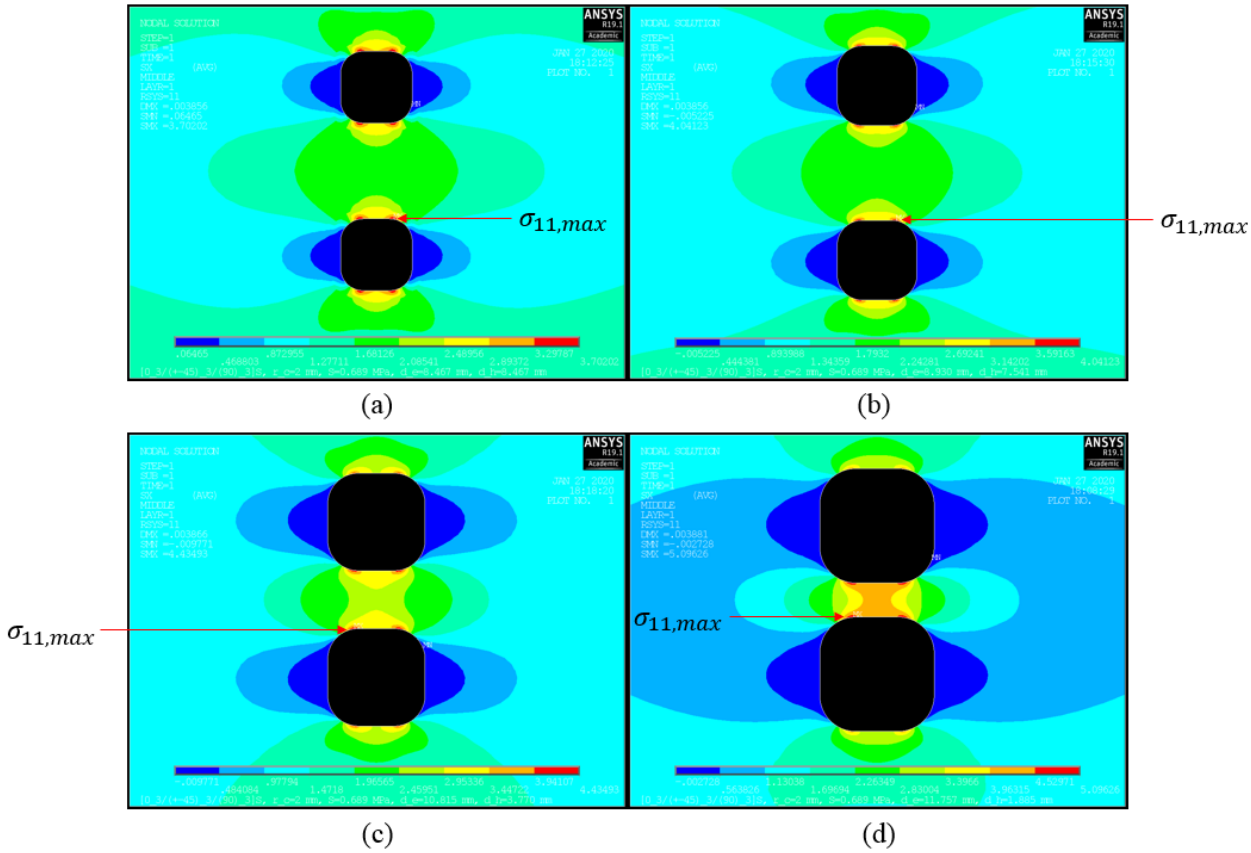

Figure 5.26: 0° lamina σ_{11} stress field interaction and maximum σ_{11} stress locations for two axisymmetric square holes with $r_c = 2$ mm: (a) $d_h = 8.467$ mm (equidistant), (b) $d_h = 7.541$ mm, (c) $d_h = 3.770$ mm, (d) $d_h = 1.885$ mm.

Using $d_e = d_h = 8.467$ mm as the baseline in Table 5.8, it can be seen that for a 10.94% reduction in d_h, there exists a 9.16% increase in maximum σ_{11} stress, for a 55.47% reduction in

d_h, there exists a 19.8% increase in maximum σ_{11} stress, and for a 77.74% reduction in d_h, there exists a 37.66% increase in maximum σ_{11} stress.

Table 5.8: Effect of hole-to-hole proximity on the 0° lamina maximum σ_{11} stress for two axisymmetric square holes with $r_c = 2$ mm.

Hole Edge-to-Edge Distance, d_h (mm)	**Hole 1 Edge-to-Laminate Edge Distance, d_e (mm)**	**$\sigma_{11,max}$ (MPa)**
8.467 (Equidistant)	8.467 (Equidistant)	3.702
7.541	8.930	4.041
3.770	10.815	4.435
1.885	11.757	5.096

As the two holes become close enough, the stress fields surrounding each hole begin to coalesce. Consequently, the magnitude of the stresses in the area between both holes increases. From a practical design standpoint, holes within such close proximity as seen in Fig. 5.26d are rarely encountered, if at all. However, it is worthwhile to be aware of the high stresses which can result from holes within such proximity.

The maximum stress results for two axisymmetric holes are given below in Table 5.9. In general, for a given corner radius, the maximum stress increases in all laminas as the holes become closer. This trend is consistent with results from both Esp [4] and Kheradiya [5]. As in previous results, the maximum σ_{11} stress is always found in the 0° laminas, and the magnitude of the maximum stress in the ±45° laminas is equivalent.

Table 5.9: Maximum σ_{11} stress in each lamina for two axisymmetric square holes with rounded corners and two axisymmetric circular holes.

Corner Radius, r_c (mm)	Hole 1 Edge-to-Laminate Edge Distance, d_e (mm)	Hole Edge-to-Edge Distance, d_h (mm)	Two Axisymmetric Square Holes: $\sigma_{11,max}$ (MPa)			
			0° Lamina	45° Lamina	-45° Lamina	90° Lamina
0.25	8.467 (Equidistant)	8.467 (Equidistant)	5.361	5.241	5.241	1.688
	8.930	7.541	7.131	6.922	6.922	2.900
	10.815	3.770	7.777	7.503	7.503	3.150
	11.757	1.885	8.129	7.633	7.633	3.118
1	8.467 (Equidistant)	8.467 (Equidistant)	4.128	3.428	3.428	0.774
	8.930	7.541	4.866	4.160	4.160	1.303
	10.815	3.770	5.333	4.535	4.535	1.436
	11.757	1.885	5.709	4.739	4.739	1.470
2	8.467 (Equidistant)	8.467 (Equidistant)	3.702	2.910	2.910	0.535
	8.930	7.541	4.041	3.271	3.271	0.874
	10.815	3.770	4.435	3.602	3.602	0.984
	11.757	1.885	5.096	3.865	3.865	1.013
3	8.467 (Equidistant)	8.467 (Equidistant)	3.916	2.702	2.702	0.450
	8.930	7.541	4.078	2.894	2.894	0.679
	10.815	3.770	4.192	3.175	3.175	0.784
	11.757	1.885	5.038	3.539	3.539	0.827
			Two Axisymmetric Circular Holes: $\sigma_{11,max}$ (MPa)			
3.175 (Circle)	8.467 (Equidistant)	8.467 (Equidistant)	4.157	2.690	2.690	0.440
	8.930	7.541	4.296	2.860	2.860	0.652
	10.815	3.770	4.371	3.110	3.110	0.756
	11.757	1.885	5.216	3.501	3.501	0.802

It is worthwhile to note the transformation and the resulting interaction of the σ_{11} stress fields in the 0° and 45° laminas for the two holes at their closest proximity, $d_h = 1.885$ mm, as this is where the greatest stresses in the laminate are developed for any given r_c. As the corner radius increases, the stress fields coalesce, giving rise to an increase in stress magnitude which is greater than that which is seen for a single independent square hole with rounded corners. As expected, this is due to the "hole-to-hole proximity effect". This behavior can be seen below for $r_c = 2$ mm in Figs. 5.27 and 5.28.

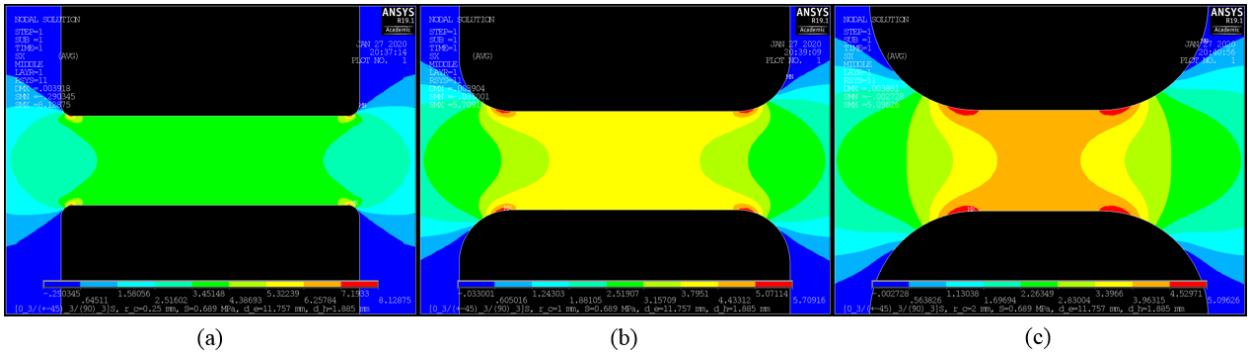

(a) (b) (c)

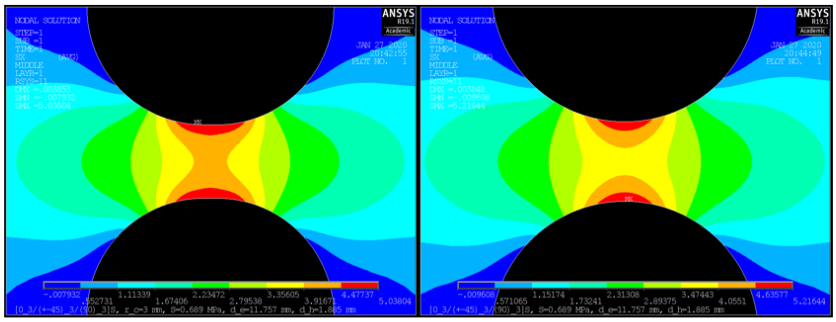

(d) (e)

Figure 5.27: 0° lamina σ_{11} stress field transformation and interaction, and maximum σ_{11} stress locations for two axisymmetric square holes for $d_h = 1.885$ mm: (a) $r_c = 0.25$ mm, (b) $r_c = 1$ mm, (c) $r_c = 2$ mm, (d) $r_c = 3$ mm, (e) $r_c = 3.175$ mm (circle).

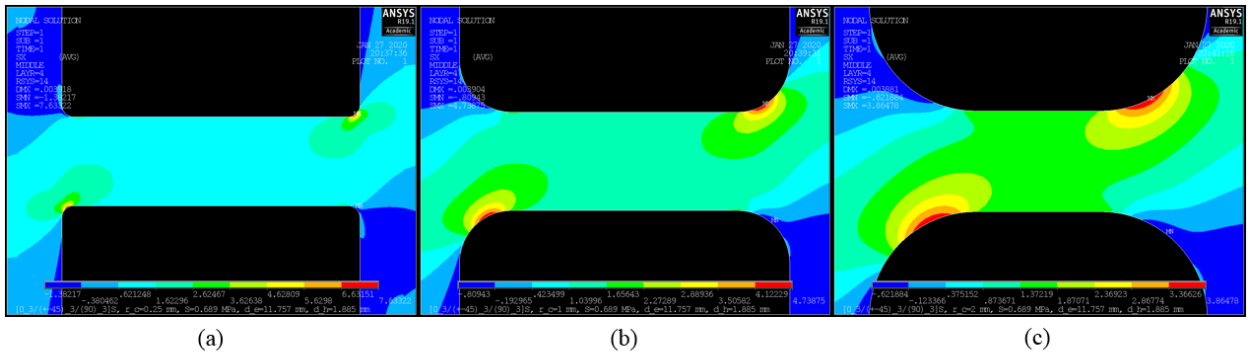

(a) (b) (c)

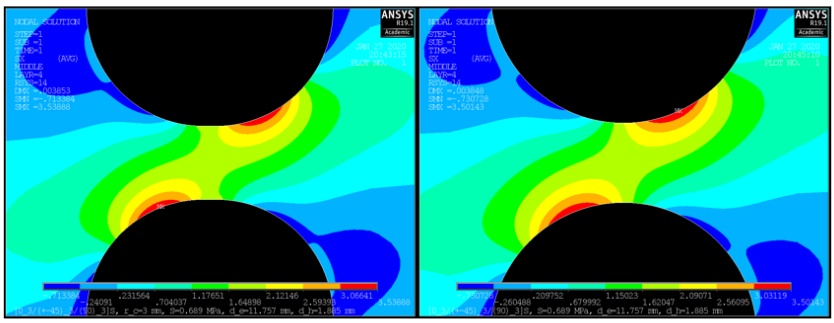

(d) (e)

Figure 5.28: 45° lamina σ_{11} stress field transformation and interaction, and maximum σ_{11} stress locations for two axisymmetric square holes for $d_h = 1.885$ mm: (a) $r_c = 0.25$ mm, (b) $r_c = 1$ mm, (c) $r_c = 2$ mm, (d) $r_c = 3$ mm, (e) $r_c = 3.175$ mm (circle).

5.2.5 Stress Concentration Factors

It is important to illustrate that for all cases of two axisymmetric square holes, that due to the symmetry present in the spacing of the holes about the central axis, secondary bending is not present, and thus no contribution is found in the resultant stresses or SCFs. Further, as in the case of the single centered hole, only extension in the x-direction is present, along with some Poisson effect. This can be seen below in Fig. 5.29. However, the "edge effect" and the "hole-to-hole proximity effect" are present in all hole spacing configurations.

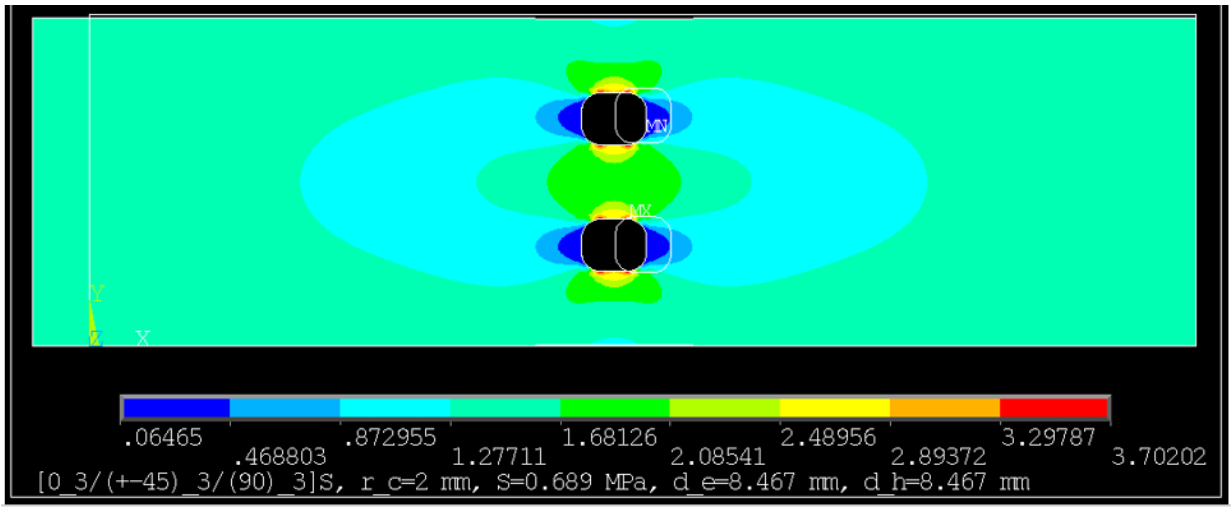

Figure 5.29: Two axisymmetric square holes with $d_e = d_h = 8.467$ mm (equidistant) and $r_c = 2$ mm, with no secondary bending and x-direction extension only.

The stress concentration factors for each lamina for the two axisymmetric holes are given below in Table 5.10. As in previous sections, the highest SCFs are always found in the ±45° laminas, due to division by the lower value of stress found in the ±45° laminas with no hole using Eqn. 4.6.

Table 5.10: Lamina SCFs for two axisymmetric square holes with rounded corners and two axisymmetric circular holes.

Corner Radius, r_c (mm)	Hole 1 Edge-to-Laminate Edge Distance, d_e (mm)	Hole Edge-to-Edge Distance, d_h (mm)	Two Axisymmetric Square Holes: $K_{t,\theta}$			
			$\theta = 0°$	$\theta = 45°$	$\theta = -45°$	$\theta = 90°$
0.25	8.467 (Equidistant)	8.467 (Equidistant)	4.145	9.360	9.360	4.895
	8.930	7.541	5.513	12.363	12.363	8.413
	10.815	3.770	6.013	13.401	13.401	9.138
	11.757	1.885	6.285	13.633	13.633	9.043
1	8.467 (Equidistant)	8.467 (Equidistant)	3.192	6.123	6.123	2.244
	8.930	7.541	3.762	7.430	7.430	3.780
	10.815	3.770	4.123	8.099	8.099	4.165
	11.757	1.885	4.414	8.463	8.463	4.265
2	8.467 (Equidistant)	8.467 (Equidistant)	2.862	5.198	5.198	1.550
	8.930	7.541	3.125	5.842	5.842	2.537
	10.815	3.770	3.429	6.433	6.433	2.853
	11.757	1.885	3.940	6.902	6.902	2.937
3	8.467 (Equidistant)	8.467 (Equidistant)	3.028	4.826	4.826	1.304
	8.930	7.541	3.153	5.168	5.168	1.970
	10.815	3.770	3.241	5.670	5.670	2.274
	11.757	1.885	3.895	6.320	6.320	2.397
			Two Axisymmetric Circular Holes: $K_{t,\theta}$			
3.175 (Circle)	8.467 (Equidistant)	8.467 (Equidistant)	3.214	4.805	4.805	1.275
	8.930	7.541	3.321	5.107	5.107	1.891
	10.815	3.770	3.379	5.554	5.554	2.192
	11.757	1.885	4.033	6.253	6.253	2.328

The SCFs for each lamina as a function of hole edge-to-edge distance are plotted below in Figs. 5.30-5.32. As one may expect, the SCF increases as the two holes become closer to one another, for all values of r_c.

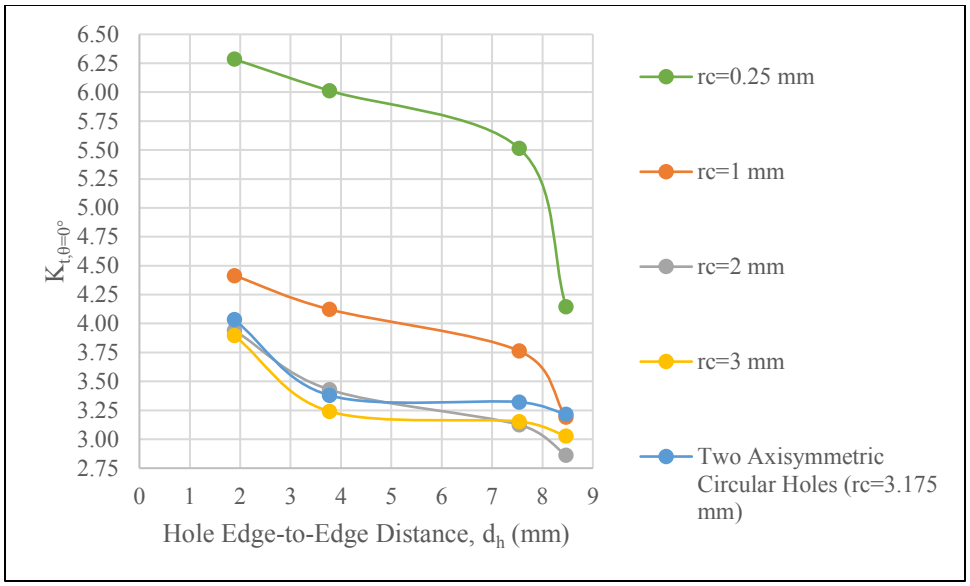

Figure 5.30: 0° lamina SCF for two axisymmetric square holes with rounded corners and two axisymmetric circular holes.

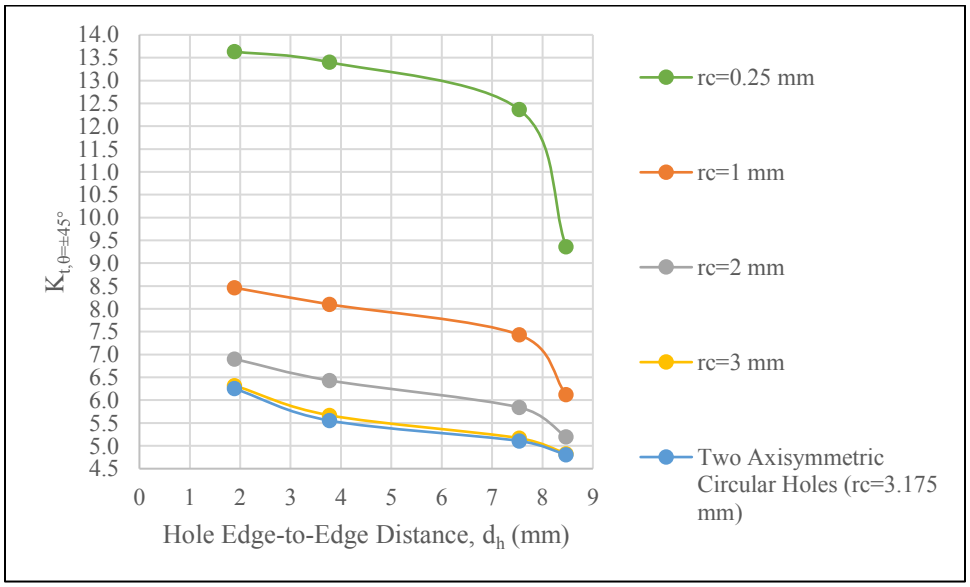

Figure 5.31: ±45° lamina SCF for two axisymmetric square holes with rounded corners and two axisymmetric circular holes.

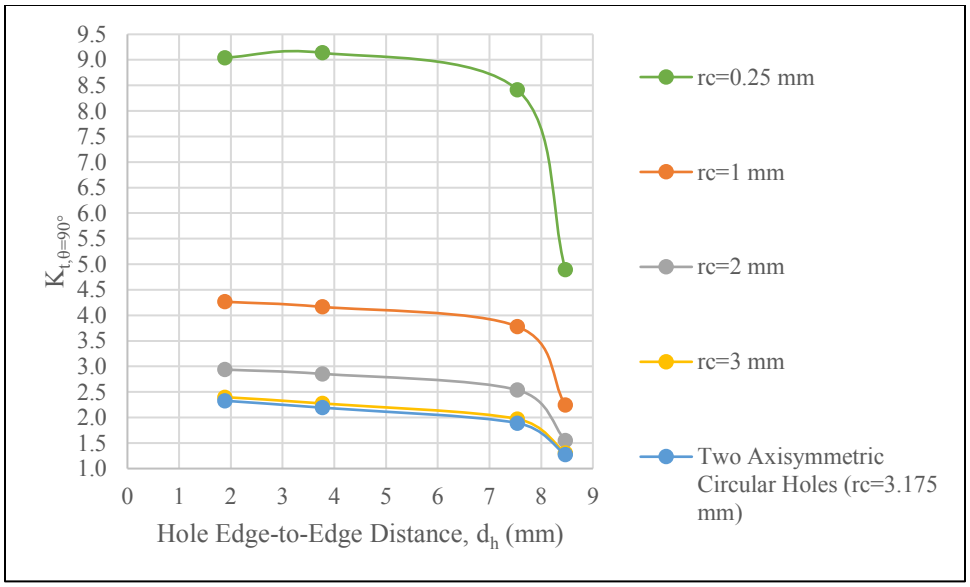

Figure 5.32: 90° lamina SCF for two axisymmetric square holes with rounded corners and two axisymmetric circular holes.

Since both square holes are always spaced equally from each other about the central axis of the laminate, symmetry conditions are present. As well as that which is created by the fiber orientation angle, certain σ_{11} stress field values at each of the four corners of the square hole are expected to be equivalent. However, certain symmetry conditions are only present for the equidistant hole and edge spacing. Once the holes approach one another, symmetry conditions are lost due to influence from the "hole-to-hole proximity effect". The symmetry equivalencies for two axisymmetric square holes with rounded corners can be seen below in Fig. 5.33, where the dashed blue line between the two holes represents the central axis.

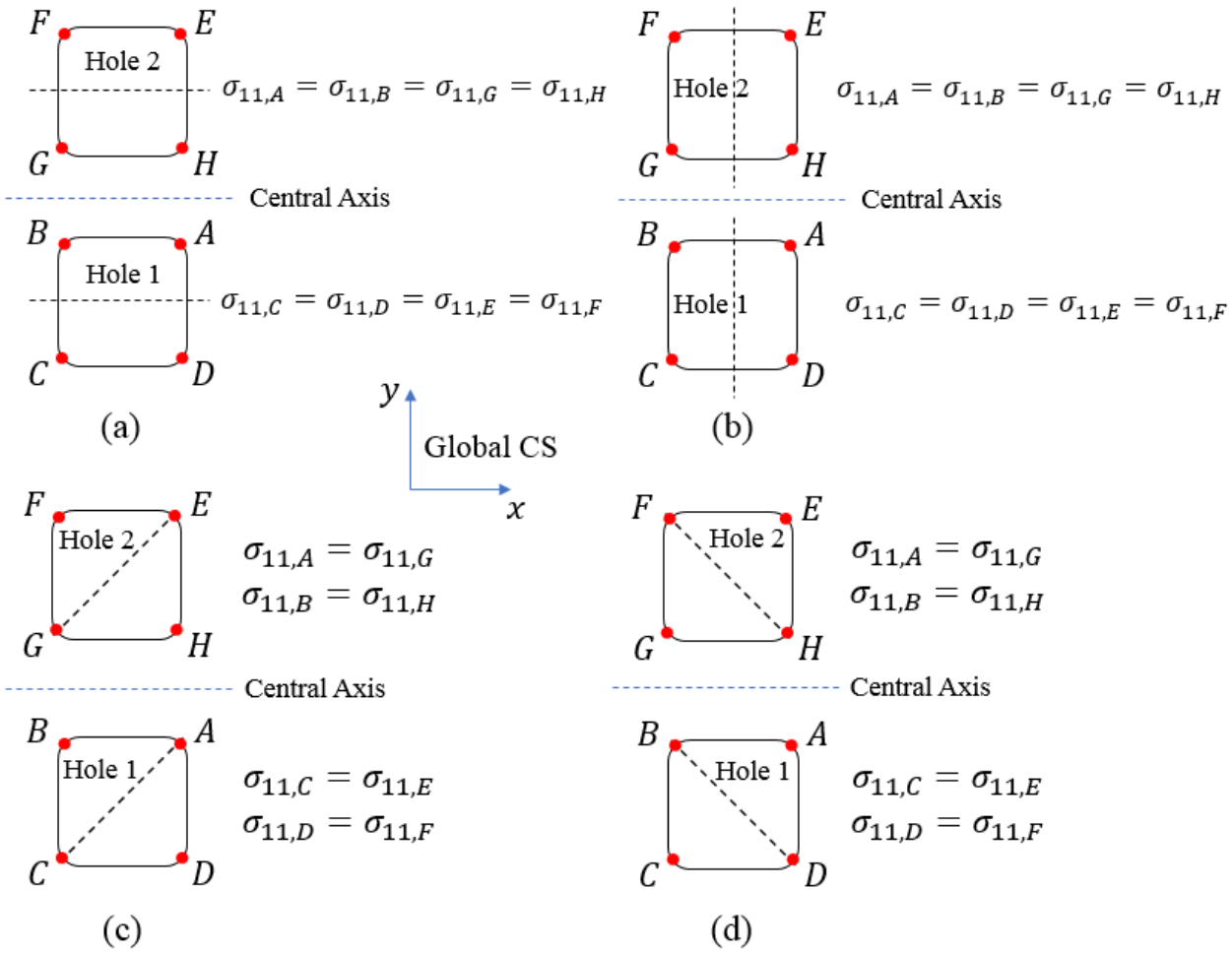

Figure 5.33: σ_{11} stress symmetry conditions based on fiber orientation directions for two axisymmetric square holes: (a) 0° fiber, (b) 90° fiber, (c) 45° fiber, (d) -45° fiber.

The σ_{11} stress values at each of the four corners of the two axisymmetric square holes for $r_c = 2$ mm are given below in Table 5.11. It should be noted that for the case of equidistant hole and edge spacing, that points $A, B, G,$ and H are slightly greater than points $C, D, E,$ and F, which are the points closest to the edges of the laminate. This would seem to indicate that the "hole-to-hole proximity effect" has a greater influence than the "edge effect", all other things being equal.

Table 5.11: σ_{11} stress at points A through H for two axisymmetric square holes with $r_c = 2$ mm.

Two Axisymmetric Square Holes										
Hole Edge-to-Edge Distance, d_h (mm)	**Hole Edge-to-Laminate Edge Distance, d_e (mm)**	**Fiber Orientation Angle, θ (°)**	**σ_{11} (MPa)**							
			Hole 1				**Hole 2**			
			A	***B***	***C***	***D***	***E***	***F***	***G***	***H***
8.467 (Equidistant)	8.467 (Equidistant)	0	3.702	3.702	3.696	3.696	3.696	3.696	3.702	3.702
7.541	8.930		4.041	4.041	4.022	4.022	4.022	4.022	4.041	4.041
3.770	10.815		4.435	4.435	4.147	4.147	4.147	4.147	4.435	4.435
1.885	11.757		5.096	5.096	4.311	4.311	4.311	4.311	5.096	5.096
8.467 (Equidistant)	8.467 (Equidistant)	45	0.087	2.910	0.110	2.749	0.110	2.749	0.087	2.910
7.541	8.930		-0.368	3.271	-0.340	3.019	-0.340	3.019	-0.368	3.271
3.770	10.815		-0.413	3.602	-0.363	3.163	-0.363	3.163	-0.413	3.602
1.885	11.757		-0.339	3.865	-0.296	3.370	-0.296	3.370	-0.339	3.865
8.467 (Equidistant)	8.467 (Equidistant)	-45	2.910	0.087	2.749	0.110	2.749	0.110	2.910	0.087
7.541	8.930		3.271	-0.368	3.019	-0.340	3.019	-0.340	3.271	-0.368
3.770	10.815		3.602	-0.413	3.163	-0.363	3.163	-0.363	3.602	-0.413
1.885	11.757		3.865	-0.339	3.370	-0.296	3.370	-0.296	3.865	-0.339
8.467 (Equidistant)	8.467 (Equidistant)	90	0.535	0.535	0.325	0.325	0.325	0.325	0.535	0.535
7.541	8.930		0.874	0.874	0.704	0.704	0.704	0.704	0.874	0.874
3.770	10.815		0.984	0.984	0.773	0.773	0.773	0.773	0.984	0.984
1.885	11.757		1.013	1.013	0.836	0.836	0.836	0.836	1.013	1.013

The behavior of the symmetry found at the various points of the two axisymmetric square holes with rounded corners using the normalized σ_{11} stress values can be easily understood in graphical form, which is shown below for the various laminas, in Figs. 5.34-5.37.

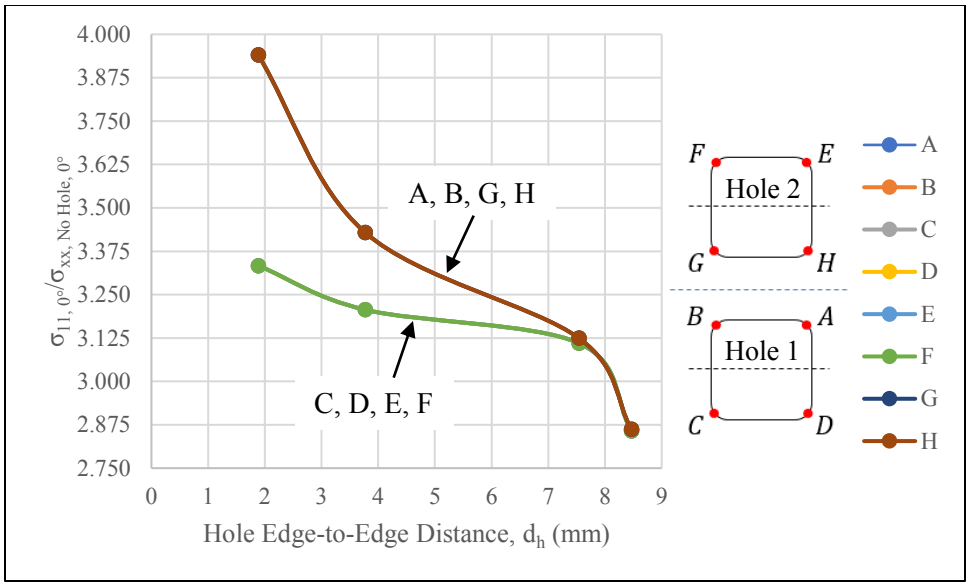

Figure 5.34: Normalized 0° lamina σ_{11} stress at points A through H for two axisymmetric square holes with rounded corners for $r_c = 2$ mm.

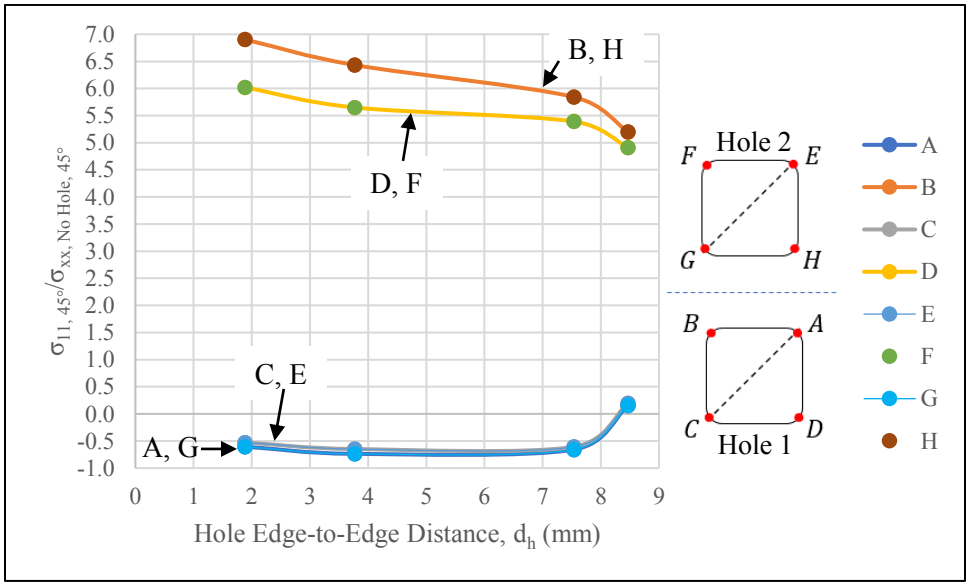

Figure 5.35: Normalized 45° lamina σ_{11} stress at points A through H for two axisymmetric square holes with rounded corners for $r_c = 2$ mm.

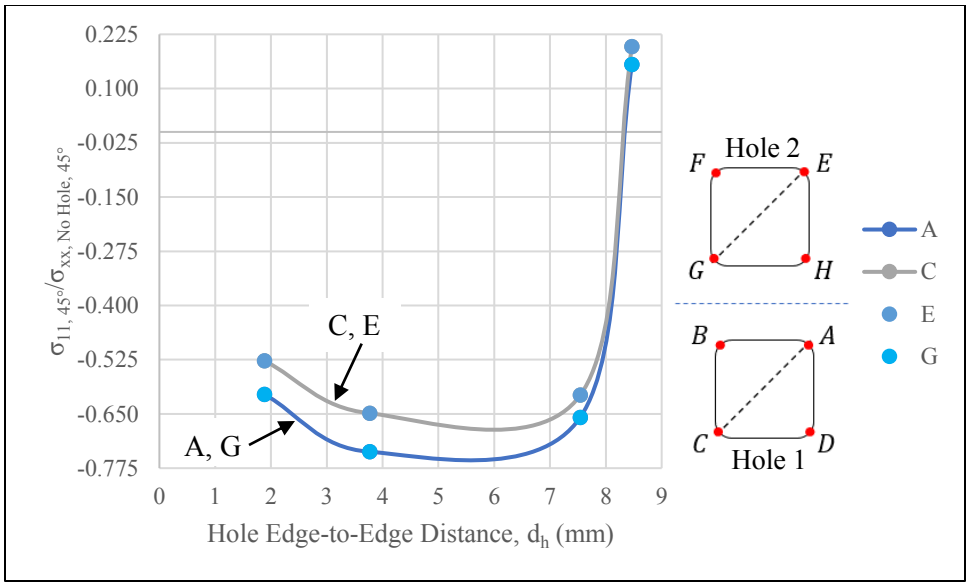

Figure 5.36: Enlarged view of the normalized 45° lamina σ_{11} stress at points A, C, E, and G, for two axisymmetric square holes with rounded corners for $r_c = 2$ mm.

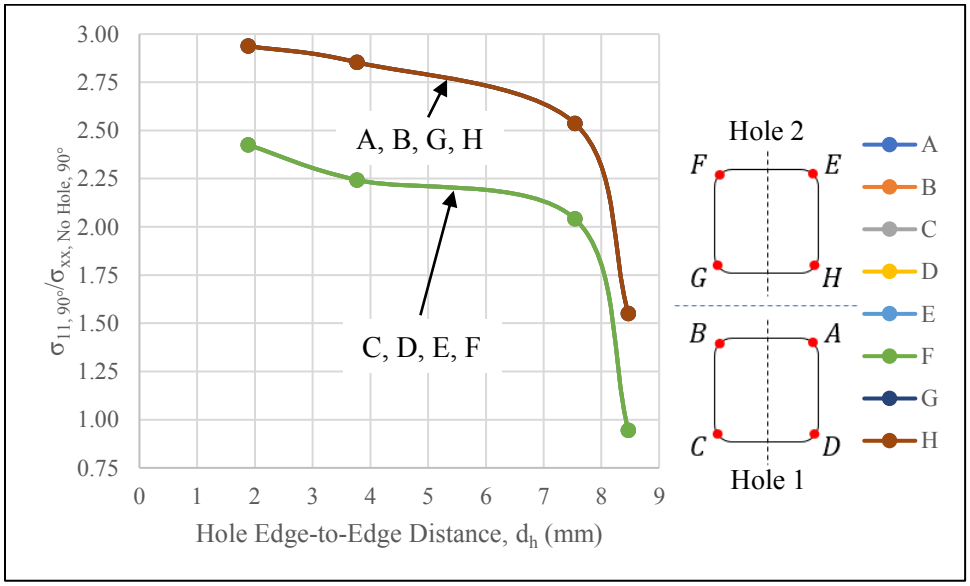

Figure 5.37: Normalized 90° lamina σ_{11} stress at points A through H for two axisymmetric square holes with rounded corners for $r_c = 2$ mm.

Again, the maximum σ_x stress in the laminate can be obtained by using the values from Table 4.17 as the elastic constants for the laminate, in order to model it as an isotropic material. The maximum laminate σ_x stress for all cases of both the two axisymmetric square holes with

rounded corners and the two axisymmetric circular holes are given below in Table 5.12, along with the laminate SCFs based on the gross area of the quasi-isotropic laminate.

Table 5.12: Maximum laminate σ_x stress using laminate elastic constants, and SCFs based on the gross area of the laminate.

Corner Radius, r_c (mm)	**Hole Edge-to-Edge Distance, d_h (mm)**	**Two Axisymmetric Square Holes: $\sigma_{x,max}$ (MPa)**	**Two Axisymmetric Square Holes: K_{tg}**
0.25	8.467 (Equidistant)	2.996	4.346
	7.541	3.876	5.622
	3.770	4.220	6.120
	1.885	4.402	6.384
1	8.467 (Equidistant)	2.250	3.263
	7.541	2.608	3.783
	3.770	2.856	4.143
	1.885	3.058	4.435
2	8.467 (Equidistant)	2.003	2.905
	7.541	2.167	3.144
	3.770	2.378	3.449
	1.885	2.722	3.948
3	8.467 (Equidistant)	2.100	3.046
	7.541	2.179	3.160
	3.770	2.239	3.247
	1.885	2.691	3.904
		Two Axisymmetric Circular Holes: $\sigma_{x,max}$ (MPa)	**Two Axisymmetric Circular Holes: K_{tg}**
3.175 (Circle)	8.467 (Equidistant)	2.225	3.228
	7.541	2.292	3.324
	3.770	2.331	3.382
	1.885	2.783	4.036

The SCFs for the quasi-isotropic laminate are graphed and shown below in Fig. 5.38.

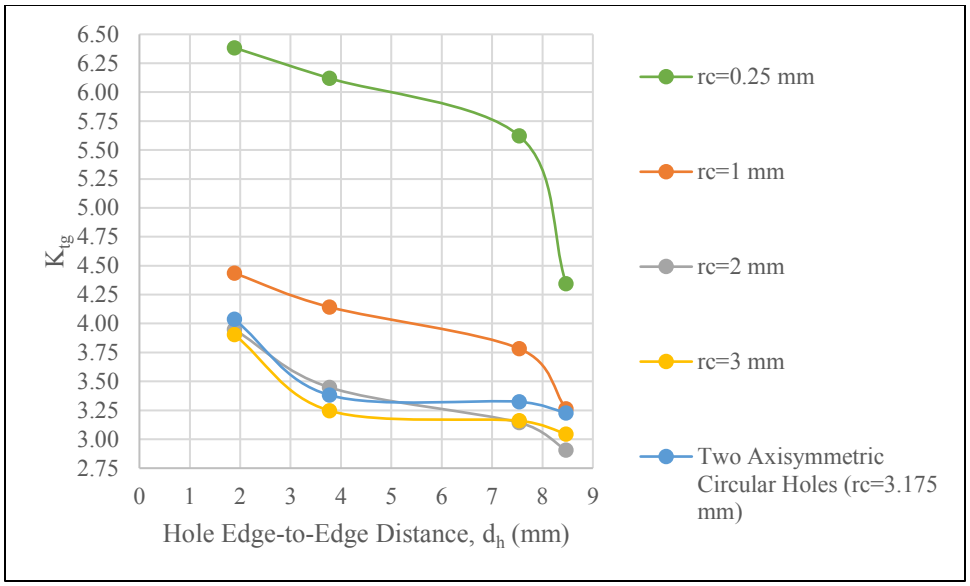

Figure 5.38: Laminate SCFs for the two axisymmetric square holes with rounded corners and the two axisymmetric circular holes.

It can be seen in Fig. 5.38 that once the square hole corners become sufficiently rounded ($r_c > 2$ mm), the hole edge-to-edge distance has less influence upon the magnitude of maximum laminate stress for $3.770 \text{ mm} \leq d_h \leq 7.541$ mm, and thus SCF. Also, once $r_c > 1$ mm, the influence of d_h upon the magnitude of maximum laminate stress for $1.984 \text{ mm} \leq d_h \leq 3.770$ mm becomes appreciable. A corner radius of $r_c = 3$ mm elicits a lower SCF than a circular hole for all values of d_h.

5.3 Conclusions

For both the two asymmetric square holes and the two axisymmetric square holes, the maximum σ_{11} stress in the laminate is always found in the 0° lamina, regardless of hole spacing configuration and corner radius. A much greater degree of symmetry with respect to the σ_{11} stress found at the square hole corner points is present in the two axisymmetric square holes, as opposed to the two asymmetric square holes. This is due to the symmetry present in the geometrical spacing of the two axisymmetric holes about the central axis.

In general, a decrease in hole edge-to-edge distance, d_h, elicits an increase in maximum σ_{11} stress for all laminas, irrespective of fiber orientation, hole edge-to-laminate edge distance, d_e, and corner radius, r_c. For the equidistant spacing of two axisymmetric square holes with $r_c =$

2 mm, the maximum stress is found on the inside corners of Hole 1 and Hole 2, suggesting that influence from the "hole-to-hole proximity effect" is greater than the "edge effect".

For an equivalent d_h and r_c between two axisymmetric square holes and two asymmetric square holes, the presence of the laminate edge ("edge effect") in the case of the two asymmetric square holes produces an increase in maximum σ_{11} stress in the 0° lamina. This can be seen below in Table 5.13 for various d_h and $r_c = 2$ mm. It is interesting to note that the largest percent increase maximum σ_{11} stress between the two configurations coincides with the lowest maximum σ_{11} stress in the 0° lamina. One should recall that secondary bending is present for the two asymmetric holes, and not for the two axisymmetric holes.

Table 5.13: Influence of the "edge effect" and the "hole-to-hole proximity effect" on maximum σ_{11} stress in the 0° lamina for two square holes with $r_c = 2$ mm.

Hole Edge-to-Edge Distance, d_h (mm)	**Hole Configuration**	**$\sigma_{11,max}$ (MPa)**	**% Increase**
7.541 (Hole 2 Centered for Asymmetric Case Only)	Two Axisymmetric	4.041	28.99
	Two Asymmetric	5.411	
3.770	Two Axisymmetric	4.435	27.31
	Two Asymmetric	5.838	
1.885	Two Axisymmetric	5.096	25.59
	Two Asymmetric	6.400	

CHAPTER 6: DAMAGE INITIATION ANALYSIS

An introduction to composite damage is given, followed by a background on continuum damage mechanics which includes an explanation of the Hashin criteria. A damage analysis for a single centered square hole with rounded corners and a single centered circular hole is then given. This is followed by a damage analysis for two asymmetric square holes with rounded corners and two axisymmetric square holes with rounded corners. Lastly, a conclusion is given.

6.1 Introduction

Composites do not possess the same capability to redistribute stress around local areas of stress concentration when compared to their metallic counterparts. In metals, stress redistribution is made possible by the yielding of the material surrounding the local areas of stress concentration. Composites are restricted in their ability to redistribute stress in this manner. Instead, damage is created at local areas of stress concentration. As discussed briefly in Section 2.5, this can occur in micro-failure modes such as fiber fracture, fiber buckling, matrix cracking, delamination (common), and fiber-matrix interfacial shear. It is important to be aware that damage occurs at a very small scale, and thus a robust model is one that incorporates multiple orders of magnitude, and can transition from micro to meter scale. In this way, an understanding of damage initiation and evolution can be more readily attained.

6.2 Composite Damage Analysis

In this study, ANSYS Mechanical APDL 19.1 was used to investigate the initiation and evolution of damage within the quasi-isotropic laminate. ANSYS possesses the capability to model progressive composite damage using various damage evolution laws, which are based upon different mathematical damage models. Such models include the continuum damage mechanics (CDM) method and the material property degradation (MPDG) method. This study focuses on the former method. The main difference between the two approaches is that CDM is based upon the progressive dissipation of discrete amounts of energy and can be thought of as a

"toughness reduction" model, whereas MPDG models composite damage using "instant stiffness reduction", hence its material degradation name. In ANSYS, CDM, which models gradually increasing damage, can be seen as superior in some ways to MPDG. The latter can only qualify a mesh element as damaged or undamaged (a consequence of modeling damage with a step function), whereas CDM can qualify and quantify damage evolution within an element, as well as throughout the mesh. For the various failure modes, ANSYS can plot either the nodal or the elemental contours of the failure index. It uses a color scale to quantify and qualify the initiation of any damage within a particular element on a scale of roughly zero (no damage predicted) to unity or above (damage predicted). Similarly, ANSYS can also plot either the nodal or elemental contours of the damage variable, and represent the presence of any damage within a particular element on a color scale of zero (no damage) to unity (total failure; complete loss of stiffness). Any value between zero and unity indicates that damage is present within the lamina. Both the failure indices and the damage variables are discussed in the following section.

6.2.1 Damage Initiation

Many types of damage initiation criteria have been developed based upon theory which governs the behavior of the fiber-matrix interface. Each type possesses its own ease of use, advantages, and limitations. The appeal of the Hashin criteria is that unlike traditional alternatives such as Tsai-Wu, which informs of only the initiation of damage, it is able to not only quantify damage initiation, but reveals the type of damage predicted (fiber or matrix) and whether it is due to tensile or compressive stresses. In order to model composite damage evolution, ANSYS requires the user to first select a damage initiation criterion. ANSYS allows the user to select from failure criteria which include: maximum stress, maximum strain, Puck, Hashin, LaRc03, LaRc04, and up to nine user-defined criteria. It should be noted that the criteria are damage method specific. The Hashin criteria only works with progressive damage analysis (PDA) such as the CDM method, and the remaining failure criteria only work with the MPDG method. For this study, the two-dimensional Hashin damage initiation criteria was used in conjunction with CDM. The Hashin criteria proposes four separate modes of failure, each with its own equation. It is important to be aware of the fact that these criteria are applied at the lamina level, and accordingly, they involve strength parameters and stress components, σ_{ij}, measured at the lamina level. These failure modes and their governing equations are as follows:

(1) For fiber tension failure,

$$I_{Fft} = \left(\frac{\sigma_{11}}{F_{1t}}\right)^2 + \alpha\left(\frac{\tau_{12}}{F_{12}}\right)^2 \quad if\ \sigma_{11} \geq 0 \tag{6.1}$$

where I_{Fft} is the failure index for fiber failure in tension, σ_{11} is the stress in the longitudinal direction of the fibers, F_{1t} is the fiber tensile strength, α is a weight factor which controls the influence of shear stress on fiber failure, τ_{12} is the shear stress in the 12-plane, and F_{12} is the shear failure stress in the 12-plane. For this study, it is assumed that $\alpha = 0$. Barbero and Shahbazi [21] pointed out that fiber tension is a misnomer encountered in the literature, in that this failure mode represents the *longitudinal tensile failure* of the composite lamina.

(2) For fiber compression failure,

$$I_{Ffc} = \left(\frac{\sigma_{11}}{F_{1c}}\right)^2 \quad if\ \sigma_{11} < 0 \tag{6.2}$$

where I_{Ffc} is the failure index for fiber failure in compression, F_{1c} is the fiber compressive strength, and all other variables are as defined previously. In a similar fashion to the above, this mode represents *longitudinal compressive failure* of the composite lamina.

(3) For matrix tension failure,

$$I_{Fmt} = \left(\frac{\sigma_{22}}{F_{2t}}\right)^2 + \left(\frac{\tau_{12}}{F_{12}}\right)^2 \quad if\ \sigma_{22} \geq 0 \tag{6.3}$$

where I_{Fmt} is the failure index for matrix failure in tension, σ_{22} is the stress in the transverse direction of the fibers, F_{2t} is the matrix tensile strength, and all other variables are as defined above. This mode represents the *transverse tensile* and *in-plane shear failure* of the composite lamina.

(4) For matrix compression failure,

$$I_{Fmc} = \left(\frac{\sigma_{22}}{2F_4}\right)^2 + \left[\left(\frac{F_{2c}}{2F_{23}}\right)^2 - 1\right]\frac{\sigma_{22}}{F_{2c}} + \left(\frac{\tau_{12}}{F_{12}}\right)^2 \quad if\ \sigma_{22} < 0 \tag{6.4}$$

where I_{Fmc} is the failure index for matrix failure in compression, F_{23} is the shear failure stress in the 23-plane, F_{2c} is the matrix compressive strength, and all other variables are as defined above. For this study, $F_4 = 1/2F_{2c}$. This mode represents the *transverse compressive failure* of the composite lamina.

The damage failure (or more appropriately, initiation) indexes, I_{Fft}, I_{Ffc}, I_{Fmt}, and I_{Fmc} govern the onset of damage for a particular damage mode within a given lamina. Damage is predicted to occur when the initiation failure index is equal to or exceeds unity; $I_F \geq 1$. Barbero and Shahbazi [21] also indicated that "failure" is not the most accurate way to describe such phenomena. For a laminate which has been properly designed and manufactured, no catastrophic failure typically occurs at that physical location. Instead, small amounts of damage appear, and evolve as the displacement (or load) continues to be increased.

For the various failure modes, ANSYS is able to display the associated damage variables. These are as follows: d_{mt}, d_{mc}, d_{ft}, and d_{fc}, which correspond to the damage variable for matrix tension, matrix compression, fiber tension, and fiber compression, respectively. The accumulation of damage within any given lamina can then be considered using three "global damage variables" as below [28]

$$d_f = 1 - (1 - d_{ft})(1 - d_{fc}) \tag{6.5}$$

$$d_m = 1 - (1 - d_{mt})(1 - d_{mc}) \tag{6.6}$$

$$d_s = 1 - (1 - d_{ft})(1 - d_{fc})(1 - d_{mt})(1 - d_{mc}) \tag{6.7}$$

where d_f is the global fiber damage variable, d_m is the global matrix damage variable, and d_s is the global shear damage variable. When any given damage variable becomes greater than zero, damage has occurred in the lamina.

The user must also provide the associated Hashin criteria material strengths when using the CDM method, as these values govern largely the onset of material damage. The extent of composite damage is determined by the applied displacement (or load), stacking sequence, holes or notches and their consequent SCFs, and material properties. These composite material properties are given below in Table 6.1. It should be noted that some values are *in situ*, meaning that they can only be acquired during the time of the experiment, thereby necessitating laboratory testing. The material strength values F_{2t} and F_{12} are *in situ*. All of the values were taken from a research paper by Barbero and Shahbazi [21], in which experimental data from a physical specimen was used in tandem with ANSYS to effectively determine these values, as mentioned briefly in Section 2.5. Without the benefit of such experimental tension test data from a physical specimen, it becomes necessary to appeal to an alternative method in order to acquire these parameters, namely searching existing research publications for a complete set of data. Barbero [27] noted that from a practical standpoint, the major drawback of CDM is the requisite need for additional experimentation in order to determine these model specific parameters. It is important to note the large difference in magnitude between the fiber tensile strength and the matrix tensile strength, as seen below in Table 6.1. These two values govern largely their respective Hashin failure criterion.

Table 6.1: HyE 9082Af, Fiberite strength values needed for CDM damage modeling in ANSYS [21].

Fiber Tensile Strength, F_{1t} (MPa)	**Fiber Compressive Strength, F_{1c} (MPa)**
1020	-620
Matrix Tensile Strength, F_{2t} (MPa)	**Matrix Compressive Strength, F_{2c} (MPa)**
80	-140
Z Tensile Failure Stress, F_{3t} (MPa)	**Z Compressive Strength, F_{3c} (MPa)**
80	-140
XY Shear Failure Stress, F_{12} (MPa)	**XZ Shear Failure Stress, F_{13} (MPa)**
48	48
YZ Shear Failure Stress, F_{23} (MPa)	
52.7	

6.2.2 Damage Evolution

The CDM method is governed by two types of variables for each damage mode; the dissipation of energy per unit area (fracture toughness), G_c, and the viscosity damping coefficient of the material, η. Once damage is initiated, the damage variables increase gradually, as they are dictated by the amount of energy dissipated within the material. The values of G_c and η must be determined beforehand via standard laboratory tests. The fracture toughness is described by the following equation:

$$G_c = \int_0^{U_e^f} \sigma_e dU_e \tag{6.8}$$

where σ_e is the equivalent stress (equal to σ_x for the case of an in-plane uniaxial stress state in the x-direction), U_e is the equivalent displacement (for an in-plane uniaxial stress state, $U_e = L_c\epsilon_x$ where L_c is the length of the element in the x-direction, and ϵ_x is the strain), and U_e^f is the ultimate equivalent displacement, where the total material stiffness is lost for the specific failure mode. The graph for Eqn. 6.8 is shown below in Fig. 6.1, and as implied by Eqn. 6.8, the fracture toughness is simply the area under the equivalent stress curve. The fracture toughness values used in the CDM modeling are given below in Table 6.2.

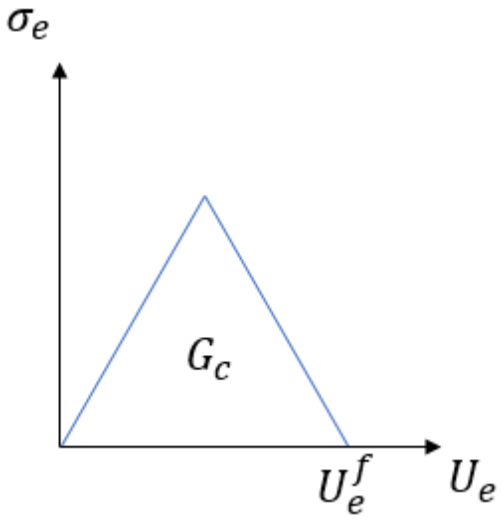

Figure 6.1: Fracture toughness.

Table 6.2: Fracture toughness values used for CDM damage modeling in ANSYS [21].

Fiber Tensile Damage Dissipation Energy, G_c^{ft} (kJ/m^2)	**Fiber Compressive Damage Dissipation Energy, G_c^{fc} (kJ/m^2)**
1000000	1000000
Matrix Tensile Damage Dissipation Energy, G_c^{mt} (kJ/m^2)	**Matrix Compressive Damage Dissipation Energy, G_c^{mc} (kJ/m^2)**
25	1000000

Because ANSYS can encounter difficulty in converging upon a solution, the CDM model incorporates damping coefficients, η, for each of the damage modes, which are used to retard the damage accumulation and overcome any such incident. Convergence difficulties arise due to the softening of the material. Control of the damage evolution rate is gained via adjustment of the damping coefficient; the lower the damping value, the more pronounced the damage accumulation. For a specific damage mode, the damage evolution is internally regularized by the following:

$$d'_{t+\Delta t} = \frac{\eta}{\eta + \Delta t} d'_t + \frac{\Delta t}{\eta + \Delta t} d_{t+\Delta t} \tag{6.9}$$

where Δt is the time step, $d'_{t+\Delta t}$ is the regularized damage variable at the current time, $d_{t+\Delta t}$ is the un-regularized damage variable at the current time and is used for material degradation, and d'_t is the regularized damage variable at the previous time (end of last substep). The viscous damping coefficients are $\eta_{ft}, \eta_{fc}, \eta_{mt}$, and η_{mc} for the fiber tensile, fiber compressive, matrix tensile, and matrix compressive damage modes, respectively. The viscous damping coefficient values used in the current study are given below in Table 6.3.

Table 6.3: Viscous damping coefficient values used for CDM damage modeling in ANSYS [21].

Fiber Tensile Damage Viscosity Damping Coefficient, η_{ft}	**Fiber Compressive Damage Viscosity Damping Coefficient, η_{fc}**
0.001	0.001
Matrix Tensile Damage Viscosity Damping Coefficient, η_{mt}	**Matrix Compressive Damage Viscosity Damping Coefficient, η_{mc}**
0.005	0.001

In order to create an adequate amount of damage, sufficient displacement must be imposed on the ANSYS model. The software will fail to converge upon a solution if too large of a displacement is applied in any given displacement step. However, this can be overcome by adding additional lines of code which allow for the adjustment of the convergence values (force and displacement) and their tolerance. But, it is recommended by most sources that the total applied displacement be split into manageable increments, such that it can be applied *gradually* and more *precisely*. Therefore, multiple displacement steps (referred to as load steps by ANSYS documentation) must be used in order to split the displacement up into increments which are small enough to ensure nonlinear solution convergence, and a more well-behaved model. Although a sufficient distributed force could be applied to the model in order to create damage, it was discovered that in some problems an applied displacement typically results in a more gradual failure, and thus it is easier to detect the exact initiation time of damage. Such conditions mimic an actual tension test which would be performed in a laboratory, and are therefore more appropriate. However, it must be noted that this is *not* a tension test. One simply endeavors to apply only enough displacement to initiate and create an adequate amount of damage; that which is detectable (qualifiable) and measurable (quantifiable). Substeps are used to discretize each displacement step, a number which must be specified by the user. Typically, the number of substeps is chosen to be large enough such that damage can be shown to evolve gradually. Further, a greater number of substeps facilitates the detection of the exact time and location of damage onset. The time rate of change of displacement in the x-direction is given by $\dot{U}_x = U_x/T$ (mm/sec), which in this study, is taken as $\dot{U}_x = 0.1$ mm/sec.

It is useful to know the equivalent applied remote force at which the lamina will begin to experience damage, and it can be easily obtained from some of the basic principles of mechanics. The parameters needed to ascertain the equivalent applied remote force are given below in Table 6.4.

Table 6.4: Quasi-isotropic laminate properties.

Length, L (mm)	**Laminate Modulus, E_x (MPa)**	**Area, A (mm^2)**
127	23857.1	116.129

To begin, the strain (in mm/mm) in the x-direction of the laminate is simply

$$\epsilon_x = \frac{\Delta L}{L_o} = \frac{U_x}{L_o} \tag{6.10}$$

where U_x is the applied external displacement in mm, and L_o is the initial length (in the x-direction) of the laminate in mm. One may take $L = L_o$ in Table 6.4. Using Hooke's law, the equivalent applied remote stress in MPa is then

$$\sigma_x = E_x \epsilon_x \tag{6.11}$$

where E_x is the laminate modulus in the longitudinal direction (parallel to the direction of the applied displacement). Finally, from the definition of stress, one can arrive at the equivalent applied remote force in Newtons as

$$F_x = A\sigma_x \tag{6.12}$$

where A is the cross-sectional area of the laminate in mm^2.

6.3 Single Square Hole Transverse to Applied Displacement

The damage initiation and evolution due to an incrementally applied displacement for a single square hole is investigated in this section. The hole geometry is the same as that of Chapter 4, Section 4.1.1, except that only a single centered square hole (Table 6.5) is considered here.

6.3.1 Geometry and Displacement

The geometry and displacement configuration for the single centered square hole is shown below in Fig. 6.2. The hole edge-to-laminate edge distance, d_e, the height of the square hole, h, and the corner radius, r_c, are all held constant at 15.875 mm, 6.35 mm, and 2 mm, respectively. The center of the square hole is located at the mid-length of the laminate, at $x = L/2$. A through D are the four corner points around the periphery of the square hole. One end of

the laminate is fixed at $x = L$, and an incremental in-plane horizontal displacement, U_x, is applied uniformly along the width of the free end of the laminate ($x = 0$) from $y = 0$ to $y = W$.

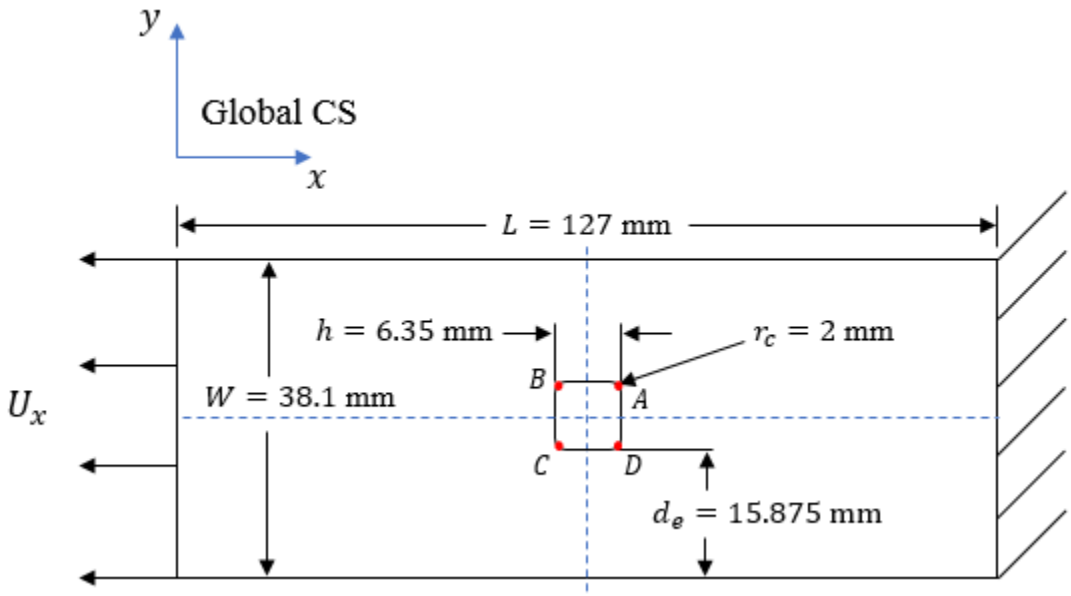

Figure 6.2: Geometry and displacement condition for the single centered square hole with rounded corners.

The case for the spacing of the single centered square hole with $r_c = 2$ mm is given below in Table 6.5.

Table 6.5: Damage analysis case for the single centered square hole with $r_c = 2$ mm.

Case	Hole Edge-to-Laminate Edge Distance, d_e (mm)	Square Hole Height, h (mm)
1	15.875 (Centered)	6.35

For the case of the single centered square hole, eight displacement steps are used, each containing 100 substeps. The number of substeps was chosen such that an adequate amount of damage evolution could be shown, without severely hindering the computation time. The damage displacement parameters, which include the number of displacement steps, the number of substeps, and the applied external in-plane displacement increment are given below in Table 6.6.

Table 6.6: CDM displacement parameters and ANSYS runtime for the single centered square hole with $r_c = 2$ mm.

Single Centered Square Hole					
Hole Edge-to-Laminate Edge Distance, d_e (mm)	**Displacement Step**	**# of Substeps**	**Applied Displacement, U_x (mm)**	**Displacement Step End Time, T (sec)**	**ANSYS Runtime**
15.875 (Centered)	1	100	0.10	1	2 hr 56 min 4 sec
	2	100	0.20	2	
	3	100	0.30	3	
	4	100	0.40	4	
	5	100	0.50	5	
	6	100	0.60	6	
	7	100	0.70	7	
	8	100	0.80	8	

6.3.2 Meshing

The mesh used for CDM analysis of the single centered square hole with rounded corners is the same that was used for the stress analysis in Chapter 4, Section 4.1.2, Fig. 4.2a. For convenience, it is shown below in Fig. 6.3.

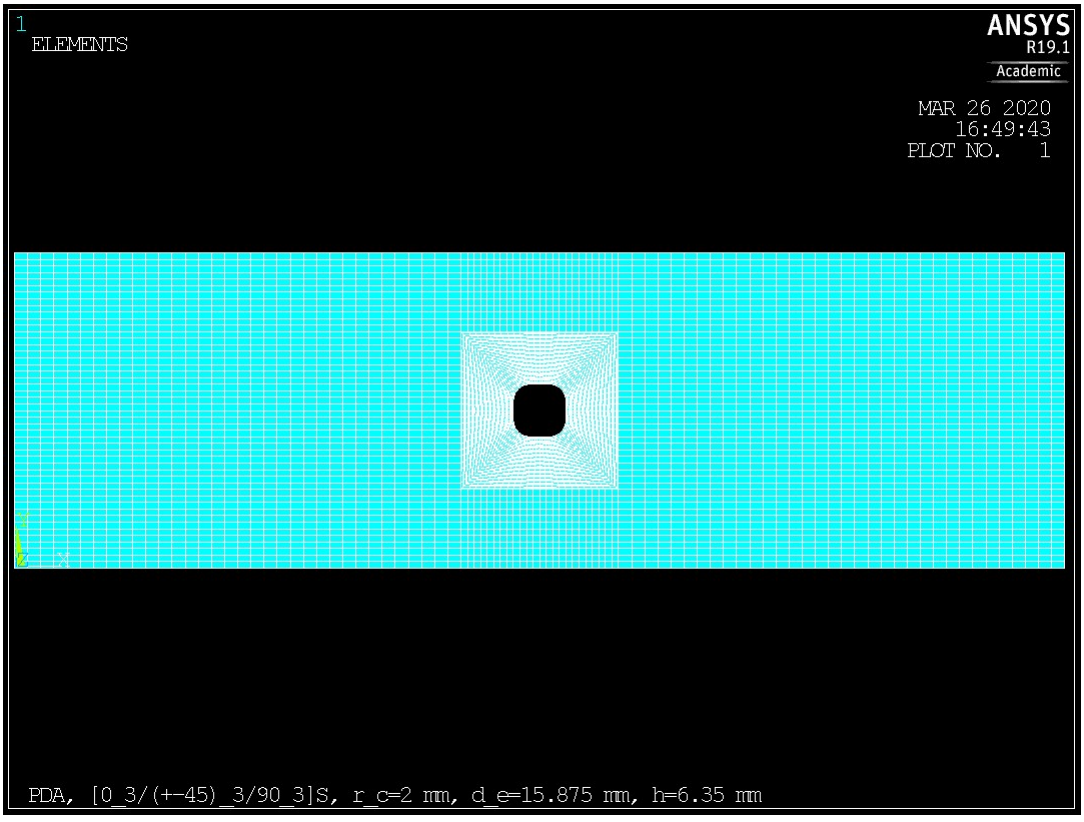

Figure 6.3: Mapped meshing for the single centered square hole with $r_c = 2$ mm.

6.3.3 Results

The failure indices which predict the initiation of damage in their respective laminas for the single centered square hole with $r_c = 2$ mm are given below in Table 6.7.

Table 6.7: Hashin failure indices for matrix and fiber failure in tension for the single centered square hole with $d_e = 15.875$ mm and $r_c = 2$ mm.

Single Centered Square Hole					
Displacement Step	**Substep**	**Failure Mode/Lamina**	**ANSYS Failure Index (Matrix Tension), I_{Fmt}**	**ANSYS Failure Index (Fiber Tension), I_{Fft}**	**Time, T (sec)**
3	47	Matrix Tension, MT/±45°	1.0008	N/A	2.47
3	79	Matrix Tension, MT/90°	1.0066	N/A	2.79
3	91	Fiber Tension, FT/±45°	N/A	1.0034	2.91
5	2	Matrix Tension, MT/0°	1.0022	N/A	4.02
5	4	Fiber Tension, FT/0°	N/A	1.0032	4.04

The maximum displacement applied to the laminate is $U_x = 0.80$ mm. Correspondingly, the maximum displacement of each lamina is $U_x = 0.80$ mm. Once the Hashin failure index reaches unity, damage is predicted by theory to occur, and the appearance of damage is expected in the following substeps. It should be noted that the appearance of the damage was not seen immediately following the failure index reaching unity, but some substeps thereafter. This difference is a small fraction of the elapsed time for the first two matrix failure modes, but somewhat larger for the 0° lamina matrix tension and fiber tension modes. This is thought to be due to the failure index being a prediction, or indicator that damage was likely to occur once the criterion was satisfied. Also, this can be attributed to the large amount of substeps used. Had a fewer amount of substeps been used, the damage would appear immediately after the failure index reached unity. One should note that fiber tension damage is predicted to occur in the ±45° lamina shortly after matrix tension damage. This agrees with intuition, as the fibers would be forced to carry more load upon any damage to the matrix. Similarly, this behavior is also seen in the 0° lamina. However, the 0° lamina fibers fail immediately after the matrix, which is due to the fact that the fibers are parallel to the direction applied displacement, and therefore carry most of the resultant stress.

The matrix tensile failure index for the 45° lamina can be seen below in Fig. 6.4. In order to illustrate the connection between the locations of stress concentration and the failure index

reaching unity, a comparison between the σ_{22} stress field and I_{Fmt} is made in Fig. 6.5. It can be seen in Fig. 6.5b that the failure index reaches a value of $I_{Fmt} = 1.00077$ at the periphery of the rounded corners, specifically at the locations of stress concentration depicted in Fig. 6.5a. This is consistent with intuition, as one expects damage to initiate at the locations of the highest stress.

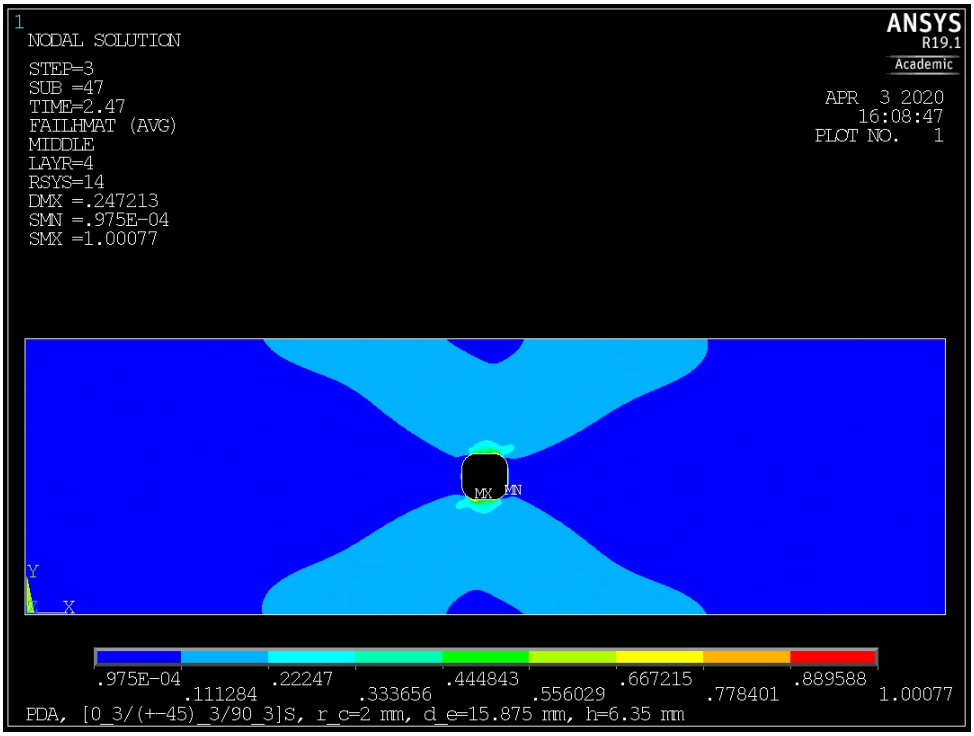

Figure 6.4: Matrix tensile failure index, $I_{Fmt} = 1.00077$ for the 45° lamina in the single centered square hole with $r_c = 2$ mm laminate.

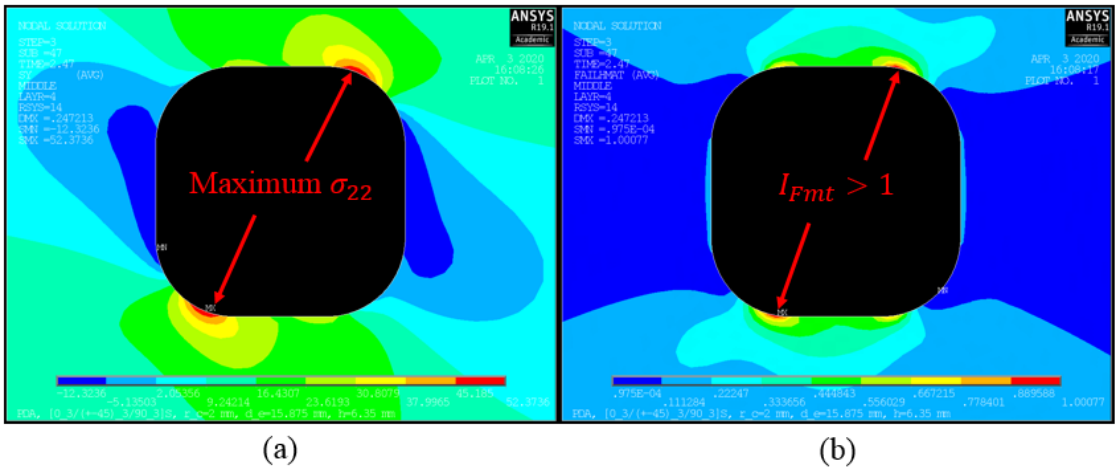

Figure 6.5: Single centered square hole with $r_c = 2$ mm: (a) σ_{22} stress field at $I_{Fmt} = 1.00077$, (b) enlarged view of the matrix tensile failure index, $I_{Fmt} = 1.00077$ for the 45° lamina.

Damage begins first at $U_x = 0.260$ mm in the ±45° laminas, and is due to matrix tensile failure. The amount of applied external tensile force required to initiate this damage is 5671.9 N. Fiber tensile failure modes do not occur until $U_x = 0.493$ mm, owing to the two order of magnitude difference in the fiber tensile strength, as compared to the matrix tensile strength seen in Table 6.1. Fiber tensile damage initiation in the 0° laminas occurs at $U_x = 0.493$ mm and in the ±45° laminas at $U_x = 0.609$ mm. The corresponding loads are 10754.8 N and 13285.3 N. The displacement step sequence for the damage modes is given below in Table 6.8.

Table 6.8: Displacement step sequence of damage initiation for the single centered square hole with $d_e = 15.875$ mm and $r_c = 2$ mm.

Single Centered Square Hole							
Displacement Step	**Substep**	**Failure Mode/Lamina**	**Applied Displacement, U_x (mm)**	**Strain, ϵ_x (mm/mm)**	**Equivalent Applied Remote Stress, σ_x (MPa)**	**Equivalent Applied Remote Force, F_x (N)**	**Time, T (sec)**
3	60	Matrix Tension, MT/±45°	0.260	0.00205	48.841	5671.9	2.60
3	91	Matrix Tension, MT/90°	0.291	0.00229	54.665	6348.1	2.91
5	38	Matrix Tension, MT/0°	0.438	0.00345	82.279	9554.9	4.38
5	93	Fiber Tension, FT/0°	0.493	0.00388	92.611	10754.8	4.93
7	8	Fiber Tension, FT/±45°	0.609	0.00480	114.401	13285.3	6.08

It can be seen in Table 6.8 that damage initiates first in the ±45°, 90°, and 0° laminas, and is due to matrix tensile failure. Again, this is because the matrix tensile strength and xy shear failure strength values are much lower than the fiber tensile strength, and thus it is much easier to meet the failure criterion, as seen in Eqn. 6.3. The equivalent applied remote force, F_x, versus the displacement, U_x, data from Table 6.8 is shown below in Fig. 6.6.

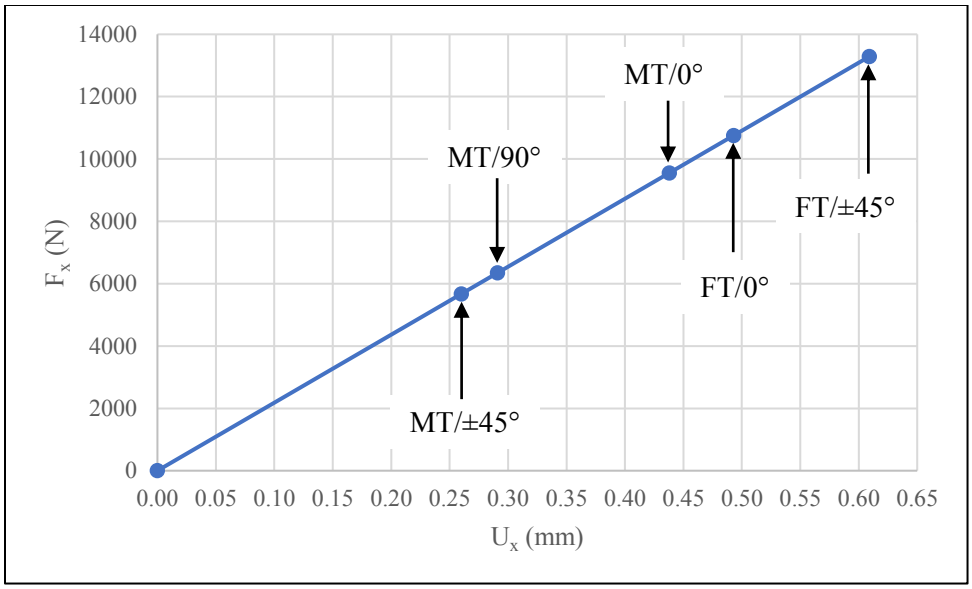

Figure 6.6: Equivalent applied remote force, F_x, versus applied displacement, U_x, for the single centered square hole with $r_c = 2$ mm.

To further validate the connection between stress concentration location and its effect upon damage initiation location, the σ_{22} stress field and the matrix tension damage variable, d_{mt}, at $T = 4.38$ seconds for the 0° lamina are shown below in Fig. 6.7a and 6.7b, respectively. Similarly, the σ_{11} stress field and the fiber tension damage variable, d_{ft}, at $T = 6.08$ seconds for the 0° lamina are also shown below in Fig. 6.7c and 6.7d, respectively. It can be seen that damage initiates in the general location of stress concentration, which is at corners *A* through *D* of the square hole periphery.

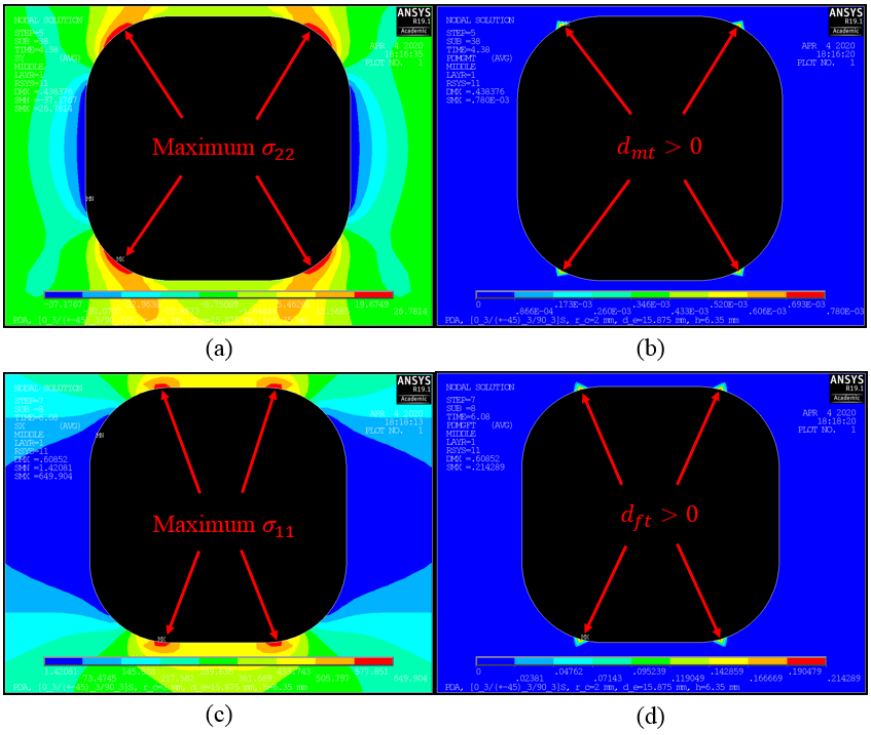

Figure 6.7: 0° lamina in the single centered square hole with $r_c = 2$ mm laminate: (a) σ_{22} stress field depicting locations of stress concentration at $T = 4.38$ sec, (b) matrix tension damage variable, d_{mt}, depicting location of damage initiation at $T = 4.38$ sec, (c) σ_{11} stress field depicting locations of stress concentration at $T = 6.08$ sec, (d) fiber tension damage variable, d_{ft}, depicting location of damage initiation at $T = 6.08$ sec.

The magnitude of the fiber tension and matrix tension damage variables for the different laminas at the time of damage onset (see Table 6.8) and maximum displacement ($T = 8$ sec, $U_x = 0.80$ mm) are given below in Table 6.9.

Table 6.9: Matrix damage variable at damage onset and maximum displacement for the single centered square hole with $r_c = 2$ mm.

Single Centered Square Hole				
Failure Mode/Lamina	**ANSYS Matrix Damage Variable, $d_{mt,onset}$**	**ANSYS Fiber Damage Variable, $d_{ft,onset}$**	**ANSYS Maximum Matrix Damage Variable, $d_{mt,max}$**	**ANSYS Maximum Fiber Damage Variable, $d_{ft,max}$**
Matrix Tension, MT/±45°	0.00016	N/A	0.7898	N/A
Matrix Tension, MT/90°	0.00042	N/A	0.7536	N/A
Matrix Tension, MT/0°	0.00078	N/A	0.5697	N/A
Fiber Tension, FT/0°	N/A	0.00093	N/A	0.5328
Fiber Tension, FT/±45°	N/A	0.00078	N/A	0.2049

The first failure mode and corresponding damage evolution for the composite laminas can be seen below in Figs. 6.8 and 6.9.

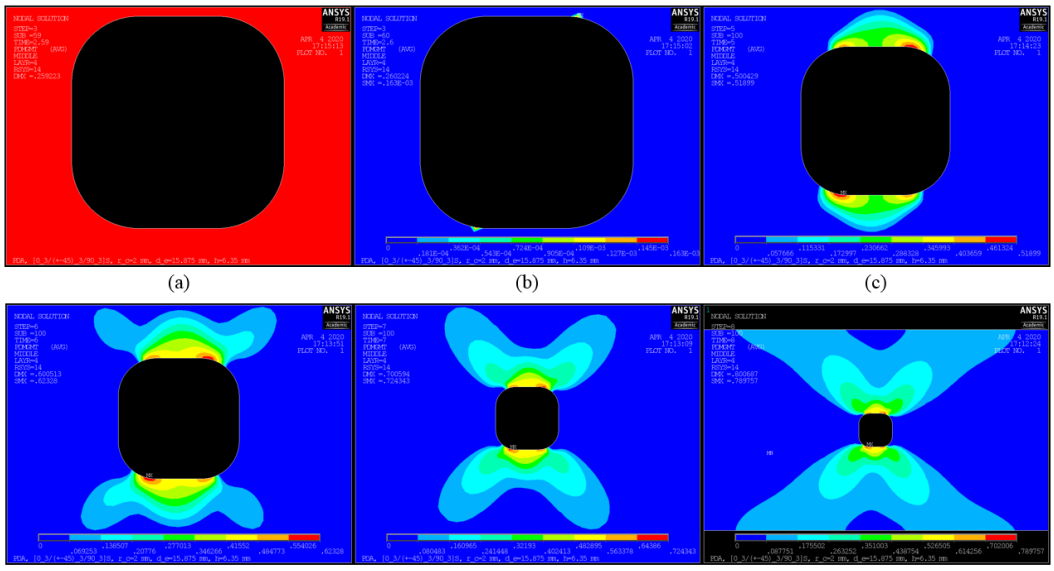

Figure 6.8: Damage evolution of matrix tensile damage variable, d_{mt}, in 45° lamina for $d_e = 15.875$ mm: (a) before damage, $U_x = 0.259$ mm, (b) damage onset, $U_x = 0.260$ mm, (c) damage evolution, $U_x = 0.500$ mm, (d) damage evolution, $U_x = 0.601$ mm, (e) damage evolution, $U_x = 0.701$ mm, (f) maximum damage, $U_x = 0.801$ mm.

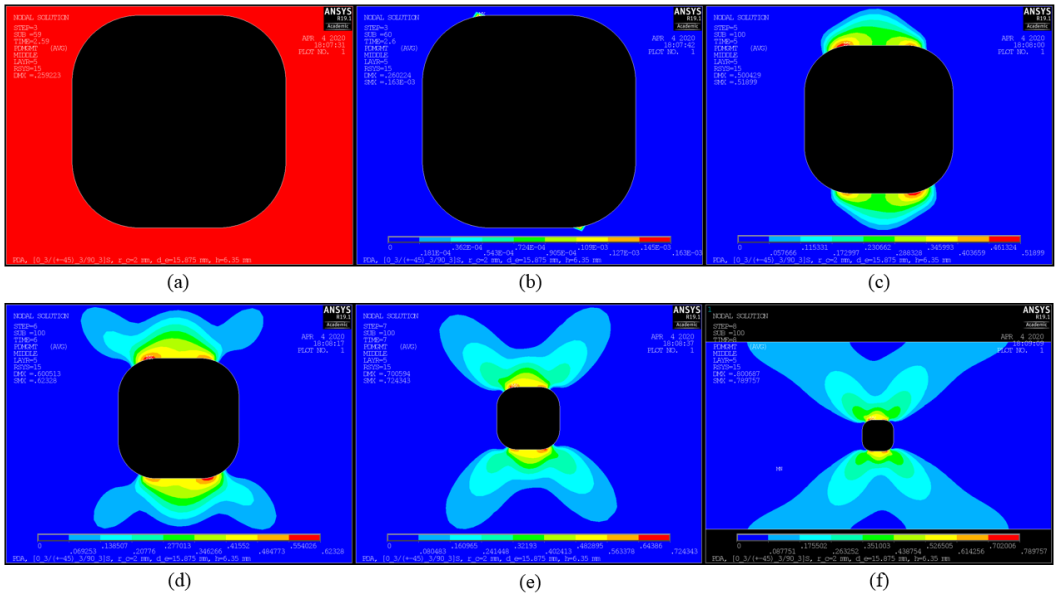

Figure 6.9: Damage evolution of matrix tensile damage variable, d_{mt}, in -45° lamina for $d_e = 15.875$ mm: (a) before damage, $U_x = 0.259$ mm, (b) damage onset, $U_x = 0.260$ mm, (c) damage evolution, $U_x = 0.500$ mm, (d) damage evolution, $U_x = 0.601$ mm, (e) damage evolution, $U_x = 0.701$ mm, (f) maximum damage, $U_x = 0.801$ mm.

6.4 Single Circular Hole Transverse to Applied Displacement

The damage initiation and evolution due to an incrementally applied displacement for a single circular hole is investigated in this section. The hole geometry is the same as that of Chapter 4, Section 4.2.1, except that only a single centered circular hole (Table 6.10) is considered here.

6.4.1 Geometry and Displacement

The geometry and displacement configuration for the single centered circular hole is shown below in Fig. 6.10. The diameter of the hole, d, and the hole edge-to-laminate edge distance, d_e, are held constant at 6.35 mm and 15.875 mm, respectively. This geometry is equivalent to a square hole with rounded corners, where $r_c = 3.175$ mm. The center of the circular hole is located at the mid-length of the laminate, at $x = L/2$. A and B are points of interest on the hole periphery. One end of the laminate is fixed at $x = L$, and an incremental in-plane horizontal displacement, U_x, is applied uniformly along the width of the free end of the laminate ($x = 0$) from $y = 0$ to $y = W$.

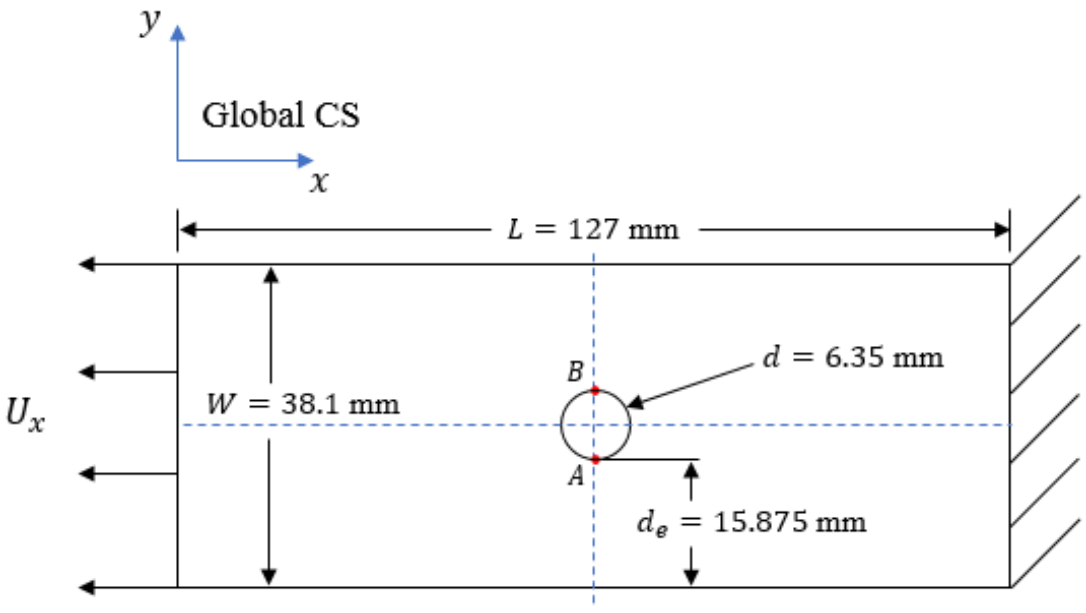

Figure 6.10: Geometry and displacement condition for the single centered circular hole.

The case for the spacing of the single centered circular hole is given below in Table 6.10.

Table 6.10: Damage analysis case for the single centered circular hole.

Case	Hole Edge-to-Laminate Edge Distance, d_e (mm)	Hole Diameter, d (mm)
1	15.875 (Centered)	6.35

For the case of the single centered circular hole, eight displacement steps are used, each containing 100 substeps. The number of substeps was chosen such that an adequate amount of damage evolution could be shown, without severely hindering the computation time. The damage displacement parameters, which include the number of displacement steps, the number of substeps, and the applied external in-plane displacement increment are given below in Table 6.11.

Table 6.11: CDM displacement parameters and ANSYS runtime for the single centered circular hole with $d = 6.35$ mm.

Single Centered Circular Hole					
Hole Edge-to-Laminate Edge Distance, d_e (mm)	Displacement Step	# of Substeps	Applied Displacement, U_x (mm)	Displacement Step End Time, T (sec)	ANSYS Runtime
15.875 (Centered)	1	100	0.10	1	3 hr 29 min 6 sec
	2	100	0.20	2	
	3	100	0.30	3	
	4	100	0.40	4	
	5	100	0.50	5	
	6	100	0.60	6	
	7	100	0.70	7	
	8	100	0.80	8	

6.4.2 Meshing

The mesh used for CDM analysis of the single centered circular hole is the same that was used for the stress analysis in Chapter 4, Section 4.2.2, Fig. 4.12a. For convenience, it is shown below in Fig. 6.11.

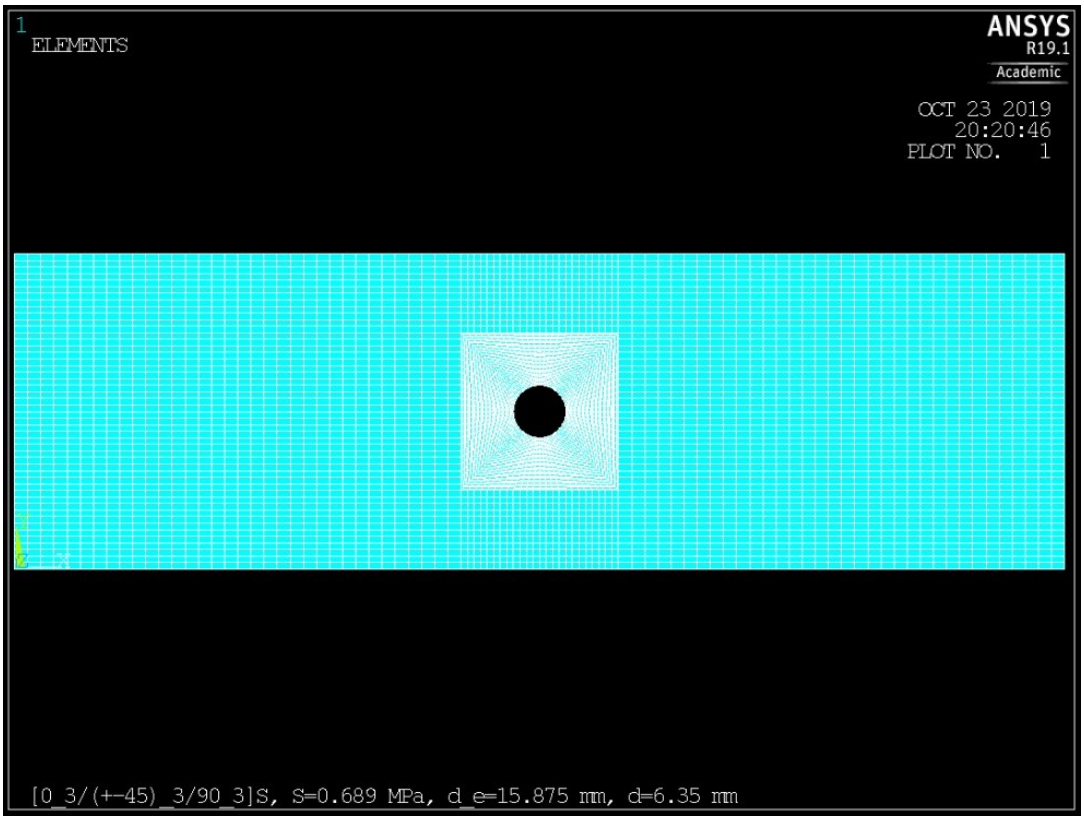

Figure 6.11: Mapped meshing for the single centered circular hole with $d = 6.35$ mm.

6.4.3 Results

The failure indices which predict the initiation of damage in their respective laminas for the single centered circular hole are given below in Table 6.12. Remark is due here, in that the damage initiation sequence is slightly different than for the single centered square hole with $r_c = 2$ mm in Section 6.3.3. Here damage is predicted to initiate due to fiber tension failure in the 0° lamina *before* the matrix tension failure mode. This is attributed to the higher SCF found in the 0° lamina of the laminate which contains the single centered circular hole. From Table 4.10, for a single centered square hole with $r_c = 2$ mm and a single centered circular hole ($r_c = 3.175$ mm), $K_{t,\theta=0^\circ} = 2.882$ and 3.102, respectively. Therefore, since the fibers in the 0° lamina carry the majority of the stresses in the laminate, it is reasonable to expect a higher SCF to dictate an earlier damage initiation time. With the exception of the 0° lamina failure modes, the damage initiates in the same failure mode/lamina sequence as in Section 6.3.3, albeit with different displacement step and substep values.

Table 6.12: Hashin failure indices for matrix and fiber failure in tension for the single centered circular hole with $d_e = 15.875$ mm and $d = 6.35$ mm.

Single Centered Circular Hole					
Displacement Step	**Substep**	**Failure Mode/Lamina**	**ANSYS Failure Index (Matrix Tension), I_{Fmt}**	**ANSYS Failure Index (Fiber Tension), I_{Fft}**	**Time, T (sec)**
3	40	Matrix Tension, MT/±45°	1.0013	N/A	2.40
3	80	Matrix Tension, MT/90°	1.0031	N/A	2.80
4	77	Fiber Tension, FT/±45°	N/A	1.0036	3.77
5	53	Fiber Tension, FT/0°	N/A	1.0044	4.53
5	56	Matrix Tension, MT/0°	1.0025	N/A	4.56

The matrix tensile failure index for the 45° lamina can be seen below in Fig. 6.12. As in Section 6.3.3, a comparison between the σ_{22} stress field and I_{Fmt} is made in Fig. 6.13. It can be seen in Fig. 6.13b that the failure index reaches a value of $I_{Fmt} = 1.0013$ at the periphery of the hole, near the locations of stress concentration depicted in Fig. 6.13a. As with the single centered square hole, damage initiates in close proximity to the locations of the highest stress.

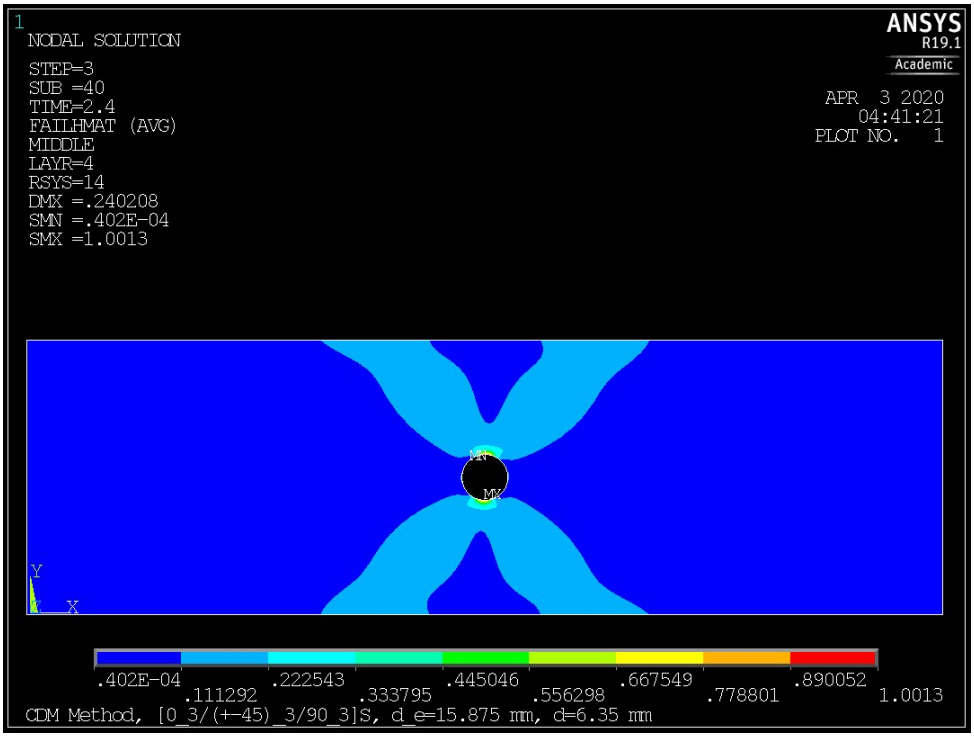

Figure 6.12: Matrix tensile failure index, $I_{Fmt} = 1.0013$ for the 45° lamina in the single centered circular hole with $d = 6.35$ mm laminate.

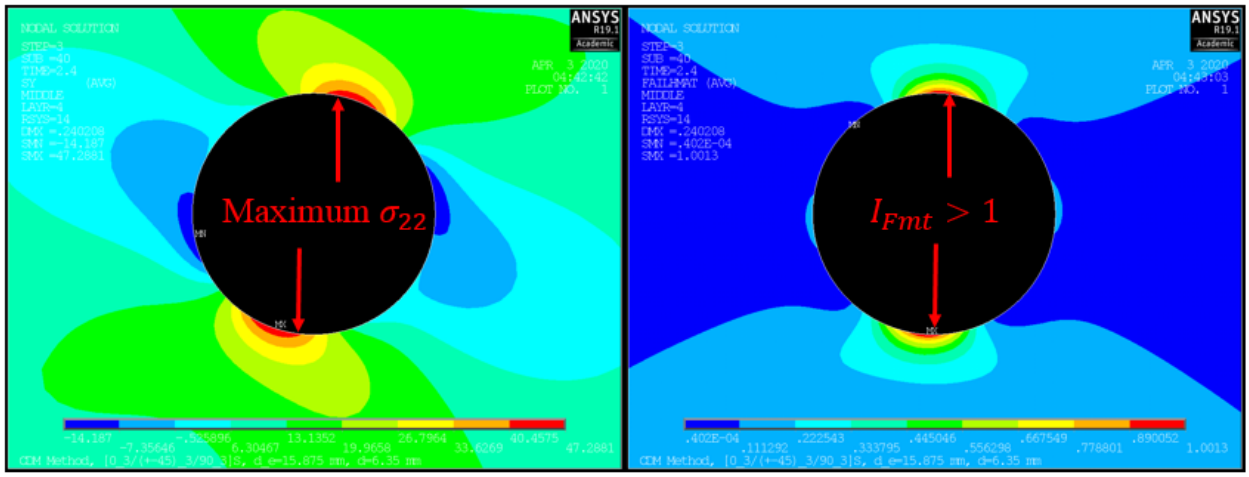

Figure 6.13: Single centered circular hole: (a) σ_{22} stress field at $I_{Fmt} = 1.0013$, (b) enlarged view of the matrix tensile failure index, $I_{Fmt} = 1.0013$ for the 45° lamina.

It can be seen below in Table 6.13 that damage occurs in the same failure mode/lamina sequence as in Section 6.3.3, but with different displacement step and substep values.

Table 6.13: Displacement step sequence of damage development for the single centered circular hole with $d_e = 15.875$ mm and $d = 6.35$ mm.

Single Centered Circular Hole							
Displacement Step	**Substep**	**Failure Mode/Lamina**	**Applied Displacement, U_x (mm)**	**Strain, ϵ_x (mm/mm)**	**Equivalent Applied Remote Stress, σ_x (MPa)**	**Equivalent Applied Remote Force, F_x (N)**	**Time, T (sec)**
3	48	Matrix Tension, MT/±45°	0.248	0.00195	46.587	5410.1	2.48
3	86	Matrix Tension, MT/90°	0.286	0.00225	53.725	6239.1	2.86
5	82	Matrix Tension, MT/0°	0.482	0.00380	90.544	10514.8	4.82
6	28	Fiber Tension, FT/0°	0.528	0.00416	99.185	11518.3	5.28
7	68	Fiber Tension, FT/±45°	0.669	0.00527	125.672	14594.2	6.68

The equivalent applied remote force, F_x, versus the displacement, U_x, data from Table 6.13 is shown below in Fig. 6.14.

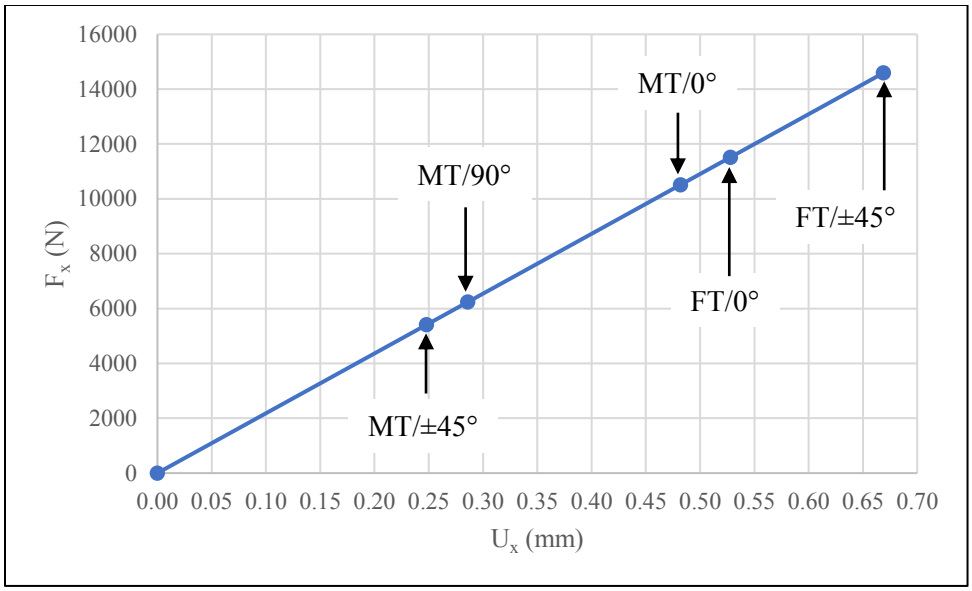

Figure 6.14: Equivalent applied remote force, F_x, versus applied displacement, U_x, for the single centered circular hole with $d = 6.35$ mm.

To further validate the connection between stress concentration location and its effect upon damage initiation location, the σ_{22} stress field and the matrix tension damage variable, d_{mt}, at $T = 2.86$ seconds for the 0° lamina are shown below in Fig. 6.15a and 6.15b, respectively. Similarly, the σ_{11} stress field and the fiber tension damage variable, d_{ft}, at $T = 5.28$ seconds for the 0° lamina are also shown below in Fig. 6.15c and 6.15d, respectively. It can be seen that damage initiates in the general location of stress concentration, which is at points A and B on the circular hole periphery.

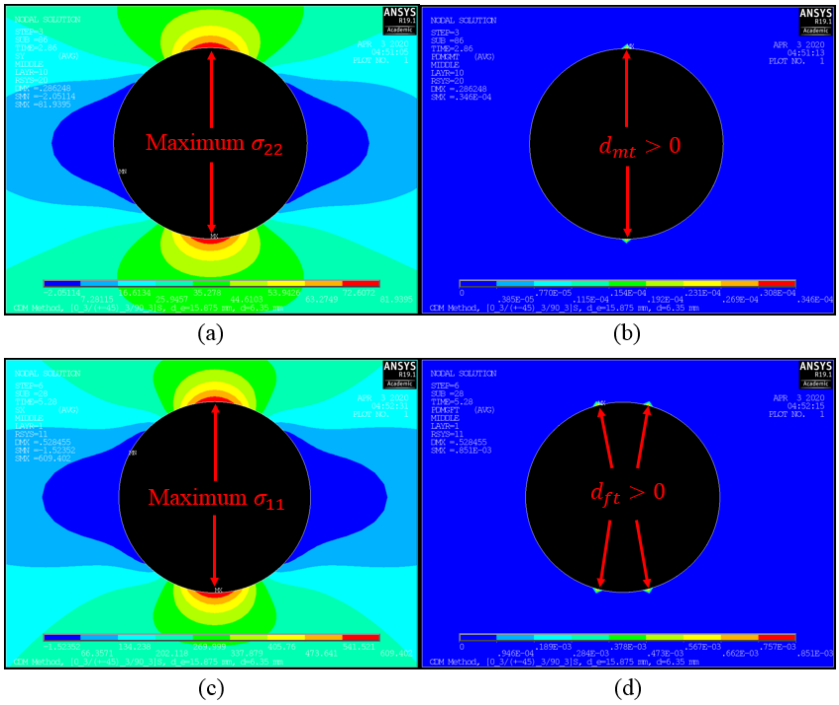

Figure 6.15: Single centered circular hole with $r_c = 2$ mm: (a) σ_{22} stress field depicting locations of stress concentration at $T = 2.86$ sec in the 45° lamina, (b) matrix tension damage variable, d_{mt}, depicting location of damage initiation at $T = 2.86$ sec in the 45° lamina, (c) σ_{11} stress field depicting locations of stress concentration at $T = 5.28$ sec in the 0° lamina, (d) fiber tension damage variable, d_{ft}, depicting location of damage initiation at $T = 5.28$ sec in the 0° lamina.

The magnitude of the fiber tension and matrix tension damage variables for the different laminas at the time of damage onset (see Table 6.13) and maximum displacement ($T = 8$ sec, $U_x = 0.80$ mm) are given below in Table 6.14.

Table 6.14: Matrix damage variable at damage onset and maximum displacement for the single centered circular hole with $d = 6.35$ mm.

Single Centered Circular Hole				
Failure Mode/Lamina	**ANSYS Matrix Damage Variable, $d_{mt,onset}$**	**ANSYS Fiber Damage Variable, $d_{ft,onset}$**	**ANSYS Maximum Matrix Damage Variable, $d_{mt,max}$**	**ANSYS Maximum Fiber Damage Variable, $d_{ft,max}$**
Matrix Tension, MT/±45°	0.00187	N/A	0.78321	N/A
Matrix Tension, MT/90°	0.00003	N/A	0.74726	N/A
Matrix Tension, MT/0°	0.00027	N/A	0.51409	N/A
Fiber Tension, FT/0°	N/A	0.00085	N/A	0.50898
Fiber Tension, FT/±45°	N/A	0.00020	N/A	0.19791

The first failure mode and corresponding damage evolution for the composite laminas can be seen below in Figs. 6.16 and 6.17.

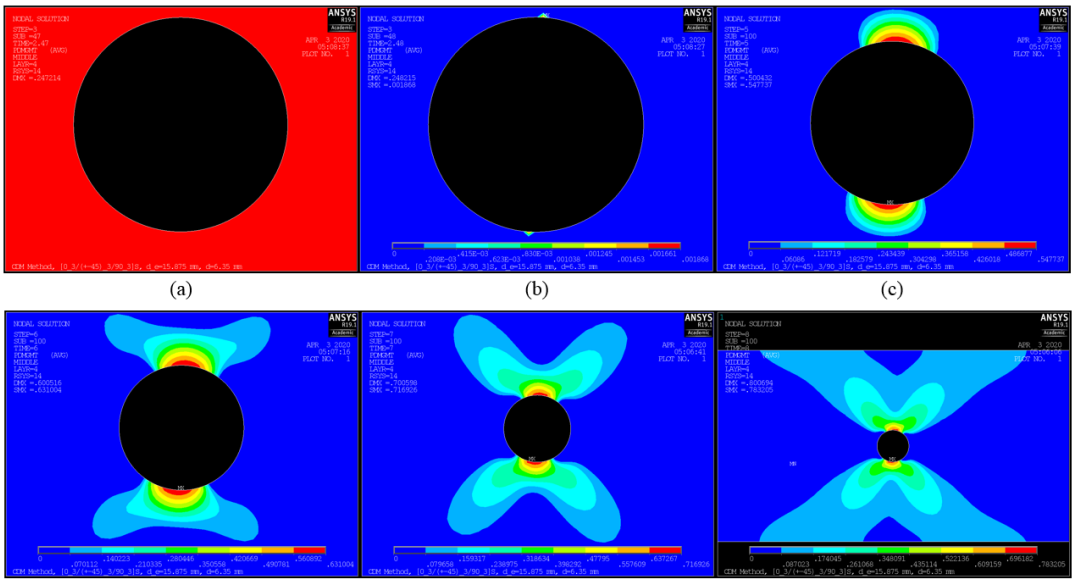

(a) (b) (c)

(d) (e) (f)

Figure 6.16: Damage evolution of matrix tensile failure mode in 45° lamina for $d_e = 15.875$ mm: (a) before damage, $U_x = 0.247$ mm, (b) damage onset, $U_x = 0.248$ mm, (c) damage evolution, $U_x = 0.500$ mm, (d) damage evolution, $U_x = 0.601$ mm, (e) damage evolution, $U_x = 0.701$ mm, (f) maximum damage, $U_x = 0.801$ mm.

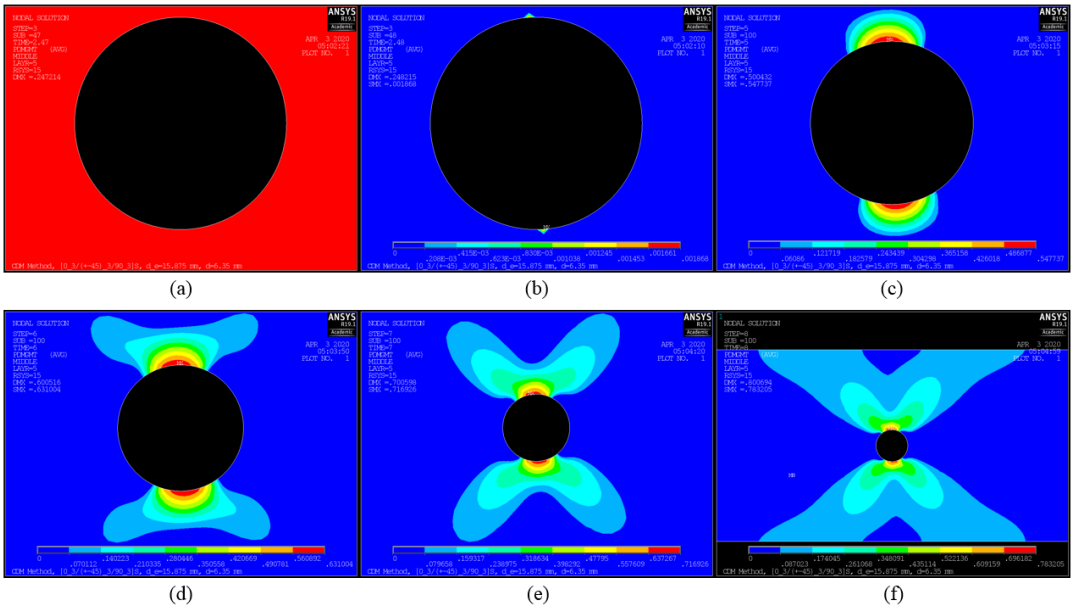

(a) (b) (c)

(d) (e) (f)

Figure 6.17: Damage evolution of matrix tensile failure mode in -45° lamina for $d_e = 15.875$ mm: (a) before damage, $U_x = 0.247$ mm, (b) damage onset, $U_x = 0.248$ mm, (c) damage evolution, $U_x = 0.500$ mm, (d) damage evolution, $U_x = 0.601$ mm, (e) damage evolution, $U_x = 0.701$ mm, (f) maximum damage, $U_x = 0.801$ mm.

6.5 Two Asymmetric Square Holes Transverse to Applied Displacement

The damage initiation and evolution due to an incrementally applied displacement for two asymmetric square holes with rounded corners is investigated in this section. The hole geometries and spacings are the same as that of Chapter 5, Section 5.1.1, except that only a corner radius of $r_c = 2$ mm is considered here.

6.5.1 Geometry and Displacement

The geometry and displacement configuration for the two asymmetric square holes is shown below in Fig. 6.18. The hole edge-to-edge distance, d_h, is varied, while the Hole 1 edge-to-laminate edge distance, d_e, and the corner radius for both holes, r_c, are held constant at 1.984 mm and 2 mm, respectively. For all values of d_h, the centers of the holes are located at the mid-length of the laminate, at $x = L/2$. A through H are points of interest on the corners of the hole peripheries. One end of the laminate is fixed at $x = L$, and an incremental in-plane horizontal displacement, U_x, is applied uniformly along the width of the free end of the laminate ($x = 0$) from $y = 0$ to $y = W$.

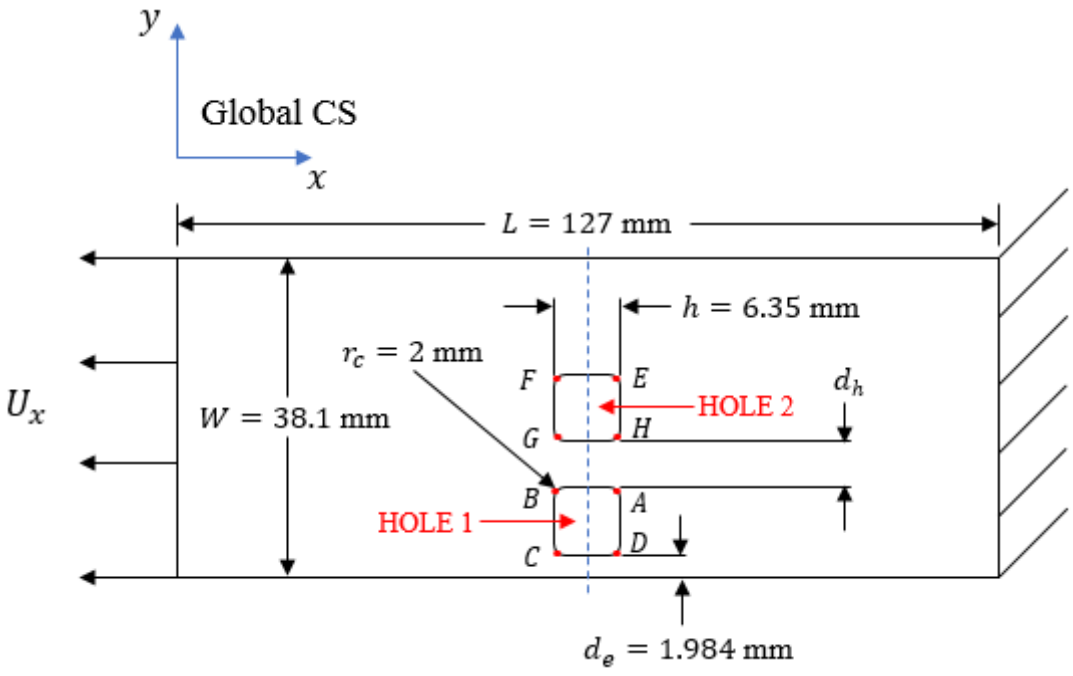

Figure 6.18: Geometry and displacement condition for two asymmetric square holes with rounded corners.

The various cases for the spacing of the two asymmetric square holes with rounded corners are given below in Table 6.15.

Table 6.15: Damage analysis cases for two asymmetric square holes with $r_c = 2$ mm.

Case	Hole Edge-to-Laminate Edge Distance, d_e (mm)	Hole Edge-to-Edge Distance, d_h (mm)	Square Hole Height, h (mm)
1	1.984	7.541 (Hole 2 Centered)	6.35
2		3.770	
3		1.885	

For all cases of the two asymmetric square holes, four displacement steps are used, each containing 25 substeps. The number of substeps was chosen such that an adequate amount of damage evolution could be shown, without severely hindering the computation time. The damage displacement parameters, which include the number of displacement steps, the number of substeps, and the applied external in-plane displacement increment are given below in Table 6.16.

Table 6.16: CDM displacement parameters and ANSYS runtime for two asymmetric square holes with $r_c = 2$ mm.

Two Asymmetric Square Holes					
Hole Edge-to-Edge Distance, d_h (mm)	Displacement Step	# of Substeps	Applied Displacement, U_x (mm)	Displacement Step End Time, T (sec)	ANSYS Runtime
7.541 (Hole 2 Centered)	1	25	0.10	1	6 hr 42 min 36 sec
	2	25	0.20	2	
	3	25	0.30	3	
	4	25	0.40	4	
3.770	1	25	0.10	1	4 hr 58 min 12 sec
	2	25	0.20	2	
	3	25	0.30	3	
	4	25	0.40	4	
1.885	1	25	0.10	1	5 hr 53 min 32 sec
	2	25	0.20	2	
	3	25	0.30	3	
	4	25	0.40	4	

6.5.2 Meshing

The mesh used for CDM analysis is the same that was used for the stress analysis in Chapter 5, Section 5.1.2, Fig. 5.2. It is shown again for convenience below in Fig. 6.19.

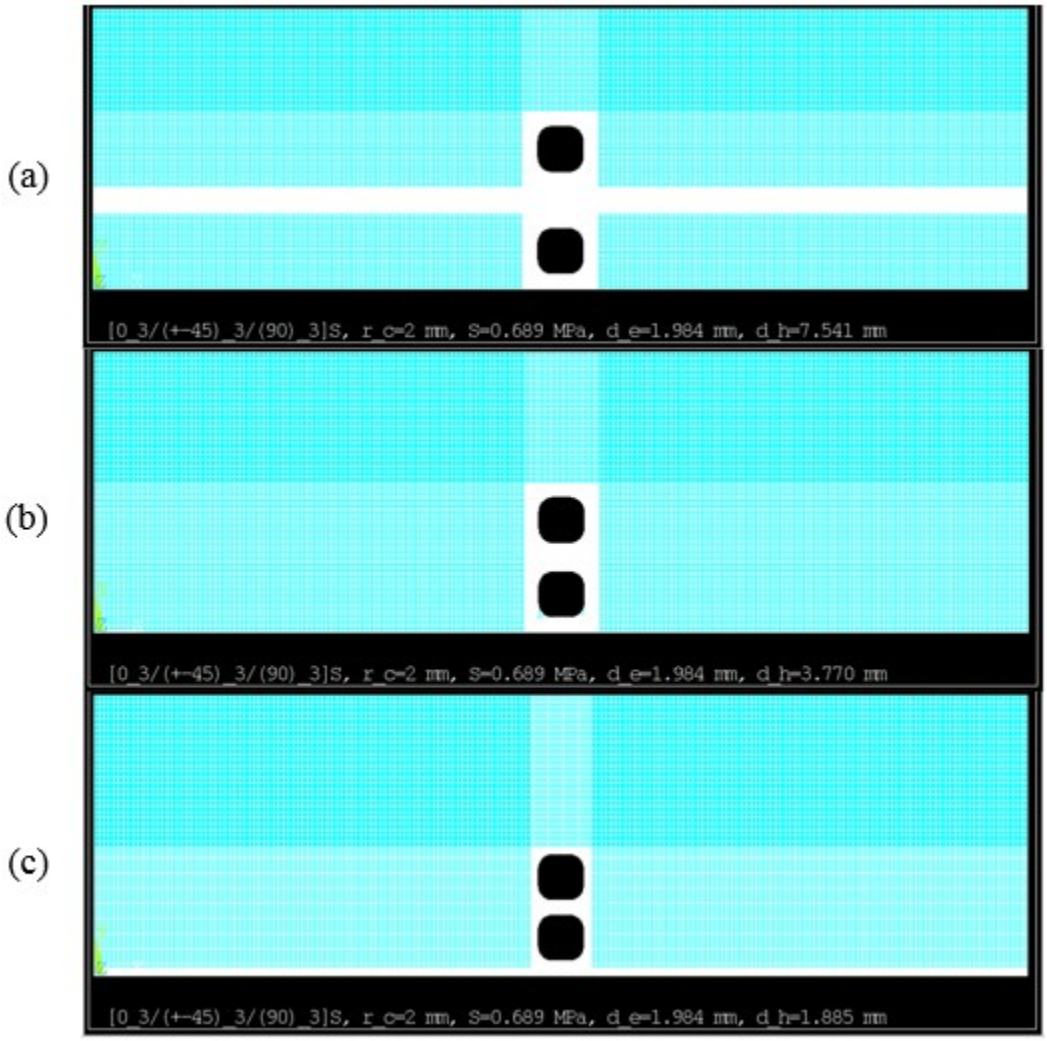

Figure 6.19: Mapped meshing for two asymmetric square holes with $r_c = 2$ mm and $d_e = 1.984$ mm: (a) $d_h = 7.541$ mm (Hole 2 centered), (b) $d_h = 3.770$ mm, (c) $d_h = 1.885$ mm.

6.5.3 Results

The failure indices which predict the initiation of damage in their respective laminas for the two asymmetric square holes with $r_c = 2$ mm are given below in Table 6.17. It can be seen that for all matrix failure modes, the damage initiation time decreases with decreasing hole edge-to-edge distance. This is expected, as the "hole-to-hole proximity effect" increases the maximum

stresses found at the hole peripheries, thereby initiating damage sooner. Only matrix failure modes are considered here.

Table 6.17: Hashin failure indices for matrix failure in tension for two asymmetric square holes with $r_c = 2$ mm.

Two Asymmetric Square Holes					
Hole Edge-to-Edge Distance, d_h (mm)	**Displacement Step**	**Substep**	**Failure Mode/Lamina**	**ANSYS Failure Index (Matrix Tension), I_{Fmt}**	**Time, T (sec)**
7.541 (Hole 2 Centered)	2	23	Matrix Tension, MT/±45°	1.0265	1.92
	3	6	Matrix Tension, MT/90°	1.0270	2.24
	4	4	Matrix Tension, MT/0°	1.0227	3.16
3.770	2	20	Matrix Tension, MT/±45°	1.0100	1.80
	3	3	Matrix Tension, MT/90°	1.0323	2.12
	3	21	Matrix Tension, MT/0°	1.0052	2.84
1.885	2	17	Matrix Tension, MT/±45°	1.0176	1.68
	2	22	Matrix Tension, MT/90°	1.0081	1.88
	3	18	Matrix Tension, MT/0°	1.0171	2.72

The matrix failure indices for the 0°, 45°, and 90° laminas for the various values of d_h can be seen below in Fig. 6.20. It can be seen that for decreasing hole edge-to-edge distance, the failure index fields intensify between the two square holes. As in Section 6.4.3, a comparison between the σ_{22} stress field and I_{Fmt} is made in Fig. 6.21. One finds in Fig. 6.21b that when $d_h = 1.885$ mm, the failure index for the 45° lamina reaches a value of $I_{Fmt} = 1.0176$ at the periphery of the hole, specifically at the locations of stress concentration as seen in Fig. 6.21a. Again, this is consistent with intuition, as one expects damage to initiate at the locations of the highest stress.

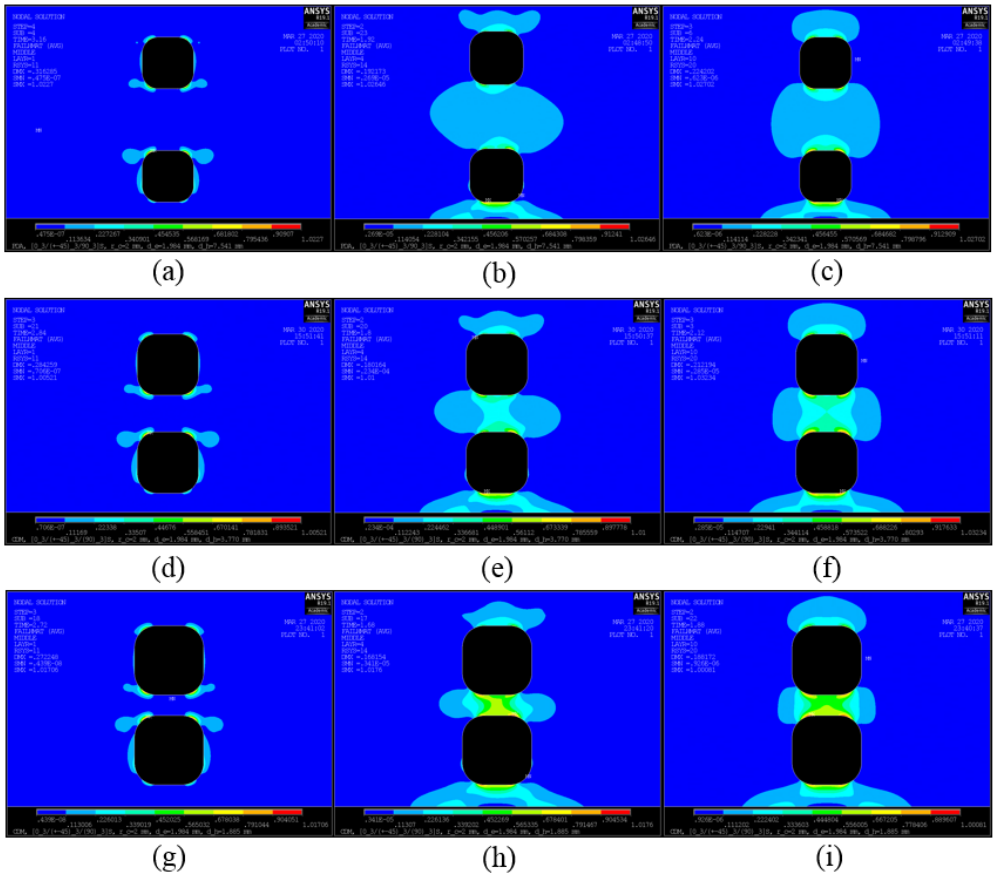

Figure 6.20: Matrix failure indices, I_{Fmt}, for two asymmetric square holes with $r_c = 2$ mm: (a) 0° lamina, $d_h = 7.541$ mm (Hole 2 centered), (b) 45° lamina, $d_h = 7.541$ mm (Hole 2 centered), (c) 90° lamina, $d_h = 7.541$ mm (Hole 2 centered), (d) 0° lamina, $d_h = 3.770$ mm, (e) 45° lamina, $d_h = 3.770$ mm, (f) 90° lamina, $d_h = 3.770$ mm, (g) 0° lamina, $d_h = 1.885$ mm, (h) 45° lamina, $d_h = 1.885$ mm, (i) 90° lamina, $d_h = 1.885$ mm.

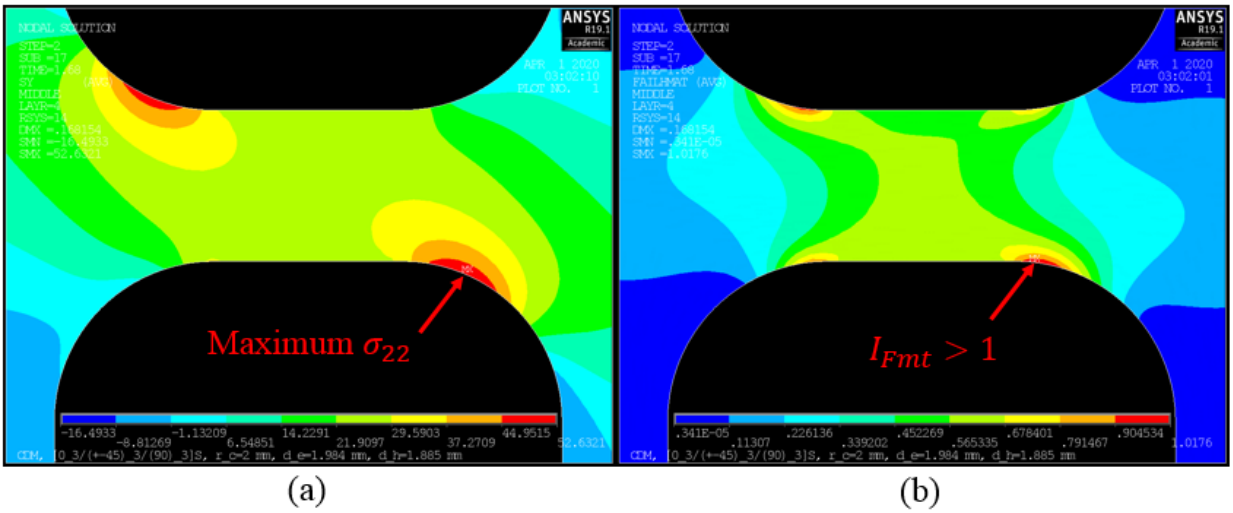

Figure 6.21: Location of maximum σ_{22} stress and matrix tension failure index, I_{Fmt}, in the 45° lamina for two asymmetric square holes with $d_h = 1.885$ mm and $r_c = 2$ mm: (a) σ_{22} stress field at $I_{Fmt} = 1.0176$, (b) enlarged view of the matrix tensile failure index, $I_{Fmt} = 1.0176$.

The damage initiation analysis of the failure modes and corresponding values for the two asymmetric square holes with $r_c = 2$ mm are given below in Table 6.18. It can be seen that damage initiates sooner for all failure modes and laminas with decreasing hole edge-to-edge distance. Again, this is due to the "hole-to-hole proximity effect". The amount of equivalent applied stress required to initiate damage for any given lamina decreases with decreasing hole edge-to-edge distance.

Table 6.18: Displacement step sequence of damage development for two asymmetric square holes with $r_c = 2$ mm.

Two Asymmetric Square Holes								
Hole Edge-to-Edge Distance, d_h (mm)	**Failure Mode/Lamina**	**Displacement Step**	**Substep**	**Applied Displacement, U_x (mm)**	**Strain, ϵ_x (mm/mm)**	**Equivalent Applied Remote Stress, σ_x (MPa)**	**Equivalent Applied Remote Force, F_x (N)**	**Time, T (sec)**
7.541 (Hole 2 Centered)	Matrix Tension, MT/±45°	2	24	0.196	0.00154	36.819	4275.7	1.96
	Matrix Tension, MT/90°	3	7	0.228	0.00180	42.830	4973.8	2.28
	Matrix Tension, MT/0°	4	6	0.324	0.00255	60.864	7068.0	3.24
3.770	Matrix Tension, MT/±45°	2	22	0.188	0.00148	35.316	4101.2	1.88
	Matrix Tension, MT/90°	3	4	0.216	0.00170	40.576	4712.0	2.16
	Matrix Tension, MT/0°	3	23	0.292	0.00230	54.853	6370.0	2.92
1.885	Matrix Tension, MT/±45°	2	17	0.168	0.00132	31.559	3664.9	1.68
	Matrix Tension, MT/90°	2	23	0.192	0.00151	36.067	4188.5	1.92
	Matrix Tension, MT/0°	3	19	0.276	0.00217	51.847	6020.9	2.76

The equivalent applied remote force, F_x, versus the applied displacement, U_x, data from Table 6.18 is shown below in Fig. 6.22.

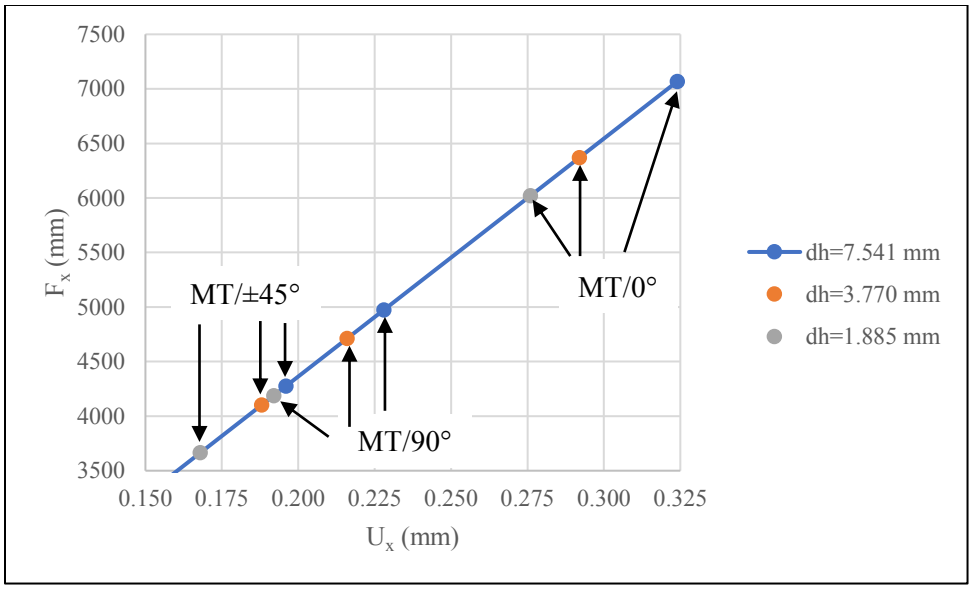

Figure 6.22: Equivalent applied remote force, F_x, versus applied displacement, U_x, for two asymmetric square holes with $r_c = 2$ mm.

To again illustrate the connection between stress concentration location and its effect upon damage initiation location, the σ_{22} stress field and the matrix tension damage variable, d_{mt}, at $T = 1.68$ seconds for the 45° lamina when $d_h = 1.885$ mm are shown below in Fig. 6.23a and 6.23b, respectively. Similarly, the σ_{22} stress field and the matrix tension damage variable, d_{mt}, at $T = 2.76$ seconds for the 0° lamina when $d_h = 1.885$ mm are also shown below in Fig. 6.23c and 6.23d, respectively. It can be seen that damage initiates in the general location of stress concentration, which is at point A for the 45° lamina, and points A and B for the 0° lamina.

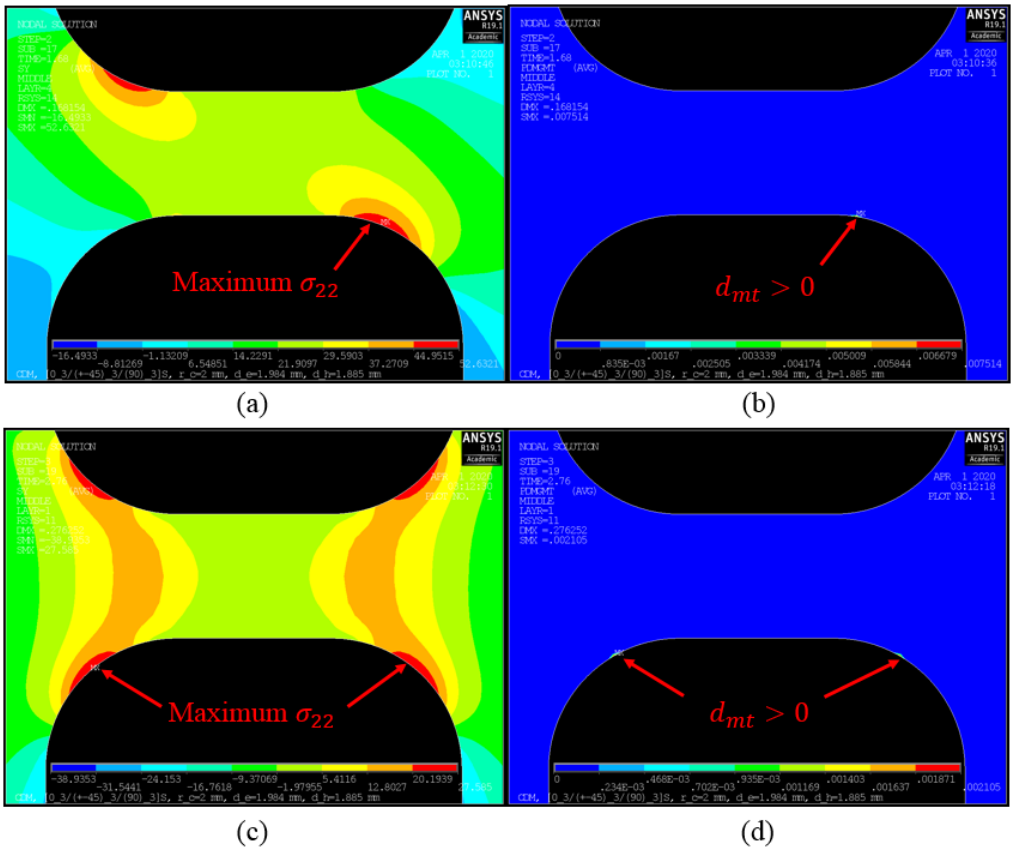

Figure 6.23: Two asymmetric square holes with $d_h = 1.885$ mm and $r_c = 2$ mm: (a) σ_{22} stress field depicting locations of stress concentration at $T = 1.68$ sec in the 45° lamina, (b) matrix tension damage variable, d_{mt}, depicting location of damage initiation at $T = 1.68$ sec in the 45° lamina, (c) σ_{22} stress field depicting locations of stress concentration at $T = 2.76$ sec in the 0° lamina, (d) matrix tension damage variable, d_{mt}, depicting location of damage initiation at $T = 2.76$ sec in the 0° lamina.

The magnitude of the matrix tension damage variable for the different laminas and values of d_h at the time of damage onset (see Table 6.18) and maximum displacement ($T = 4$ sec, $U_x = 0.40$ mm) are given below in Table 6.19. It can be seen that $d_{mt,max}$ increases with decreasing d_h for equivalent failure modes and laminas. This is due to the increased stress concentrations at the hole peripheries which arise from the "hole-to-hole proximity effect" and the "edge effect".

Table 6.19: Matrix damage variable at damage onset and maximum displacement for two axisymmetric square holes with $r_c = 2$ mm.

Two Asymmetric Square Holes			
Hole Edge-to-Edge Distance, d_h (mm)	**Failure Mode/Lamina**	**ANSYS Matrix Damage Variable, $d_{mt,onset}$**	**ANSYS Maximum Matrix Damage Variable, $d_{mt,max}$**
7.541 (Hole 2 Centered)	Matrix Tension, MT/±45°	0.0065	0.5539
	Matrix Tension, MT/90°	0.0080	0.4695
	Matrix Tension, MT/0°	0.0038	0.2205
3.770	Matrix Tension, MT/±45°	0.0117	0.5843
	Matrix Tension, MT/90°	0.0123	0.5060
	Matrix Tension, MT/0°	0.0005	0.3126
1.885	Matrix Tension, MT/±45°	0.0075	0.6370
	Matrix Tension, MT/90°	0.0107	0.5715
	Matrix Tension, MT/0°	0.0021	0.3674

6.6 Two Axisymmetric Square Holes Transverse to Applied Displacement

The damage initiation and evolution due to an incrementally applied displacement for two axisymmetric square holes with rounded corners is investigated in this section. The hole geometries and spacings are the same as that of Chapter 5, Section 5.2.1, except that only a corner radius of $r_c = 2$ mm is considered here.

6.6.1 Geometry and Displacement

The geometry and displacement configuration for the two axisymmetric square holes is shown below in Fig. 6.24. The hole edge-to-edge distance, d_h, is varied, while the hole height, h, and corner radius for both holes, r_c, are held constant at 6.35 mm and 2 mm, respectively. For all values of d_e and d_h, the centers of the holes are located at the mid-length of the laminate, at $x = L/2$. A through H are points of interest on the corners of the hole peripheries. One end of the laminate is fixed at $x = L$, and an incremental in-plane horizontal displacement, U_x, is applied uniformly along the width of the free end of the laminate ($x = 0$) from $y = 0$ to $y = W$.

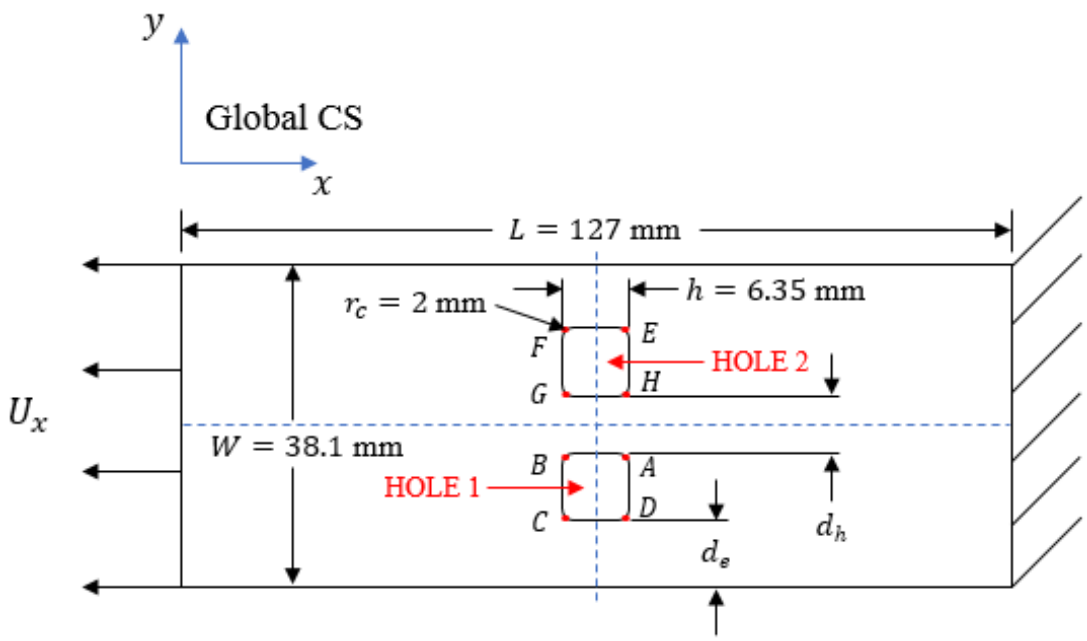

Figure 6.24: Geometry and displacement condition for two axisymmetric square holes with rounded corners.

The various cases for the spacing of the two axisymmetric square holes with rounded corners are given below in Table 6.20.

Table 6.20: Damage analysis cases for two axisymmetric square holes with $r_c = 2$ mm.

Case	Hole Edge-to-Edge Distance, d_h (mm)	Hole 1 Edge-to-Laminate Edge Distance, d_e (mm)	Square Hole Height, h (mm)
1	8.467 (Equidistant)	8.467 (Equidistant)	6.35
2	7.541	8.930	
3	3.770	10.815	
4	1.885	11.757	

For all cases of the two axisymmetric square holes, four displacement steps are used, each containing 25 substeps. This number of substeps was chosen such that an adequate amount of damage evolution could be shown, without severely hindering the computation time. The damage displacement parameters, which include the number of displacement steps, the number of substeps, and the applied external in-plane displacement increment are given below in Table 6.21.

Table 6.21: CDM displacement parameters and ANSYS runtime for two axisymmetric square holes with $r_c = 2$ mm.

Two Axisymmetric Square Holes					
Hole Edge-to-Edge Distance, d_h (mm)	**Displacement Step**	**# of Substeps**	**Applied Displacement, U_x (mm)**	**Displacement Step End Time, T (sec)**	**ANSYS Runtime**
8.467 (Equidistant)	1	25	0.10	1	11 min 22 sec
	2	25	0.20	2	
	3	25	0.30	3	
	4	25	0.40	4	
7.541	1	25	0.10	1	1 hr 15 min 20 sec
	2	25	0.20	2	
	3	25	0.30	3	
	4	25	0.40	4	
3.770	1	25	0.10	1	1 hr 35 min 36 sec
	2	25	0.20	2	
	3	25	0.30	3	
	4	25	0.40	4	
1.885	1	25	0.10	1	3 hr 45 min 54 sec
	2	25	0.20	2	
	3	25	0.30	3	
	4	25	0.40	4	

6.6.2 Meshing

The mesh used for CDM analysis is the same that was used for the stress analysis in Chapter 5, Section 5.2.2, Fig. 5.21. It is shown again for convenience below in Fig. 6.25.

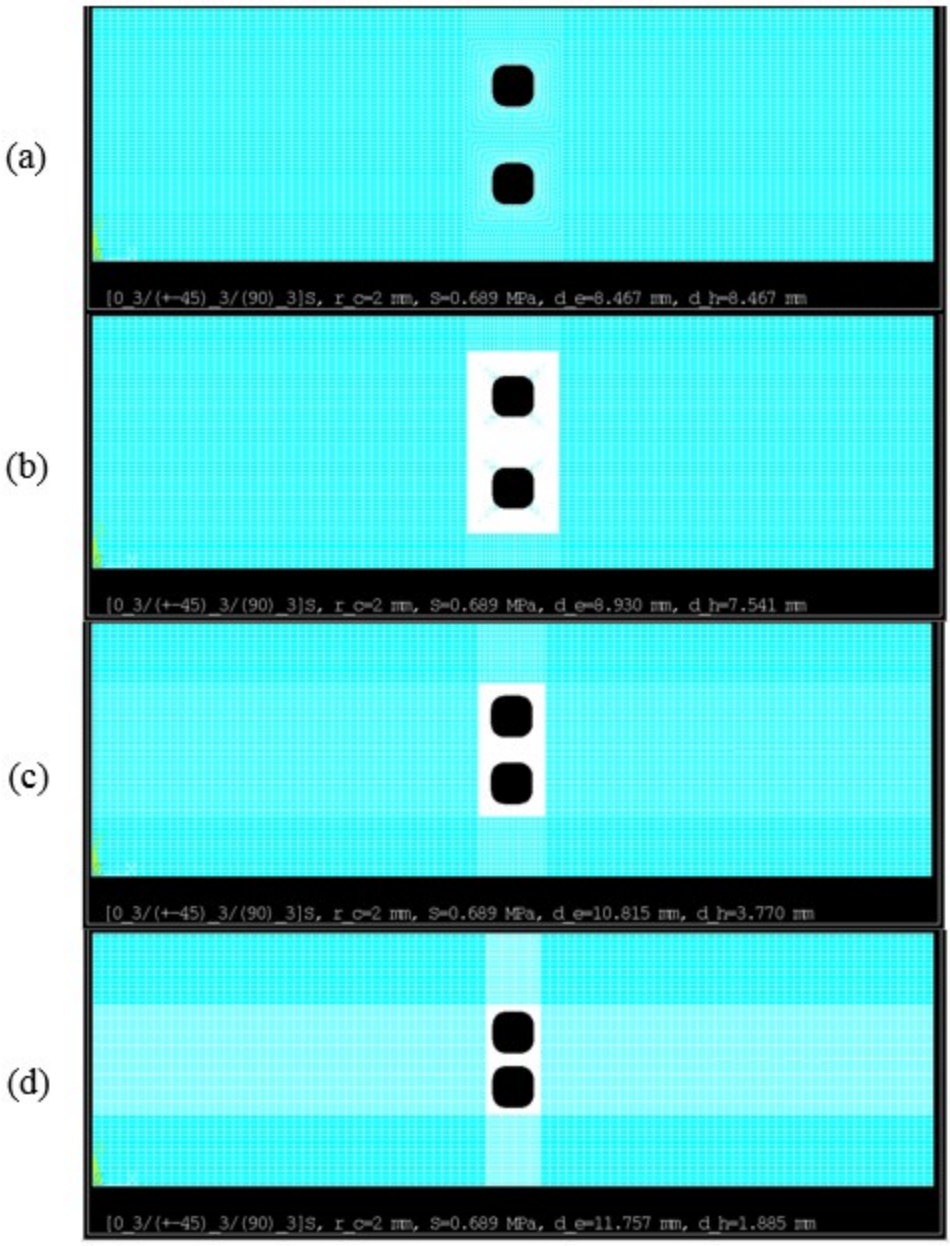

Figure 6.25: Mapped meshing for two axisymmetric square holes with $r_c = 2$ mm: (a) $d_h = 8.467$ mm (equidistant), (b) $d_h = 7.541$ mm, (c) $d_h = 3.770$ mm, (d) $d_h = 1.885$ mm.

6.6.3 Results

The failure indices which predict the initiation of damage in their respective laminas for the two axisymmetric square holes with $r_c = 2$ mm are given below in Table 6.22. It can be seen that the matrix fails in the same failure mode/lamina sequence that occurred in the two asymmetric square holes with $r_c = 2$ mm. As in Section 6.5.3, for all matrix failure modes, the

damage initiation time decreases with decreasing hole edge-to-edge distance. Again, this is expected, as the "hole-to-hole proximity effect" increases the maximum stresses found at the hole peripheries, thereby initiating damage sooner. It should be noted that for $d_h = 8.467$ mm, the failure index for matrix tension in the 0° lamina does not reach a value of unity, and therefore damage is not predicted to initiate. Only matrix failure modes are considered here.

Table 6.22: Hashin failure indices for matrix failure in tension for two axisymmetric square holes with $r_c = 2$ mm.

Two Axisymmetric Square Holes					
Hole Edge-to-Edge Distance, d_h (mm)	**Displacement Step**	**Substep**	**Failure Mode/Lamina**	**ANSYS Failure Index (Matrix Tension), I_{Fmt}**	**Time, T (sec)**
8.467 (Equidistant)	3	14	Matrix Tension, MT/±45°	1.0041	2.56
	3	21	Matrix Tension, MT/90°	1.0084	2.84
	4	25	Matrix Tension, MT/0°	0.9077	4.00
7.541	3	9	Matrix Tension, MT/±45°	1.0213	2.36
	3	15	Matrix Tension, MT/90°	1.0114	2.60
	4	14	Matrix Tension, MT/0°	1.0079	3.56
3.770	3	4	Matrix Tension, MT/±45°	1.0262	2.16
	3	10	Matrix Tension, MT/90°	1.0329	2.40
	4	6	Matrix Tension, MT/0°	1.0065	3.24
1.885	2	23	Matrix Tension, MT/±45°	1.0186	1.92
	3	4	Matrix Tension, MT/90°	1.0051	2.16
	4	3	Matrix Tension, MT/0°	1.0127	3.12

The matrix failure indices for the 0°, 45°, and 90° laminas for the various values of d_h can be seen below in Fig. 6.26. It can be seen that for decreasing hole edge-to-edge distance, the failure index fields intensify between the two square holes. As in Section 6.5.3, a comparison between the σ_{22} stress field and I_{Fmt} is made in Fig. 6.27. One finds in Fig. 6.27b that when $d_h = 1.885$ mm, the failure index for the 45° lamina reaches a value of $I_{Fmt} = 1.0186$ at the periphery of the hole, specifically at the locations of stress concentration as seen in Fig. 6.27a.

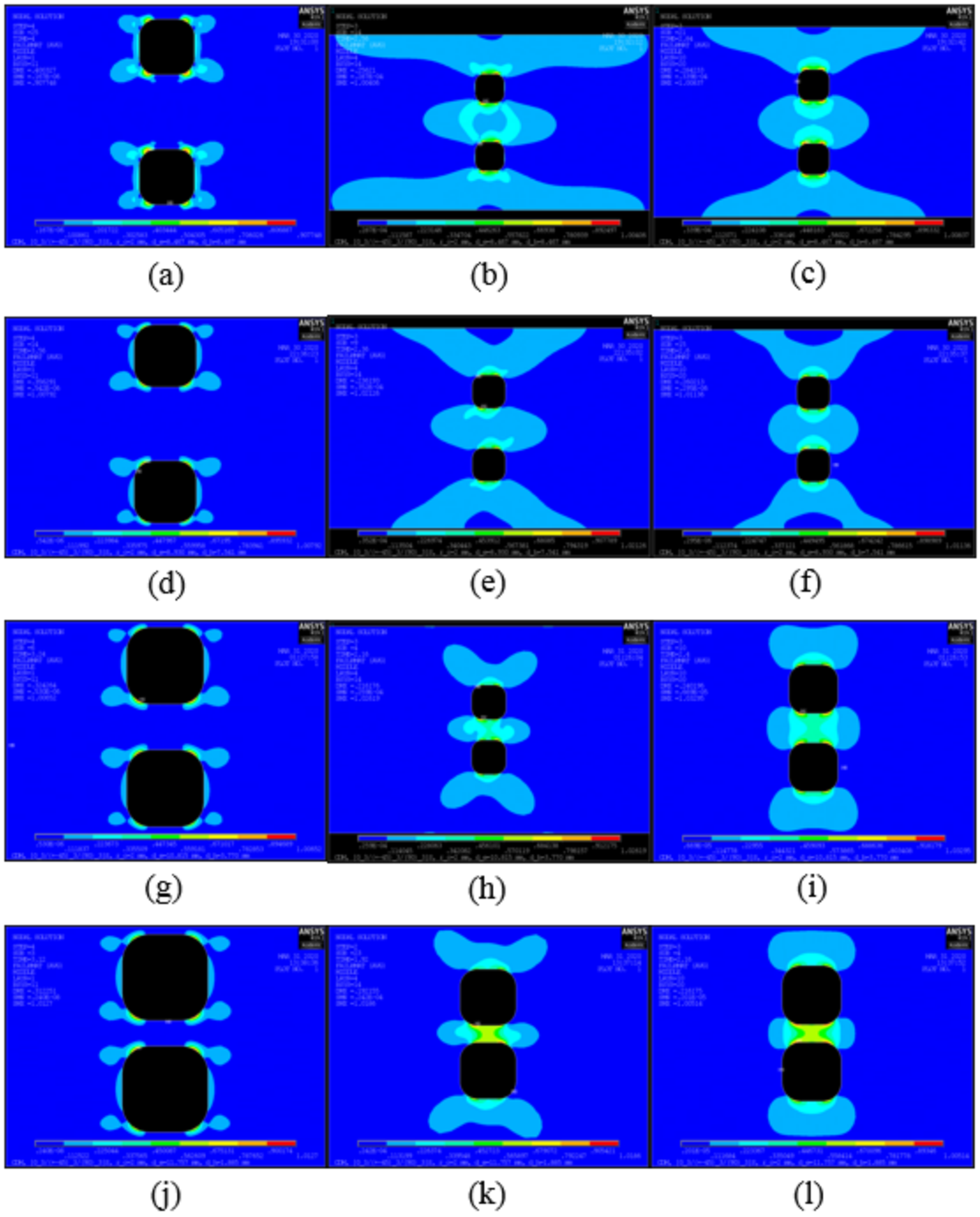

Figure 6.26: Matrix failure indices, I_{Fmt}, for two axisymmetric square holes with $r_c = 2$ mm: (a) 0° lamina, $d_h = 8.467$ mm (equidistant), (b) 45° lamina, $d_h = 8.467$ mm (equidistant), (c) 90° lamina, $d_h = 8.467$ mm (equidistant), (d) 0° lamina, $d_h = 7.541$ mm, (e) 45° lamina, $d_h = 7.541$ mm, (f) 90° lamina, $d_h = 7.541$ mm, (g) 0° lamina, $d_h = 3.770$ mm, (h) 45° lamina, $d_h = 3.770$ mm, (i) 90° lamina, $d_h = 3.770$ mm, j) 0° lamina, $d_h = 1.885$ mm, (k) 45° lamina, $d_h = 1.885$ mm, (l) 90° lamina, $d_h = 1.885$ mm.

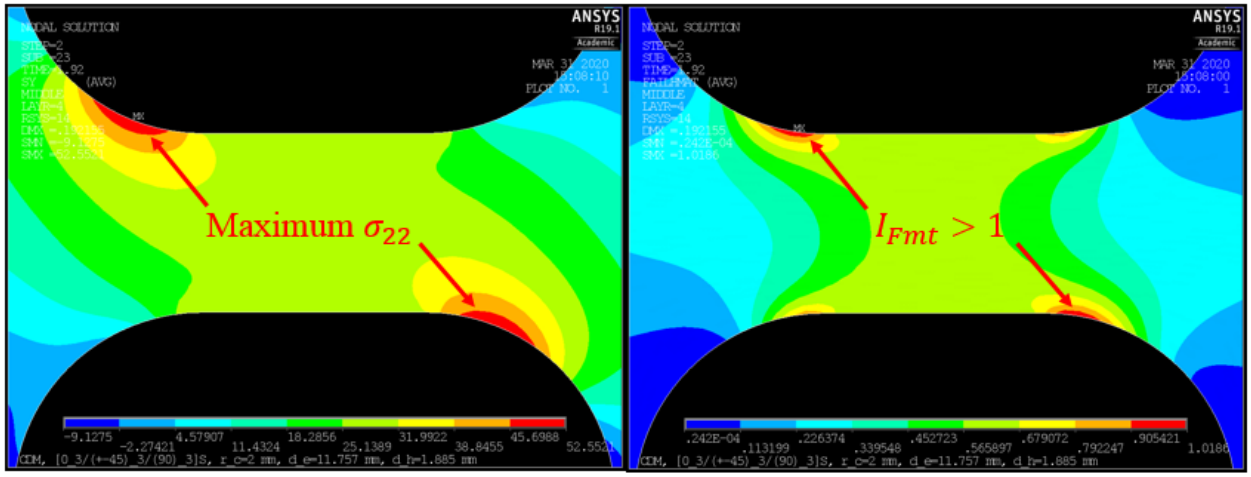

Figure 6.27: Location of maximum σ_{22} stress and matrix tension failure index, I_{Fmt}, in the 45° lamina for two axisymmetric square holes with $d_h = 1.885$ mm and $r_c = 2$ mm: (a) σ_{22} stress field at $I_{Fmt} = 1.0186$, (b) enlarged view of the matrix tensile failure index, $I_{Fmt} = 1.0186$.

The damage initiation analysis of the failure modes for the two axisymmetric square holes with $r_c = 2$ mm and corresponding values are given below in Table 6.23. As in Section 6.5.3, damage initiates sooner for all failure modes and laminas with decreasing hole edge-to-edge distance. The amount of equivalent applied stress required to initiate damage for any given lamina decreases with decreasing hole edge-to-edge distance. Also, damage due to matrix tension does not appear in the 0° lamina for $d_h = 8.467$ mm, as its failure index did not reach a value of unity in Table 6.22.

Table 6.23: Displacement step sequence of damage development for two axisymmetric square holes with $r_c = 2$ mm.

Two Axisymmetric Square Holes								
Hole Edge-to-Edge Distance, d_h (mm)	**Failure Mode/Lamina**	**Displacement Step**	**Substep**	**Applied Displacement, U_x (mm)**	**Strain, ϵ_x (mm/mm)**	**Equivalent Applied Remote Stress, σ_x (MPa)**	**Equivalent Applied Remote Force, F_x (N)**	**Time, T (sec)**
8.467 (Equidistant)	Matrix Tension, MT/±45°	3	22	0.288	0.00227	54.101	6282.7	2.88
	Matrix Tension, MT/90°	4	4	0.316	0.00249	59.361	6893.5	3.16
	Matrix Tension, MT/0°	N/A	N/A	N/A	N/A	N/A	N/A	N/A
7.541	Matrix Tension, MT/±45°	3	11	0.244	0.00192	45.836	5322.8	2.44
	Matrix Tension, MT/90°	3	17	0.268	0.00211	50.344	5846.4	2.68
	Matrix Tension, MT/0°	4	19	0.376	0.00296	70.632	8202.4	3.76
3.770	Matrix Tension, MT/±45°	3	5	0.220	0.00173	41.327	4799.3	2.20
	Matrix Tension, MT/90°	3	11	0.244	0.00192	45.836	5322.8	2.44
	Matrix Tension, MT/0°	4	9	0.336	0.00265	63.118	7329.8	3.36
1.885	Matrix Tension, MT/±45°	2	23	0.192	0.00151	36.067	4188.5	1.92
	Matrix Tension, MT/90°	3	5	0.220	0.00173	41.327	4799.3	2.20
	Matrix Tension, MT/0°	4	5	0.320	0.00252	60.112	6980.8	3.20

The equivalent applied remote force, F_x, versus the applied displacement, U_x, data from Table 6.23 is shown below in Fig. 6.28.

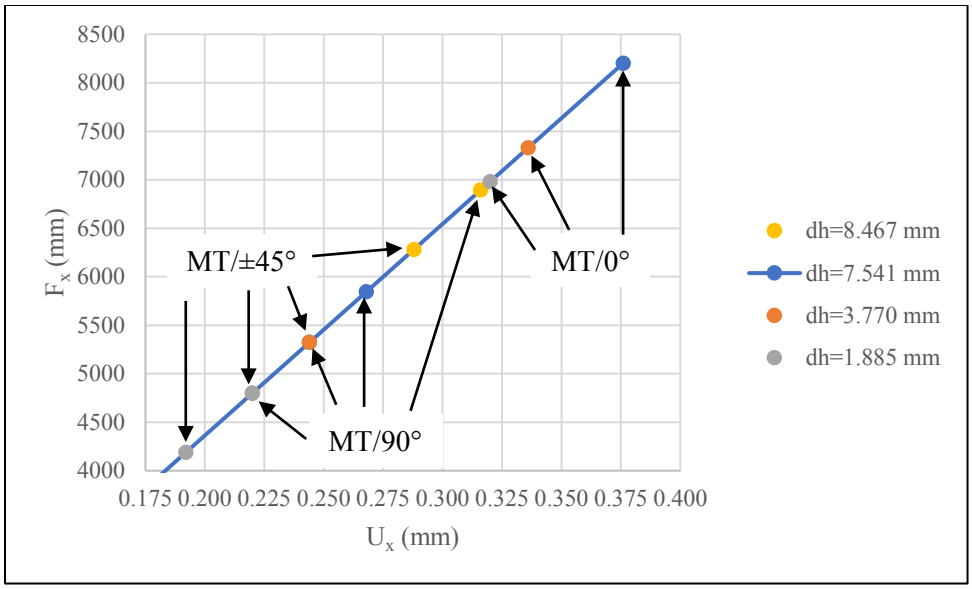

Figure 6.28: Equivalent applied remote force, F_x, versus applied displacement, U_x, for two axisymmetric square holes with $r_c = 2$ mm.

To again illustrate the connection between stress concentration location and its effect upon damage initiation location, the σ_{22} stress field and the matrix tension damage variable, d_{mt}, at $T = 1.92$ seconds for the 45° lamina when $d_h = 1.885$ mm are shown below in Fig. 6.29a and 6.29b, respectively. Similarly, the σ_{22} stress field and the matrix tension damage variable, d_{mt}, at $T = 3.20$ seconds for the 0° lamina when $d_h = 1.885$ mm are also shown below in Fig. 6.29c and 6.29d, respectively. It can be seen that damage initiates in the general location of stress concentration, which is at points A and G for the 45° lamina, and points A, B, G, and H for the 0° lamina.

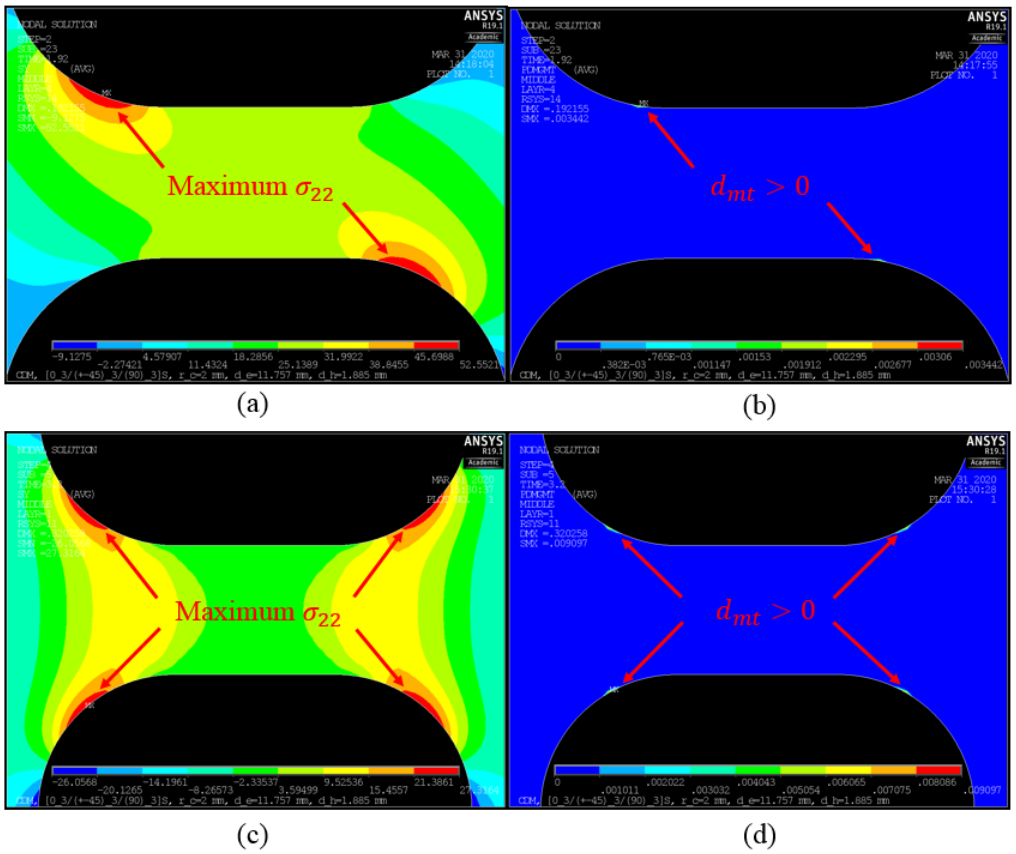

Figure 6.29: Two axisymmetric square holes with $d_h = 1.885$ mm and $r_c = 2$ mm: (a) σ_{22} stress field depicting locations of stress concentration at $T = 1.92$ sec in the 45° lamina, (b) matrix tension damage variable, d_{mt}, depicting location of damage initiation at $T = 1.92$ sec in the 45° lamina, (c) σ_{22} stress field depicting locations of stress concentration at $T = 3.20$ sec in the 0° lamina, (d) matrix tension damage variable, d_{mt}, depicting location of damage initiation at $T = 3.20$ sec in the 0° lamina.

The magnitude of the matrix tension damage variable for the different laminas and values of d_h at the time of damage onset (see Table 6.23) and maximum displacement ($T = 4$ sec, $U_x = 0.40$ mm) are given below in Table 6.24. It can be seen that $d_{mt,max}$ increases with decreasing d_h for equivalent failure modes and laminas. This is due to the increased stress concentrations at the hole peripheries which arise from the "hole-to-hole proximity effect".

Table 6.24: Matrix damage variable at damage onset and maximum displacement for two axisymmetric square holes with $r_c = 2$ mm.

Two Axisymmetric Square Holes			
Hole Edge-to-Edge Distance, d_h (mm)	**Failure Mode/Lamina**	**ANSYS Matrix Damage Variable, $d_{mt,onset}$**	**ANSYS Matrix Damage Variable, $d_{mt,max}$**
8.467 (Equidistant)	Matrix Tension, MT/±45°	0.0081	0.3227
	Matrix Tension, MT/90°	0.0035	0.2414
	Matrix Tension, MT/0°	N/A	N/A
7.541	Matrix Tension, MT/±45°	0.0057	0.4299
	Matrix Tension, MT/90°	0.0028	0.3566
	Matrix Tension, MT/0°	0.0036	0.0686
3.770	Matrix Tension, MT/±45°	0.0059	0.4958
	Matrix Tension, MT/90°	0.0103	0.4262
	Matrix Tension, MT/0°	0.0046	0.1852
1.885	Matrix Tension, MT/±45°	0.0034	0.5683
	Matrix Tension, MT/90°	0.0102	0.4921
	Matrix Tension, MT/0°	0.0091	0.2395

6.7 Conclusions

Damage initiation occurs at a lower load for the case of a single centered circular hole than it does for the single centered square hole with $r_c = 2$ mm. The mode of damage initiation is with matrix tension (MT) failure in the ±45° lamina. The "hole-to-hole proximity effect" gives rise to an increased amount of damage in two square hole configurations, which occurs at an earlier time than for the case of single holes.

Upon the presence of both the "hole-to-hole proximity effect" and the "edge effect" for the two asymmetric square holes with $r_c = 2$ mm, damage initiation begins earlier versus two axisymmetric square holes with $r_c = 2$ mm. Further, total damage occurs to a greater extent in the former. This would seem to indicate that the presence of the "edge effect" in the case of the two asymmetric square holes gives rise to an additional amount of damage, which begins sooner.

In general, damage initiates at the periphery of the hole (or holes) for all hole configurations, regardless of hole shape, hole-to-hole proximity, and hole edge-to-laminate edge distance. Further, damage initiation occurs in the neighborhood of the local stress concentration

areas, suggesting that damage initiation location is governed largely by maximum stress location within any particular lamina.

For equivalent failure modes and laminas, the maximum amount of damage in the first two matrix failure modes is only slightly greater for the single centered square hole with $r_c = 2$ mm than for the single centered circular hole. In general, the single centered square hole experiences only a minimal increase in the amount of damage for all failure modes and laminas. The percentage increase in the maximum amount of damage experienced for the various failure modes and laminas between the single centered square hole and the single centered circular hole is given below in Table 6.25.

Table 6.25: Matrix and fiber damage variable comparison between the single centered square hole with $r_c = 2$ mm and the single centered circular hole with $d = 6.35$ mm.

Failure Mode/Lamina	**Single Centered Square Hole**		**Single Centered Circular Hole**		$d_{mt,max}$ **% Increase**	$d_{ft,max}$ **% Increase**
	ANSYS Maximum Matrix Damage Variable, $d_{mt,max}$	**ANSYS Maximum Fiber Damage Variable,** $d_{ft,max}$	**ANSYS Maximum Matrix Damage Variable,** $d_{mt,max}$	**ANSYS Maximum Fiber Damage Variable,** $d_{ft,max}$		
Matrix Tension, MT/±45°	0.78976	N/A	0.78321	N/A	0.84	N/A
Matrix Tension, MT/90°	0.75358	N/A	0.74726	N/A	0.85	N/A
Matrix Tension, MT/0°	0.56973	N/A	0.51409	N/A	10.82	N/A
Fiber Tension, FT/0°	N/A	0.53284	N/A	0.50898	N/A	4.69
Fiber Tension, FT/±45°	N/A	0.20493	N/A	0.19791	N/A	3.55

For the case of two asymmetric holes with $d_h = 7.541$ mm (Hole 2 centered), the presence of Hole 1 at the laminate edge causes a 24.62% decrease in the load required to initiate damage due to matrix tension in the ±45° lamina, as compared to a single centered square hole with $r_c = 2$ mm. Similarly, there is a 21.65% decrease in the load required to initiate damage due to matrix tension in the 90° lamina, as compared to a single centered square hole with $r_c = 2$ mm.

For equivalent hole edge-to-edge distances, damage initiates sooner for two asymmetric square holes than for two axisymmetric square holes with $r_c = 2$ mm. This is due to contribution from secondary bending as well as the "edge effect", which serve to increase local stresses at the

hole periphery, thereby satisfying the Hashin failure criteria at a lower load. The percentage increase in the load required to initiate damage for the various failure modes and laminas between the two asymmetric square holes and the two axisymmetric holes is given below in Table 6.26.

Table 6.26: Damage initiation comparison between two asymmetric square holes and two axisymmetric square holes with $r_c = 2$ mm.

Hole Edge-to-Edge Distance, d_h (mm)	Failure Mode/Lamina	Two Asymmetric Square Holes		Two Axisymmetric Square Holes		F_x % Increase
		Displacement, U_x (mm)	Equivalent Applied Remote Force, F_x (N)	Displacement, U_x (mm)	Equivalent Applied Remote Force, F_x (N)	
7.541	Matrix Tension, MT/±45°	0.196	4275.7	0.244	5322.8	24.49
	Matrix Tension, MT/90°	0.228	4973.8	0.268	5846.4	17.54
	Matrix Tension, MT/0°	0.324	7068.0	0.376	8202.4	16.05
3.770	Matrix Tension, MT/±45°	0.188	4101.2	0.220	4799.3	17.02
	Matrix Tension, MT/90°	0.216	4712.0	0.244	5322.8	12.96
	Matrix Tension, MT/0°	0.292	6370.0	0.336	7329.8	15.07
1.885	Matrix Tension, MT/±45°	0.168	3664.9	0.192	4188.5	14.29
	Matrix Tension, MT/90°	0.192	4188.5	0.220	4799.3	14.58
	Matrix Tension, MT/0°	0.276	6020.9	0.320	6980.8	15.94

Similarly, for equivalent hole edge-to-edge distances, the maximum amount of damage is greater for two asymmetric square holes than for two axisymmetric square holes with $r_c = 2$ mm. This is due to contribution from secondary bending as well as the "edge effect", which serve to increase local stresses at the hole periphery. The percentage increase in the maximum amount of damage experienced for the various failure modes and laminas between the two asymmetric square holes and the two axisymmetric square holes is given below in Table 6.27.

Table 6.27: Matrix damage variable comparison between two asymmetric square holes and two axisymmetric square holes with $r_c = 2$ mm.

Hole Edge-to-Edge Distance, d_h (mm)	Failure Mode/Lamina	Two Asymmetric Square Holes		Two Axisymmetric Square Holes		$d_{mt,max}$ % Increase
		ANSYS Matrix Damage Variable, $d_{mt,onset}$	ANSYS Maximum Matrix Damage Variable, $d_{mt,max}$	ANSYS Matrix Damage Variable, $d_{mt,onset}$	ANSYS Maximum Matrix Damage Variable, $d_{mt,max}$	
7.541	Matrix Tension, MT/±45°	0.0065	0.5539	0.0057	0.4299	28.84
	Matrix Tension, MT/90°	0.0080	0.4695	0.0028	0.3566	31.66
	Matrix Tension, MT/0°	0.0038	0.2205	0.0036	0.0686	221.43
3.770	Matrix Tension, MT/±45°	0.0117	0.5843	0.0059	0.4958	17.85
	Matrix Tension, MT/90°	0.0123	0.5060	0.0103	0.4262	18.72
	Matrix Tension, MT/0°	0.0005	0.3126	0.0046	0.1852	68.79
1.885	Matrix Tension, MT/±45°	0.0075	0.6370	0.0034	0.5683	12.09
	Matrix Tension, MT/90°	0.0107	0.5715	0.0102	0.4921	16.13
	Matrix Tension, MT/0°	0.0021	0.3674	0.0091	0.2395	53.40

It is worth recognizing the large percentage increase between the two asymmetric square holes and the two axisymmetric square holes for the 0° lamina when $d_h = 7.541$ mm. Again, this is due to the additional presence of the "edge effect" in the two asymmetric square holes configuration. In general, there exists a decreasing percentage increase in the maximum amount of damage for decreasing hole edge-to-edge distance, d_h, for all matrix failure modes and laminas. This is due to the increase in stress concentration at the hole peripheries which arises from the "hole-to-hole proximity effect". This increase in stress concentration results in a greater amount of total damage at maximum displacement ($U_x = 0.40$ mm).

CHAPTER 7: CONCLUSIONS

The conclusion to the thesis is given, followed by recommendations for future work.

7.1 Conclusions

The primary research problem was to understand the effect of multiple holes upon stress concentrations within a quasi-isotropic composite laminate using finite element analysis (FEA). The effects of hole shape, corner radius size, hole edge-to-edge proximity, and hole edge-to-laminate edge proximity upon stress concentrations are taken into consideration.

The second research problem was to gain insight into the damage initiation caused by the stress concentrations due to multiple holes (also using the finite element analysis approach). Local damage initiation due to the "hole-to-hole proximity effect", hole shape, and the "edge effect" are explored.

The maximum σ_{11} stress in the laminate is always found in the 0° lamina for any given single or multiple hole configuration and corner radius, r_c. The largest SCF is always found in the ±45° lamina for any given single or multiple hole configuration and corner radius, owing to division by the lower value of the applied lamina stress found in the ±45° laminas with no hole.

For an offset hole, its distance from the central axis of the lamina or laminate creates an eccentricity of the applied tensile load, which induces secondary bending. This effect increases the magnitude of the maximum stresses in both circular holes and square holes, irrespective of corner radius size. The presence of the laminate edge gives rise to marked increases in maximum σ_{11} stress, most notably in the 0° lamina.

The location of the maximum σ_{11} stress in the 0° lamina is always found in the neighborhood of the rounded corners for any given single or multiple square hole configuration and corner radius.

Symmetry conditions are present in all fiber orientations for a single centered square hole with rounded corners for any given corner radius, which are reduced as the hole moves away from the central axis. Similarly, symmetry conditions are present in all fiber orientations for two

axisymmetric square holes with rounded corners for any given corner radius, which remain constant for all hole-to-hole spacings. Symmetry conditions are present in the 0° and 90° fiber orientations for two asymmetric square holes with rounded corners for any given corner radius, which remain constant for all hole spacings.

For the transition of the single square hole with rounded corners to a circular hole there is a decreasing-increasing behavior found in the maximum σ_{11} stress and consequent SCF for the 0° laminas and for the laminate, and thus a minimum value of corner radius exists for which there is a corresponding minimum $\sigma_{11,max}$ and SCF. This behavior is also found in both types of the two offset square hole configurations. Further, for all single and multiple hole configurations, corner radii exist which elicit a lower SCF than that of a circular hole of equivalent size.

In terms of damage initiation and evolution, hole-to-hole proximity governs the initiation time and extent of local damage for both the two asymmetric and two axisymmetric square hole configurations. Multiple square holes with rounded corners ($r_c = 2$ mm) which are within sufficient distance of one another give rise to premature damage initiation and accelerated damage evolution, as compared to a single square hole of equal geometry. The additional presence of the "edge effect" elicits an even greater amount of total damage, which initiates sooner than for hole configurations without its presence. In general, damage initiates at the periphery of the hole (or holes) for all hole configurations, regardless of hole shape, hole-to-hole proximity, and hole edge-to-laminate edge distance. Further, damage initiation occurs in the neighborhood of the local stress concentration areas, suggesting that damage initiation location is governed largely by maximum stress location within any particular lamina.

In terms of failure modes, the laminate fails in the ±45° lamina due to matrix tension, regardless of single or multiple hole configuration. For the single centered square hole and single centered circular hole, damage within the laminate always initiates with the same lamina/failure mode sequence, albeit at different displacements. In general, damage within the laminate initiates with the same lamina/failure mode sequence for all hole configurations.

The findings of this work indicate that the "hole-to-hole proximity effect" and the "edge effect" can have considerable influence upon maximum stress concentration, damage initiation, and damage evolution found within a quasi-isotropic laminate. The "stacking" of multiple effects can quickly increase the maximum stress found in the laminas and laminate, resulting in high stress magnification regions. These local regions of high stress concentration lead to premature

damage initiation, and result in a greater total amount of damage in the laminas, as compared to hole configurations which do not possess the same type, or severity of effects. For these reasons, it is critical that such phenomena be taken into consideration when designing components manufactured from such types of laminates.

In a general sense, knowledge of maximum σ_{11} stress locations based upon fiber and central axis symmetry relationships provide insight into the exact locations of laminate damage initiation. Local regions of intense stress field magnification are of primary concern to initial design efforts, an understanding of which provides a more accurate means of predicting laminate damage initiation, subsequent evolution, and ultimate laminate failure.

In terms of stress concentration, to mitigate the "hole-to-hole proximity effect", holes should be spaced such that they possess a hole edge-to-edge distance of $d_h > 3.770$ mm. Similarly, to mitigate the "edge effect", holes should have a hole edge-to-laminate edge distance of $d_e > 3.969$ mm.

With regard to damage initiation time and damage extent, to mitigate the "hole-to-hole proximity effect", holes should be spaced such that they possess a hole edge-to-edge distance of $d_h > 3.770$ mm. In general, the presence of multiple simultaneous effects such as the "edge effect" and the "hole-to-hole proximity effect" accelerates the damage initiation time and extent of total damage. Consequently, one should seek to avoid situations where multiple effects are present, as they work in tandem to greatly increase maximum stresses.

Ideally, holes would be spaced such that there is never concern for these effects, however design efforts may warrant tightly spaced holes or hole patterns, or closeness to a component edge/boundary. Additionally, machining errors may produce components with holes which are out of tolerance. When such occurrences become unavoidable, the above guidelines are a good general rule of thumb, however, one must bear in mind that no two manufactured laminates are perfectly identical. Micro-defects in composite manufacturing can produce local regions of fiber-rich or matrix-rich areas, or air voids (among other defects) which can lead to a difference in the stress behavior from specimen to specimen.

The SCF findings of this study can also be applied to any isotropic material, as the quasi-isotropic laminate behaves identically in-plane. However, these results can only be applied to another finite width plate of equivalent dimensions, and holes of equal dimension.

With further regard to design efforts, it is perfectly acceptable to place a hole, or holes, within some general proximity of an edge or to each other. The findings of this work should not dissuade the designer from such an occurrence. However, what remains critical is knowledge of the applied load to the component, as the SCFs will dictate the maximum stress realized within the component. Further, the inherent strength of the fiber, matrix, and laminate will ultimately govern the time of damage initiation and failure of the laminas, and laminate. When designing for failure, one should endeavor to minimize the stress or stresses that dictate the failure mode of interest. Since the low strength of the matrix is what gives rise to initial damage, one should either choose a matrix with a higher strength (if possible), or seek to minimize the σ_{22} and τ_{12} stresses.

7.2 Recommendations

The opportunity for much additional work exists in this particular area. The scope for this thesis was originally so large that a great deal was removed (much to the dismay of the author) due to time constraints. Multiaxial loading, both tensile (or compressive) and bending moment, have not been considered, nor were hygrothermal effects. Configurations beyond two holes were not considered, nor were additional layup sequences. Laminates which are not flat plates (i.e. possessing some degree of curvature) were also not investigated. Optimal hole relief patterns were not examined. Hole size effects were not explored, nor were other hole geometries. Also, stress distributions, maximum stress locations, and SCFs due to σ_{22} and τ_{12} stresses were not studied. Laminates of varying overall dimension were also not explored. All of these are topics to be recommended for future work.

REFERENCES

[1] T. Ngo, "Introduction to Composite Materials.", *Fiber Composites*, IntechOpen, 2020.

[2] T. Palucka and B. Bensaude-Vincent, "Composites: An Overview.", Cal Tech, n.d., Available: https://authors.library.caltech.edu/5456/1/hrst.mit.edu/hrs/materials/public/Composites/Composites_Overview.htm

[3] P. K. Mallick, *Fiber Reinforced Composites: Materials, Manufacturing, and Design*, 3rd ed., CRC, 2008.

[4] B. Esp, "Stress Distribution and Strength Prediction of Composite Laminate with Multiple Holes", Ph.D Dissertation, The University of Texas at Arlington, 2007.

[5] M. Kheradiya, "Effects of Edge Distance, Hole Size Ratio and Hole Spacing on Peak Stresses of Composite Laminate with Multiple Holes", Master's Thesis, The University of Texas at Arlington, 2008.

[6] W. D. Pilkey and D. F. Pilkey, *Peterson's Stress Concentration Factors*, 3rd ed., John Wiley & Sons, 2008.

[7] G. Kirsch, "Die Theorie Der Elastizitaet und Die Beduerfnisse Der Festigkeitslehre," ZVDI, 1898, mentioned by S. Timoshenko in *History of Strength of Materials*, McGraw-Hill Book Co., New York, 1953.

[8] W. C. Young, R. G. Budynas, and A. M. Sadegh, *Roark's Formulas for Stress and Strain*, 8th ed., McGraw Hill, New York, 2012.

[9] S. P. Timoshenko and J. N. Goodier, *Theory of Elasticity*, 2nd ed., McGraw-Hill, New York, 1951.

[10] R. I. Stephens, A. Fatemi, R. R. Stephens, and H. Fuchs, *Metal Fatigue in Engineering*, 2nd ed., John Wiley & Sons, 2001.

[11] Massachusetts Institute of Technology, Department of Mechanical Engineering, Laboratory Module No. 4 "Isotropic Linear Elastic Stress Concentration", 2.002 Mechanics and Materials II, Spring 2004.

[12] R. B. Heywood, *Designing by Photoelasticity*, London, Chapman and Hall, 1952.

[13] S. C. Tan, *Stress Concentrations in Laminated Composites*, 1st ed., Boca Raton FL: CRC Press, 1994.

[14] S. C. Tan, "Finite-Width Correction Factors for Anisotropic Plate Containing a Central Opening", *Journal of Composite Materials*, vol. 22, (November 1988b), pp. 1080-1097.

[15] C. Soutis, N. A. Fleck, and P. T. Curtis, "Hole-Hole Interaction in Carbon Fibre/Epoxy Laminates Under Uniaxial Compression", *Composites*, vol. 22**,** No. 1, (January 1991), pp. 31-38.

[16] S. G. Lekhnitskii, *Theory of Elasticity of an Anisotropic Body*, 1977, English translation, Moscow, Mir Publishers, 1981.

[17] R. E. Rowlands, I. M. Daniel, and J. B. Whiteside, "Geometric and Loading Effects on Strength of Composite Plates with Cutouts", eds. C. Berg, F. McGarry, and S. Elliott, ASTM STP546-EB *Composite Materials: Testing and Design (Third Conference)*. West Conshohocken, PA: ASTM International, 1974, pp. 361-375.

[18] T. D. Jong, "Stresses around Rectangular Holes in Orthotropic Plates", *Journal of Composite Materials*, vol. 15 (July 1981), p.311.

[19] C. P. Cannon, "Stress Concentrations around a Square Cutout in a Composite Plate", Master's Thesis, The University of Texas at Arlington, 2012.

[20] K. Bakhshandeh, I. Rajabi, and F. Rahimi, "Investigation of Stress Concentration Factor for Finite-Width Orthotropic Rectangular Plates with a Circular Opening Using Three-Dimensional Finite Element Model", *Journal of Mechanical Engineering*, vol. 54, 2008, p. 140-147.

[21] E. J. Barbero and M. Shahbazi, "Determination of Material Properties for ANSYS Progressive Damage Analysis of Laminated Composites", *Journal of Composite Structures*, vol. 176 (2017), p. 768-779.

[22] A. E. A. El-Sisi, H. M. El-Emam, H. A. Salim, and H. E. M. Sallam, "Efficient 3D Modeling of Damage in Composite Materials", *Journal of Composite Materials*, 2014.

[23] J. Varna, R. Joffe, N. V. Akshantala, and R. Talreja, "Damage in Composite Laminates with Off-Axis Plies", *Composites Science and Technology*, vol. 59, Issue 14, (November 1999), pp. 2139-2147.

[24] G. H. Staab, *Laminar Composites*, 2nd ed., Butterworth-Heinemann, 2016.

[25] M. K. Thompson and J. M. Thompson, *ANSYS Mechanical APDL for Finite Element Analysis*, Elsevier, 2017.

[26] ASTM A36 Steel Plate, MatWeb Material Property Data, Available: http://www.matweb.com/search/DataSheet.aspx?MatGUID=afc003f4fb40465fa3df05129f0e88e6 (accessed Sept. 9, 2019)

[27] E. J. Barbero, *Finite Element Analysis of Composite Materials Using ANSYS*®, 2nd ed., CRC, 2014.

[28] D. Mohr, "Damage of Fiber-Reinforced Composites", Lecture #13, ETH Zürich, Fall 2015.